Understanding the growth and convective instability of mushy layers, with application to young sea ice

Joseph Hitchen

Hertford College

University of Oxford

A thesis submitted for the degree of

Doctor of Philosophy

Trinity 2017

Acknowledgements

First and foremost, thanks need to go to my supervisor, Dr. Andrew Wells. It is safe to say that without his guidance, encouragement, and attention to detail, this journey would have turned out very differently. Within the group, thanks should also go to Jamie Parkinson for his helpful conversations and useful discussions, and to Kevin Thielen for his unhelpful conversations and useless distractions. Slightly further afield, Tomos David was a great housemate for two years and has shown me what a real academic-to-be looks like. I should also mention Dirk Notz, Chris MacMinn, and David Rees Jones for their comments on an early version of the paper that later became chapter 4. Finally, NERC are due thanks for their role in this adventure - without their (financial) support, none of this would have been possible.

However, it will be apparent to all who know me that physics has always been playing second fiddle to rowing. Everyone I've met through NCBC, OUWLRC, HCBC, and OURCs has a some small role in this experience and while there are far too many to name individually, it would be amiss not to mention a few people who stand out from the crowd: Eleanor Law, whose role in the last eights years is indescribable; Ian Maconnachie, for getting me into OURCs, and then onto two wheels; Stefany Wragg, for guiding me through the role of Captain of Coxes, and then through the writing process; Stuart Walter, travelling partner and *worst RowSab ever*; and Yosiane White, for all the joint crisis management.

Finally, thanks go to my parents, Phil & Leslie, for making me the person I am and giving me all the support that I need. When they first told my uncle I would be studying ice, Uncle John replied: "I don't see how you could possible do that for *three* years". After one of Phil's attempts to understand my research, he remarked: "Next time I see Uncle John, I will have to tell him three years isn't going to be enough".

Abstract

Sea ice is salt-water ice which forms at the poles when the oceans solidify, and it plays a vital role in polar climate and ecosystems. In particular, the salt fluxes from growing sea ice are a major contributor to the cold halocline in the Arctic, and to the Arctic and Southern Ocean circulations more generally. Sea ice is not a pure solid - it has a microstructure of solid ice crystals and concentrated brine, known as a mushy layer. Segregation occurring during solidification means that the colder interstitial fluid closer to the ice surface also has a larger salinity than the warmer, fresher, underlying ocean. This creates a tendency for convection which drives the observed salt fluxes from growing ice, and provides nutrients fluxes for algae within the sea ice.

This thesis aims to characterise the early growth and convective onset in sea ice through a broad investigation of the relevant parameters. The study makes use of the mushy layer equations which describe the transport of mass, energy, salinity, and momentum through a reactive, porous medium. Whilst motivated by sea ice, the results are presented generally, and may have implications for convection problems in Earth sciences and engineering. I investigate the dependence on the dimensionless parameters that characterise the system; with particular focus on the (dimensionless) liquidus gradient and the Biot number. The liquidus gradient describes the ratio of salinity to thermal scales, while the Biot number measures the rate of effective thermal conduction by the surface boundary. This is an aspect which has not previously been considered in growing mushy layers.

I identify two clear limiting regimes for growth. When salinity variations are relatively large compared to thermal variations the mushy layer has a high porosity. A second regime, referred to as the *Stefan regime*, features comparatively smaller salinity variation and substantial internal solidification, with high porosity confined to a narrow region at the mush base. Most sea ice systems straddle the transition between these regimes. Inefficient cooling, as modelled by the Biot number delays the mushy layer growth and slows internal solidification. Regions of high porosity play a key role in convective dynamics due to their high permeability, reducing the requirements for convective onset but also leading to localisation of convective flow near the base of sea ice. Imperfect conduction is also shown to delay convective onset in a pure porous medium, which has geophysical implications, including for carbon sequestration.

Contents

1 Introduction and Background **1**

1.1 Thesis Structure . . . 3
1.2 Background on Sea Ice . . . 4
1.2.1 Sea Ice Growth . . . 4
1.2.2 Binary Alloys . . . 6
1.2.3 Sea Ice Properties . . . 9
1.3 Solidification & Mushy Layers . . . 10
1.4 Convection Models . . . 14
1.4.1 Steady State Thermohaline Convection . . . 14
1.4.2 Boundary Condition Effects . . . 16
1.4.3 Two-Domain Convection . . . 20
1.4.4 Boundary Layer Convection . . . 21
1.4.5 Convection During Steady Mush Growth . . . 25
1.4.6 Time-Dependent Mushy Layer Convection . . . 28
1.5 Observations . . . 31
1.6 Summary and Openings . . . 31

2 Model **33**

2.1 Mushy Layer Equations . . . 34
2.1.1 Conservation of Mass . . . 35
2.1.2 Conservation of Energy . . . 36
2.1.3 Conservation of Solvents . . . 38
2.1.4 Conservation of Momentum . . . 39
2.1.5 Liquid Layer Limit . . . 41
2.2 Initial and Boundary Conditions . . . 42
2.2.1 Surface Conditions . . . 42
2.2.2 Interface Conditions . . . 46
2.3 Non-Dimensionalisation . . . 48
2.3.1 Considering the Concentration Ratio . . . 53
2.4 Thermohaline Coupling . . . 53
2.5 A Solution to the Thermal Diffusion Equation . . . 55
2.6 Summary . . . 57

3 Diffusive solidification **59**
3.1 Simplified Model with Low Solid Fraction 60
3.1.1 Method 60
3.1.2 Results 64
3.1.3 Summary and Discussion 72
3.2 Mush with Perfect Boundary Conduction 73
3.2.1 Method 73
3.2.2 Results 75
3.2.3 Summary and Discussion 88
3.3 Mush with Imperfect Boundary Conduction 89
3.3.1 Method 89
3.3.2 Results 92
3.3.3 Summary and Discussion 102
3.4 Discussion and Conclusions 103

4 Porous Boundary Convection **105**
4.1 Model 105
4.1.1 Dynamical Equations 106
4.1.2 Base-State Solution 108
4.2 Stability Analysis 108
4.2.1 Energy Stability Method 109
4.2.2 Linearised dynamics 112
4.3 Numerical Method 112
4.4 Results 113
4.4.1 High Biot Number Limit 116
4.4.2 Low Biot Number Limit 120
4.5 Conclusion 123

5 Mushy Layer Convection **127**
5.1 Linearised Perturbation Equations 128
5.2 Impact of the Liquidus Gradient on Stability 133
5.2.1 Comparison with Wettlaufer et al. (1997) 139
5.3 Understanding Convective Confinement 140
5.4 Effects of the Stefan number 142
5.5 Effects of Imperfect Boundary Conduction 145
5.5.1 Comparison with Notz and Worster (2008) 149
5.6 Summary and Conclusions 154

6 Discussion and Conclusions **159**
6.1 Summary of Key Results 161
6.1.1 Diffusive Growth of a Mushy Layer 161
6.1.2 Convection in a Deep Porous Layer 164
6.1.3 Convection in Growing Mushy Layers 166
6.1.4 Overall Summary 168
6.2 Implications 169
6.3 Suggestions for Future Work 170

Appendices

A Nomenclature **175**
A.1 Modifiers 175
A.2 Physical Quantities 175
A.3 Coordinates, Physical Lengths and Physical Times 176
A.4 Profiles and Reference Values 177
A.5 Dimensionless Quantities and Characteristic Lengths 178
A.6 Miscellaneous 179

Bibliography **181**

1

Introduction and Background

Sea ice is found in both the Arctic and Southern Oceans where the extremely cold temperatures every winter lead to the surface of the ocean freezing over. It is distinct from icebergs, which are formed as fresh water ice in a glacier or ice shelf, and subsequently break off into the ocean. It is also different to fresh water ice which forms when lakes or other fresh water bodies freeze, due to the high salt concentration of sea water which dramatically changes the solidification dynamics (Worster, 2000). The goal of this thesis is to understand aspects of how the salinity of sea ice affects its growth, development and structure, and how these evolve over time.

In the polar winter, recent observations show that sea ice cover can reach as much as 15.7 million square kilometres in the Arctic and 18.8 million square kilometres in the Antarctic, but in the summer it can be as little as 4.3 and 3.6 million square kilometres respectively (Comiso, 2010). This means that every year, more than 25 million square kilometres of sea ice forms and melts, and with the summer minimum decreasing at a faster rate than the winter maximum, this figure is increasing. Recent years have seen sharp declines in both Arctic and Antarctic summer ice cover due to global temperature rises and some authors are predicting that summer ice may disappear completely in the near future (Haas et al., 2008; Overland and Wang, 2013).

In the first year of ice growth, Antarctic ice reaches a depth of $0.5 - 0.6$m but Arctic ice grows to an average of 1.3m (Haas et al., 2008). The ice partially melts in the polar summers, but some remains after the summer as multi-year ice and continues

to grow in successive winters. In the 1980s, the average depth of multi-year ice was 3.64m but there has been a gradual decline in depth due to climate change and the current average is 1.89m (Kwok and Rothrock, 2009).

The same set of physical processes affecting ice growth can be found at both poles, but their relative importance and effect on the regional ice cover differs. The Antarctic sea ice extends from 75^oS to 55^oS; it has a reduced thickness and a larger variability in ice extent when compared to Arctic ice (Dieckmann and Hellmer, 2010). Winds blowing away from the Antarctic continent move ice forming near the coast towards warmer latitudes where ice growth is slower. However this allows for more ice growth in the open water left behind as *polynyas* (Morales Maqueda et al., 2004). In the Arctic basin, there are no obstructions to the ice all the way up to 90^oN and there is a smaller oceanic heat flux than in the Southern Ocean (Martinson, 1990), leading to almost three times as much multi-year ice in the Arctic and thicker single year ice (Dieckmann and Hellmer, 2010).

While sea ice is primarily found in the polar regions, it has an impact far beyond its physical extent. Brine rejected by growing ice into a cold, less-saline layer leads to convective instability which creates a cold, salty mixed layer. Fresh water released when the ice melts then contributes to a sharp salinity gradient near the top of the ocean known as the *cold halocline layer* and prevents mixing between the intermediate and surface layers of the Arctic ocean (Brandon et al., 2010). Another impact is the formation of Arctic deep water by ice growth over shallow continental shelves. Brine rejection from growing ice generates dense water masses on these shelves which flows down the continental shelf, entraining water from intermediate layers as they go, and eventually penetrating to the bottom of the ocean to form the Arctic deep water (Jones et al., 1995). This process is also important in the Southern Ocean where it contributes to the formation of Antarctic Bottom Water, with sea ice melt also being a major factor in the transformation of Circumpolar Deep Water to Antarctic Intermediate Water (Abernathey et al., 2016).

Sea ice can affect interactions between the ocean and atmosphere, the most well known mechanism being the ice-albedo feedback, resulting from the differing albedos of ice and open water (Budyko, 1969; Ebert and Curry, 1993). In this process, increased ice cover results in more reflected solar radiation, lower temperatures and further ice growth. Conversely, decreased ice cover results in more solar radiation being absorbed by the ocean, which warms and promotes further ice melting. The

presence of melt ponds on the surface of the ice can complicate this picture by increasing the absorption of solar energy in an otherwise ice-covered area (Taylor and Feltham, 2004). Many other interactions moderated by sea ice are biogeochemical in nature and this role of sea ice is reviewed in Vancoppenolle et al. (2013). One example of these processes is the strong link between melting first-year ice in spring and bromination events in the atmosphere, which then impact on levels of tropospheric ozone (Lieb-Lappen and Obbard, 2015), although the mechanisms involved are not yet fully understood. Sea ice also provides a vital habitat in both the Arctic and Antarctic for numerous different species, ranging from algae living within the ice (Krembs et al., 2001), to the iconic polar bear in the Arctic and multiple species of penguin in Antarctic (Tynan et al., 2010), with a whole ecosystem in-between (Bluhm et al., 2010).

1.1 Thesis Structure

There have been various investigations into the convective desalination of sea ice (see Worster and Rees Jones, 2015, for a summary) but the onset of convection in time-dependent growth remains an unstudied field. In this thesis, I aim to form a simple model of growing sea ice and to determine its stability properties to build insight into the dominant physical mechanisms.

The remainder of this chapter begins by providing some background information into sea ice growth processes, the behaviour of binary alloys, and the physical properties of sea ice. I then review the relevant literature for the solidification of binary alloys (§1.3) and convective processes (§1.4), including convection in mushy layers growing at a steady rate (§1.4.5) and in those grown from a suddenly cooled boundary (§1.4.6). There is a brief review of some relevant experimental studies and field observations not covered by the previous two sections in §1.5. The dynamical equations for mushy layers are discussed in chapter 2, as well as the boundary conditions and non-dimensionalisation used throughout the remainder of the thesis. Chapter 3 considers the development of mushy layers before convective onset, with a particular focus on the rate of ice growth, the amount of solidification which occurs, and how these respond to the efficiency of atmospheric cooling. In chapter 4, I investigate the effects of imperfect boundary conductivity on convective onset in a uniform, infinitely deep porous medium. This builds fundamental insight into the convective process, which is used to understand the more complex convective instability in growing mushy layers in chapter 5. Finally, the key findings of the study are summarised in chapter 6 and potential directions for future investigation are suggested.

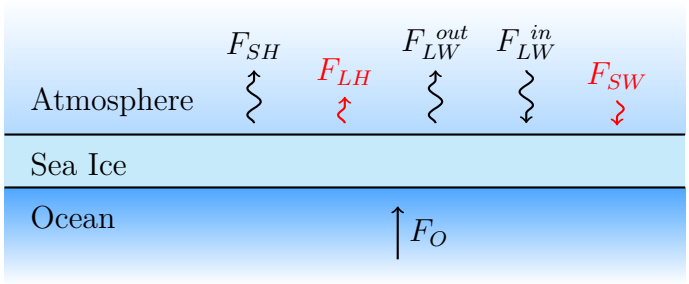

Figure 1.1: Thermal forcing on growing sea ice. The heat flux from the ocean F_O includes both advective and diffusive fluxes while the atmospheric fluxes are: F_{LW}, incoming and outgoing longwave radiation; F_{SW}, net incoming shortwave radiation (noting that some is reflected); F_{SH}, outgoing sensible heat; F_{LH}, outgoing latent heat. Forcings in red are generally negligible during the polar winters with the main thermal balance between those in black and ice growth. For young sea ice, sensible heat losses are the dominant form of thermal transport, while thicker ice loses more heat through longwave fluxes (Maykut and Untersteiner, 1971).

1.2 Background on Sea Ice

1.2.1 Sea Ice Growth

The growth of sea ice is governed by both dynamic and thermodynamic processes. The thermodynamic processes control the formation of the ice itself while the dynamic process are important when looking at large scale ice motion, mechanical deformation, and the effects of gaps in the ice such as *leads* and *polynyas* (Petrich and Eicken, 2010).

In the polar winters, thermodynamic processes cool the ocean's surface (see figure 1.1). Incoming solar radiation is minimal at high latitudes in winter but longwave thermal radiation is very important with outgoing radiation from the ice being balanced in part by incoming radiation from the clouds and atmosphere (Maykut and Untersteiner, 1971). There are also energy fluxes due to the loss of sensible heat (through atmospheric convection) and latent heat (through evaporation).

This cooling leads to the formation of small ice crystals known as *frazil ice* which clump together to form thin layers of *grease ice* (Petrich and Eicken, 2010). As further heat is removed, the grease ice thickens into *pack ice* (Arrigo et al., 2010). However, the ice is not a pure solid - it is a porous medium with both solid ice crystals and liquid brine phases in local thermodynamic equilibrium known as a *mushy layer* (Feltham et al., 2006). The properties of mushy layers are described in

more detail in §1.3 and §2.

While the ice is growing, the interstitial fluid nearer the surface is colder and saltier (due to the rejection of salt by the growing solid matrix) than fluid nearer the underlying ocean. Movement of the liquid phase can therefore lead to a net transport of salt downwards, desalinating the ice. Fluid motion within the ice can be caused by volume expansion upon freezing (Chiareli et al., 1994), or forced by pressure changes due to shear flow in the ocean (Feltham et al., 2002; Neufeld and Wettlaufer, 2008) but the primary mechanism is convective overturning (Notz and Worster, 2009). An unstable density gradient is formed within the ice since the cold, salty interstitial brine near the surface is denser than the warmer, fresher brine below. When disturbed, this density gradient leads to a convective instability and once the overturning is established, warmer, fresher ocean water entering the ice will be cooled and partially solidify, increasing the salinity of the remaining brine before it is advected back into the ocean. Since the proportion of fresh water retained is greater than the proportion of salt retained, the growing sea ice is desalinated (Petrich and Eicken, 2010).

Once the pack has formed, dynamical process such as ocean currents and wind stresses, cause movement and deformation of the ice. Dynamical processes that continually move ice away from a certain area create ice-free regions known as *polynyas* (Tynan et al., 2010; Morales Maqueda et al., 2004). These can be created either by winds blowing off a coastline (latent heat polynyas) or by ocean upwelling in deeper water (sensible heat polynyas). Latent heat polynyas are important because they provide a constant source of newly forming ice which migrates and increases the total ice extent. Ice movement also creates *leads*, which are gaps in the ice created by divergent motion of the pack (Weeks, 2010). Leads differ from polynyas since they are typically short lived, while a polynya will often be present throughout the winter. The open water in latent heat polynyas and leads has a large temperature difference with the atmosphere, driving rapid solidification and brine rejection (Weeks, 2010), while the ice free periods (including those from sensible heat polynyas) provide breathing holes for marine mammals and are a vital part of the polar ecosystem (Dieckmann and Hellmer, 2010).

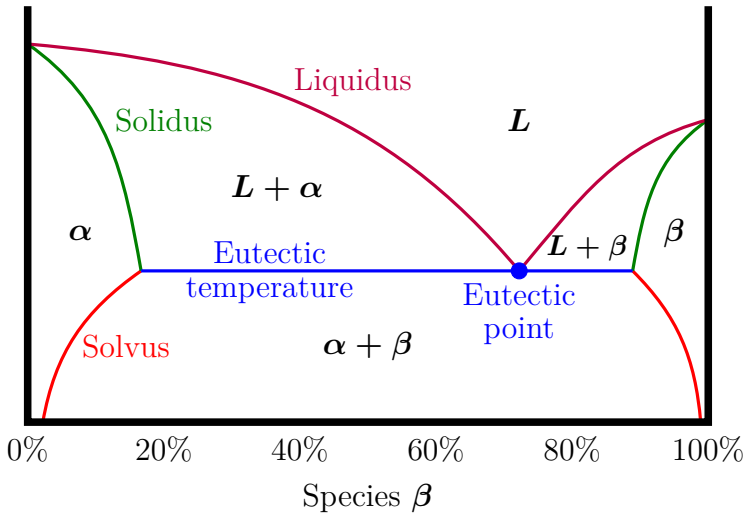

Figure 1.2: Schematic phase diagram for a binary alloy with solid components α and β, where L represents a liquid solution of the two. The liquidus curve (purple) is the line below which solid will start to form and the solidus curve (green) is the line below which liquid is unable to exist. The minimum of the liquidus curve is known as the *eutectic point* (blue), the concentration at which it occurs is the *eutectic concentration* and the temperature is the *eutectic temperature*. This diagram follows Stefanescu (2002).

1.2.2 Binary Alloys

Sea ice is grown from sea water, which is a chemical mixture which contains multiple chemical species that affect the freezing temperature, and is known as a *multicomponent alloy*. In the simplest case, a multicomponent alloy has just two chemical components and is known as a *binary alloy* (Worster, 2000). For example, a solution of sodium chloride in water is a binary alloy. Rather than having a simple freezing point, a binary alloy has a pair of temperatures called the *liquidus* and *solidus* which depend on the composition of the alloy, as shown in figure 1.2. The liquidus is the temperature to which a liquid mixture of the two components can be cooled before one component starts to solidify. Likewise, the solidus is the temperature to which a solid mixture can be heated before it will start to melt. Chemical systems with these properties are also known as *eutectic systems*, with the minimum of the liquidus curve known as the *eutectic point*.

Materials in a phase-change equilibrium exist in a state where the rate of molecules attaching and detaching from the lattice is equal. The lattice will be formed primarily of the more abundant *major species*, with inclusions of the less abundant *minor species* (for example, water is the major species for sea ice and salts are the minor species). The presence of a minor species in the liquid near the interface

reduces the rate of attachment by preventing molecules of the major species from colliding with the lattice, but leaves the rate of detachment unchanged. To maintain the equilibrium, the system must be cooled to reduce the energy of liquid molecules when they collide with the lattice and increase their probability of attaching. Since the lattice mainly contains the major species, growing the solid preferentially removes more of the major species and therefore increases the concentration of the minor component in the remaining the liquid. This increases the blocking effect caused by the presence of the minor species and prevents further lattice growth until the system has been cooled enough to overcome the increased blocking, which manifests itself as increased concentration decreasing the liquidus temperature. Further details on this process can be found in Alexander et al. (2005).

Minor species molecules in the lattice are more weakly bound than major species molecules because they disrupt the regular crystalline structure. Individual molecules will therefore be less likely to attach to the lattice whilst also being more likely to detach. To maintain an equilibrium between the total rates of attachment and detachment for the minor species, the concentration of minor species molecules in the fluid needs to be higher than in the lattice. This will increase the number of collisions between the lattice and minor species molecules in the fluid and therefore increase the total rate of attachment so that it balances the relatively high rate of detachment. For any given temperature, this manifests itself in a solidus concentration which is lower than the liquidus concentration, as seen in figure 1.2. Alexander et al. (2005) also contains more information about this process.

When a binary alloy is cooled to below the liquidus temperature for its initial concentration, the solid and liquid phases will exist in equilibrium with the system neither fully liquid nor fully solidified until the eutectic temperature is reached. The solid phase will exist at the solidus concentration, while the remaining liquid will have an increased concentration as dictated by the liquidus curve. The relative abundance of the two phases can be determined by applying conservation laws to the two components.

A good example of a binary alloy is a simple mixture of water and sodium chloride which has a eutectic temperature of -21.1^oC at a eutectic salinity of 233psu, and in the first instance, sea water can be well approximated by this combination. The liquidus temperature of a $NaCl - H_2O$ mixture is approximated by:

$$T_L{}^{Salt\ Water} = -5.92 \times 10^{-2}\hat{S} - 9.37 \times 10^{-6}\hat{S}^2 - 5.33 \times 10^{-7}\hat{S}^3,$$

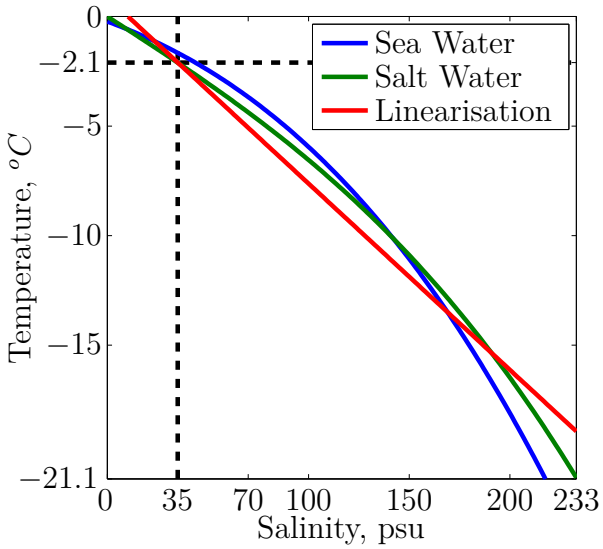

Figure 1.3: The liquidus temperature of sea water (blue) lies very close to the liquidus temperature of a $NaCl - H_2O$ binary alloy (green) when the temperature is above -21.1^oC, which is the eutectic temperature for salt water. In this study, we will use a linear approximation to the full liquidus curve which is given by (1.2.1) and shown in red, with the reference values indicated with dashed lines. (Data from Assur, 1960, and Lide, 2005, via Notz, 2005.)

---

as calculated by Notz (2005) using data from Lide (2005). Here, T_L is the liquidus temperature (measured in ^oC) and $\hat{S}$ is the salinity (measured in psu).

However, the presence of other ions such as ${SO_4}^{2-}$ and Mg^{2+} (Assur, 1960), means that the liquidus temperature for sea water differs from a $NaCl - H_2O$ mixture, and is given by:

$$T_L{}^{Sea\ Water} = -0.226 - 3.35 \times 10^{-2}\hat{S} - 1.94 \times 10^{-4}\hat{S}^2 - 4.24 \times 10^{-7}\hat{S}^3,$$

using data from Assur (1960) presented in Notz (2005). This curve is plotted in figure 1.3 for comparison to the liquidus temperature for simple salt water. The effect of these additional ions is also noticeable when the $NaCl - H_2O$ eutectic is reached because their presence disrupts the formation of $NaCl - 2H_2O$ crystals via the mechanisms described above for a two-component system. As a result, sea water will remain partially liquid well below the $NaCl - H_2O$ eutectic, and the true eutectic of sea water lies below -46^oC (Assur, 1960).

These non-linear relationships are not very amenable to manipulation so in this study, we will use a linearisation yielding a liquidus temperature in the form:

$$T_L = T_{L\infty} - \Gamma\left(\hat{S} - \hat{S}_\infty\right), \tag{1.2.1}$$

with a representative ocean salinity of $\hat{S}_\infty = 35$psu and a corresponding sea water liquidus temperature of $T_{L\infty} = -2.1^oC$. The liquidus gradient used is $\Gamma = 0.085^oC/$psu. This linearisation has a root-mean-square error (RMSE) of 23.4% between 35psu and 233psu when compared to the sea water liquidus curve, and a maximum error of 39.3% at 59psu. A visual comparison is provided in figure 1.3. Since we trying to gain broad understanding of the dynamics of sea ice growth rather than trying to faithfully recreate the minutiae of a specific observation, this error will be acceptable for our purposes.

For both sea water and salt water, there is almost no ion content in the solid phase (Petrich and Eicken, 2010), and the solidus concentration can be considered zero for any temperature.

1.2.3 Sea Ice Properties

Sea ice properties depend on the material properties of both the pure ice and liquid brine, which I will discuss here. Unless otherwise referenced, data in this section has been taken from Chapter 2 of *Sea Ice* written by Petrich & Eicken and edited by Thomas & Dieckmann (Petrich and Eicken, 2010).

The liquid filled pores in the solid matrix are typically spaced at $0.3 - 0.5$mm intervals, with the pores themselves on a similar scale. Flow through the porous medium is governed by a permeability function $\hat{\Pi}(\chi)$ which relates the permeability, $\hat{\Pi}$, to the liquid fraction, χ. Field measurements and theory provide some support for a permeability function of the form $\hat{\Pi}_0\chi^3$, where the reference permeability is $\hat{\Pi}_0 = 2 \times 10^{-8}\text{m}^2$, (Freitag, 1999). This model is widely used but I will also discuss alternatives in §2.1.4. It is thought that flow through the ice is restricted to regions with a porosity greater than 0.05 and below this threshold the pores would be too disconnected to allow efficient fluid motion (Golden et al., 2007).

The density of pure ice is $\rho_s = 917\text{kgm}^{-3} - 0.1403T$, where T is the temperature in ^oC. The density of brine, ρ_l, below zero degrees Celsius is a non-linear function of temperature and salinity, $\hat{S}$, although is well approximated by:

$$\rho_l = \rho_0 \left[1 - \alpha T + \beta \hat{S}\right] \tag{1.2.2}$$

with reference density $\rho_0 = 1000.3\text{kgm}^{-3}$ (Notz, 2005), thermal expansivity $\alpha = 3.87 \times 10^{-5}\text{K}^{-1}$, and saline contractivity $\beta = 7.86 \times 10^{-4}\text{psu}^{-1}$ (Jenkins, 2011). Notz

(2005) notes that the temperature variation (which he neglects) has less than a 2% impact on the density between 0^oC and -20^oC. He also provides a second order correction to the salinity contribution, $2.8008 \times 10^{-4}\hat{S}^2$, which has a maximum impact of 1.3% at 233psu.

As reported in Notz (2005), the thermal conductivity of brine is approximated by $k_l = (0.523 + 0.013T)\mathrm{Wm^{-1}K^{-1}}$, with T in ^oC, and decreases by 50% between 0^oC and -20^oC. Ice has a higher thermal conductivity of $k_s = (2.21 - 0.01T)\mathrm{Wm^{-1}K^{-1}}$ and shows a much smaller change over the same temperature range. The experimentally determined specific heat capacity of brine below 0^oC is given by $c_{pl} = (4217.2 - 3.4T)\mathrm{Jkg^{-1}K^{-1}}$ while the heat capacity of ice is $c_{ps} = (2112.2 + 7.7T)\mathrm{Jkg^{-1}K^{-1}}$. Some of these formulae have been truncated after the second term, with further terms given in the original source. The latent heat of fusion for ice is $L = 333.4\mathrm{kJkg^{-1}}$ (Petrich and Eicken, 2010).

All of the properties discussed here take different values in the solid and liquid phases and some vary with temperature. Since our aim is to determine the key dynamical mechanisms that control ice growth and convection, we will ignore these discrepancies and assume that the physical properties of the sea ice are independent of phase, temperature, and salinity, except in buoyancy terms where density variations are necessary to drive convection. This follows the spirit of the Boussinesq approximation. It removes a number of non-linearities in the dynamical equations discussed in chapter 2 and is a reasonable first order approximation since there are no order-of-magnitude variations.

We will use values similar to the liquid values in subsequent calculations which are: the reference density, $\rho_0 = 1000\mathrm{kgm^{-3}}$; thermal conductivity, $k = 0.5\mathrm{Wm^{-1}K^{-1}}$; and specific heat capacity $c_p = 4000\mathrm{Jkg^{-1}K^{-1}}$. Other values are unaffected. These reference values combine to give a thermal diffusivity of $\kappa = k/c_p\rho_0 = 1.3 \times 10^{-7}\mathrm{m^2s^{-1}}$. The diffusivity of salt in water is $D = 6.8 \times 10^{-10}\mathrm{m^2s^{-1}}$ and the ratio of the two is given by the Lewis number, $\mathcal{L}_e = \kappa/D = 190$.

1.3 Solidification & Mushy Layers

In 1891, Josef Stefan published a thermodynamic model for the thickness of polar ice as a function of time (Stefan, 1891). This model and related solidification problems

have become known as *Stefan* problems.

The original Stefan problem considered a single component, semi-infinite fluid, of initial temperature T_∞, being cooled from above. Heat is removed by conduction into a surface heat sink of temperature T_c, below the freezing point of the fluid. An important combination for determining the rate of solidification was the ratio of latent heat to specific heat, $\mathcal{S}_t = L/c_p(T_\infty - T_c)$; a combination which has become known as the *Stefan number*. For sea ice with a 20K temperature scale, the Stefan number will be 4.2 but can vary between 2.4 and 16.6 for temperature scales of 35K and 5K respectively.

The solution to the Stefan problem also makes use of the similarity solution to the thermal diffusion problem, whereby the spatial and temporal variations can be collapsed onto a single, self-similar coordinate given by $\tilde{z} = \hat{z}/2\sqrt{\kappa\hat{t}}$, where $\hat{t}$ is the time since cooling began and $\hat{z}$ is the depth. We therefore note that for problems deriving influence from the Stefan problem, one of the relevant length scales will be the thermal diffusion length scale, $\sqrt{\kappa\hat{t}}$. This length scale grows in time and is a measure of the distance a thermal anomaly could have spread diffusively since $\hat{t} = 0$.

When a binary alloy is cooled, the compositional component can also affect the rate of solidification. For example, Huppert and Worster (1985) considered the time-dependent solidification of an aqueous Na_2CO_3 solution cooled from below. They showed theoretically that the slow rate of chemical diffusion relative to the faster thermal diffusion leads to an increased salinity close to the solid: salt is rejected from the growing solid but unable to diffuse away at the same rate as the thermal energy being transferred. This build up of salinity at the boundary decreases the local liquidus temperature and so decreases the overall rate of solid formation. However, when the salinity of the system is small, they found that the compositional boundary layer was not sufficiently large to significantly alter the local liquidus temperature and the rate of solidification was controlled by thermal diffusion.

At the solid-liquid interface, the local liquidus temperature and the actual temperature are equal, but the slower rate of salt diffusion means that the compositional boundary layer has a much smaller extent than the thermal boundary layer. The sharp decrease in salinity, and hence liquidus temperature, away from the boundary means that some of the fluid in the compositional boundary layer is below its

local liquidus temperature. This effect is known as *constitutional supercooling* (see Worster, 2000, for a review).

Constitutional supercooling was first investigated by Mullins and Sekerka (1964) for solidification at a steady rate, who found that it can trigger a *morphological instability* in the solidification front. Where a perturbation moves ahead of the front, the salinity gradient ahead of the perturbation is sharpened and diffusion can remove salt faster from this region than from the surrounding interface. This reduces the resistance to further solid growth around the perturbation and the solidification front can advance faster here than in neighbouring regions, triggering an instability in the planar front. Morphological instabilities are not limited to the solidification of binary alloys and occur in a wide variety of geophysical, geological and industrial solidification problems. A good review can be found in Langer (1980).

The developing morphological instability in the solidification front quickly leads to the formation of dendrites similar to those in figure 1.4. Instead of attempting to accurately model the complex interfaces, Hills et al. (1983) proposed a volume averaged set of equations (see §2.1) for the dendritic region. This region has solid ice crystals in local thermodynamic equilibrium with the concentrated brine that fills the pores between them, and is known as a *mushy layer* (Worster, 1992a). While the global system may not be in equilibrium, the assumption of local thermodynamic equilibrium is used because diffusion on the ice pore scale will occur on a much faster time-scale than diffusion on a macroscopic scale, and the pore scale geometry quickly relaxes back to local equilibrium.

As well as showing theoretically how the presence of a compositional boundary layer affects growth in the two-component Stefan problem, Huppert and Worster (1985) also performed a number of experiments on the mushy layer which forms when $NaNO_3$ is solidified. The results demonstrated experimentally that mushy layers still follow the self similarity of thermal diffusion. They also showed that the growth rate decreases as the initial concentration is increased and increases as the temperature difference between the interface and cooling surface increases.

Worster (1986) extended the Stefan problem to include a mushy region between the solid and liquid regions. He showed that the mushy layer equations could be collapsed onto the same self-similarity coordinate as the thermal diffusion and Stefan problems, and found that the mushy layer grows at a much faster rate than

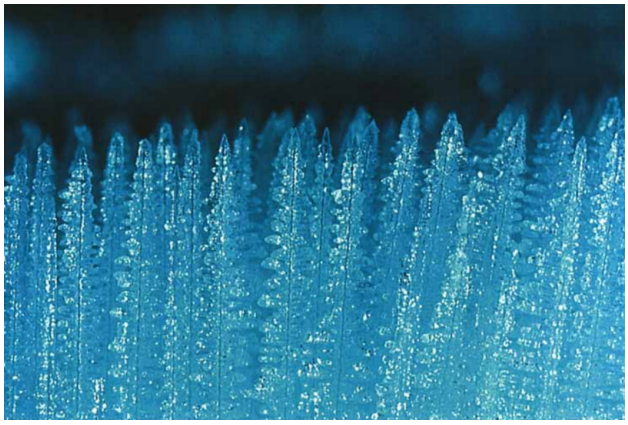

Figure 1.4: A reproduction of figure 19b of Huppert (1990), showing dendrites of NH_4Cl formed while solidifying an aqueous solution. *This figure has been altered for online publication due to copyright restrictions.*

the entirely solid region behind the growing mushy region. The presence of a mushy layer slightly suppresses the growth of the solid, but the absence of an entirely solid region does little to impact the growth of the mushy region. His calculated growth rates agreed well with the results of Huppert and Worster (1985) and confirmed that the ice growth rate can be increased by increasing the temperature difference between the interfacial and cooling temperatures, or lowering the initial temperature. He predicts that increasing the concentration in a mushy layer will result in a larger liquid fraction over a greater range, which they attribute to the need for pores to accommodate salt from the mush. This result was later confirmed experimentally by Aussillous et al. (2006) using magnetic resonance imaging techniques.

Shirtcliffe et al. (1991) measured the solid fraction during the solidification of aqueous $NaNO_3$ suddenly cooled from below and found decreasing solid fraction further from the cooling plate, in reasonable agreement with the model of Worster (1986). Chiareli and Worster (1992) then extended the model used by Worster (1986) to include the effects of the two phases having separate densities. This is significant because when the two phases have different densities, the growing solid forces fluid out of (in to) the mushy layer as the material expands (contracts) upon solidification. The extended model was also compared to the experimental result of Shirtcliffe et al. (1991) and offered noticeably improved agreement between the model and the experimental results.

Chiareli et al. (1994) investigated the effects of the phase density ratio more generally and found that expansion upon solidification (as occurs in salt water) increases

the growth rate of the mushy layer as well as the solid fraction at the surface. They also introduced the segregation coefficient which is the ratio of solidus to liquidus concentrations for a given temperature. A non-zero value means that salt is absorbed into the solid matrix as it forms. This reduces the build up of salt within the mushy layer and Chiareli et al. (1994) observe more solid formation throughout the mushy layer as the segregation coefficient increases.

1.4 Convection Models

As sea ice grows, both the changes in salinity caused by the solidification and the cooling itself create a density gradient within the interstitial fluid that leads to convective overturning. The convection occurs in both the liquid and mushy phases and flows freely across the mush-liquid interface. Here, I present a brief review of the convective processes relevant to sea ice growth.

1.4.1 Steady State Thermohaline Convection

An influential early study of thermal convection was provided by Lord Rayleigh (1916) in his theoretical study of a viscous fluid between two rigid, horizontal plates separated by a distance, $\hat{d}$, as illustrated in figure 1.5. He identified a key dimensionless number, which represents the ratio of buoyancy forcing to viscous dissipation, as the parameter controlling the stability of the system. This parameter has become known as the *Rayleigh number*, $\mathcal{R}_a = g\alpha\Delta T\hat{d}^3/\kappa\nu$, where ΔT is the temperature difference between the two plates, g is acceleration due to gravity and ν is the kinematic viscosity of the fluid. A larger Rayleigh number indicates that there is more gravitational potential energy in the system which is able to drive convection, compared to the stabilising impact of diffusive processes, which dissipate fluctuations in temperature or momentum.

The modified problem of convection in a porous medium was considered by Horton and Rogers (1945) and independently by Lapwood (1948). Conservation of momentum is governed by Darcy's law for flow in a porous medium rather than the Navier-Stokes equation which is used for pure fluids. Both papers found that the stability was still controlled by a Rayleigh-like parameter known as the *porous Rayleigh number*, $\mathcal{R}_p = g\alpha\Delta T\hat{\Pi}_0\hat{d}/\kappa\nu$. The porous Rayleigh number is related to the standard Rayleigh number:

$$\mathcal{R}_p = \mathcal{D}_a\mathcal{R}_a,$$

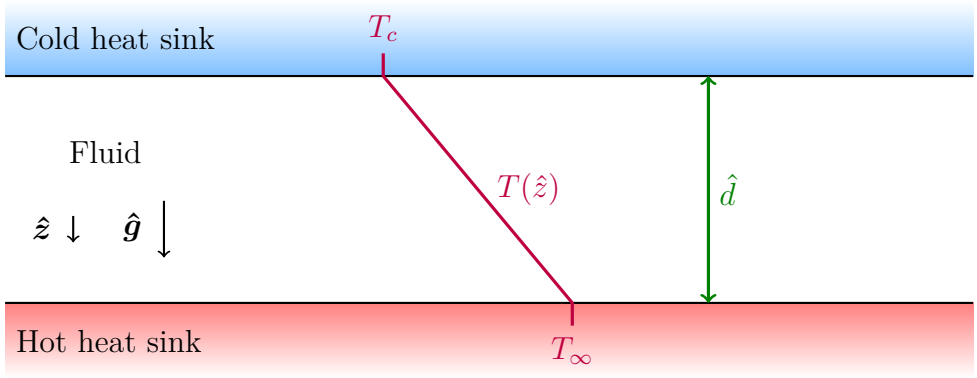

Figure 1.5: A diagram showing the setup of a simple convection problem where a fluid is cooled from the top and heated from the bottom. The domain has a total depth of $\hat{d}$ and there is a temperature difference across the domain of $\Delta T = T_\infty - T_c$. The fluid has a thermal expansivity, α, thermal diffusivity, κ, and viscosity, ν. Acceleration due to gravity, $\boldsymbol{g}$, acts vertically downwards and for convection in a porous medium, the permeability is given by $\hat{\Pi}_0$.

where the *Darcy number*, $\mathcal{D}_a = \hat{\Pi}_0/\hat{d}^2$, is the ratio of the permeability scale compared to the macroscopic size of a porous medium.

Pure compositional convection is mathematically identical to thermal convection and the next level of complexity considers thermohaline convection which features contributions to the density from both thermal and compositional components. Stommel et al. (1956) observed that continuous motion could be sustained in a vertical tube if its base was open to cold, fresh water and its top to warm, salty water. They attributed this to the exchange of thermal energy through the tube to the surroundings, but the inability to exchange salt in the same way. The residual salinity gradients then drive the convective exchange. Stern (1960) examined this result analytically and found if the density contribution from one component is unstable, an apparently stable stratification can start convecting as a result of the differences in diffusivity for thermal and compositional components, with thermal exchange able to occur at a much faster rate than salt exchange. Sani (1963) found that the differing diffusivities lead to two new modes known as *salt finger* and *diffusive* convection as a result of parcels exchanging heat with their surroundings but retaining their salt content. A good review of these effects is given by Linden (2000) but I will briefly summarise their explanations.

Salt finger convection occurs with a stable thermal gradient but destabilising salinity gradient. In this mode, a parcel which is displaced downwards (upwards) will rapidly adjust to the ambient temperature but will retain its previous salt content, due

to heat diffusing faster than salt. As a result it will be saltier (fresher) than the surrounding fluid and negatively (positively) buoyant, resulting in further downward (upward) movement and the growth of the instability. This is the mechanism behind the behaviour observed by Stommel et al. (1956) and considered analytically by Stern (1960).

The diffusive-convection mode found by Sani (1963) occurs in the opposite setting when the thermal gradient is destabilising but the salinity gradient is stabilising. In this instance, a parcel displaced downwards (upwards) is now colder and fresher (warmer and saltier) than its surroundings. The quick thermal transfer results in a parcel which is then at the same temperature as its surroundings but fresher (saltier), and therefore positively (negatively) buoyant. When the parcel returns to its original position, it will still be positively (negatively) buoyant since it is now warmer (colder) than its surroundings but will have the same salt content. The parcel will therefore move past the initial position, come to rest on a new density plane and the process will then repeat. If the gradients are severe enough, the maximum displacement can grow with each iteration, leading to an oscillatory instability. This is often called *overstability*.

Nield (1968) performed a similar analysis of thermohaline convection in a porous medium. Through a linear stability analysis, he was able to confirm that both salt-finger and diffusive convection are possible in porous media. The stability bounds for these convective modes can be expressed as a combination of the porous Rayleigh number, the ratio of thermal and salinity scales, $\beta\Delta\hat{S}/\alpha\Delta T$, and the Lewis number, $\mathcal{L}_e = \kappa/D$, which represents the ratio of thermal and saline diffusivities when the boundaries are held fixed.

It is important to note however, that both salt finger and diffusive convection require decoupled thermal and salinity fields, so these modes will only be possible in the compositional boundary layer and not within a mushy layer where T and $\hat{S}$ are thermodynamically coupled.

1.4.2 Boundary Condition Effects

The previous section focused on results found using Dirichlet boundary conditions which assume the boundaries are perfectly conducting (isothermal) and perfectly impervious (no normal flux). However, in many settings the boundaries apply a more general forcing to the fluid, and Dirichlet boundary conditions are not

Vertical Velocity		Thermal		$\mathcal{R}_c$	k_c
Upper	Lower	Upper	Lower		
D	D	D	D	$4\pi^2 = 39.48$	$\pi = 3.14$
D	D	D	N	27.10	2.33
D	D	N	N	12	0
D	N	D	D	27.10	2.33
D	N	N	D	17.65	1.75
D	N	D	N	$\pi^2 = 9.87$	$\pi/2 = 1.57$
D	N	N	N	3	0
N	N	Any		0	0

Table 1.1: A reproduction of table 1 from Nield (1968) giving the critical Rayleigh number and wavenumber for thermal convection in a porous medium with a variety of boundary condition combinations. The boundary conditions are applied to the perturbation only and the base state is not affected. 'D' indicates a Dirichlet condition (constant temperature or no normal flow) and 'N' indicates a Neumann condition (no thermal flux or constant pressure/no normal stress).

appropriate. Neumann boundary conditions can also be used and represent a perfectly insulating or no stress boundary when applied to the temperature and velocity fields respectively, amongst others. More generally, Robin boundary conditions can be used where the thermal or momentum flux depends linearly on the temperature or velocity at the boundary.

Lapwood (1948) also considers the case where the upper boundary is held at a constant pressure. For the impervious case, the critical Rayleigh number is $4\pi^2 = 39.48$ while for a constant pressure boundary the critical Rayleigh number is 27.10. Similarly, the critical wavenumber decreases from π to 2.3, representing wider convective cells, but Lapwood does not attempt to explain this difference.

Nield (1968) also looked at the effect of different boundary conditions for thermal convection in a porous layer, as summarised in table 1.1. He considered both Neumann and Dirichlet conditions for the thermal and velocity perturbations in a number of combinations.

Where Lapwood (1948) found that a Neumann condition applied to the velocity decreases the critical Rayleigh number to 27.10, Nield (1968) found the same critical Rayleigh number when applying a Neumann condition to the thermal perturbation. Adding a second Neumann condition caused a further decrease in the critical Rayleigh number, with the exact result depending on whether the two conditions

were applied to the same field or at the same boundary. Using a third Neumann condition (i.e. two thermal and one velocity) further decreases the Rayleigh number and for four Neumann conditions, the critical Rayleigh number drops to 0 and any vertically constant perturbation is allowed.

Kubitschek and Weidman (2003) investigated convection in a porous cuboid with insulating side walls, an isothermal upper boundary and an imperfectly conducting lower boundary. The temperature of the heat sink for the lower boundary was held constant but heat is transferred through Newtonian cooling where the rate of heat transfer is set by the temperature difference across the boundary, and a cooling parameter, $\mathfrak{h}$:

$$k\frac{\partial T}{\partial \hat{z}} = \mathfrak{h}\,(T - T_c)$$

Non-dimensionally, this imperfect conduction is characterised by the Biot number, $\mathcal{B}_i = \mathfrak{h}\hat{d}/k$, which is the ratio of the cooling parameter and the system depth, $\hat{d}$, to the thermal conductivity, k. A larger Biot number represents faster heat transfer across the boundary with an infinite Biot number representing a perfectly conducting (Dirichlet) boundary, while a Biot number of zero represents a perfect insulating (Neumann) boundary. By varying the Biot number, it is possible to alter the effective conductivity of the boundary and investigate the transition between the two extremes.

By increasing the Biot number applied to the perturbation only, they were able to produce a smooth, monotonic transition from a critical Rayleigh number of 27.10 with a Neumann condition to a critical Rayleigh number of 39.48 with a Dirichlet condition. This was accompanied by a similar smooth increase in the critical wavenumber between the corresponding limits. While this setup is physically implausible since the base state would also be affected by changes to the boundary conductivity, it is useful for gaining insight and they link the Biot number to the stability of the system, with a larger Biot number having a stabilising effect on the perturbations.

Barletta et al. (2015) took this further and applied a Robin boundary condition to both the thermal and vertical velocity perturbations on the upper and lower boundaries, representing the most general case possible. They vary the Biot numbers (and the velocity equivalents) in a number of different ways, showing the smooth transitions between Dirichlet and Neumann boundary conditions, and the results in

table 1.1, as the extremes. The running theme to their results was that decreasing one or more Biot numbers would decrease the critical Rayleigh number and critical wavenumber of the system and so promote convection. They surmise that decreasing the Biot number makes the boundary less restrictive to convection, with perfectly conducting and perfectly impervious boundaries being the most restrictive, while perfectly insulating and constant pressure/no stress boundaries are the most liberal. This makes sense since a lower Biot number means a shallower gradient at the boundary and therefore less diffusive dissipation of the profile in question, which in turn makes it easier for convection to occur. As a result, the decreasing critical Rayleigh number with increasing number of Neumann boundary conditions found by Nield (1968) and shown in table 1.1 can be explained by noting that each Neumann condition removes a dissipative barrier to convection.

Imperfect conduction will also affect the thermal base state which is being perturbed. For a fixed difference between the two external heat sinks, imperfect conduction results in a temperature difference across each boundary and so decreases the temperature difference across the fluid itself, but in a steady state system the temperature profile will remain linear. Kubitschek and Weidman (2003) account for this change in temperature by defining a *Biot-modified Rayleigh number*, given by $\mathcal{R}_p\mathcal{B}_i/(1+\mathcal{B}_i)$, which corrects for the known change in base-state temperature range as the boundary conduction is varied. This amounts to a redefinition of the temperature scale for the stability problem to use the actual temperature difference between the boundaries rather than the driving temperature difference between the heat sinks. However, we note such a transformation may not be possible in systems which do not begin in equilibrium since the vertical structure of the base-state may change over time, and it may cause complications if other parameters in the system also depend on the this temperature scale.

Robin boundary conditions have also been considered for convection problems in a number of other physical settings including the vertical side walls of a box (Nygård and Tyvand, 2010), the walls of a horizontal pipe (Barletta and Storesletten, 2011), and the ends of a vertical cylinder (Barletta and Storesletten, 2013).

1.4.3 Two-Domain Convection

Section 1.4.1 considered convection in boxes which consisted of a single medium. However, sea ice consists of a porous layer in contact with an underlying fluid and there are many other settings where both media are present and active, such as metallurgy, magma/mantle dynamics and submerged sediments. The first study to consider convection in a porous layer underlying a fluid layer was Sun (1973) in his PhD thesis, followed independently by Nield (1977). Subsequently, Chen and Chen (1988) discovered bimodal behaviour of the system when the liquid layer is thin. In this configuration, there are two stability minima for the critical Rayleigh number as a function of wavelength.

The first of these modes is known as the *boundary layer mode*, with convection occurring almost exclusively within the fluid layer. There are only small intrusions into the porous layer close to the boundary, with the majority of the porous layer unaffected by convection. The second mode is the *porous layer mode* (later *mushy layer mode*) with convection occurring throughout the full height of the domain. Convection in the porous layer mode occurs at a significantly larger wavelength than the boundary layer mode, reflecting their different vertical extents and the preference of convecting systems for square aspect ratios.

Chen and Chen (1988) found that the relative stability of the two modes depends on the thickness of the liquid layer relative to the porous layer. For thin liquid layers, the porous layer mode is more unstable than the boundary layer mode and the system is strongly bimodal. However, when the liquid layer is suitably thick the boundary layer mode becomes more unstable, and for a very thick liquid layer the bimodal behaviour is no longer present, with the porous layer mode subsumed into the boundary layer mode. This may explain why the bimodal behaviour was missed by Sun (1973) and Nield (1977).

In the same paper, Chen and Chen (1988) also studied thermohaline convection of the two-layer system and found that while the bimodal behaviour persisted, the boundary layer mode was significantly more stable than the porous layer mode. They observed an optimum depth ratio for convection to occur and that past this ratio, secondary cells began to form in the liquid layer. They postulated that the optimum depth ratio was a result of these secondary cells and the increased motion in the liquid layer suppressing convection, but did not investigate this further.

This bimodal behaviour was then observed experimentally by Chen and Chen (1989), who also investigated the rate of heat transfer in supercritical states. Numerical simulations of the supercritical convection by Chen and Chen (1992) showed good agreement between the experimental heat transfer rates and their numerical model. Various studies have continued this investigation and a good review can be found in Dixon and Kulacki (2017a,b).

1.4.4 Boundary Layer Convection

The previous sections discussed systems that are in an equilibrium state before convection begins, but such systems neglect the transient nature of most real-life systems. A particularly important transient system for our application is an initially uniform state that is exposed to a sudden change in buoyancy forcing at one boundary. As this buoyancy forcing spreads into the fluid and gravitational potential energy builds up, a convective instability can occur.

The thermal (or compositional) profiles during this initial transience naturally differ from the equilibrium state and so the criteria for convection during this period also differs from the stability criteria of an equilibrium state, although the criteria will approach this limit as time progresses and the system itself approaches equilibrium. As a result, it is possible for a transient state to be more unstable (have a lower critical Rayleigh number) than the final state, representing a convective mode which is unstable for a short period of time before becoming stable again as the underlying buoyancy profiles begin to interact with the unchanged boundary (Slim and Ramakrishnan, 2010).

With a view to combining the models of time-dependent convection with the solidification models in §1.3, I will focus solely on convection within a semi-infinite or *deep pool* system. These systems represent the initial transience of a physically finite system where the evolving base state is not interacting with the other boundary, and as such, require that $\hat{d} \gg \sqrt{\kappa \hat{t}}$, where $\hat{d}$ represents the physical size of the system. This is known as *boundary layer convection* since the instability is confined to a small region near the primary boundary. A variety of stability methods have been applied when studying it.

The stability of a suddenly cooled fluid was studied first by Foster (1965). The moment at which an instability develops is poorly defined in a time-dependent

problem and Foster used the *amplification method* which looks at the root-mean-square growth of a perturbation. Starting from a white noise initial condition, Foster declared the instability as occurring when the averaged velocity amplitude reached an arbitrary threshold of 100 times its initial value. Foster found that the critical Rayleigh number, $\mathcal{R}_c$, of this instability scaled as $\hat{t}^{-3/2}$ while the critical wavenumber, k_c, scaled as $\hat{t}^{-1/2}$, both of which are consistent with a thermal diffusion length scale of $\sqrt{\kappa\hat{t}}$ acting as the characteristic scale of the convective system.

The scaling of the critical Rayleigh number can also be explained by considering a Rayleigh number defined using the thermal diffusion length scale, $\sqrt{\kappa\hat{t}}$, so that $\mathcal{R}_a$ grows proportional to $\hat{t}^{3/2}$. Using this length scale, the temperature profiles become static in time because the vertical scale grows in unison with their spread and a stability criteria calculated for this profile will therefore be constant in time. Transforming back to a system with an externally imposed length scale, $\hat{d}$, and a Rayleigh number which does not evolve in time, the time-dependence must shift to the stability criteria and so scale as $\hat{t}^{-3/2}$.

Caltagirone (1980) solved the analogous problem for a porous medium and he found that the scaling of the critical wavenumber is still consistent with the thermal diffusion length scale, but the critical Rayleigh number now scales as $\hat{t}^{-1/2}$. This can be explained, analogously to the pure liquid case, by noting that the porous Rayleigh number is proportional to the depth, $\hat{d}$, rather than the cube of the depth, $\hat{d}^3$.

Following Foster (1965), Caltagirone (1980) initially used the amplification method and offered two definitions of when the instability occurred. The first was when the thermal amplitude returned to its initial value after an initial period of decay as stable modes in the initial white noise decay and unstable modes grow. This criteria is similar to Foster's criteria but with a lower threshold. The second defined the instability as the point when the growth or decay of the amplitude was zero. By construction, a system will always meet the second criteria before it meets the first criteria, so the second criteria produces smaller critical Rayleigh numbers.

As well as using the amplification method, Caltagirone introduced the non-linear *energy method*. While the amplification method determines whether a numerically defined perturbation is able to grow, the energy method analytically provides a lower bound on the conditions for a perturbation to grow and then seeks perturbations

Author	Method	$c_1 = \mathcal{R}_c\sqrt{t}$	$c_2 = \mathrm{k}_c\sqrt{t}$
Caltagirone (1980)	Energy (Global)	9.6*	-
Yoon and Choi (1989)	Propagation	12.43	0.915
Ennis-King et al. (2005)	Energy (Global)	5.5	-
	Amplification of θ	8.7	0.57
Riaz et al. (2006)	Dominant mode	12.1	0.85
Hassanzadeh et al. (2006)	Amplification of θ	7.7 - 11.4	-
Slim and Ramakrishnan (2010)	Energy (Local)	6.92	0.37 ± 0.01
Kim and Choi (2012)	Propagation	12.9	0.900
Tilton et al. (2013)	Frozen time	7.45	0.435
	Propagation	11.18	0.817
	Self-sim. amp. of w	7.28	0.438
	Self-sim. amp. of θ	10.57	0.795

Table 1.2: A list of studies into convection driven by thermal/compositional boundary layers in porous media and the methods used. * This value was reported by Ennis-King et al. (2005) rather than the original work and they believe the original work to be erroneous.

which meet these requirements using variational methods. This is a much more powerful technique since it places a strong lower bound on the stability of the problem - perturbation growth below this bound is not possible - compared to the empirical bounds from the amplification method. The amplification method can be affected by the choice of initial perturbation and decisions on when an instability is deemed to have occurred.

Caltagirone does not attach numerical values to the proportionality between $\mathcal{R}_c$ and $\hat{t}^{-1/2}$, but Ennis-King et al. (2005) report a value of 9.64 for Caltagirone's energy bound, which they believe to be erroneous. This value and those found by the studies discussed subsequently are presented in table 1.2 for comparison.

Yoon and Choi (1989) introduced the *propagation method*. This method takes advantage of the similarity solution for diffusive growth by transforming into self-similar coordinates and then using the quasi-static stability analysis (QSSA) method in this new frame. The QSSA method considers linear perturbations which have a sinusoidal horizontal structure and an exponential rate of growth/decay. For comparison, the *frozen time* method takes the time-evolving temperature profiles from the laboratory frame and treats them as a static base state for the purposes of QSSA analysis. Yoon and Choi (1989) claim their method is superior to the frozen time method because their coordinate transformation ensures that any perturbations

they find are self-similar. However, the vertical spreading of a perturbation with the increasing thermal diffusion length scale represents an increase in the energy of the perturbation even if the amplitude remains unchanged, which increases the energy barriers for such perturbations to grow. As a result, the propagation method produces critical Rayleigh numbers higher than those found with less restrictive methods.

Where previous studies focussed on thermal convection, the problem was re-framed as solutal convection in carbon sequestration by Ennis-King et al. (2005). For this study, they followed Caltagirone (1980) in using both the amplification and energy methods, and defined the amplification instability as when the perturbations first begin to grow, rather than reaching a set amplitude. They found that the critical Rayleigh number found by the amplification method is 50% higher than the critical Rayleigh number from the energy method, but both of their results are lower than the results of Yoon and Choi (1989) using the propagation method.

Riaz et al. (2006) introduced the *dominant mode* method which transforms the dynamical equations into self-similar coordinates before looking at the moments of the vertical diffusion operator in this new frame. The first mode of this operator is then used as the basis of a leading-order approximation to the full stability problem.

A more recent innovation was a variation on the energy method by Slim and Ramakrishnan (2010). Previous versions of the energy method average Darcy's law globally and use a single-valued coupling parameter to couple this average dissipation to the energy functional. Instead, Slim and Ramakrishnan (2010) opt to apply Darcy's law locally through the use of a Lagrange multiplier field, which provides a more rigorous application of the constraint. This method is discussed in more detail in §4.2.

Slim and Ramakrishnan (2010) also use the frozen time method and while they do not discuss the results of this method in depth, they do note that the frozen time method produced much closer results to their energy method than the other methods used in previous studies. This method had not previously been applied to the porous-media problem and had faced criticism when applied to the fluid case, most notably by Gresho and Sani (1971). The basis of this criticism appears to be that it produced different critical Rayleigh numbers and different subsequent evolution to the amplification method they also used. However, table 1.2 suggests

that the critical Rayleigh numbers from the frozen time method (as reported by Tilton et al., 2013), fall within the range of suggested Rayleigh numbers found using a variety of methods. Frozen time methods should only be applied to instantaneous growth and not the subsequent evolution as well, which will invariably be affected by the continued diffusion of the base state. A further criticism is that neutral modes have zero growth by definition, and hence evolve on a slower timescale than the background state. This creates an apparent contradiction with the assumption that the background state is static. However, I argue that the method can be usefully interpreted as follows. Without objection, the frozen time method can be used to find perturbations growing or decaying much faster than the base state. Any inaccuracy would occur as the perturbation growth rate is decreased towards the stability threshold. It would therefore be possible to interpolate from these fast-evolving perturbations on each side of the stability curve to a neutral perturbation. A reasonable assumption is that a bound found by such an interpolation would be close to that found by setting the growth rate to zero, noting that for Rayleigh-Benard and Horton-Rogers-Lapwood convection, the growth rate is linear in the Rayleigh number.

To summarise the results in table 1.2, the studies all recover the same dependence of $\mathcal{R}_c$ and k_c on $\hat{t}$ but the methods produce different coefficients of proportionality, along with a selection of other studies. As yet, there is no consensus as to exactly how the instability should be defined or which is the "best" method to use. For example, some methods focus on any deviation from the background state which is growing, whilst others only consider large perturbation amplification. A number of recent works, such as Kim and Choi (2012), have identified the self-similar coordinates as the most relevant to the problem but methods which make them an integral part of the solution method overly restrict the range of allowed perturbations compared to methods formulated in Cartesian coordinates. They are also harder to generalise to problems which contain additional length scales, where the similarity transformation may no longer be applicable. Of the methods considered, only the energy method offers a robust lower bound for the onset of convection.

1.4.5 Convection During Steady Mush Growth

Mushy layers contain both thermal and concentration gradients and so can support a convective instability, an aspect which has been studied extensively in settings where the mushy layer is growing at a constant rate, G. While being a step away from many environmental applications, this has found uses in metallurgy, and can

occur in systems were material is pulled between two heat exchangers at a constant rate, see Peppin et al. (2008) for an example. The steady growth can make the system easier to analyse than the transient case, particularly when analysed in coordinates moving with the solidification front, $\hat{z} - G\hat{t}$. As a result, the instability from initially steady growth has received more attention than time-dependent mushy layer convection.

The steady growth configuration in a moving frame is known as the directional solidification setting and the possibility was first studied by Fowler (1985). This preliminary study was able to find an approximate critical Rayleigh number for the *near eutectic* limit, where the initial concentration is close to the eutectic concentration, and by assuming the mushy layer is thin relative to the thermal diffusion length scale. However, the author recommended further numerical investigation and suggested the possibility of a subcritical branch below this linear bifurcation.

Worster (1992b) followed this with a numerical study of linear perturbations in a coupled mush-liquid system. He demonstrated that the bi-modal behaviour observed by Chen and Chen (1988) for a porous-liquid system also exists in the mush-liquid system, with narrow convection cells in the compositional boundary layer as the boundary layer mode, and wide convection cells over the full depth of the system in the mushy layer mode. Worster also investigated how changing the Darcy number and the Lewis number affected the relative stability of these two modes. Decreasing the Darcy number was found to make the the boundary layer mode more unstable relative to the mushy layer mode, by increasing the relative mobility of the liquid region. Decreasing the Lewis number also destabilises the boundary layer mode, due to the increasing thickness of the compositional boundary layer. He drew parallels between this result and Chen and Chen (1988) finding that increasing the thickness of the liquid layer decreased the critical Rayleigh number of the boundary layer mode.

Amberg and Homsy (1993) searched for sub-critical behaviour in the same near-eutectic, thin-layer limit of Fowler (1985), and without consideration of the adjacent liquid layer. They performed a weakly non-linear analysis and found that the linear bifurcation can exhibit both supercritical and subcritical behaviour. For 2-D rolls, the presence of subcritical behaviour depends on the combination $\left(\partial\hat{\Pi}/\partial\phi\right)/\delta\mathcal{C}$, which relates the rate of permeability change with solid fraction, ϕ, to the non-dimensional mush thickness, δ, and the concentration ratio, $\mathcal{C}$. The system will exhibit subcritical behaviour when this exceeds a certain threshold, with local outflow

moving cold, salty water to a warmer, fresher region. The parcel's temperature will equilibrate quickly but the salt content will not, leading to a parcel which is above its liquidus temperature and resulting in dissolution to restore local thermodynamic equilibrium. For 3-D hexagonal convection, they found that the linear bifurcation is always transcritical, with states that have outflow at the hexagon's centre always being subcritical and inflow at the hexagon's centre always being supercritical. The subcritical tendency was once again controlled by the combination $\left(\partial\hat{\Pi}/\partial\phi\right)/\delta\mathcal{C}$.

Anderson and Worster (1996) also observed a mechanism specific to mushy layers when considering linear stability in a near-eutectic system with a large superheat, that results in a thin mushy layer. The authors observed a linear, oscillatory mode which occurs at the same wavenumbers as the non-oscillating linear instability but which occurs at a lower Rayleigh number than the non-oscillating mode in some circumstance. This instability takes the form of waves of dissolution and solidification which propagate horizontally through the mushy layer as it grows, and appears to be most pronounced when the near-eutectic and thin-layer approximations are most accurate. As a result, this mode can only occur in a mushy layer because it requires the solidification dynamics to form the waves, but it remains a linear stability mode so cannot be related to the subcritical behaviour found by Amberg and Homsy (1993).

The strongly non-linear development of convection in mushy layers can lead to the formation of solid-free chimneys (or channels) which focus the flow out of the mushy layer, as discussed in Worster (1997). These chimneys have been studied experimentally in a range of settings (eg. Copley et al., 1970) and they are created by a non-linear feedback between solidification and the flow, where flow through the mushy layer draws salt towards the outflow region, leading to an increased salinity. The increase in salinity causes dissolution and a decrease in the solid fraction which in turn, helps focus the outflow through region and leads to the development of the channels. See Rees Jones and Worster (2013) or Wells et al. (2013) for a review and further information.

Other useful innovations in this field include the discussion of tangential stress on the mush-liquid interface by Le Bars and Worster (2006) and the introduction of a deformable interface by Roper et al. (2008).

1.4.6 Time-Dependent Mushy Layer Convection

Tait and Jaupart (1992) performed an experimental investigation into the solidification of a $NH_4Cl - H_2O$ mixture following a sudden change in temperature (similar to that discussed in §1.4.4). The first part of the study looked at the evolving temperature profiles and they found good agreement with theoretical results following Worster (1986), although the theory underestimated the temperature close to the cold plate and overestimated it further away. This discrepancy was more noticeable after a larger time had elapsed or if the viscosity was lower - cellulose polymer was added to noticeable increase the viscosity without affecting the dynamics (Tait and Jaupart, 1989).

As time progressed, Tait and Jaupart (1992) observed channel formation and convective overturning which had the effect of suppressing mush growth, with the suppression strongest for lower viscosities. They also investigate the convective onset criteria for channel formation (a non-linear process), and produce a critical Rayleigh number of 25. These results are also presented in Emms and Fowler (1994) after further analysis which suggest the Rayleigh number, as determined by the experiments, is between 9 and 22, varying with superheat and viscosity but with no clear trends. *Superheat* is the name given to the difference between the initial temperature and the initial liquidus temperature.

Emms and Fowler (1994) was also the first study to perform a stability analysis on a growing mushy layer, rather than the more common directional solidification setting discussed in §1.4.5. To simplify the dynamics, they employed the *near eutectic* approximation, where the initial concentration is assumed to be close to the eutectic concentration. This has the effect of ensuring that the solid fraction remains small throughout the liquid layer such that $\chi \approx 1$, although time derivatives of χ and ϕ are retained. They also noted that salt finger convection in the liquid will occur more readily than convection within the mushy layer. The fluid will therefore be in a more turbulent regime. A simple parameterisation was used to model convection within the liquid layer, reducing it to a set of boundary fluxes on the mushy layer interface.

Their investigation used the frozen time method and focussed on parameters corresponding to the solidification of aqueous NH_4Cl cooled isothermally from below. The only time dependence in their calculated stability criteria arises from the advance of the mushy layer interface. Hence analogously to the behaviour

discussed in §1.4.4, we observe a critical Rayleigh number that decreases with $1/\sqrt{\kappa\hat{t}}$ when measured using an external length scale. Emms and Fowler (1994) found that the critical Rayleigh number decreases as the superheat increases, although they provide no explanation for this result.

This line of investigation was next picked up by a series of studies using the propagation method, which requires that perturbations are self-similar and spread vertically in line with the mushy layer growth, as well as growing in amplitude. Hwang and Choi (2000) parameterised the effects of the liquid layer, following the example of Emms and Fowler (1994), and use parameters appropriate for the solidification of aqueous NH_4Cl. While Hwang and Choi (2000) do not explicitly state they are working in the near-eutectic regime, they note that "the porosity of the mushy layer is higher than 0.95". The base-state and perturbation liquid fraction profiles are calculated, but there is no direct impact of these profiles on the flow since permeability is not included in their momentum equation. For small values of the superheat, the critical Rayleigh number found by this study is higher than the critical Rayleigh number found by Emms and Fowler (1994), but there is good agreement between the two sets of results for large superheats. Hwang and Choi (2000) note that mushy layer growth is more aggressive with a smaller superheat so the time-dependence of the base state will be more significant, and suggest this as the reason for the discrepancy when the superheat is small.

A later study by Hwang and Choi (2004) extended their previous study by incorporating the liquid layer into the analysis which allowed them to observe the boundary layer mode directly, rather than using a parameterisation. They found that decreasing the rate of salt diffusion in the liquid layer causes a transition from the boundary layer mode to the mushy layer mode as slower salt diffusion inhibits the salt finger convection. They also found that the boundary layer mode is more pronounced with a larger superheat.

This study was followed up by Hwang and Choi (2008), which found good agreement between their fully dynamic liquid layer and the parameterised liquid layer of Emms and Fowler (1994). Hwang and Choi (2008) then looked at the convective onset time, defined as when the critical Rayleigh number defined on the thermal diffusion length scale, $\mathcal{R}_p \propto \sqrt{\kappa\hat{t}}$, exceeds a calculated threshold. Previous studies had used a critical Rayleigh number based on the mushy layer depth and had not quantified the effects of a changing mushy layer depth on the stability criteria. They found

that the onset time exhibits a minimum as the superheat is increased, without there being a corresponding minimum in the critical Rayleigh number itself.

The next paper by Hwang and Choi (2009) considered the effects of a Beavers-Joseph condition for fluid stress at the interface (Beavers and Joseph, 1967). Using this condition decreases the applied stress at the interface, decreases the critical Rayleigh number and reduces the maximum between mushy layer mode to boundary layer mode, with a smooth transition between the modes for a free-slip interface.

Hwang (2013) extended the previous method by adding permeability effects to the momentum equation, allowing the mushy layer structure to directly impact the fluid flow. The study departs from the parameters appropriate for a $NH_4Cl - H_2O$, instead using a set of values which allow a comparison to Worster (1992b) and correspond to an unspecified aqueous solution where the chemical component solidifies. The focus of the investigation is on the concentration ratio which is known to affect the porosity of a mushy layer (Worster, 1991). Hwang (2013) finds that both the critical Rayleigh number and critical wavenumber decrease as the concentration ratio increases, approaching a limit for large values of $\mathcal{C}$. He suggests this trend is due to convective confinement by the varying porosity but he does not look for a quantitative description. The trend is also in qualitative agreement with the results of Worster (1992b) in a directional solidification setting. Hwang (2013) also observes that the critical Rayleigh number and critical wavenumber decrease as the superheat is increased, over a small range of superheat values, and relates this to the size of the compositional boundary layer.

Convection in a growing mushy layer is an underdeveloped field compared to mushy layer convection in a directional solidification setting. The majority of the theoretical studies have confined themselves to a single method which is known to overestimate stability bounds (see table 1.2) and only one has considered the effects of porosity differences throughout the layer. There is clear scope for further research here to understand the behaviours observed by the previous studies, to widen the range of parameters investigated, and to apply these generalised results to sea ice. The studies have also focused on a perfectly conducting boundary and have not considered thermal forcing more appropriate for sea ice.

1.5 Observations

Measurements of the thermal evolution of thick ice are numerous, using instruments such as ice mass balance buoys (Perovich et al., 2008), samples from ice cores (Zhou et al., 2013), and other techniques (see Hunke et al., 2011, for a review). However, in-situ observations of the early stages of sea ice growth are limited because of the logistical difficulties of operating on thin ice. Two key studies consider very thin ice in-situ: Wettlaufer et al. (2000) discusses ice growth in a natural lead; and Notz and Worster (2008) investigates the refreezing of an artificial hole created in land-fast pack ice. Both of these studies provide estimates of the ice depth and temperature profiles. Notz and Worster (2008) also give measurements of the ice solid fraction and salinity, using techniques developed by Notz et al. (2005).

There are also a number of laboratory experiments which provide useful information about convection in sea ice. Most notable is the study of Wettlaufer et al. (1997), which investigates ice growth with a range of salinities and temperature differences. They also describe in detail the solidification of a 70psu salt solution cooled from -1.8^oC to -20^oC, and provide an indication of convective onset. Niedrauer and Martin (1979) demonstrated the circulation from convection in growing sea ice through the advection of injected dyes. Cottier et al. (1999) measured the detailed patterns of salt drainage that had occurred from ice cores. A more recent study by Middleton et al. (2016) used Schlieren optical methods to directly observe convection in the compositional boundary layer as well as the plumes coming out of brine channels. A good review of these laboratory observations and others is also given by Hunke et al. (2011), who summarise the relevant findings.

1.6 Summary and Openings

In summary, for a system with both thermal and saline gradients, there are three possible forms of convective instability - direct, salt finger and diffusive - depending on whether one or both of the gradients are destabilising. Furthermore, when a porous layer is coupled to a liquid layer, the convection can either occur in the liquid mode, with only weak flow in the porous layer, or in the porous mode, with significant flow in both layers. In mushy layers, a convective instability can also arise from the feedback of solidification and interstitial flow, but salt finger and diffusive convection cannot occur because the thermal and saline fields are coupled through local thermodynamic equilibrium.

There has been significant progress in the study of time-dependent convection of porous layers, largely driven by the application to carbon sequestration, but the time-dependent stability of mushy layers remains an under-developed field. Work in the area has so far been focussed on $NH_4Cl - H_2O$ systems cooled from below and with the dense NH_4Cl solidifying since this can be related to laboratory experiments. However, analytical studies have been limited and there is clear scope for further investigation in this area. This is particularly true in relation to the way porosity changes affect the stability of the mushy layer, and the way that imperfect thermal conduction by the surface boundary affects both mushy layer development and convective onset. Considering these effects and applying the results to polar conditions can further our understanding of the polar regions and contribute to future models of sea ice.

2
Model

The investigation of growing sea ice will use mushy layer dynamics to describe the thermodynamic processes (Feltham et al., 2006), combined with a Darcy or Darcy-Brinkman equation for momentum transfer, depending on the setting. I will consider a semi-infinite liquid initially at rest and at a uniform temperature T_∞, and salinity $\hat{S}_\infty$. At $\hat{t} = 0$, cooling begins with the surface at $\hat{z} = 0$ exposed to a heat sink with a temperature of T_c, while being impermeable to mass or salt fluxes, as illustrated in figure 2.1. When the temperature at the upper boundary falls below the liquidus temperature, solidification will begin to occur with a mushy layer forming next to the boundary and growing down into the liquid. Sufficiently deep within the fluid, the properties will be unaffected by the cooling occurring above and so will tend to their initial values as $\hat{z} \to \infty$.

In this chapter, §2.1 derives the mushy layer equations from conservation principles and shows how they can also be used to describe the liquid layer. Next, §2.2 describes the initial conditions, as well as the boundary conditions at the surface and at depth. It also discusses the conditions needed on the mush-fluid interface for a two-domain solution. The equations from the previous two sections are non-dimensionalised in §2.3. The chapter finishes with two short sections - one showing how the salinity equations can be re-written in terms of the liquidus temperature (§2.4), and the other discussing the solution to the thermal diffusion equation (§2.5) - and a brief summary of how these equations are used going forwards (§2.6).

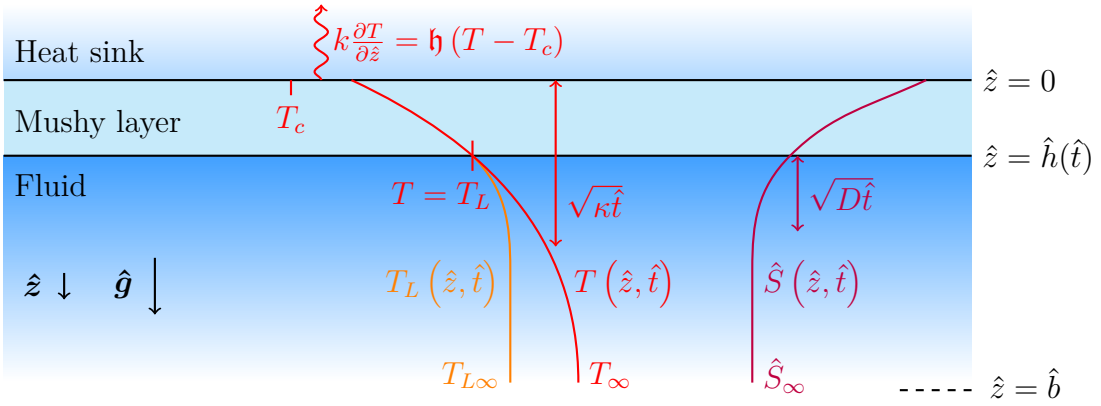

Figure 2.1: A box of fluid exists with an initial temperature of T_∞, initial salinity $\hat{S}_\infty$ and a very large depth, $\hat{b}$, such that the bottom boundary does not affect the dynamics. Cooling begins from $\hat{t} = 0$ through Newtonian cooling (2.2.6) at $\hat{z} = 0$ to a heat sink with a temperature of T_c, with the cooling propagating vertically downwards (the direction of increasing $\hat{z}$). When the temperature falls below the initial liquidus temperature, $T_{L\infty}$, a mushy layer begins to form adjacent to the surface that has a time evolving thickness, $\hat{h}(\hat{t})$. The temperature profile has a characteristic size given by the thermal diffusion length scale, $\sqrt{\kappa\hat{t}}$, where κ is the thermal diffusivity, although the Newtonian cooling factor, $\mathfrak{h}$, also affects the temperature close to the surface. If there is salt diffusion, a compositional boundary layer exists close to the mushy-fluid interface with a characteristic size of $\sqrt{D\hat{t}}$, for saline diffusivity D.

Where there is an ambiguity between dimensional and non-dimensional quantities using the same symbol, dimensional quantities will be indicated with a hat, $\hat{}$, and non-dimensional quantities will not have a hat.

2.1 Mushy Layer Equations

In this section I describe the derivation of the mushy layer equations, following the example of Worster (1992a). I will initially consider separate material properties in each phase, and then make the assumption that these properties are equal at appropriate points in the derivation.

The mushy layer equations treat a mix of solid crystals and concentrated brine arising from a morphological instability (see §1.3) as a new continuum phase by averaging the material properties over a representative control volume. This control volume is assumed to be small compared to the macroscopic scale we are interested in measuring, but large enough to encompass multiple dendrites and the fluid between them on the microscopic scale. On the microscopic scale, we also assume

that the system is in local thermodynamic equilibrium such that the temperature, T, is uniform in both phases throughout the control volume, and the salinity, $\hat{S}$, is uniform throughout the liquid phase. The assumption of local thermodynamic equilibrium also results in the temperature and salinity being coupled through the liquidus relationship, (1.2.1).

An important property of the control volume is the relative abundance of the two phases. This is described by the liquid fraction, χ, which represents the proportion of the volume occupied by the liquid phase. The liquid fraction ranges from 0 (completely solidified) to 1 (completely liquid). The corresponding abundance of the solid phase is given by $\phi = 1 - \chi$.

As well as the liquid fraction, thermal properties are defined for the control volume as a whole and this is done by taking the phase-weighted mean of those properties in the two phases. Using density as an example, the density of the control volume, $\overline{\rho}$, is given by:

$$\overline{\rho} = \chi\rho_l + (1-\chi)\rho_s,$$

where ρ_l and ρ_s are the densities of the liquid and solid phases respectively. The phase-weighted average of other properties are defined in the same way and also denoted with an overbar.

Since the conservation equations derived below are valid for any liquid fraction between zero and one, they also describe the conservation equations for a pure fluid which can be found by setting the special case $\chi = 1$. They therefore provide the full description needed for a one-domain solution to a mushy and liquid system, if a suitable momentum equation is used.

2.1.1 Conservation of Mass

The equation describing conservation of mass within the mushy layer is formed by considering the phase-weighted mass flux into and out of the control volume. This phase weighted mass flux is given generally by $\chi\rho_l\hat{\boldsymbol{u}}_l + (1-\chi)\rho_s\hat{\boldsymbol{u}}_s$, where $\hat{\boldsymbol{u}}_l$ is the velocity of the interstitial fluid through the pore space and $\hat{\boldsymbol{u}}_s$ is the velocity of the solid matrix. However we consider settings where the solid matrix is stationary

and material transport only occurs in the liquid phase, with $\hat{\boldsymbol{u}}_s = 0$. Conservation of mass for a control volume, $\hat{V}$, can then be expressed as:

$$\frac{\partial}{\partial \hat{t}} \int_{\hat{V}} \left[\chi \rho_l + (1-\chi)\rho_s\right] \, d\hat{V} = - \oint_{\partial \hat{V}} \chi \rho_l \hat{\boldsymbol{u}}_l \cdot \boldsymbol{n} d(\partial \hat{V}),$$

where $\partial \hat{V}$ is the surface of the volume, and $\boldsymbol{n}$ is the normal unit vector. Using the divergence theorem, the differential form of this expression is:

$$\hat{\boldsymbol{\nabla}} \cdot \hat{\boldsymbol{u}} = (r_\rho - 1) \frac{\partial \chi}{\partial \hat{t}}. \tag{2.1.1}$$

Here, $r_\rho = \rho_s/\rho_l$ is the ratio of solid to liquid densities and more generally, r_Y will denote the ratio of Y in the solid phase to Y in the liquid phase. The phase-weighted volume flux, $\hat{\boldsymbol{u}} = \chi \hat{\boldsymbol{u}}_l$, is know as the *Darcy flux*, and while it is a volume flux rather than a true velocity, we will also refer to it as the velocity of bulk transport for convenience.

From (2.1.1), we see that solidification, $\partial\chi/\partial\hat{t} < 0$, (or melting with $\partial\chi/\partial\hat{t} > 0$) is a source (sink) of material transport if the density of the solid phase is lower than the density of the liquid phase. This can drive expansion or contraction flow as discussed in Chiareli and Worster (1992) and Chiareli et al. (1994). However, for simplicity we will work in the Boussinesq approximation, where all densities are considered equal except where multiplied by gravity in the buoyancy terms, so there is no expansion or contraction of the material on solidification and the Darcy velocity is incompressible:

$$\hat{\boldsymbol{\nabla}} \cdot \hat{\boldsymbol{u}} = 0. \tag{2.1.2}$$

2.1.2 Conservation of Energy

To describe conservation of energy within the mushy region, we start by considering the phase-weighted enthalpy density, $\overline{\rho \hat{H}}$, and the ways it can be transported into or out of a control volume.

The advective flux of enthalpy is given simply by $\chi \rho_l \hat{H}_l \hat{\boldsymbol{u}}_l$, with no transport by the stationary solid phase, while the rate of thermal diffusion is given by $-\overline{k}\hat{\boldsymbol{\nabla}} T$, where k is the thermal conductivity. In general, the thermal conductivity may be anisotropic and represented by a matrix, but we will assume isotropy and that thermal conductivity is a constant scalar in each phase. We also note that the enthalpies of the two phases are not required to be equal, $\hat{H}_l \neq \hat{H}_s$, but for a system in

local thermodynamic equilibrium, the temperature must be the same in both phases.

With these fluxes, the divergent form of the continuity equation is:

$$\frac{\partial \overline{\rho \hat{H}}}{\partial \hat{t}} + \hat{\boldsymbol{\nabla}} \cdot \left(\rho_l \hat{H}_l \hat{\boldsymbol{u}} \right) = \hat{\boldsymbol{\nabla}} \cdot \left(\overline{k} \hat{\boldsymbol{\nabla}} T \right). \tag{2.1.3}$$

By expanding the derivatives and using (2.1.1) to rewrite the advective term, we find that:

$$\overline{\rho \frac{\partial \hat{H}}{\partial \hat{t}}} + \rho_l \hat{\boldsymbol{u}} \cdot \hat{\boldsymbol{\nabla}} \hat{H}_l + \rho_s L \frac{\partial \chi}{\partial \hat{t}} = \hat{\boldsymbol{\nabla}} \cdot \left(\overline{k} \hat{\boldsymbol{\nabla}} T \right), \tag{2.1.4}$$

where $L = \hat{H}_l - \hat{H}_s$ represents the *latent heat* of phase change (specifically the *enthalpy of fusion*), which we assume is unaffected by changes in temperature and salinity. This expression contains both the enthalpy and the temperature but these profiles are linked through the definition of the specific heat capacity:

$$c_p = \frac{\partial \hat{H}}{\partial T}.$$

The heat capacity can be different in the solid and liquid phases, but again for simplicity we will assume it remains constant during changes in temperature and salinity. Substituting this expression into (2.1.4) leads to:

$$\overline{\rho c_p} \frac{\partial T}{\partial \hat{t}} + (\rho c_p)_l \, \hat{\boldsymbol{u}} \cdot \hat{\boldsymbol{\nabla}} T + \rho_s L \frac{\partial \chi}{\partial \hat{t}} = \hat{\boldsymbol{\nabla}} \cdot \left(\overline{k} \hat{\boldsymbol{\nabla}} T \right). \tag{2.1.5}$$

By expanding the phase-weighted properties, the full equation for conservation of energy in the mushy layer becomes:

$$\begin{aligned} \left[1 + \left(r_{\rho c_p} - 1 \right) (1 - \chi) \right] \frac{\partial T}{\partial \hat{t}} + \hat{\boldsymbol{u}} \cdot \hat{\boldsymbol{\nabla}} T + \frac{r_\rho L}{c_{pl}} \frac{\partial \chi}{\partial \hat{t}} \\ = \kappa \hat{\boldsymbol{\nabla}} \cdot \left[\left[1 + (r_k - 1)(1 - \chi) \right] \hat{\boldsymbol{\nabla}} T \right], \end{aligned} \tag{2.1.6}$$

where $\kappa = k_l / \rho_l c_{pl}$ is the thermal diffusivity of the liquid phase, and we have neglected the temperature dependence of k_l. With the assumption of equal thermal properties, this equation reduces to:

$$\frac{\partial T}{\partial \hat{t}} + \hat{\boldsymbol{u}} \cdot \hat{\boldsymbol{\nabla}} T + \frac{L}{c_{pl}} \frac{\partial \chi}{\partial \hat{t}} = \kappa \hat{\nabla}^2 T. \tag{2.1.7}$$

We know from the physical data discussed in §1.2.3 that r_k is 4.27 and r_{c_p} is 0.50. By assuming thermal properties in the solid are equal to their corresponding values in the liquid, we will underestimate the thermal conductivity and overestimate

the specific heat capacity. Both of these assumptions have the effect of artificially reducing the thermal transport through the mush.

It is also possible to solve for the phase-weighted enthalpy $\overline{\hat{H}}$ as one of the dynamical variables. In this formalism, we take (2.1.3) and expand the advective derivative but not the temporal derivative leading to:

$$\frac{1}{c_{pl}}\frac{\partial \overline{\hat{H}}}{\partial \hat{t}} + \hat{\boldsymbol{u}} \cdot \hat{\boldsymbol{\nabla}} T = \kappa \hat{\nabla}^2 T, \tag{2.1.8}$$

where we have assumed thermal properties are the same in the two phases, and used the definition of the specific heat capacity to replace the liquid enthalpy with the temperature in the advective term. To relate the temperature to the enthalpy, we substitute the definition of the latent heat into the definition of $\overline{\hat{H}}$ to get:

$$\overline{\hat{H}} = c_{pl} T - L(1 - \chi), \tag{2.1.9}$$

again using the definition of the specific heat capacity. We note that using this expression in (2.1.8), directly leads to (2.1.7).

2.1.3 Conservation of Solvents

Concentration of salt and other tracers is formed in a very similar way to concentration of energy. We look at the evolution of the phase-weighted volumetric salinity, $\overline{\rho \hat{S}}$, which can be transported by advection, $\overline{\rho \hat{S} \hat{\boldsymbol{u}}}$, or diffusion, $-\overline{\rho D \hat{\boldsymbol{\nabla}} \hat{S}}$, where D represents the salt diffusivity. However, macroscopic transport can only occur within the liquid phase since the solid matrix is stationary, $\hat{\boldsymbol{u}}_s = 0$, and there is no diffusion within the solid phase, $D_s = 0$. We also assume that salt is not absorbed into the solid matrix, with $\hat{S}_s = 0$. Conservation of salt is given by:

$$\frac{\partial \overline{\hat{S}}}{\partial \hat{t}} = \frac{\partial \chi \hat{S}}{\partial \hat{t}} = \hat{\boldsymbol{\nabla}} \cdot \left(\chi D \hat{\boldsymbol{\nabla}} \hat{S} \right) - \hat{\boldsymbol{u}} \cdot \hat{\boldsymbol{\nabla}} \hat{S}, \tag{2.1.10}$$

where we have dropped the $_l$ label on the salinity in the liquid phase because there is no salinity in the solid phase, and used (2.1.2) to expand the advective flux. This equation can either be solved directly for $\overline{\hat{S}}$, or it can be expanded in terms of χ and $\hat{S}$ to allow for further analytical manipulation.

In the liquid region, the temperature and salinity are completely uncoupled. In the mushy region local thermodynamic equilibrium creates a solidification feedback

that ties the temperature with the liquidus temperature, and hence with the salt content, through the liquidus relationship:

$$T = T_L(\hat{S}). \tag{2.1.11}$$

Recalling from §1.2.2 that a linear approximation to the liquidus relationship is given by:

$$T_L(\hat{S}) = T_{L\infty} - \Gamma(\hat{S} - \hat{S}_\infty), \tag{1.2.1 revisited}$$

where $T_{L\infty}$ is the liquidus temperature at the reference salinity, $\hat{S}_\infty$, and Γ is the liquidus gradient. We note that the simple model used for this study does not model the effects of pressure on the liquidus temperature. Using (1.2.1) to replace the liquid salinity in the definition of the bulk salinity leads to:

$$\chi = \frac{\Gamma\overline{\hat{S}}}{\Gamma\hat{S}_\infty + T_{L\infty} - T_L}. \tag{2.1.12}$$

This equation is called the *Lever Rule* and allows the liquid fraction of a mushy layer to be calculated from the liquidus temperature, T_L, (equal to the physical temperature) and bulk salinity, $\overline{\hat{S}}$.

2.1.4 Conservation of Momentum

Conservation of momentum in a pure Newtonian fluid is governed by the Navier-Stokes equation, as described in Vallis (2006):

$$\frac{\partial\hat{\boldsymbol{u}}}{\partial\hat{t}} + \hat{\boldsymbol{u}}\cdot\hat{\boldsymbol{\nabla}}\hat{\boldsymbol{u}} + \frac{1}{\rho_0}\hat{\boldsymbol{\nabla}}\hat{p} - g\frac{\rho-\rho_0}{\rho_0}\boldsymbol{e_z} = \nu\hat{\nabla}^2\hat{\boldsymbol{u}}, \tag{2.1.13}$$

where ν is the kinematic viscosity, $\hat{p}$ is the pressure, g is the gravitational acceleration, ρ_0 is the reference density, and $\boldsymbol{e_z}$ is the vertical, downward, unit vector. The Navier-Stokes equation describes the behaviour of the interstitial fluid well on a microscopic pore scale but the walls of the pores exert substantial viscous forces on the fluid. These forces dominate the large scale dynamics but cannot be described by the traditional Navier-Stokes equation when applied on the macroscopic scale so other momentum transfer models must be considered.

In porous regions, fluid flow is normally modelled using Darcy's law which averages the Stokes viscous forces over a number of pore spaces (Gray, 1975), leading to:

$$\frac{\nu\hat{\boldsymbol{u}}}{\hat{\Pi}(\chi)} = -\frac{\hat{\boldsymbol{\nabla}}\hat{p}}{\rho} + g\frac{\rho-\rho_0}{\rho_0}\boldsymbol{e_z}, \tag{2.1.14}$$

with the permeability $\hat{\Pi}(\chi)$ representing the resistance to flow arising from the solid matrix, which depends on the size and shape of the pores. Mushy layer models of sea ice typically assume a permeability function of the form:

$$\hat{\Pi}(\chi) = \hat{\Pi}_0 \chi^3, \tag{2.1.15}$$

where the reference permeability has a value of $\hat{\Pi}_0 = 2 \times 10^{-8} \mathrm{m}^2$. This form has been used in a number of other studies including Worster (1992b) and Wells et al. (2010), and is in line with the field observations of Freitag (1999), who directly measured the permeability of sea ice cores to find the reference value quoted. However, direct measurements are difficult since the ice cores will interact with the measurement fluid. More recently, Rees Jones and Worster (2014) have suggested an alternative reference value of $\hat{\Pi}_0 = 2.24 \times 10^{-9} \mathrm{m}^2$, based on comparisons between their model and observations of Wettlaufer et al. (1997). Another popular description of the permeability is the Carmen-Kozeney function:

$$\hat{\Pi}(\chi) = \frac{\hat{\Pi}_0 \chi^3}{(1-\chi)^2}. \tag{2.1.16}$$

This has been used in a modified form by Katz and Worster (2008) and Wells et al. (2013) and has the added benefit of better representing liquid regions by diverging to infinity as $\chi \to 1$. However, it also adds complexity to the problem. Some studies, such as Feltham et al. (2002), note that the permeability of sea ice shows anisotropy due to the preferred vertical alignment of ice crystals, but we will not consider such details here.

Equations (2.1.13) and (2.1.14) both work well in their respective purely liquid and purely porous domains but are not valid in the other domain. The Darcy-Brinkman equation is a modification to Navier-Stokes to extend its applicability to both fluid and porous regions. Various forms exist in the literature but we will use the form derived by Le Bars and Worster (2006):

$$\frac{\partial \hat{\boldsymbol{u}}}{\partial \hat{t}} + \hat{\boldsymbol{u}} \cdot \hat{\boldsymbol{\nabla}} \left(\frac{\hat{\boldsymbol{u}}}{\chi} \right) + \frac{\chi}{\rho_0} \hat{\boldsymbol{\nabla}} \hat{p} - g \frac{\chi (\rho - \rho_0)}{\rho_0} \boldsymbol{e_z} = \nu \hat{\nabla}^2 \hat{\boldsymbol{u}} - \frac{\nu \chi \hat{\boldsymbol{u}}}{\hat{\Pi}(\chi)}. \tag{2.1.17}$$

The left-hand side of Navier-Stokes has been altered here so that pressure and buoyancy forces act purely on the liquid phase, whilst the right-hand side contains both Stokes viscosity and Darcy-like terms. As the porosity tends to zero, $\chi \to 0$, this recovers Darcy's law (2.1.14), while for a fully porous material $\chi = 1$, we recover Navier-Stokes (2.1.13), assuming the permeability diverges in this limit, $\hat{\Pi} \to \infty$.

We approximate the fluid density by a simple, linear equation of state:

$$\rho_l = \rho_0 \left[1 - \alpha T + \beta \hat{S}\right], \qquad \text{(1.2.2 revisited)}$$

where $\alpha = 3.87 \times 10^{-5}\mathrm{K}^{-1}$ is the thermal expansion coefficient and $\beta = 7.86 \times 10^{-4}\mathrm{psu}^{-1}$ is the saline contraction coefficient (Jenkins, 2011). As mentioned in §1.2.3, this is a linearisation of the full, non-linear equation of state but is accurate to within 2% over the range of temperatures and salinities considered. The buoyancy term in (2.1.17) becomes:

$$g\frac{\chi\left(\rho - \rho_0\right)}{\rho_0}\boldsymbol{e_z} = g\chi\left[\beta\left(\hat{S} - \hat{S}_\infty\right) - \alpha\left(T - T_\infty\right)\right]\boldsymbol{e_z}, \qquad (2.1.18)$$

2.1.5 Liquid Layer Limit

As mentioned at the start of this section, these continuity equations are also valid for a pure fluid. In this special case, there is no solid so $\chi = 1$ everywhere.

In the limit of a pure liquid, the Darcy flux, defined as the average bulk transport, is simply equal to the liquid velocity, since there is no solid to inhibit the bulk mass flux. As such we find that incompressibility (2.1.2) also holds in the liquid region.

In the absence of any solid or solidification, the thermodynamics simplify greatly and we find that (2.1.7) reduces to a simple diffusion-advection equation:

$$\frac{\partial T}{\partial \hat{t}} + \hat{\boldsymbol{u}} \cdot \hat{\boldsymbol{\nabla}} T = \kappa \hat{\nabla}^2 T. \qquad (2.1.19)$$

We also find that the enthalpy, $\overline{\hat{H}}$, as defined in (2.1.9), becomes equal to the specific heat, $c_{pl}T$.

The salinity equation (2.1.10) also reduces to a simple diffusion-advection equation.

$$\frac{\partial \hat{S}}{\partial \hat{t}} + \hat{\boldsymbol{u}} \cdot \hat{\boldsymbol{\nabla}} \hat{S} = D \hat{\nabla}^2 \hat{S}, \qquad (2.1.20)$$

with the bulk salinity, $\overline{\hat{S}}$, now equal to the liquid salinity, $\hat{S}$.

To find the limit of the Darcy-Brinkman equation, we also need to note that a pure fluid is infinitely permeable ($\hat{\Pi} \to \infty$ as $\chi \to 1$). This means that the Darcy-like term in (2.1.17) vanishes and we return to the Navier-Stokes equation given in (2.1.13).

2.2 Initial and Boundary Conditions

To complete the model, we need to specify the initial conditions as well as the boundary conditions at the external and internal interfaces.

As mentioned at the start of this chapter and illustrated in figure 2.1, the fluid will initially be at rest with a constant temperature and salinity.

$$T = T_\infty, \qquad \hat{S} = \hat{S}_\infty, \qquad \hat{\boldsymbol{u}} = 0, \qquad \text{when } \hat{t} \leq 0. \qquad \text{(2.2.1a-c)}$$

We will also work in the deep pool limit where the physical box depth is much larger than the thermal diffusion length scale, $\hat{b} \gg \sqrt{\kappa \hat{t}}$. In this limit all profiles tend to their initial values at depth:

$$T \to T_\infty, \qquad \hat{S} \to \hat{S}_\infty, \qquad \hat{\boldsymbol{u}} \to 0, \qquad \text{as } z \to \infty, \qquad \text{(2.2.2a-c)}$$

2.2.1 Surface Conditions

Conservation of mass at the surface provides a simple balance which states that the normal component of the velocity at the surface must be equal to any mass flux across the surface. The main contributors to a surface mass flux would be evaporation removing water molecules from the liquid or precipitation adding water molecules. However, for simplicity we will assume these processes are not occurring, leading to the condition:

$$\hat{\boldsymbol{u}} \cdot \boldsymbol{n} = 0. \qquad \text{(2.2.3)}$$

Both shortwave solar and longwave thermal radiation transfer energy between the atmosphere and the ice or ocean. Incoming thermal radiation from the atmosphere, F_{LW}^{in}, is present throughout the year and delivers roughly 170 Wm^{-2} to perennial ice in winter (Maykut, 1978). This partially balances the outgoing thermal emission given by the Stefan-Boltzmann Law:

$$F_{LW}^{out} = \epsilon \sigma_{sb} {T_S}^4,$$

where F_{LW}^{out} is the outgoing longwave energy flux (in Wm^{-2}), T_S is the surface temperature (in Kelvin), ϵ is the emissivity of sea ice (measured to be very close to 1 by Chao et al., 2015), and $\sigma_{sb} = 5.67 \times 10^{-8}$ $\text{Wm}^{-2}\text{K}^{-4}$ is the Stefan-Boltzmann constant. Maykut (1978) gives the surface temperature of perennial ice as $-30^o C$, which gives an outgoing thermal flux of roughly 200 Wm^{-2} and therefore a net outgoing flux on the order of 30 Wm^{-2}, which is in line with SHEBA observations

reported by Stramler et al. (2011). Over open water, the temperature must be greater than the liquidus temperature of the ocean and this results in a larger outgoing and net thermal fluxes. Solar radiation is absent from November to February in the Arctic (Maykut, 1978) but small amounts are present at the start and end of the growth season. We will not consider solar radiation explicitly, but note that the effective solar flux (once albedo effects are considered) could be included as a constant correction to the incoming thermal radiation.

Sea ice and open ocean also lose energy through direct exchange with the lower atmosphere. The primary direct exchange is through the movement of sensible heat where thermal energy is transferred directly to the atmosphere, F_{SH}. This transfer is typically approximated via a turbulent flux scaling law (Roberts et al., 2012) that is linearly proportional to the temperature difference between the surface of the ice/ocean and the air it is in direct contact with, and also to the surface wind speed:

$$F_{SH} = \rho_a c_{pa} C_s u_w \left(T_S - T_{la}\right),$$

where $\rho_a = 1.3$ kgm^{-3} and $c_{pa} = 1.01 \times 10^3$ Jkg^{-1}K^{-1} are the density and specific heat capacity of the atmosphere, and $C_s = 2.5 \times 10^{-3}$ is the sensible heat transfer coefficient (Andreas, 1980). The wind speed, u_w, is measured at 10m and is typically a couple of meters per second, while T_{la} and T_S are the air and surface temperatures respectively. With a temperature difference of 20^oC and a wind speed of 3m/s, we get a sensible heat flux of 200 Wm^{-2} which is larger than the outgoing radiative flux. However, this is strongly dependent on the difference between surface and atmospheric temperatures, which will decrease as the growth season progresses and the ice thickens.

There is also a secondary direct exchange in the form of latent heat fluxes through evaporation or sublimation. This occurs when the specific humidity of the atmosphere is not in equilibrium or varies close to the surface and water molecules evaporate to address this imbalance. The transition from liquid to gaseous phases has an associated cost in the form of *enthalpy of vapourisation* or *latent heat*, but this is different from the primary use of "latent heat" in this thesis which refers to the *enthalpy of fusion*. In the conditions investigated by Maykut (1978), sensible heat fluxes are three times larger than latent heat fluxes for open water, but this ratio rapidly increases with ice depth and with just 10cm of ice, latent heat fluxes are an order of magnitude smaller than sensible heat fluxes. As a first approximation,

we will not include the effect of latent heat fluxes.

Our surface thermal balance will therefore consist of thermal conduction from the upper surface down into the ice or ocean, F_C, sensible heat fluxes and longwave radiative exchange:

$$F_C = F_{LW}^{in} - F_{LW}^{out} - F_{SH},$$

where F_C is negative when there is a net outgoing flux but the other fluxes are all positive. We can expand these definitions to get:

$$F_C = \epsilon\sigma_{sb}T_{ua}^4 - \epsilon\sigma_{sb}T_S^4 - \rho_a c_{pa} C_s u_w \left(T_S - T_{la}\right).$$

Here, we have defined an effective upper atmosphere temperature by inverting the Stefan-Boltzmann law, $T_{ua} = \left(F_{LW}^{in}/\epsilon\sigma_{sb}\right)^{1/4}$, which is equal to -40^oC for a flux of $170\mathrm{Wm}^{-2}$. This is not necessarily the same as the lower atmosphere temperature, T_{la}, used in the sensible heat flux. We now expand the longwave fluxes in terms of the temperature difference $T_S - T_{ua}$ to get:

$$F_C \approx -4\epsilon\sigma_{sb}T_{ua}^3 \left(T_S - T_{ua}\right) - \rho_a c_{pa} C_s u_w \left(T_S - T_{la}\right),$$

where we have used the fact that $|T_S - T_{ua}| \ll T_{ua}, T_S$ to neglect higher powers of $(T_S - T_{ua})$. With some algebra, this rearranges to:

$$F_C = -\mathfrak{h}\left(T_S - T_c\right), \tag{2.2.4}$$

$$\mathfrak{h} = 4\epsilon\sigma_{sb}T_{ua}^3 + \rho_a c_{pa} C_s u_w, \qquad T_c = \frac{4\epsilon\sigma_{sb}T_{ua}^4 + \rho_a c_{pa} C_s u_w T_{la}}{4\epsilon\sigma_{sb}T_{ua}^3 + \rho_a c_{pa} C_s u_w} \tag{2.2.5a,b}$$

We now have an equation for the heat flux conducted down into the ice which depends on only two parameters: the effective temperature of the atmospheric heat sink, $T_c \sim -25^oC$, and the effective thermal conductivity of the atmospheric exchange, $\mathfrak{h} \sim 10\ \mathrm{Wm}^{-2}\mathrm{K}^{-1}$. However, it should be noted that in a physical setting, both T_c and u_w will vary with weather conditions on the synoptic scale.

The second parameter, $\mathfrak{h}$ controls the rate of heat loss to the atmosphere, with a large value representing efficient thermal transfer and a high effective conductivity for the boundary. In the limit of $\mathfrak{h} \to \infty$, a boundary condition of the form in (2.2.4) becomes degenerate with a perfectly conducting, isothermal boundary, $T_S = T_c$. Alternatively, small values of $\mathfrak{h}$ represent very inefficient thermal transfer and a low effective conductivity for the boundary. At this extreme, we have $\mathfrak{h} \to 0$ and (2.2.4)

becomes degenerate with a perfectly insulating, no flux boundary, $F_C = 0$.

Finally, we need to express F_C in terms of our dynamical variables. In the absence of mass transport across the boundary, all the cooling must be balanced by the conductive flux, $-\overline{k}\hat{\boldsymbol{\nabla}}T$. As before, we neglect any variation in k and take the normal component of the gradient to get:

$$k\frac{\partial T}{\partial z} = \mathfrak{h}\,(T_S - T_c) \qquad \text{at } \hat{z} = 0, \tag{2.2.6}$$

We also need to consider salt conservation at the surface, with the balance given by:

$$\boldsymbol{n}\cdot\hat{\boldsymbol{u}}\hat{S} - D\chi\frac{\partial \hat{S}}{\partial z} = F_{Sal},$$

where F_{Sal} is the salt flux across the boundary, and represents the direct transfer of salt molecules into (or out of) the mushy layer. Without either salt diffusion, $D = 0$, or mass transfer across the boundary, it is trivial to show that F_{Sal} should be zero, representing the absence of salt transfer across the boundary. However, when salt diffusion is present, the picture is more complicated. The salinity gradient in the diffusive term is coupled to the thermal gradient through the liquidus relationship, yielding $\partial\hat{S}/\partial\hat{z} = -1/\Gamma\ \partial T/\partial\hat{z}$. Cooling is represented by a positive thermal gradient, which implies a negative salinity gradient and therefore a downward diffusive salt flux.

There are a number of ways the salt balance can be maintained. Firstly, an upwelling flow can bring salt from within the mushy layer towards the surface at a rate which exactly balances the downward diffusion. However, the upwelling flow would require a mass flux out of the mushy layer to maintain conservation of mass. An alternative resolution requires the direct addition of salt from the atmosphere such as to balance the diffusive flux but the mechanisms which would create such a flux are unclear. The final, and most likely, resolution is the formation of layer of pure solid such that $\chi = 0$ at the surface (Worster, 1986; Gewecke and Schulze, 2011). This means that the salt effectively drains from the surface of the mushy layer to leave a pure solid. As time passes, the purely solid region grows as a larger area has been drained of salt by diffusion. However, the thickness of this purely solid layer is typically substantially smaller than the underlying mush (Worster, 1986; Gewecke and Schulze, 2011).

When we consider salt diffusion and the conservation of salt directly in §3.1, we will assume the condition:

$$D\chi\frac{\partial\hat{S}}{\partial z} = 0, \tag{2.2.7}$$

without explicitly trying to resolve the slender layer of pure solid, but we will remain aware of the issues involved and the potential breakdown of our mushy layer model close to the surface boundary.

2.2.2 Interface Conditions

When working with a two-domain solution in chapters 3 and 5, we also need to consider the interface between the porous and liquid regions and the boundary conditions which need to be applied there.

Since we have no sources of mass in our system, the mass fluxes on either side of the interface must be equal:

$$[\hat{\boldsymbol{u}}\cdot\boldsymbol{n}]^{+}_{-} = 0, \qquad \text{for } \hat{z} = \hat{h}(\hat{t}), \tag{2.2.8a}$$

where $\boldsymbol{n}$ is the unit vector normal to the interface.

Schulze and Worster (2005) describe the thermohaline boundary conditions which need to be applied at the mush-liquid interface in the absence of salt diffusion for general fluid and solid motion. Since our ice is growing relative to the solid matrix and is spreading into the liquid layer, our setting represents a freezing interface with inflow, and I will describe their results for this setting here, as well as the necessary generalisations in the presence salt diffusion.

Since the system is in local thermodynamic equilibrium, the temperature across the interface must be continuous. In our particular setting, we also know that the mushy layer will grow to remove any supercooling in the liquid phase. The interface between the mushy and liquid regions can therefore be found where the temperature in the liquid region is first equal to the liquidus temperature. If the temperature in the liquid fell below the liquidus temperature, the fluid would be supercooled and the mush would rapidly grow into this region, while if the temperature was above the liquidus, the immediately adjacent mushy region would not able to sustain any solid and the mush would melt back.

This further implies continuity of liquid salinity across the interface, since temperature is continuous and salinity is constrained by the liquidus temperature on either side:

$$[T]^+_- = \left[\hat{S}\right]^+_- = 0, \qquad T|_+ = T_L\left(\hat{S}\right)\Big|_+, \qquad \text{for } \hat{z} = \hat{h}(\hat{t}). \qquad \text{(2.2.8b-d)}$$

Balancing the thermal and salt fluxes at the boundary gives:

$$\begin{aligned}\left[\left(\rho_l \hat{H}_l \hat{\boldsymbol{u}} - \overline{k}\hat{\boldsymbol{\nabla}}T\right)\cdot\boldsymbol{n}\right]^+_- &= \rho_0 L\,[\chi]^+_- \frac{\partial \hat{h}}{\partial \hat{t}},\\ \left[\left(\rho_l \hat{S}\hat{\boldsymbol{u}} - D\chi\hat{\boldsymbol{\nabla}}\hat{S}\right)\cdot\boldsymbol{n}\right]^+_- &= \left[\hat{S}\chi\right]^+_- \frac{\partial \hat{h}}{\partial \hat{t}}, \qquad \text{for } \hat{z} = \hat{h}(\hat{t}).\end{aligned}$$

These can immediately be simplified by noting that salinity, normal velocity and temperature are all continuous across the interface, and that temperature is proportional to the enthalpy of the liquid phase, $\hat{H}_l$. This gives:

$$\begin{aligned}\left[-\overline{k}\boldsymbol{n}\cdot\hat{\boldsymbol{\nabla}}T\right]^+_- &= \rho_0 L\,[\chi]^+_- \frac{\partial \hat{h}}{\partial \hat{t}},\\ \left[-D\chi\boldsymbol{n}\cdot\hat{\boldsymbol{\nabla}}\hat{S}\right]^+_- &= \left[\hat{S}\chi\right]^+_- \frac{\partial \hat{h}}{\partial \hat{t}}, \qquad \text{for } \hat{z} = \hat{h}(\hat{t}).\end{aligned}$$

In the absence of salt diffusion, $D = 0$, and noting that $\hat{S}$ and $\partial\hat{h}/\partial\hat{t}$ are non-zero, there cannot be a jump in liquid fraction across the interface, leading to:

$$\chi|_- = 1, \qquad \text{for } \hat{z} = \hat{h}(\hat{t}). \qquad \text{(2.2.8e)}$$

When salt diffusion is present, we follow Worster (1986) and make the assumption of marginal equilibrium:

$$\left.\frac{\partial T}{\partial \hat{z}}\right|_+ = \left.\frac{\partial T_L}{\partial \hat{z}}\right|_+ = -\Gamma \left.\frac{\partial \hat{S}}{\partial \hat{z}}\right|_+, \qquad \text{for } \hat{z} = \hat{h}(\hat{t}).$$

With this assumption Worster (1986) demonstrates that (2.2.8e) remains valid provided $k_l \geq k_s$ and is therefore the correct condition for this study to use for any value of D, since we have assumed that $k_l = k_s$.

These results also mean that the thermal, salinity and liquidus fluxes become continuous across the interface:

$$\left[\boldsymbol{n}\cdot\hat{\boldsymbol{\nabla}}T\right]^+_- = 0 \qquad \text{For all } D \text{ and } \hat{z} = \hat{h}(\hat{t}), \qquad \text{(2.2.8f)}$$

$$\left[\boldsymbol{n}\cdot\hat{\boldsymbol{\nabla}}\hat{S}\right]^+_- = \left[\boldsymbol{n}\cdot\hat{\boldsymbol{\nabla}}T_L\right]^+_- = 0 \qquad \text{For } D > 0 \text{ and } \hat{z} = \hat{h}(\hat{t}). \qquad \text{(2.2.8g,h)}$$

An additional boundary condition is also needed for the fluid shear-stress in the liquid phase. This presents some difficulty since the fluid is continuous between the two layers and there is a transition region at the bottom of the porous region where the fluid is still affected by motion in the liquid layer through the shear stress. The Darcy-Brinkman equation allows the problem to be solved on a single-domain for the two regions, but a two-domain solution requires approximating the fluid stress at the boundary and is discussed at length in Le Bars and Worster (2006). However, such a boundary condition is not required in the current work since we will not consider a two-domain solution in a setting which has fluid flow.

2.3 Non-Dimensionalisation

The thermal diffusion length scale, $\sqrt{\kappa \hat{t}}$, provides a natural scale for non-dimensionalisation, but using a time-evolving scale introduces complexity into the problem as the coordinate transformations become non-trivial. It is therefore convenient for initial non-dimensionalisation and analysis to use a fixed, time-independent length scale, $\hat{d}$. This scale can be considered as a physical length scale (such as mixed-layer depth of the ocean or the depth of some experimental apparatus), or the thermal diffusion length after some chosen interrogation time. We will scale this distance out of the problem in favour of the thermal diffusion length scale during later stages of the analysis. This chosen length scale also has an associated thermal diffusion time and velocity scale, $\hat{d}^2/\kappa$ and $\kappa/\hat{d}$ respectively. A diagram of the non-dimensional system is shown in figure 2.2.

The non-dimensional temperature, enthalpy, and salinities are defined as:

$$\theta = \frac{T - T_c}{T_\infty - T_c}, \qquad H = \frac{\hat{H} - c_{pl} T_c}{c_{pl}(T_\infty - T_c)}, \qquad \overline{S} = \frac{\overline{\hat{S}}}{\hat{S}_\infty} \qquad S = \frac{\hat{S}}{\hat{S}_\infty}. \tag{2.3.1a-d}$$

The temperature scale used, $\Delta T = T_\infty - T_c$, is the temperature scale across the whole system - from the deep fluid to the surface heat sink - while the salinity scale used is the initial salinity of the system. This means that both the temperature and salinity will tend towards 1 at depth and the boundary conditions (2.2.2) become:

$$\theta \to 1, \qquad S \to 1, \qquad \boldsymbol{e_z} \cdot \boldsymbol{u} \to 0, \qquad \text{as } z \to \infty. \tag{2.3.2a-c}$$

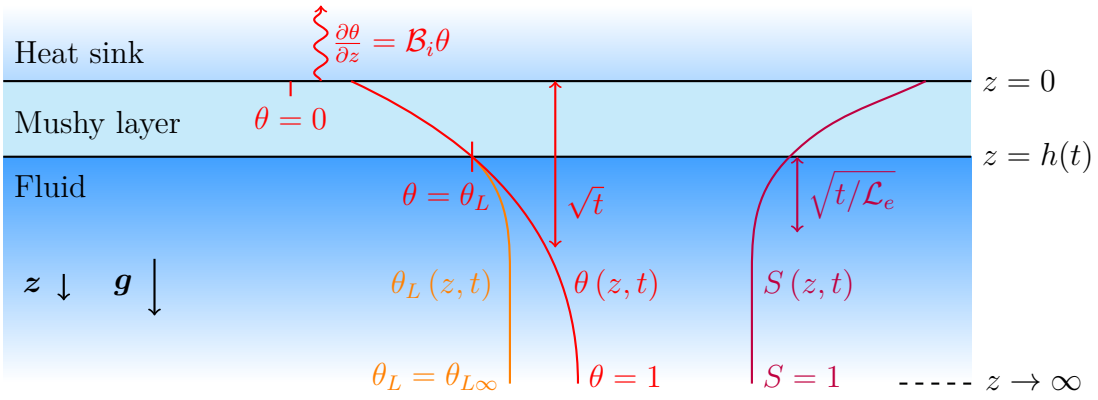

Figure 2.2: A non-dimensional version of figure 2.1. The temperature profile runs between 0 at the surface and 1 at depth, while the salinity and liquidus reference values are now 1 and $\theta_{L\infty}$ respectively. The thermal diffusion length scale is proportional to $\sqrt{t}$ and the saline diffusion length scale to $\sqrt{t/\mathcal{L}_e}$. For linearised heat transfer, the constant of proportionality is $\mathcal{B}_i$. A full description of the non-dimensional parameters used can be found in the main text.

The interface conditions applied at the boundary between the liquid and mushy regions (2.2.8a-c, f-h, d-e, in order) become:

$$[\boldsymbol{u}\cdot\boldsymbol{n}]^+_- = [\theta]^+_- = [S]^+_- = [\boldsymbol{n}\cdot\boldsymbol{\nabla}\theta]^+_- = [\boldsymbol{n}\cdot\boldsymbol{\nabla}S]^+_- = [\boldsymbol{n}\cdot\boldsymbol{\nabla}\theta_L]^+_- = 0,$$
$$\theta|_+ = \theta_L(S)|_+, \qquad \chi|_- = 1 \qquad \text{for } z = h(t). \qquad \text{(2.3.2d-k)}$$

At the surface, the boundary conditions (2.2.6, 2.2.7 and 2.2.3 respectively) become:

$$\frac{\partial\theta}{\partial z} = \mathcal{B}_i\theta, \qquad \frac{\chi}{\mathcal{L}_e}\frac{\partial S}{\partial z} = 0, \qquad \boldsymbol{e_z}\cdot\boldsymbol{u} = 0, \qquad \text{where } z = 0. \qquad \text{(2.3.2l-n)}$$

Here, we have introduced the *Lewis number*, $\mathcal{L}_e = \kappa/D$ and the *Biot number*, $\mathcal{B}_i$. The Lewis number represents the ratio of thermal to saline diffusion and a larger Lewis number means that the rate of thermal diffusion has increased relative to the rate of salt diffusion. An infinite Lewis number occurs when the saline diffusivity, D, is zero and there is no salt diffusion in this limit. Meanwhile, the Biot number is given by:

$$\mathcal{B}_i = \frac{\mathfrak{h}\hat{d}}{k_l} = \frac{\hat{d}}{\hat{d}_b}, \qquad \text{(2.3.3)}$$

where we define the boundary cooling length scale as $\hat{d}_b = k_l/\mathfrak{h}$. The Biot number represents the rate of heat transfer into the heat sink compared to thermal diffusion within the porous layer, and can be interpreted as an effective thermal conductivity of the surface boundary, $\mathfrak{h}\hat{d}$, relative to the thermal conductivity of the liquid, k_l.

This combination $\mathfrak{h}\hat{d}$ does not necessarily represent a physical conductivity of the adjacent medium, but instead is equivalent to an effective conductivity for general, linearised heat transfer across the surface boundary and into the heat sink at $z < 0$. The Biot number can alternatively be considered as the ratio of a length scale associated with the imperfect boundary cooling, $\hat{d}_b$, and the representative length scale of the domain (currently $\hat{d}$ and later $\sqrt{\kappa\hat{t}}$). An infinite Biot number represents an effective conductivity equivalent to a perfect thermal conductor at the boundary, and a Biot number of zero represents a boundary which does not conduct heat, equivalent to a perfect insulator. The length scale $\hat{d}_b$ is inversely proportional to the Biot number, so an infinite (zero) Biot number has a associated length scale of zero (infinity).

The dynamical equations of the system are also non-dimensionalised, with the thermal equations (2.1.7), (2.1.8) and (2.1.9) now given by:

$$\frac{\partial\theta}{\partial t} + \boldsymbol{u}\cdot\boldsymbol{\nabla}\theta + \mathcal{S}_t\frac{\partial\chi}{\partial t} = \nabla^2\theta, \qquad \frac{\partial H}{\partial t} + \boldsymbol{u}\cdot\boldsymbol{\nabla}\theta = \nabla^2\theta, \qquad H = \theta - \mathcal{S}_t(1-\chi). \tag{2.3.4a-c}$$

These equations introduce the Stefan number, $\mathcal{S}_t = L/c_{pl}(T_\infty - T_c)$, which represents the ratio of latent to specific heat in the system. A larger Stefan number means that the latent heat represents a greater proportion of the total energy in the system and that the release of energy caused by solidification will have a greater impact on the dynamics of the system. For brevity, we have dropped the overbar on the non-dimensional enthalpy, H, and the phase-weighted nature of this field is implied.

The salinity equation, (2.1.10) non-dimensionalises to:

$$\frac{\partial\overline{S}}{\partial t} = \frac{\partial\chi S}{\partial t} = \frac{1}{\mathcal{L}_e}\boldsymbol{\nabla}\cdot(\chi\boldsymbol{\nabla}S) - \boldsymbol{u}\cdot\boldsymbol{\nabla}S. \tag{2.3.5}$$

We also need to consider the non-dimensional form of the liquidus relationship (1.2.1) and the Lever rule (2.1.12) since these equations provide the coupling between the thermal and saline fields in the mushy layer.

$$\theta_L = \theta_{L\infty} - \Lambda\,(S-1)\,, \qquad \chi = \frac{\Lambda\overline{S}}{\Lambda + \theta_{L\infty} - \theta}. \tag{2.3.6a,b}$$

Here, we have introduced two non-dimensional parameters, the dimensionless initial liquidus temperature, $\theta_{L\infty}$, and the dimensionless liquidus gradient, Λ:

$$\theta_{L\infty} = \frac{T_{L\infty} - T_c}{T_\infty - T_c} \qquad \Lambda = \frac{\Gamma\hat{S}_\infty}{T_\infty - T_c}. \tag{2.3.7a,b}$$

A larger value of $\theta_{L\infty}$ indicates that the initial temperature of a fluid is closer to its initial liquidus temperature. The dimensionless liquidus gradient, Λ relates the size of the freezing point depression, $\Gamma\hat{S}_\infty$, to the temperature scale and therefore is a measure of the size of salinity effects in the system. A large liquidus gradient means that the freezing point depression caused by the salt content is large compared to the temperature range of the system and so it will have a larger impact on the solidification dynamics. Conversely, a small liquidus gradient means that the salt content has a much smaller impact on the liquidus temperature and the solidification dynamics, with the limit of $\Lambda \to 0$ representing a pure fluid with no salt content.

When non-dimensionalising the Darcy-Brinkman equation (2.1.17), we need to define the non-dimensional permeability, $\Pi(\chi)$, which is given by $\hat{\Pi}(\chi) = \hat{\Pi}_0 \Pi(\chi)$, and the non-dimensional pressure, p, given by $\hat{p} = \rho_0 g \alpha \Delta T \hat{d}\,[p - zT_c/\Delta T]$. The second term here arises from the fact that the reference density is measured when $T = 0^oC$, which differs from the non-dimensional zero-value which occurs when $T = T_c$, leading to an accumulation of hydrostatic pressure with depth. The Darcy-Brinkman equation then becomes:

$$\frac{1}{\mathcal{P}_r}\left[\frac{\partial \boldsymbol{u}}{\partial t} + \boldsymbol{u}\cdot\boldsymbol{\nabla}\left(\frac{\boldsymbol{u}}{\chi}\right)\right] + \mathcal{R}_a\chi\left[\boldsymbol{\nabla}p + (\theta - \beta^* S)\,\boldsymbol{e_z}\right] = \nabla^2\boldsymbol{u} - \frac{\chi\boldsymbol{u}}{\mathcal{D}_a\Pi(\chi)}. \tag{2.3.8}$$

which introduces four new dimensionless parameters: the compressibility ratio β^*, the Prandtl number $\mathcal{P}_r$, the thermal Rayleigh number $\mathcal{R}_a$, and the Darcy number $\mathcal{D}_a$. The compressibility ratio, $\beta^* = \beta\hat{S}_\infty/\alpha\Delta T$, indicates whether thermal or saline density effects are dominant, with a large value indicating the density is mainly controlled by the salinity and a smaller value indicating that thermal variations are the main source of density differences. The Prandtl number, $\mathcal{P}_r = \nu/\kappa$, represents the ratio of viscous to thermal diffusion, with a larger Prandtl number indicating that viscous dissipation is faster than thermal dissipation. The Rayleigh number is given by:

$$\mathcal{R}_a = \frac{g\alpha\Delta T\hat{d}^3}{\kappa\nu}. \tag{2.3.9}$$

This combination measures the ratio of thermal buoyancy forcing to viscous and thermal dissipation in the system, with a larger value indicating stronger buoyancy forcing and a smaller value indicating stronger dissipation. We can also use the Rayleigh number to define a convective length scale:

$$\hat{d}_c = \left(\frac{\kappa\nu}{g\alpha\Delta T}\right)^{1/3},$$

which represents the length over which thermal buoyancy anomalies can propagate before they are dissipated. The Darcy number is defined as:

$$\mathcal{D}_a = \frac{\hat{\Pi}_0}{\hat{d}^2}, \tag{2.3.10}$$

and measures the size of the typical pore relative to the size of the system. A larger Darcy number indicates larger pores and higher permeability, with a smaller Darcy number indicates smaller pores and lower permeability. The Rayleigh number and Darcy number can be combined to give the *porous Rayleigh number*, and an associated convective lengthscale:

$$\mathcal{R}_p = \mathcal{R}_a \mathcal{D}_a = \frac{g\alpha\Delta T\hat{\Pi}_0\hat{d}}{\kappa\nu}, \qquad \hat{d}_p = \frac{\kappa\nu}{g\alpha\Delta T\hat{\Pi}_0} \tag{2.3.11a,b}$$

Using this definition, the non-dimensional formulation of Darcy's Law (2.1.14) becomes:

$$\boldsymbol{u} = -\mathcal{R}_p\chi^3\left[\hat{\boldsymbol{\nabla}}p + (\theta - \beta^* S)\,\boldsymbol{e_z}\right], \tag{2.3.12}$$

and we can see that $\mathcal{R}_p$ is the direct analogue of $\mathcal{R}_a$ when considering thermal convection in a porous medium rather than a fluid. In sea ice and most binary alloys used for mushy layer experiments, changes to salinity in the fluid during solidification or melting have a significant impact on the buoyancy since the compression ratio, β^*, is typically greater than one. The coupling of the thermal and salinity fields means that the buoyancy effects from the two fields work in unison and it is common to combine them in the definition of the Rayleigh number. To do this, a characteristic salinity scale for buoyancy is defined as the salinity variation associated with the thermal variation and the liquidus relationship, $\Delta\hat{S} = -\Delta T/\Gamma$. The density changes from both fields is then given by $\alpha\Delta T - \beta\Delta\hat{S} = (\alpha + \beta/\Gamma)\Delta T$, and this combined density scale is used in the definition of the *mushy Rayleigh number* and the associated *mushy convective length*:

$$\mathcal{R}_m = \frac{g\left(\alpha + \beta/\Gamma\right)\Delta T\hat{\Pi}_0\hat{d}}{\kappa\nu}, \qquad \hat{d}_m = \frac{\kappa\nu}{g\left(\alpha + \beta/\Gamma\right)\Delta T\hat{\Pi}_0}. \tag{2.3.13a,b}$$

This was first introduced by Worster (1991) for convection in a directional solidification setting and we will make use of this definition in chapter 5. Most expressions of the mushy Rayleigh number are written in terms of the salinity scale, with $(\beta + \Gamma\alpha)\Delta\hat{S}$, but the two definitions are equivalent when $\Delta T = -\Gamma\Delta\hat{S}$. There may, however, be some difference between the numerical values found in this study compared to previous results due to the differing temperature scales used, as discussed in the next section.

2.3.1 Considering the Concentration Ratio

Most previous studies of mushy layer have tended to use the concentration ratio, $\mathcal{C}$, and the superheat θ_∞, in place of the liquidus gradient, Λ, and initial liquidus temperature, $\theta_{L\infty}$, respectively. They are typically defined as:

$$\mathcal{C} = \frac{\hat{S}_\infty - \hat{S}_s}{\hat{S}_c - \hat{S}_\infty} = \frac{\Lambda}{\theta_{L\infty}}, \qquad \theta_\infty = \frac{T_\infty - T_{L\infty}}{T_{L\infty} - T_c} = \frac{1}{\theta_{L\infty}} - 1, \qquad (2.3.14a,b)$$

where $\hat{S}_c$ is the salinity corresponding to the cooling temperature, T_c, and $\hat{S}_s$ is the salinity of the solid phase. The cooling temperature and cooling salinity, $\hat{S}_c$, are typically taken to be the eutectic point. This definition is used in Worster (1991), Feltham and Worster (1999) and Hwang (2013) amongst others but a small number of studies (including Worster, 1997, 2000; Rees Jones and Worster, 2013) have used the alternative definitions:

$$\mathcal{C} = \frac{\hat{S}_c - \hat{S}_s}{\hat{S}_c - \hat{S}_\infty} = \frac{\Lambda}{\theta_{L\infty}} + 1, \qquad \theta_\infty = \frac{T_\infty - T_c}{T_{L\infty} - T_c} = \frac{1}{\theta_{L\infty}}.$$

While these definitions are written in terms of salinities, the difference between them is better understood in terms of temperature - the two definitions use the same temperature scale of $T_{L\infty} - T_c$ but differ in choice of zero for the non-dimensional temperature. In the former definition, $T_{L\infty}$ is chosen as the zero-temperature with the cooling boundary at $\theta = -1$, and in the latter definition, the zero temperature is the cooling temperature, T_c, while the liquidus reference becomes $\theta = +1$.

The difference with the current work comes from the choice of temperature scale, with this work preferring the global temperature difference, $T_\infty - T_c$, over the mushy-layer temperature difference, $T_{L\infty} - T_c$. I choose this different scale because it avoids the diverging superheat ($\theta_\infty \to \infty$) as $T_{L\infty} \to T_c$ and provides better isolation of varying the initial salinity since it no longer affects the temperature scale.

Where this work refers to $\mathcal{C}$ or θ_∞, it will use the more common usage given in (2.3.14).

2.4 Thermohaline Coupling

The liquidus relationship (2.3.6a) provides a link between the salinity of a fluid parcel and the liquidus temperature of the same parcel which allows us to write equations involving the liquid salinity, S, in terms of the liquidus temperature,

θ_L. This is particularly useful within the mushy layer where local thermodynamic equilibrium dictates that the temperature is equal to the liquidus temperature.

The salinity equation, (2.3.5), can be re-written as:

$$\chi\frac{\partial\theta_L}{\partial t}+\boldsymbol{u}\cdot\boldsymbol{\nabla}\theta_L-(\Lambda+\theta_{L\infty}-\theta_L)\frac{\partial\chi}{\partial t}=\frac{1}{\mathcal{L}_e}\boldsymbol{\nabla}\cdot[\chi\boldsymbol{\nabla}\theta_L]\,. \tag{2.4.1}$$

I have written this in terms of the liquidus temperature θ_L to keep generality, but in the mushy phase, we can eliminate θ_L by enforcing the liquidus constraint, $\theta_L=\theta$.

In the liquid phase, we can only state that $\theta_L\leq\theta$, and without a strict equality, we cannot eliminate θ_L from the system. However, we can simplify the system by noting that $\chi=1$ throughout the liquid layer, leading to:

$$\frac{\partial\theta_L}{\partial t}+\boldsymbol{u}\cdot\boldsymbol{\nabla}\theta_L=\frac{1}{\mathcal{L}_e}\nabla^2\theta_L. \tag{2.4.2}$$

This is, perhaps unsurprisingly, a simple diffusion-advection equation with the liquidus temperature standing in as a proxy for salinity in a non-dimensionalised form of (2.1.20).

We also need to re-write the salinity boundary conditions so that they can be applied to the new dynamical liquidus equations:

$$\begin{aligned}&[\theta_L]^+_-=0, && [\boldsymbol{n}\cdot\boldsymbol{\nabla}\theta_L]^+_-=0, && \theta|_+=\theta_L|_+\,,\\ &&& \boldsymbol{n}\cdot\boldsymbol{\nabla}\theta_L|_+=\boldsymbol{n}\cdot\boldsymbol{\nabla}\theta|_+ && \text{at } z=h(t)\end{aligned}$$

$$\theta_L\to\theta_{L\infty} \qquad \text{as } z\to\infty.$$

This thermohaline expression of the salinity equations will be particularly useful in chapter 3 where we will use it to create an effective heat capacity for the mushy layer which includes the effects of latent heat release.

Combining (2.4.1) with (2.3.4a) allows the removal of χ as a prognostic field - it becomes diagnostic using the Lever rule (2.3.6b). The combined thermohaline evolution equation is:

$$\begin{aligned}\left(1+\frac{\mathcal{S}_t\chi}{\Lambda+\theta_{L\infty}-\theta}\right)\frac{\partial\theta}{\partial t}+\left(1+\frac{\mathcal{S}_t}{\Lambda+\theta_{L\infty}-\theta}\right)\boldsymbol{u}\cdot\boldsymbol{\nabla}\theta&\\ =\nabla^2\theta+\frac{\mathcal{S}_t}{\mathcal{L}_e\left(\Lambda+\theta_{L\infty}-\theta\right)}\boldsymbol{\nabla}\cdot[\chi\boldsymbol{\nabla}\theta]\,.&\end{aligned} \tag{2.4.3}$$

This is a dimensionless form of the effective thermal equation in Feltham et al. (2006), which has been expanded to also include salt diffusion. There is a clear impact from solidification and salinity on the heat capacity of the mushy layer, with the prefactors to both the evolution and advection terms increasing. This increase comes from the formation (or removal) of solid and the associated release (absorption) of latent heat, which increases the amount of energy which must be removed (added) to cool (warm) the mushy layer and so appears as an increased heat capacity. Note that the effect appears slightly differently in the evolution and advection terms since the reference heat capacity for static evolution includes a contribution to the heat capacity from the solid phase where as the reference heat capacity for advection does not.

The effect on the rate of thermal diffusion is less clean since the terms cannot be combined directly, but the enhancement to diffusion will typically be positive. The mechanism for this effect is similar to that described in Notz and Worster (2009) when discussing a method for brine transport in response to a thermal gradient, and is based on the diffusion of salt acting in the opposite direction to thermal diffusion. Salt diffuses against the thermal gradient, which causes dissolution of solid at the bottom of a liquid pocket and solidification at the top, as the mush adjusts to maintain local thermodynamic equilibrium at the two ends. This results in an effective upwards diffusion of solid, and therefore a similar transport of latent heat, which is the source of the effective thermal conductivity.

As $\mathcal{L}_e \to \infty$, the effective properties in (2.4.3) recover the form of temperature- and salinity-dependence given by Schwerdtfeger (1963) and Ono (1967), as discussed in Feltham et al. (2006), and have been shown to agree with empirically fitted bulk properties, such as those given by Untersteiner (1961). More recent studies to make use of these bulk properties include Butler (2011), who studied the rate at which thermal and saline fronts can propagate through a mushy layer.

2.5 A Solution to the Thermal Diffusion Equation

During the analysis, I will make use of the following solution to a general, one-dimensional diffusion equation:

$$\frac{\partial \theta}{\partial t} = \kappa^* \frac{\partial^2 \theta}{\partial z^2}.$$

When subject to the boundary condition (2.3.2l), the semi-infinite deep boundary condition (2.3.2a), a uniform initial condition ($\theta = 1$), the solution is given by:

$$\theta\left(z,t\right) = \Upsilon\left(z,t,\mathcal{B}_i,\kappa^*\right) = \operatorname{erf}\left(\frac{z}{2\sqrt{\kappa^* t}}\right) + \exp\left(\frac{-z^2}{4\kappa^* t}\right)\operatorname{erfcx}\left(\frac{z+2\mathcal{B}_i\kappa^* t}{2\sqrt{\kappa^* t}}\right), \tag{2.5.1}$$

as presented in Carslaw and Jaeger (1959). Here, $\operatorname{erfcx}\left(y\right) = \exp\left(y^2\right)\left[1-\operatorname{erf}\left(y\right)\right]$ is the scaled complimentary error function and Υ represents the general solution to the thermal diffusion equation that we will use when creating solutions in different settings. The general solution has two terms that contribute different behaviour to the solution.

For large arguments, y, the scaled complimentary error function tends to zero, $\operatorname{erfcx}\left(y\right) \rightarrow 0$, so the contribution of the second term in Υ is negligible and the solution takes the form:

$$\Upsilon\left(z,t,\mathcal{B}_i,\kappa^*\right) \approx \operatorname{erf}\left(\frac{z}{2\sqrt{\kappa^* t}}\right) \qquad \text{for } z+2\mathcal{B}_i\kappa^* t \gg \sqrt{\kappa^* t}. \tag{2.5.2}$$

I will refer to this as the perfectly conductive limit since one way to recover it is to have a perfectly conducting boundary with infinite Biot number. However, it can also be recovered at large times or distances, when $z+2\mathcal{B}_i\kappa^* t \gg \sqrt{\kappa^* t}$, with no constraint on the value of $\mathcal{B}_i$. The perfectly conductive limit depends only on the combination $z/2\sqrt{\kappa^* t}$, which is the natural, self-similar variable for the thermal diffusion equation with Dirichlet boundary conditions. It also leads us to the diffusive lengthscale, $\sqrt{\kappa^* t}$, which will appear throughout our analysis.

Studying the structure of (2.3.2l) suggests that $1/\mathcal{B}_i$ is also an important non-dimensional 'length' scale close to the surface boundary. Indeed, expanding Υ around $z = 0$ yields:

$$\Upsilon\left(z,t,\mathcal{B}_i,\kappa^*\right) \approx \operatorname{erfcx}\left(\sqrt{{\mathcal{B}_i}^2\kappa^* t}\right)\left(1+\mathcal{B}_i z + O\left(z^2\right)\right) \qquad \text{for } \mathcal{B}_i z \ll 1,$$

with first-order spatial variation clearly dependent on $\mathcal{B}_i z$. We can also read off the corresponding timescale $1/{\mathcal{B}_i}^2\kappa^*$.

We therefore have two relevant layers to the cooling problem: a deep layer which obeys the similarity solution of the thermal diffusion equation, following the $\sqrt{\kappa^* t}$ scale, and a boundary layer where the radiative cooling breaks the similarity behaviour but whose influence decays with $\mathcal{B}_i z$ and ${\mathcal{B}_i}^2\kappa^* t$.

2.6 Summary

The following chapters will each use a subset of the equations presented here for their investigations.

When investigating diffusive solidification in the next chapter, a two-domain model will be employed with thermal and salt diffusion in both phases, but there will be no velocity field, momentum transfer, or horizontal variation. Chapter 4 considers convection in an infinitely deep, non-reactive porous layer and will consider a subset of the mushy layer equations with momentum transfer but without solidification. It will also show that in this case, the effects of unequal thermal properties and thermal lag can be handled with a rescaling of the problem. Finally, chapter 5 investigates convective instability in the mushy layer, using the full dynamics of the mushy layer but parametrising the underlying liquid layer.

3
Diffusive solidification

In this chapter, I will look at the development of a mushy layer in the absence of convection or other fluid motion. This will naturally occur in settings where a binary alloy is cooled from below and rejects the dense component during solidification since both the thermal and compositional gradients are stabilising. It will also be found in the early stages of mushy layer growth where the thermal and/or compositional gradient is destabilising, but the build up of potential energy has not yet triggered the onset of convective overturning.

Diffusive growth of mushy layers has been studied previously for transient growth (e.g. Worster, 1986; Emms and Fowler, 1994) and steady-state growth (e.g. Worster, 1992b). However, in this chapter I aim to provide fresh insight into the growth and internal structure of mushy layers, particularly with respect to salt diffusion and imperfect boundary conduction, by performing a parameter sweep for a number of dynamically significant variables. This broad investigation allows us to identify regimes and limiting cases, while highlighting the results for specific parameter sets within these sweeps will allow comparisons to previous studies. Studying the depth of the mushy layer will allow us to make predictions for the growth rate of young sea ice and other mushy layers, while the internal structure has important implications for the development of convection within the mush. The internal structure of sea ice also has important implications for the mechanical and electrical properties of sea ice (Petrich and Eicken, 2010) and for biological activity in the ice (Vancoppenolle et al., 2013).

This chapter is structured in three parts, considering three different models of mushy layer development.

- In section 3.1, we consider a simplified model of the mushy layer dynamics which assumes that only a modest amount of internal solidification occurs and the liquid fraction only slightly deviates throughout the mushy layer. We use the simple model to investigate the impacts of effective thermal transport within the mush and salt diffusion.
- Section 3.2 looks at a mushy layer with appreciable solidification grown with a perfectly conducting thermal boundary condition. We will use this analysis to consider the effects of the liquidus curve and the release of latent heat within the mushy region.
- Finally, section 3.3 investigates the effect of imperfect boundary conduction on the growth of mushy layers. We will use both an extension to the simple model for imperfect conduction and numerical solutions to the full set of partial differential equations.

Since each model requires a different treatment of the dynamical equations and numerical method, the details of the model employed in each section are included within the sections themselves. A diagram of the general setup is provided in figure 2.2.

3.1 Simplified Model with Low Solid Fraction

Our first model of mushy layer growth will assume that very little solidification occurs, $\phi \ll 1$, which also means that variations in liquid fraction are small, with $\chi \approx 1$. However, we will retain the coupling of thermal and saline dynamics through changes to the small solid fraction, which will allow us to investigate the impact of solid formation and salt diffusion on the growing mushy layer.

3.1.1 Method

In the absence of salt diffusion, the bulk salinity remains constant and the Lever rule (2.3.6b) shows us that the liquid fraction remains high when $\Lambda \gg \theta_{L\infty}$. For finite Lewis number, the picture becomes more complicated, but we note that with little solidification occurring, salinity gradients and the rate of salt transport will be very small, so to a good approximation, we will still have that $\overline{S} \approx 1$, over short enough timescales. We evaluate this timescale in §3.1.1d.

3.1.1a High Liquid Fraction Regime

To determine the criteria for a high liquid fraction, we turn to the Lever rule, which states that:

$$\chi = \frac{\Lambda \overline{S}}{\Lambda + \theta_{L\infty} - \theta}. \qquad \text{(2.3.6b revisited)}$$

Salt diffusion will decrease the bulk salinity but we will assume that the bulk salinity remains largely unchanged, such that $\overline{S} \approx 1$. We will consider the validity of this approximation in §3.1.1d. The solid fraction is then given by:

$$\phi \approx \frac{\theta_{L\infty} - \theta}{\Lambda + \theta_{L\infty} - \theta}.$$

The criteria for ϕ to remain small is $\Lambda \gg (\theta_{L\infty} - \theta)$, but since $0 \leq \theta \leq \theta_{L\infty}$ in the mushy layer, it is sufficient that $\Lambda \gg \theta_{L\infty}$. This is consistent with previous studies that identify a criteria of the form $\mathcal{C} \gg 1$.

Applying the approximation $\Lambda \gg \theta_{L\infty} - \theta$ (and hence $\phi \ll 1$) to the coupled thermohaline equation (2.4.3) and neglecting flow results in:

$$(1 + \mathcal{S}_c) \frac{\partial \theta}{\partial t} = \left(1 + \frac{\mathcal{S}_c}{\mathcal{L}_e}\right) \frac{\partial^2 \theta}{\partial z^2}, \qquad (3.1.1)$$

where we have defined the compositional Stefan number:

$$\mathcal{S}_c = \frac{\mathcal{S}_t}{\Lambda} = \frac{L}{c_p \Gamma \hat{S}_\infty}.$$

This represents the ratio of latent heat to the freezing point depression and from data in §1.2.3 it has a value of approximately 30.

As discussed in §2.4, solidification and the salt content have two effects on the dynamics and the magnitude of these effects can be readily quantified in the high-liquid fraction regime. Firstly, the release of latent heat hinders the cooling of the mush by increasing the effective heat capacity to $1 + \mathcal{S}_c$, as noted by Worster (2000) and others. The second impact is the upward migration of brine pockets, and hence latent heat, through downward salt diffusion causing localised dissolution and solidification. This leads to an effective conductivity of $1 + \mathcal{S}_c/\mathcal{L}_e$. Based on the values of $\mathcal{S}_c$ and $\mathcal{L}_e$, we expect the increase in effective heat capacity to have a very large impact on the dynamics since $\mathcal{S}_c \gg 1$. The impact on the effective conductivity is often neglected since $\mathcal{L}_e \gg 1$, but is actually relatively modest with

$\mathcal{S}_c/\mathcal{L}_e = 1/6$.

Combining the two effects, we get an effective diffusivity given by:

$$\kappa^m = \frac{1 + \mathcal{S}_c/\mathcal{L}_e}{1 + \mathcal{S}_c}, \tag{3.1.2}$$

measured relative to the rate of thermal diffusion. We note that solidification reduces the thermal transport within the mushy layer, while salt diffusion enhances it.

3.1.1b Solution method

Together with the thermal (2.3.4a) and salinity (2.4.2) equations for the liquid phase, (3.1.1) completes the set of dynamical equations for our simplified system. Without any fluid motion and ignoring horizontal variation, these are all simple diffusion equations which allow a self-similar solution using the variable:

$$\tilde{z} = \frac{z}{\sqrt{t}}.$$

The time-evolving interface position, $h(t)$, is stationary in this self-similar coordinate system, and is given by:

$$\lambda = \frac{h(t)}{\sqrt{t}}. \tag{3.1.3}$$

While we have introduced λ as the self-similar interface position, the growth rate of the mush, $\partial h/\partial t$, is also proportional to λ, so we will use the terms 'interface position' and 'growth rate' interchangably when working in the self-similar coordinates.

To simplify notation, I introduce two parameters related to the non-dimensional diffusivities: $s = \sqrt{\mathcal{L}_e} = \sqrt{\kappa/D}$, for salt diffusion in the liquid phase, and $m = 1/\sqrt{\kappa^m}$, for the effective diffusivity in the mushy phase. The diffusivity of heat in the liquid phase is used as the reference value, as described in §2.3, so is scaled to 1. The solution to the diffusion equation, $\partial\theta/\partial t = a^{-2}\ \partial^2\theta/\partial z^2$, is given by $\bar{\Upsilon}\left(\tilde{z}, a\right) = \mathrm{erf}\left(a\tilde{z}/2\right)$.

Using the boundary conditions (2.3.2a,e,j&l), the temperature profiles are given by:

$$\theta\left(\tilde{z} \leq \lambda\right) = A\bar{\Upsilon}\left(\tilde{z}, m\right), \tag{3.1.4a}$$

$$\theta\left(\tilde{z} \geq \lambda\right) = 1 - \frac{1 - A\bar{\Upsilon}\left(\lambda, m\right)}{1 - \bar{\Upsilon}\left(\lambda, 1\right)}\left(1 - \bar{\Upsilon}\left(\tilde{z}, 1\right)\right), \tag{3.1.4b}$$

$$\theta_L\left(\tilde{z} \geq \lambda\right) = \theta_{L\infty} - \frac{\theta_{L\infty} - A\bar{\Upsilon}\left(\lambda, m\right)}{1 - \bar{\Upsilon}\left(\lambda, s\right)}\left(1 - \bar{\Upsilon}\left(\tilde{z}, s\right)\right). \tag{3.1.4c}$$

with two unknown parameters, A and λ. The latter of these can be found by using (2.3.2g&i) to eliminate A and give an implicit equation for λ;

$$\theta_{L\infty}\mathrm{erfcx}\left(\frac{\lambda}{2}\right) - \left(1 - \theta_{L\infty}\right)\frac{\mathrm{erf}\left(m\lambda/2\right)\exp\left(\left(m\lambda/2\right)^2\right)}{m} = \frac{\mathrm{erfcx}\left(s\lambda/2\right)}{s}. \tag{3.1.5}$$

The effects of salt diffusion within the liquid phase are fully contained within the term on the right of this equation, and which vanishes as the Lewis number, and s, increase to infinity. In this limit, the expression reduces to:

$$\frac{\theta_{L\infty}}{1 - \theta_{L\infty}}\mathrm{erfcx}\left(\frac{\lambda}{2}\right) = \frac{\mathrm{erf}\left(m\lambda/2\right)\exp\left(\left(m\lambda/2\right)^2\right)}{m}. \tag{3.1.6}$$

3.1.1c Numerical method

The reduced nature of the model in this section means that the growth rate can be found simply by using MATLAB's inbuilt `fzero` routine to solve (3.1.5) or (3.1.6) This routine is based on the algorithm in Forsythe et al. (1977) and uses a combination of the bisection, secant, and inverse quadratic interpolation methods.

3.1.1d Including Salt Diffusion

Including salt diffusion in the simplified model creates an issue at the surface. The thermal flux out of the system implies a salt flux into the system, while conservation of salt indicates that there should be no salt flux across the surface.

Physically, this is reconciled by returning to the brine-pocket model of salt diffusion. As brine pockets migrate downwards, they also transport solid upwards, which collects at the surface. Since the liquid salinity at the surface is fixed by the boundary temperature, the lever rule (2.3.6b) tells us that this decreased liquid fraction must come from a corresponding decrease in the bulk salinity, and the assumption that $\overline{S} \approx 1$ degrades. Eventually, this removal of salt leads to formation of a thin, completely solid layer at the surface, as studied by Worster (1986), and

Gewecke and Schulze (2011).

We can use this discrepancy in surface fluxes to get a measure of how accurate our approximation that $\overline{S} \approx 1$ is, and to determine a timescale over which this model remains valid. The salt flux into the mushy layer is given by:

$$\mathrm{SF} = -\frac{1}{\mathcal{L}_e}\left.\frac{\partial S}{\partial z}\right|_0 = \frac{mA}{\mathcal{L}_e \Lambda \sqrt{\pi t}},$$

and the integration constant, A, by:

$$A = \frac{1}{m\ \mathrm{erfcx}\left(\frac{\lambda}{2}\right)\exp\left(-\frac{(m\lambda)^2}{4}\right) + \mathrm{erf}\left(\frac{m\lambda}{2}\right)}.$$

By integrating this expression with respect to time, we get the total amount of salt "added" to the mushy layer by the anomalous flux through the boundary:

$$\mathrm{TSA} = \int_0^t \mathrm{SF}\ dt = \frac{2mA\sqrt{t}}{\mathcal{L}_e \Lambda \sqrt{\pi}}.$$

With more salt added, the bulk salinity $\overline{S}$ will deviate from 1 in the physical system, and the approximation that $\overline{S} \approx 1$ breaks down. This happens when the Lewis number is small, or time is large (as expected), but also when the liquidus gradient is small due to a greater amount of solidification and sharper gradients. Inhibiting thermal transport in the mush (increasing m) increases the thermal flux across the boundary and also results in a greater amount of salt added. There is also an increase in the amount of salt added as the thermal gradient, through the parameter A, increases since this will directly increase the salt flux.

A practical application of this would be to define a salt addition timescale as $t_{sa} = \pi\left(\mathcal{L}_e \Lambda / 2mA\right)^2$. We can expect the approximation $\overline{S} \approx 1$ to be accurate at leading order provided that $t \ll t_{sa}$.

3.1.2 Results

In this section we discuss the results from the simplified model. Firstly, we perform a parameter sweep without salt diffusion and consider the effects of the initial liquidus temperature, $\theta_{L\infty}$, and mushy diffusivity factor, m, on the growth rate of the ice. We then discuss the rate of salt diffusion (as measured by the Lewis number) necessary for it to have a significant effect on the dynamics. Finally, we consider a set of parameters appropriate for typical sea ice growth.

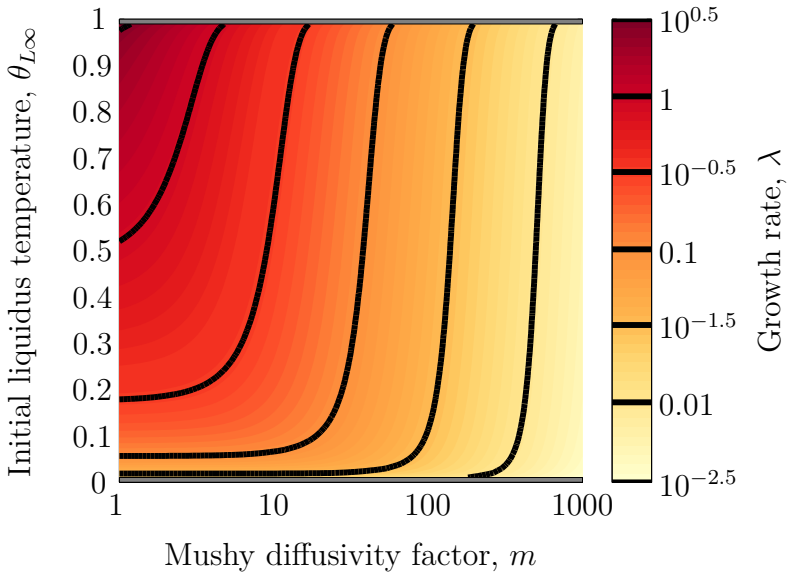

Figure 3.1: Mushy layer growth rates against the mushy diffusivity factor and initial liquidus temperature, in the absence of salt diffusion in the liquid phase, $\mathcal{L}_e \to \infty$. Increased m leads to a decreased growth rate and could be caused by increased $\mathcal{S}_c$ or decreased $\mathcal{L}_e$ in the mushy phase. An initial temperature close to the liquidus temperature (large $\theta_{L\infty}$) results in more mush growth than when the fluid starts a long way from its initial liquidus temperature (small $\theta_{L\infty}$). Contours are placed at half-powers of 10.

3.1.2a Without salt diffusion

To begin investigating the mushy layer growth using the simplified model, we first consider the case where $\mathcal{L}_e \to \infty$. Figure 3.1 plots the growth rates found by solving (3.1.6) which depends only on the two parameters to consider, $\theta_{L\infty}$ and m.

The growth rates show a clear decrease as the mushy diffusivity factor, $m = 1/\sqrt{\kappa^m}$, increases. This factor has an inverse dependence on the rate of thermal transport within the mush, κ^m, so we can see that increasing thermal transport within the mush (decreasing m) results in greater ice growth, due to the mushy layer being more effective at transferring sensible heat from the neighbouring fluid towards the top boundary.

In this simplified model and the absence of salt diffusion, the rate of thermal transport within the mush is dependent solely on the compositional Stefan number though its effect on the effective heat capacity (3.1.1). As $\mathcal{S}_c$ increases, latent heat release becomes more significant to the dynamics. This source of thermal energy within the mush inhibits the cooling rate of the liquid (by increasing m), resulting in a decreased ice growth rate. However, we note that if we allow salt diffusion

within the mushy layer, (3.1.2) tells us that salt diffusion enhances the thermal transport within the mush and this will lead to an increase in the growth rate of the mushy region.

Similarly, we can extrapolate this understanding of how changes to thermal transport affects mushy layer growth and note that many physical binary alloys, including salt water and aqueous $NaNO_3$, have an enhanced conductivity or decreased volumetric heat capacity, or both, in the solid phase relative to the liquid phase. The results of this simple model suggest that these effects will result in an enhanced growth rate as the faster thermal transport through the solid phase relative to the liquid enhances the thermal transport through the mushy layer as a whole. Indeed, this can be seen in figure 5 of Worster (1986) which uses equal thermal properties in both the solid and liquid phases, compared to figure 9 of Worster (1986) which has a solid phase with a thermal diffusivity 9.2 times greater than the liquid phase. The growth rates in the latter of these two figures are approximately double those in the first figure.

We also see in figure 3.1 that the growth rates increase as the initial liquidus temperature increases, although this effect is modest except for at the extremes of the range considered. When $\theta_{L\infty}$ is large, the initial liquidus temperature is close to the initial temperature, which means that less sensible heat needs to be removed from the fluid before mush can start to form, which increases the growth rate. As $\theta_{L\infty}$ approaches 1, the initial temperature approaches the liquidus temperature. The whole liquid therefore approaches its freezing temperature and, in the absence of an interface energy or kinematically limited crystal formation, the growth rate diverges to infinity. Small deflections of the contours are visible on the figure, but the divergence is not obvious. For small $\theta_{L\infty}$, most of the heat removed comes from sensible heat in the fluid. The growth rate approaches 0 as $\theta_{L\infty}$ approaches 0, because the fluid is no longer cooled below the liquidus temperature.

The dependence of the growth rate on the initial liquidus temperature is in agreement with previous studies. Figures 5 & 9 of Worster (1986) both plot the growth rate against different values of $T_\infty - T_{L\infty}$, representing the temperature difference across the liquid layer. He observes that increasing this temperature difference causes an increase in the growth rate, and this change is equivalent to increasing $\theta_{L\infty}$ which we also show increases the growth rate. Similarly in figure 8, he observes a decrease in the growth rate as $T_{L\infty} - T_c$ is decreased, which represents a decrease in

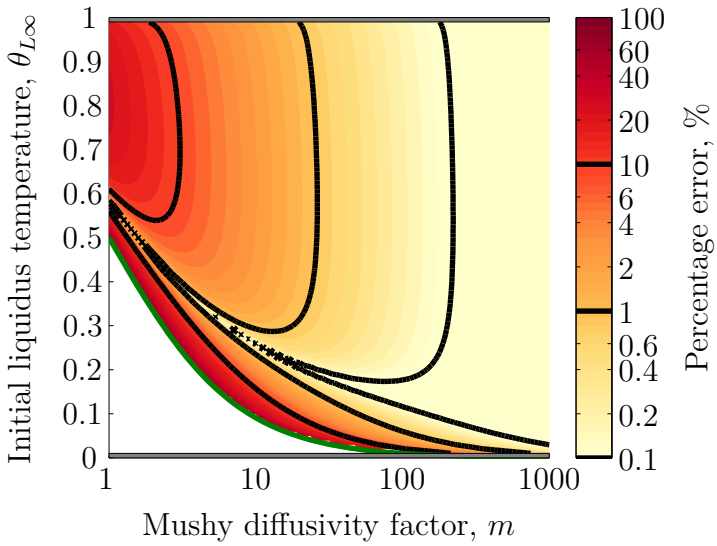

Figure 3.2: Percentage error of the approximate solution given in (3.1.8) compared to the exact solutions of (3.1.6), which are shown in figure 3.1. The black curves are the 10%, 1%, and 0.1% contours, while the green curve is give by $\theta_{L\infty}(m+1) = 1$, below which the approximate solution breaks down.

$\theta_{L\infty}$. This result is also echoed by Emms and Fowler (1994) in their figures 3 & 4, where they show that increasing the non-dimensional superheat, $\theta_\infty = 1/\theta_{L\infty} - 1$, decreases the growth rate, and by Huppert and Worster (1985) who found the same result experimentally.

When the superheat is small ($\theta_{L\infty}$ close to 1) Emms and Fowler (1994) give the approximate growth rate as:

$$\lambda = \frac{2}{m}\sqrt{\ln\left(\frac{\theta_{L\infty}}{1-\theta_{L\infty}}\right)}, \tag{3.1.7}$$

but this approximation appears to be of limited precision. Instead, we find that when the mushy diffusivity factor is large the growth rate is small, yielding $\operatorname{erfcx}(\lambda/2) \approx 1$. However, $m\lambda \sim O(1)$ so to a reasonable approximation $\operatorname{erf}(m\lambda/2) \sim 1$. We can then simplify (3.1.6) to give:

$$\lambda = \frac{2}{m}\sqrt{\ln\left(\frac{m\theta_{L\infty}}{1-\theta_{L\infty}}\right)}, \tag{3.1.8}$$

which is similar to (3.1.7) but includes a factor of m multiplying the superheat, $\theta_{L\infty}/(1-\theta_{L\infty})$. This approximation slightly overestimates the growth rates for most of the parameter space, but figure 3.2 shows that the level of agreement is generally very good, with the accuracy improving as the mushy diffusivity factor

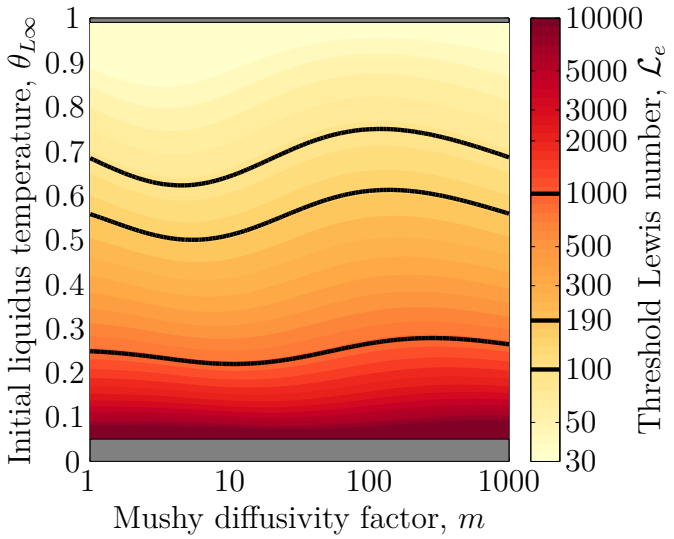

Figure 3.3: Shown here is the Lewis number above which the effect of salt diffusion in the liquid region yields less than a 1% change to the growth rate. The black contours highlight Lewis numbers of 100, 190, and 1000 (from the top), where 190 is the approximate Lewis number for salt water. Small Lewis numbers for large values of $\theta_{L\infty}$ indicate salt diffusion in the liquid has a very minimal impact on the growth rate, compared to smaller values of $\theta_{L\infty}$ where even slow salt diffusion ($\mathcal{L}_e \gg 1$) can affect the growth rate significantly. This figure assumes that there is no salt diffusion in the mushy phase.

increases.

3.1.2b Including salt diffusion

To determine the impact of salt diffusion within the liquid phase, we return to (3.1.5) and investigate the effects of finite $\mathcal{L}_e$ (ie. finite s). I solved this equation for a range of Lewis numbers and found that salt diffusion within the liquid phase always resulted in a decrease in the growth rate. This is a result of the formation of a compositional boundary layer ahead of the mush-liquid interface, which decreases the local liquidus temperature, analogous to how Huppert and Worster (1985) found a compositional boundary layer preceding a planar solidification interface. A greater amount of sensible heat then needs to be removed from the liquid before it can begin to solidify, and this decreases the growth rate in the same way that decreasing $\theta_{L\infty}$ inhibits growth.

Figure 3.3 shows the Lewis number in the liquid phase needed to give a 1% decrease in the growth rate, when compared to the growth rate for infinite Lewis number. For now, I am continuing to assume that there is no salt diffusion in the mushy

phase. The value plotted in figure 3.3 can be thought of as a threshold for the Lewis number - if the physical Lewis number is higher than the Lewis number given here, then the effects of salt diffusion within the liquid can be neglected with $< 1\%$ error in the growth rate. We can see that for large values of $\theta_{L\infty}$, very fast salt diffusion (small $\mathcal{L}_e$) is needed to impact the growth rate significantly, while for small values of $\theta_{L\infty}$, even slow salt diffusion can affect the growth rate. In sea ice, the Lewis number is 190, so we can see that salt diffusion will affect the growth rate for $\theta_{L\infty} \gtrsim 0.5$.

To understand how salt diffusion in the liquid phase and the resulting compositional boundary layer affect growth, we consider the energy budgets in the two different cases. When $\theta_{L\infty}$ is large then $T_\infty \approx T_{L\infty}$ and most of the energy removed comes from within the mush. Hence, the extra energy that needs to be removed to cool the fluid through the compositional boundary layer remains small compared to the amount of energy which can be removed from the mush. With only a small change in the energy being removed from the mush, there is a minimal change in the growth rate, even for relatively fast salt diffusion and a large compositional boundary layer. Conversely, when $\theta_{L\infty}$ is small, most of the energy being removed through the top boundary originates from the fluid layer, and there is very little energy removed from the mush. The extra energy needed to cool the fluid in the compositional boundary layer is therefore significant compared to the energy that needs to be removed from the mush to continue growth. Hence, diffusion strongly impacts the growth rate for small $\theta_{L\infty}$.

However, we also saw in §3.1.1a that salt diffusion enhances thermal transport within the mushy layer, and noted in §3.1.2a that this will increase the ice growth rate. Figure 3.4 repeats the calculation from figure 3.3 but now includes salt diffusion within the mush as well as in the liquid phase. The horizontal axis is now given in terms of the compositional Stefan number since m varies with $\mathcal{L}_e$.

We now have two competing effects. To the left of the green line in figure 3.4, the effect of salt diffusion in the liquid phase is greater than the effect of diffusion within the mush, leading to a net decrease in growth rate compared to growth without salt diffusion. The behaviour here has already been discussed in terms of the compositional boundary layer. However, to the right of this line, salt diffusion in the mush is the dominant effect, and the growth rate is increased relative to growth

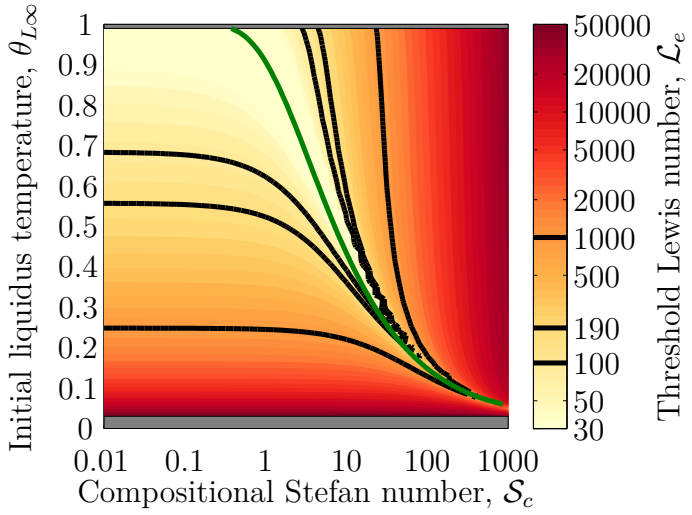

Figure 3.4: Shown here is the Lewis number above which the effect of salt diffusion in both phases becomes negligible, according to a threshold set at a 1% change to the growth rate. The black contours highlight Lewis numbers of 100, 190, and 1000 (from the top left), where 190 is the approximate Lewis number for salt water. To the left of the green line, the growth rate is decreased and to the right it is increased. As well as salt diffusion becoming more dynamically significant as $\theta_{L\infty}$ decreases (see figure 3.3), we see that its effect also increases as the compositional Stefan number increases with salt diffusion enhancing the thermal diffusion within the mush.

---

without salt diffusion. The behaviour in this regime comes from the influence of the Lewis number on the effective thermal diffusivity:

$$\kappa^m = \frac{1 + \mathcal{S}_c/\mathcal{L}_e}{1 + \mathcal{S}_c}. \qquad \text{(3.1.2 revisited)}$$

For large compositional Stefan numbers and $\mathcal{S}_c/\mathcal{L}_e > O(1)$, the amount of sensible heat corresponding to the freezing point depression is small compared to the latent heat release during solidification. The rate of sensible heat diffusion is also small compared to the effective thermal transport from salt diffusion via the movement of latent heat. The thermal balance for the mush therefore depends primarily on the rate at which the released latent heat can be diffused away through salt transport, and the effective mushy diffusivity is approximately given by $1/\mathcal{L}_e$. This therefore leads to the very strong dependence of the growth rate on changes in the rate of salt diffusion, giving high threshold Lewis numbers on the right of figure 3.4. Thus for $\mathcal{S}_c/\mathcal{L}_e \gg 1$, even slow salt diffusion can dramatically impact the dynamics.

3.1.2c Realistic values

In §3.1.1a, we assign a value to the compositional Stefan number, $\mathcal{S}_c = 30$, for 35psu salt water and in §1.2.3 we give the Lewis number, $\mathcal{L}_e$, a value of 190. This leads

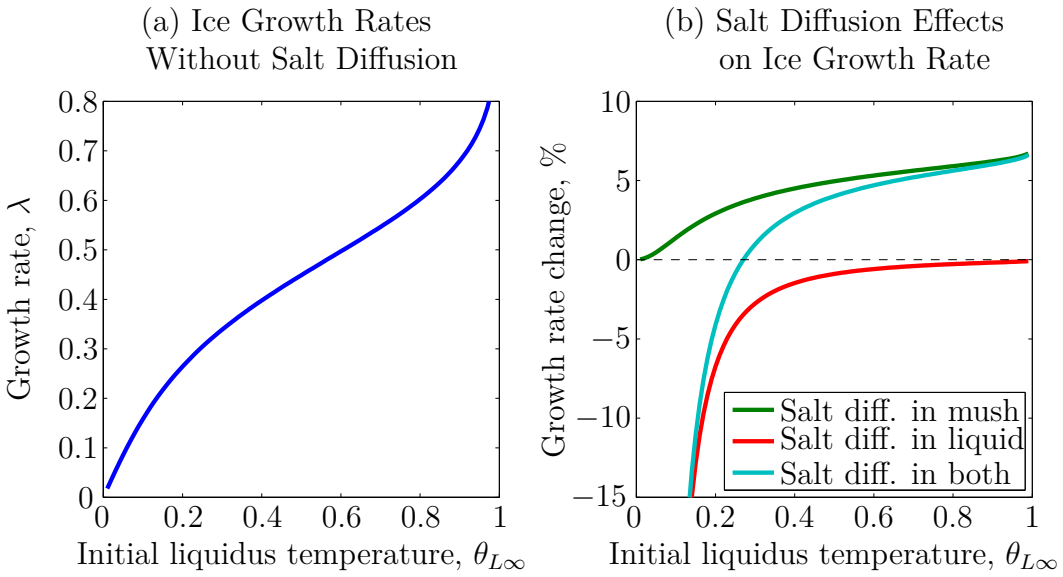

Figure 3.5: (a) Dimensionless ice growth rates, $\lambda = h(t)/2\sqrt{\kappa \hat{t}}$, for $\mathcal{S}_c = 30$, $\mathcal{L}_e = \infty$, and a range of $\theta_{L\infty}$. (b) The corrections to the growth rate when salt diffusion is included with a Lewis number of $\mathcal{L}_e = 190$. Salt diffusion in the mushy phase is the dominant correction for $\theta_{L\infty} > 0.25$ and increases the growth rate by $3 - 7\%$. Salt diffusion in the liquid phase becomes important for low values of $\theta_{L\infty}$ and can decrease the growth rate by up to 15%. The combined effect of diffusion in both phases can be approximated by the sum of the individual correction; although this is not shown in the figure.

to a mushy diffusivity factor of $m = 5.2$ with salt diffusion and $m = 5.6$ without. The growth rates for $m = 5.6$ and the effects of salt diffusion at these values are shown in figure 3.5 for a range of initial liquidus temperatures.

When salt water at 0^oC and 35psu is cooled to -20^oC, the initial liquidus temperature is $\theta_{L\infty} = 0.9$. The dimensionless ice growth rate would therefore be $\lambda = 0.69$ which corresponds to 56cm of ice growth over 60 days. However, including salt diffusion increases λ to 0.72 and adds a further 3cm to the ice depth over the same 60 day period. While there is no data available to compare the results to for a 60 day growth period, reasonable agreement can be found with the laboratory experiments of Wettlaufer et al. (1997). This study describes in detail the solidification of a 70psu salt solution when cooled from -2^oC to -20^oC, with the salt content giving an initial liquidus temperature of -4^oC. They found that there was 6.4 ± 0.2cm of ice after 400 minutes, while the simple model prediction for $\theta_{L\infty} = 0.89$, $\mathcal{S}_c = 14$, and $\mathcal{L}_e \to \infty$ is 5.1cm, which is similar but with room for improvement. However, $\Lambda = 0.37\theta_{L\infty}$ for this experiment which suggests we are outside the region of applicability for the simple model.

3.1.3 Summary and Discussion

The simplified model assumes that the solid fraction remains small throughout the mushy layer. This approximation will not always hold during sea ice growth but has allowed us to investigate a number of aspects of the system by simplifying some of the complications.

Increasing the initial liquidus temperature decreases the amount of sensible heat which must be removed from the system before it can begin to solidify; this increases the growth rate of the ice. Figure 3.1 also shows that increasing the effective mushy diffusivity, defined in (3.1.2), and therefore decreasing m, leads to a increase in the ice growth rate. The effective diffusivity depends on the release of latent heat, which contributes to a modified effective heat capacity and therefore decreases ice growth. It also depends on the diffusion of brine pockets by salt diffusion, which contributes to an effective thermal conductivity through the movement of latent heat and increases the ice growth rate. From this result, we expect that a material with a decreased heat capacity, or an increased thermal conductivity, in its solid phase will also experience an enhanced growth rate, in line with results presented in Worster (1986).

The changes to the growth rate caused by varying diffusion in the mush are much greater than those caused by varying the initial liquidus temperature, $\theta_{L\infty}$, which represents the temperature difference across the mushy layer relative to the global temperature difference. However, it was still possible to demonstrate that increasing the initial liquidus temperature increases the growth rate of the mushy layer. This is because less sensible heat needs to be removed from a fluid parcel before it reaches the liquidus temperature and can solidify, a result in line with the observations of Worster (1986) and Emms and Fowler (1994).

I also investigated the effect of salt diffusion within the liquid phase and noted that this decreases the growth rate of the ice by forming a compositional boundary layer close to the mush-liquid interface. The boundary layer decreases the local liquidus temperature and increases the amount of sensible heat which must be removed from the liquid before it can begin to solidify. This effect is greatest when $\theta_{L\infty}$ is small and the surface heat flux is predominantly used to cool the liquid. In this regime even a small change in the amount of energy which can be removed from the growing mushy layer represents a significant proportion of the solidification budget.

When salt diffusion effects in both phases are considered, the compositional boundary layer effect is dominant and decreases the growth rate for smaller $\mathcal{S}_c$. However, the increased effective transport due to salt diffusion in the mush is dominant and increases the growth rate when $\mathcal{S}_c/\mathcal{L}_e$ is larger.

This simple model makes a reasonable prediction of 61cm of ice growth over 60 days for Arctic conditions, but underestimates the ice growth over 400 minutes that was observed by Wettlaufer et al. (1997) for 70psu salt water in the lab. The low solid fraction approximation requires $\Lambda \gg \theta_{L\infty}$, but for the Wettlaufer experiment $\Lambda = 0.37\theta_{L\infty}$, and $\Lambda = 0.17\theta_{L\infty}$, for Arctic conditions so we expect the accuracy of the results to be limited.

3.2 Mush with Perfect Boundary Conduction

The second part of this investigation relaxes the requirement that the solid fraction is small and solves the mushy layer equations directly using a shooting method. The aim here will be to systematically investigate the changes in growth and internal structure to build further insight into how these interact and how they are affected by external conditions. We will ignore the effects of salt diffusion and initially focus on the case of perfect boundary conduction ($\mathcal{L}_e \to \infty$ and $\mathcal{B}_i \to \infty$ throughout this section).

This section has a number of similarities to Worster (1986), who investigated how the growth rate varied as the temperature and salinity scales are changed. As well as presenting comparible results in our non-dimensional formulation, we further Worster's results by considering the effects of varying multiple parameters simultaneously to gain better understanding of the system as a whole. Our study also provides a detailed discussion of changes to the internal structure of the mushy layer, and investigates the effects of latent heat, through the Stefan number.

3.2.1 Method

With non-negligible solid fractions the thermodynamical equations for the mushy layer now form a non-linear system but can be solved when there is a perfectly conducting upper boundary using a self-similarity transformation and a numerical shooting method (Press et al., 1992).

To formulate the equations in the self-similarity form, we start by defining the self-similar vertical coordinate $\tilde{z} = z/\sqrt{t}$. Vertical and time derivatives are expressed in this new coordinate system by:

$$\frac{\partial}{\partial z} = \frac{1}{\sqrt{t}}\frac{\partial}{\partial \tilde{z}} \qquad \frac{\partial}{\partial t} = \frac{-\tilde{z}}{2t}\frac{\partial}{\partial \tilde{z}},$$

and equation (2.3.4a) becomes:

$$0 = \frac{\partial^2 \theta}{\partial \tilde{z}^2} + \frac{\tilde{z}}{2}\frac{\partial \theta}{\partial \tilde{z}} + \frac{\mathcal{S}_t \tilde{z}}{2}\frac{\partial \chi}{\partial \tilde{z}}.$$

To evaluate $\frac{\partial \chi}{\partial \tilde{z}}$, we differentiate the Lever rule (2.3.6b) with respect to $\tilde{z}$ to get:

$$(\Lambda + \theta_{L\infty} - \theta)\frac{\partial \chi}{\partial \tilde{z}} = \chi \frac{\partial \theta}{\partial \tilde{z}}.$$

The resulting system of equations can be written as:

$$\begin{bmatrix} 1 & 0 & 0 \\ 0 & 1 & \frac{\mathcal{S}_t \tilde{z}}{2} \\ 0 & 0 & \Lambda + \theta_{L\infty} - \theta \end{bmatrix} \begin{bmatrix} \frac{\partial \theta}{\partial \tilde{z}} \\ \frac{\partial \theta_g}{\partial \tilde{z}} \\ \frac{\partial \chi}{\partial \tilde{z}} \end{bmatrix} = \begin{bmatrix} \theta_g \\ -\frac{\tilde{z}\theta_g}{2} \\ \chi \theta_g \end{bmatrix},$$

where $\theta_g = \frac{\partial \theta}{\partial \tilde{z}}$.

The system is also subject to the boundary conditions (2.3.2a,e,j,g&l), which with no salt diffusion, $\mathcal{L}_e \to \infty$, and perfect conduction, $\mathcal{B}_i \to \infty$, become:

$$\theta(0) = 0 \qquad \text{at } \tilde{z} = 0, \tag{3.2.1a}$$

$$\theta\left(\lambda^-\right) = \theta\left(\lambda^+\right) = \theta_{L\infty}, \qquad \left.\frac{\partial \theta}{\partial \tilde{z}}\right|_- = \left.\frac{\partial \theta}{\partial \tilde{z}}\right|_+ \qquad \text{at } \tilde{z} = \lambda, \tag{3.2.1b-d}$$

$$\theta \to 1 \qquad \text{as } \tilde{z} \to \infty. \tag{3.2.1e}$$

This system was solved using a shooting method (Press et al., 1992), implimented with MATLAB's `ode45` routine, which uses the Dormand-Prince fourth order Runge-Kutta method, originally described in Dormand and Prince (1980). The `ode45` routine solves an initial value problem (IVP) in $\tilde{z}$, so the surface boundary is overspecified by also setting the temperature gradient and liquid fraction at $\tilde{z} = 0$. The ODE routine was then used to integrate the dynamical equations across the mushy region to a depth determined by the initial guess of the interface position. At the interface, the output was combined with the boundary conditions (3.2.1b,d) and used to initialise a similar integration across the liquid region to some fixed depth chosen to not affect the calculation results. Finally, the values produced for the temperature and liquid fraction at the interface, as well as the far-field temperature, where used to update the interface position and the initial temperature gradient and liquid fraction, until the boundary conditions (3.2.1) are all satisfied. This updating procedure for the initial guess was done using the `fsolve` routine that uses a trust-region dogleg algorithm similar to that of Powell (1970) and Moré et al. (1980).

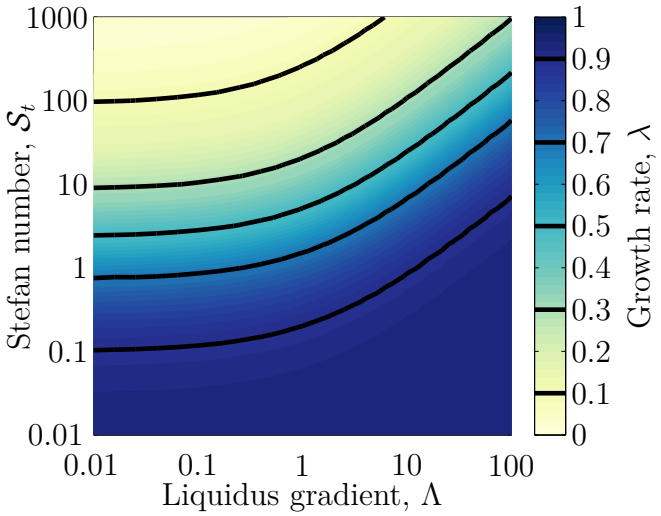

Figure 3.6: The mushy layer growth rates calculated for the full dynamics as a function of the liquidus gradient, Λ, and Stefan number, $\mathcal{S}_t$, for $\theta_{L\infty} = 0.5$. Increasing the liquidus gradient increases the ice growth rate, whilst increasing the Stefan number decreases the growth rate. For $\Lambda \lesssim 0.3$, the thermal Stefan number, $\mathcal{S}_t$, is the dominant parameter but for $\Lambda \gtrsim 0.3$ the compositional Stefan number, $\mathcal{S}_c = \mathcal{S}_t/\Lambda$, is dominant. While the position of the growth rate contours varies with the liquidus gradient, their spacing does not vary.

3.2.2 Results

Our investigation into the mushy layer dynamics in the case of a perfectly conducting boundary will focus on two interesting features illustrated in figure 3.6, which is a plot of the dimensionless mush growth rate, λ, against liquidus gradient and Stefan number. The first is the two distinct regimes for large and small values of the liquidus gradient with a transition between the two occurring approximately when $\Lambda \approx 0.3$. For small values of Λ, the growth rate is independent of Λ but for larger values, increasing Λ also increases the growth rate. This behaviour also holds for different values of $\theta_{L\infty}$, although the position of the transition varies, and an explanation in terms of the liquid fraction profiles is presented in §3.2.2a.

The second feature, which is discussed in §3.2.2c is the observation that while the growth rate contours vary with Λ, their relative spacing in $\mathcal{S}_t$ is not affected. To understand this observation, we consider the effect of latent heat on the growth rate and how it interacts with both the initial liquidus temperature and liquidus gradient.

3.2.2a Liquid fraction regimes

Figure 3.6 shows that the growth rate decreases as the Stefan number increases and increases as the liquidus gradient increases. As we saw in §3.1.2a, increasing

the Stefan number reduces the growth rate because more latent heat is released by solidification. Similarly decreasing Λ for a fixed initial liquidus temperature will increase the amount of solidification which occurs because the $\theta_{L\infty} - \theta$ term in the Lever rule (2.3.6b) becomes more significant. This increases the amount of latent heat released and depresses the growth rate. However, figure 3.6 also shows that this behaviour is not uniform throughout the parameter space and that there are two regimes of behaviour, with the transition when $\Lambda \approx 0.3$.

For $\Lambda \gtrsim 0.3$, the contours of λ are roughly parallel to the contours of $\mathcal{S}_t/\Lambda$, which defines the compositional Stefan number, $\mathcal{S}_c$. We identify this regime with the high liquid fraction regime that features in the discussion of the simplified model (see §3.1). As the liquidus gradient increases, the growth rate becomes increasing dependent on only the compositional Stefan number. In this regime, the range of temperatures in the domain is not sufficient to produce significant variations in the liquid salinity and very little solid forms, resulting in the linearised dynamics of the simple model from §3.1.

In the other regime, $\Lambda \lesssim 0.3$, we find that the contours of λ are roughly parallel to the contours of constant $\mathcal{S}_t$, indicating that the growth rate is largely independent of the liquidus gradient. We later argue that this limit approaches the two-phase Stefan problem as $\Lambda \to 0$.

The surface liquid fraction shown in figure 3.7 is a useful diagnostic tool since the liquid fraction will be lowest at the surface, allowing us to place an upper bound on the amount of solidification which occurs. The curve shown is given by:

$$\chi(0) = \frac{\Lambda}{\Lambda + \theta_{L\infty}}, \tag{3.2.2}$$

which is found from (2.3.6b) by setting $\theta = 0$ and $\overline{S} = 1$. The surface liquid fraction depends only on the ratio $\Lambda/\theta_{L\infty}$, which is linked to the $\mathcal{C}$ parameter of previous studies (see §2.3.1 and Worster, 1991). This figure also shows a transition as the liquidus gradient increases, with the mid-point of the transition occurring for $\Lambda \approx \theta_{L\infty}$.

For large liquidus gradients, the liquid fraction at the surface is:

$$\chi(0) \approx 1 - \frac{\theta_{L\infty}}{\Lambda} \qquad \text{for } \Lambda \gg \theta_{L\infty}, \tag{3.2.3a}$$

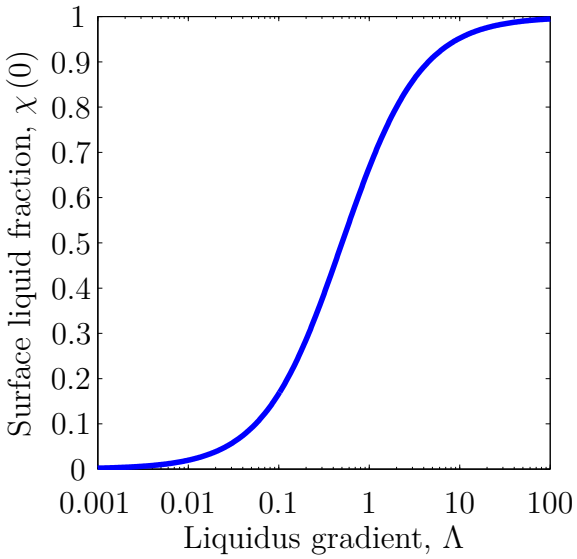

Figure 3.7: A plot of the liquid fraction at the upper boundary against the liquidus gradient, for $\theta_{L\infty} = 0.5$ and independent of $\mathcal{S}_t$. There is a clear transition from a mushy region with very little liquid (at the top of the layer) for small Λ to a mush with lots of liquid for large Λ, with the transition occurring when $\Lambda \approx \theta_{L\infty}$.

---

and we know the liquid fraction deeper in the mush must be higher than this value, supporting the link between the large liquidus gradient behaviour of figure 3.6 and the simplified dynamics in §3.1.

However, for small liquidus gradients the surface liquid fraction becomes:

$$\chi(0) \approx \frac{\Lambda}{\theta_{L\infty}} \qquad \text{for } \Lambda \ll \theta_{L\infty}, \tag{3.2.3b}$$

and the liquid fraction will vary between this and $\chi = 1$ over the depth of the mush. As a result, we cannot state that $\phi \ll 1$ through the mush and the dynamics will differ significantly from the high liquid fraction limit.

Figure 3.6 suggests the transition between regimes occurs when $\Lambda \approx 0.3$ while figure 3.7 suggests a transition around $\Lambda \approx \theta_{L\infty}\,(= 0.5)$. The transitions are smooth in both cases and are close to each other, so the results are in agreement. Figure 3.8a provides more detail by allowing us to consider the liquid fraction throughout the mushy region.

Using the red $\chi = 0.5$ contour to roughly indicate the low solid fraction regions (bluer) and high solid fraction regions (whiter), we can see that for $\Lambda > \theta_{L\infty}$ (with $\theta_L = 0.5$ in this figure), the whole mushy layer is less than 50% solidified. This

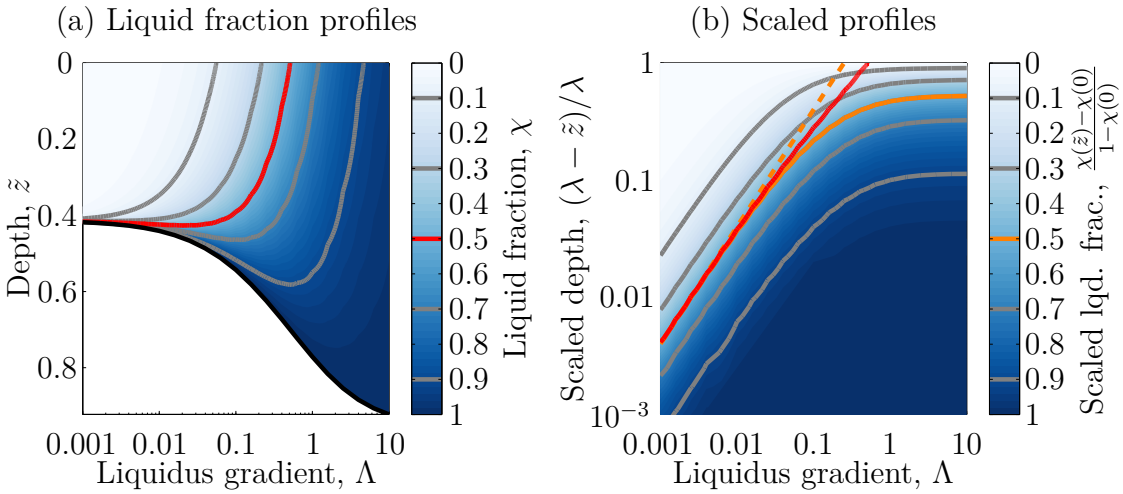

Figure 3.8: This figure shows the liquid fraction profiles at a range of liquidus gradients for $\mathcal{S}_t = 4.0$, $\theta_{L\infty} = 0.5$, and $\mathcal{L}_e = \infty$. (a) The vertical axis is the self-similar depth of the system with the black curve representing the mush-liquid interface. (b) The vertical axis has been scaled by the mushy layer depth, $(\lambda - \tilde{z})/\lambda$, and is displayed on a logarithmic scale. Note the vertical orientation is unchanged and points further down the page are still closer to the mush-liquid interface. The liquid fraction data has also been rescaled such that the liquid fraction takes a scaled value of zero at the surface and one at the interface, $(\chi(\tilde{z}) - \chi(0))/(1 - \chi(0))$. In both plots, the solid red curve represents the $\chi = 0.5$ contour while in (b) the solid orange curve represents a value of 0.5 on the compensated scale and the dashed orange curve is the limiting trend of $(1 - \tilde{z}/\lambda) = 4.0\Lambda$.

agrees with figure 3.6, where for $\Lambda \gtrsim 1$, the growth rate is only dependent on $\mathcal{S}_c$, which we would expect to find in the high liquid fraction limit (as discussed in §3.1).

However, for $\Lambda < \theta_{L\infty}$, there is a transition region with the upper part of the mush lying in the high solid fraction regime, and the lower part in the low solid fraction regime. Not until $\Lambda \approx 0.02$ do we find that the high solid fraction regime dominates the mush. This also agrees with the results in figure 3.6, which show steady behaviour for $\Lambda \lesssim 0.02$ and the transition for $0.02 \lesssim \Lambda \lesssim 1$.

To further understand this regime with small liquidus gradient, Λ, we look to figure 3.8b, which shows a compensated version of figure 3.8a, with depths scaled by the mushy layer depth and the liquid fraction scaled by the change in liquid fraction between the interface and the surface. As in figure 3.8a, we see that for small Λ the small-liquid-fraction region becomes increasingly dominant. However, we are now able to consider the behaviour close to the interface.

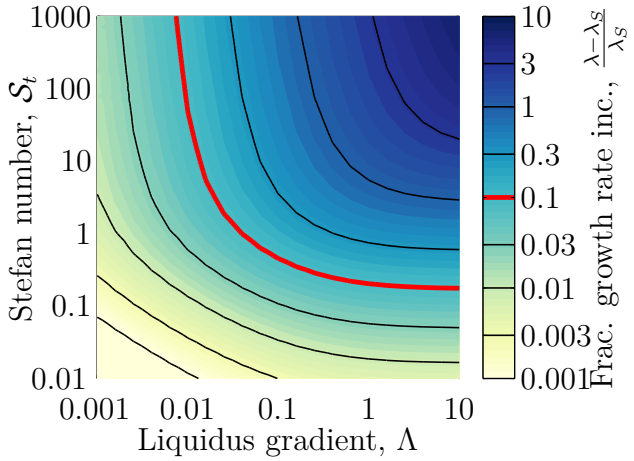

Figure 3.9: This figure plots the fractional difference of the growth rate from the growth rate given by two-phase Stefan problem for a pure fluid, λ_S, when $\theta_{L\infty} = 0.5$. The measured difference decreases as Λ decreases, indicating that this is the correct limiting behaviour. Highlighted in red is the 0.1 contour, which indicates a 10% difference.

While the size of the high liquid fraction region decreases rapidly as Λ decreases, it does not ever vanish. We can approximate the behaviour as a liquid region and a region of high solid fraction, separated by an interface region of finite thickness. Introducing the half-solidification depth, f_χ, as the fraction of the mushy layer depth which has $\chi \geq 0.5$, the rough thickness of this interface region as a fraction of the whole depth is:

$$f_\chi = 4.0\Lambda, \tag{3.2.4}$$

with the vast majority of solidification occurring within this interface region, although this will vary with $\theta_{L\infty}$ and $\mathcal{S}_t$. As $\Lambda \to 0$ this mushy interface becomes vanishingly small, with the liquid fraction jumping from 1 to 0 at the interface. It is not possible to study the zero liquidus gradient limit of $\Lambda = 0$ within the mushy layer framework because the Lever rule (2.3.6b) yields $\chi = 0$ everywhere. However, this is the same as the classic two-phase Stefan problem for a pure fluid (as discussed in §1.3) which describes a liquid and solid region separated by a sharp solidification interface. We will therefore refer to the small Λ regime as the *Stefan limit*.

To verify this explanation, figure 3.9 plots the relative difference between the mushy growth rates, λ, and those given by solving the two-phase Stefan problem for a pure fluid, λ_S. It supports the argument that this is the correct limiting behaviour

since this measure of the error decreases as Λ decreases according to:

$$\frac{\lambda - \lambda_S}{\lambda_S} \approx A\Lambda^b,$$

where A and b fitted empirically using a least-squared method. We find that $b \approx 0.8 - 0.85$ and A ranges roughly from 0.1 to 3, increasing with $\mathcal{S}_t$. The increase of A with $\mathcal{S}_t$ is unsurprising since $\mathcal{S}_t$ represents the relative size of the latent heat within the system. For large $\mathcal{S}_t$, there is a large amount of latent heat, so solidification will play a major part in determining the growth rate of the system, leading to a large A. However, for small $\mathcal{S}_t$, latent heat is only a minor feature so the growth dynamics will be far less affected by the internal solidification, leading to a small A. Indeed, for $\mathcal{S}_t = 0$ the growth rate becomes completely independent of Λ, and the amount of internal solidification plays no active role in determining the growth rate of the system, with $A = 0$.

The decreasing size of the interface region in the Stefan limit (figure 3.8b and eq. 3.2.4) explains why we do not observe any significant variation of growth rate, λ, and liquid fraction, χ, with Λ in figures 3.6 & 3.8a for small Λ. For $\Lambda \lesssim 0.02$, most of the internal solidification is confined to a region which is too small ($< 10\%$ of the total mush depth) to have a controlling influence on the dynamics of the system. As a coarse first approximation, the high liquid fraction region can be treated as a sharp interface for $\Lambda \ll 1$. The finite interface thickness does have some influence on the growth of the system, as shown by figure 3.9, but this produces $< 10\%$ change to the growth rate for $\Lambda \approx 0.02$ so it is not noticable in the earlier figures.

3.2.2b Initial liquidus temperature effects

We have so far only considered the effect of Λ on the developing mushy layer and noted two distinct limits, but we know from (2.3.6b) and (3.2.2) that $\theta_{L\infty}$ is also important in determining the liquid fraction.

Figure 3.10 plots the growth rate against both Λ and $\theta_{L\infty}$, for a fixed value of $\mathcal{S}_t$. We can immediately see that increasing $\theta_{L\infty}$ also increases the growth rate of the mushy layer. This was noted in §3.1.2a for the high liquid fraction regime, but it is clear that it holds for all values of Λ. The previous discussion argued that the difference between the initial fluid temperature and its initial freezing temperature is given by $1 - \theta_{L\infty}$, so a larger value of $\theta_{L\infty}$ means that the fluid starts closer to its

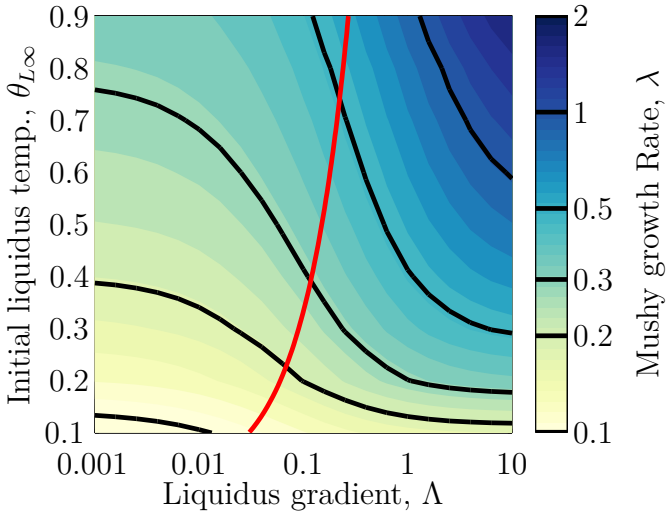

Figure 3.10: The mushy layer growth rates against Λ and $\theta_{L\infty}$ for $\mathcal{S}_t = 15.8$. Shown in red is the $\Lambda = 0.3\theta_{L\infty}$ curve which roughly indicates the inflection points of the contours of constant growth rate. This curve therefore roughly indicates the location of the transition from the Stefan limit to the high liquid fraction limit by marking their region of influence.

---

initial freezing temperature. This in turn means there is a reduction in the amount of sensible heat which needs to be removed to cool a parcel of fluid to the point where it begins to solidify, which allows more sensible and latent heat to be removed from parcels which are already solidifying. Since this explanation is independent of the liquidus gradient, increasing $\theta_{L\infty}$ always increases the growth rate, as seen in figure 3.10.

The growth rate trends in figure 3.10 can also be compared to Huppert and Worster (1985) and Worster (1986). Both studies observed (experimentally and analytically respectively) that increasing the initial concentration decreases the growth rates of the mushy layer. This will increase the liquidus gradient, defined as $\Lambda = \Gamma\hat{S}_\infty/\Delta T$, which provides a tendency to increase the growth rate as less solid forms and less latent heat is released. However, without a compensatory change in temperature scales, the initial liquidus temperature, $\theta_{L\infty} = (T_{L\infty} - T_c)/\Delta T$, will decrease as $T_{L\infty}$ decreases. As a result, there is a tendency for the growth rate to decrease because more sensible heat must be removed from fluid parcels before they can solidify. When the concentration is varied for constant temperatures, it is clearly the increased removal of sensible heat which has a greater impact on the growth rate than the decreased removal of latent heat which has a greater impact on the growth rate.

Regime	Dimensionless	Dimensional
Stefan limit	$\Lambda \ll \theta_{L\infty}$	$\Gamma\hat{S}_\infty \ll T_{L\infty} - T_c$
Transitional mid-point	$\Lambda \approx 0.3\ \theta_{L\infty}$	$\Gamma\hat{S}_\infty \approx 0.3\,(T_{L\infty} - T_c)$
High liquid frac.	$\Lambda \gg \theta_{L\infty}$	$\Gamma\hat{S}_\infty \gg T_{L\infty} - T_c$

Table 3.1: The regimes identified for a perfectly cooled mushy layer with no salt diffusion. The origin of the 0.3 factor is explained in the main text, with reference to figure 3.10.

To consider the effect that $\theta_{L\infty}$ has on the transition between the Stefan and high liquid fraction limits, we turn our attention to the contours of constant growth rate in figure 3.10. These contours necessarily have an inflection point as they shift between the two limits, which provide a good measure of centre of the transition region (in terms of growth rate behaviour) and therefore, how it responds to changes in $\theta_{L\infty}$. The red curve roughly indicates the position of these inflection points and is given by $\Lambda \approx 0.3\ \theta_{L\infty}$.

The transition therefore depends on the combination:

$$\frac{\Lambda}{\theta_{L\infty}} = \frac{\Gamma\hat{S}_\infty}{T_{L\infty} - T_c}.$$

The link between this combination and the liquid fraction was identified in Worster (1991), where it is defined as $\mathcal{C}$. This combination represents the ratio of the freezing point depression, $\Gamma\hat{S}_\infty$, to the temperature difference across a perfectly cooled mushy layer, $T_{L\infty} - T_c$, and the behaviour it governs is summarised in table 3.1. When the freezing point depression is much larger than the temperature difference across the mushy layer, $\mathcal{C}$ is large and the mushy layer is mostly liquid because only a small amount of solidification needs to occur before the salinity has been restored to local thermodynamic equilibrium. However, when the temperature difference across the mushy layer is much larger than the freezing point depression, $\mathcal{C}$ tends to 0. The mushy layer is mostly solid with a small mushy interface region because much larger amounts of solid must be formed (and larger amounts of salt rejected) to maintain local thermodynamic equilibrium.

Figure 3.11 looks at the liquid fraction profiles in the transition regions for three different values of $\theta_{L\infty}$. Note that the three graphs have differing vertical scales to accommodate changes to the growth rate.

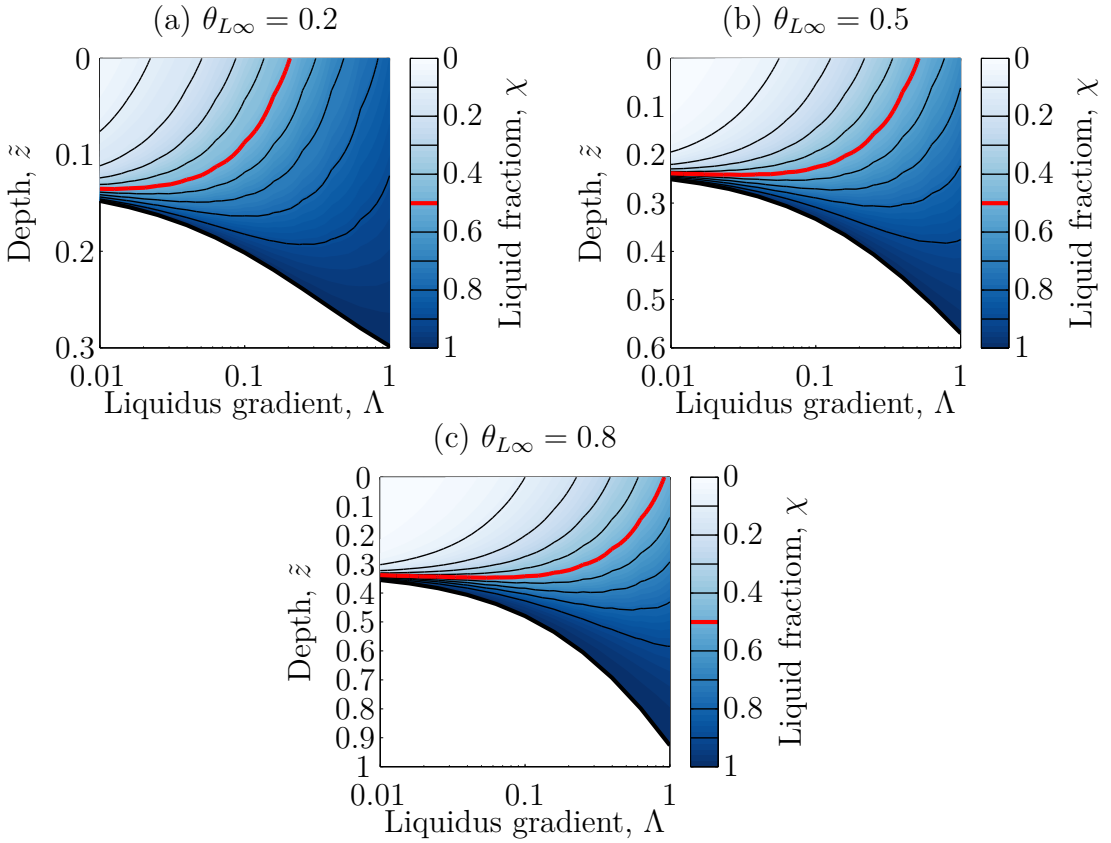

Figure 3.11: These figures show the vertical liquid fraction profiles for a range of liquidus gradients, $\mathcal{S}_t = 15.8$, and (a) $\theta_{L\infty} = 0.2$, (b) 0.5 and (c) 0.9. The black curve indicates the vertical extent of the mushy layer while the red curve highlights the $\chi = 0.5$ contour. All three graphs are plotted with the same horizontal and colour scales, but with differing vertical scales. Note that (b) also forms a portion of figure 3.8a and that these graphs cannot be collapsed onto $\mathcal{C} = \Lambda/\theta_{L\infty}$ because $\theta_{L\infty}$ affects the growth rates independently of this combination.

The increased growth rate as $\theta_{L\infty}$ increases (as seen in figure 3.10) is also apparent here, with the self-similar depth of the mushy layer clearly increasing across the three panels. Changes to the position of the transitional region are also evident. As $\theta_{L\infty}$ increases, the low liquid fraction region (left of the red curve) occupies a larger range of Λ, and more of the vertical extent for small Λ. The liquid fraction at the surface of these three figures also links back to (3.2.2), which tells us that for a fixed value of Λ, increasing $\theta_{L\infty}$ will increase the amount of solidification which occurs, with the liquid fraction decreasing both at the surface and in the interior of the mush.

Parallels can be drawn with figure 12 of Aussillous et al. (2006) in their study of solidifying water-sucrose mixture that made use of MRI imaging to measure the internal solidification. They show experimentally measured liquid fraction profiles

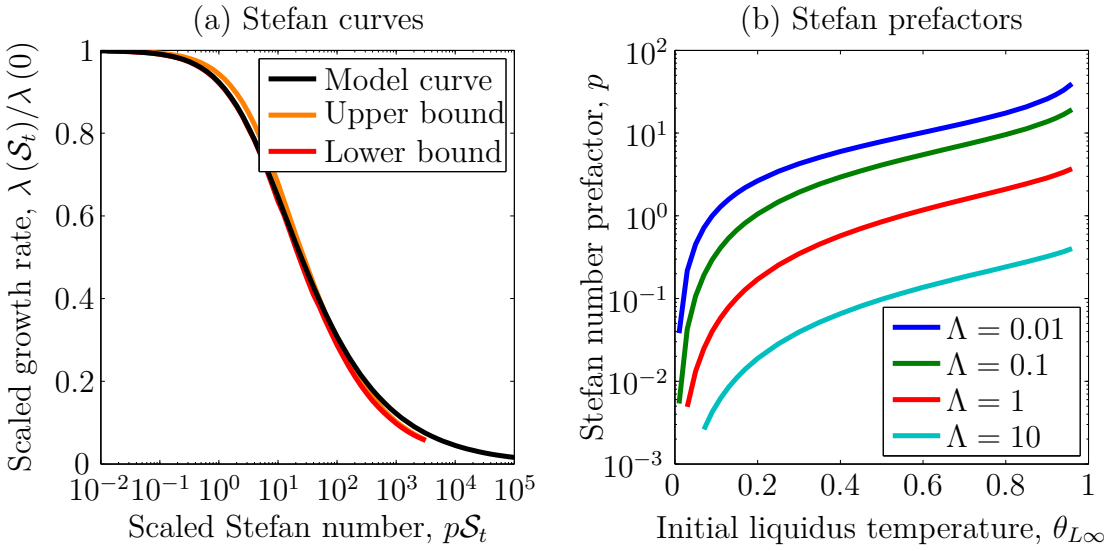

Figure 3.12: The dependence of the growth on the Stefan number exhibits the same functional form regardless of the initial liquidus temperature and liquidus gradient, and can be described by (3.2.5). (a) The functional form, $M(\mathcal{S}_t)$, (black) and the maximum (orange) and minimum (red) of the scaled Stefan-dependent curves for $0.01 \leq \theta_{L\infty} \leq 0.99$ and $0.01 \leq \Lambda \leq 100$. All curves are scaled by the growth rate at zero Stefan number for their respective values of $\theta_{L\infty}$ and Λ. (b) The shifts to the Stefan number needed to recreate the data, against $\theta_{L\infty}$ for $\Lambda = 0.01, 0.1, 1,$ and 10. Note that the shift needed increases as $\theta_{L\infty}$ increases but decreases as Λ increases.

against depth for four different initial salinities, with a clear decrease in internal solidification as the initial salinity increases. As noted before, increasing the initial salinity, $\hat{S}_\infty$, for fixed temperatures increases the dimensionless liquidus gradient, Λ, and decreases the dimensionless initial liquidus temperature, $\theta_{L\infty}$. When considering the growth rate of the mushy layer these changes had competing effects, but here they have complementary effects and both result in a decrease in internal solidification as $\hat{S}_\infty$ increases, agreeing qualitatively with the experimental observations.

3.2.2c Latent heat effects

Using the simplified model in section §3.1.2a, we noted that an increase in $\mathcal{S}_c$ leads to a decrease in the growth rate as the latent heat release inhibits thermal transport from the liquid region to the surface. The simplified model only applies when $\Lambda \gg \theta_{L\infty}$ but we can see from figure 3.6 that a greater release of latent heat (larger $\mathcal{S}_t$) results in a decreased growth rate for all values of Λ.

The decrease in the growth rate with increased Stefan number approximately collapses onto a single functional form over the full range of Λ and $\theta_{L\infty}$ considered in

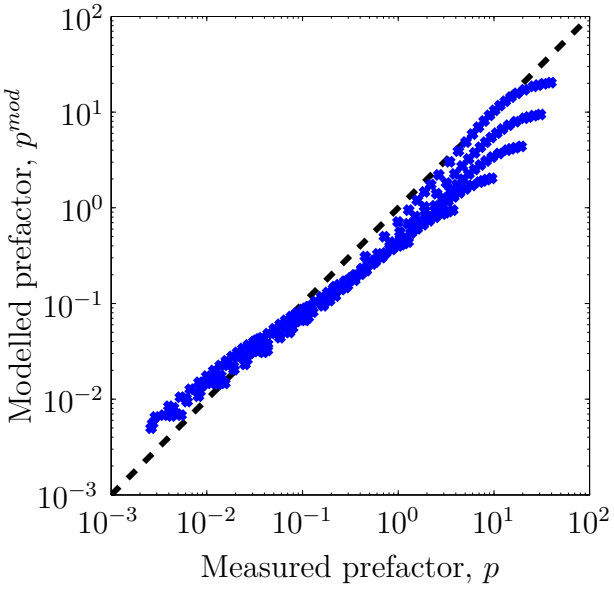

Figure 3.13: The prefactors calculated from (3.2.6) against the empirically measured prefactors, calculated by averaging the scaling needed to match the model curve $M(\mathcal{S}_t)$ over a range of growth rates. The results show relatively good agreement over five orders of magnitude in p, with $0.01 \leq \theta_{L\infty} \leq 0.99$ and $0.01 \leq \Lambda \leq 10$. The relative root-mean-square error is 48% but the model captures the general variation with $\theta_{L\infty}$ and Λ.

---

this study. This functional form, $M(\mathcal{S}_t)$, is shown by the black curve in figure 3.12a, and was found by solving the two-phase Stefan problem for a pure fluid (see §1.3). The growth rates for a mushy layer are then given by the expression:

$$\lambda(\mathcal{S}_t) = \lambda(0) M(p\mathcal{S}_t), \tag{3.2.5}$$

where $\lambda(0)$ is the mushy layer growth rate when $\mathcal{S}_t = 0$ and p is a multiplicative factor applied to the Stefan number that depends on Λ and $\theta_{L\infty}$. The growth rate for zero Stefan number, $\lambda(0)$, can be found by solving the equation $\operatorname{erf}(\lambda/2) = \theta_{L\infty}$. This is because the problem reduces to that of simple thermal diffusion, with the same diffusivity in both phases, and the solution for perfect conduction is given by (2.5.2). The zero-Stefan-number growth rate increases as $\theta_{L\infty}$ increases due to a decreased amount of sensible heat needing to be removed from the liquid before it can begin to solidify when $\theta_{L\infty}$ is larger, as discussed in §3.1.2a and §3.2.2b.

The prefactor, p, is calculated empirically using a least-squares method by comparing the Stefan numbers needed to get the same scaled growth rate, and averaging over a range of growth rates. The upper and lower bounds of the shifted results curves are also shown (orange and red respectively) in figure 3.12a to indicate the very high level

of agreement found with the model curve. While the absolute scale of p is arbitrary to within a multiplicative factor, a larger value means that latent heat has a noticable impact on the growth rate for smaller Stefan numbers. We can see in figure 3.12b that increasing $\theta_{L\infty}$ or decreasing Λ leads to larger p and a greater impact of latent heat release on the dynamics. To a good approximation, the behaviour is given by:

$$p \approx 1.3\frac{{\theta_{L\infty}}^{3/2}}{\Lambda^{2/3}} = \frac{{\theta_{L\infty}}^{5/6}}{\mathcal{C}^{2/3}}, \tag{3.2.6}$$

which was found heuristically with a power-law fit to the measured results. The accuracy of this expression plotted in figure 3.13.

By rewriting (2.3.6a) as:

$$\theta = \theta_{L\infty}\left(1 - \mathcal{C}\left(S - 1\right)\right),$$

with $\mathcal{C} = \Lambda/\theta_{L\infty}$, we can see that $\mathcal{C}$ sets the scale for salinity increases. As discussed previously, $\mathcal{C}$ is the dominant parameter in setting the amount of solidification which occurs. As $\mathcal{C}$ decreases, larger increases in salinity are needed to maintain local thermodynamic equilibrium, more solid forms, and more latent heat is released. This allows latent heat to grow in dynamical significance even when the Stefan number is held fixed, resulting in the increasing prefactor, p, as $\mathcal{C}$ decreases.

Meanwhile, increasing $\theta_{L\infty}$ increases the growth rate through the prefactor, p, in (3.2.5) by allowing a greater fraction of the heat removed to be used for cooling and solidifiying the mushy layer, rather than cooling the liquid to the liquidus temperature. However, this increased growth also increases the total amount of ice which forms and therefore increases the amount of latent heat released. As with decreasing $\mathcal{C}$, this increase in latent heat release means that it can have more dynamical impact for constant $\mathcal{S}_t$, and we get an increase in p as $\theta_{L\infty}$ increases.

3.2.2d Realistic Values

Table 3.2 shows the results for three calculations representative of real sea ice growth, using different temperature ranges.

Increasing the temperature range decreases the liquidus gradient and Stefan number, but increases the initial liquidus temperature. Decreasing the liquidus temperature tends to decrease the growth rate, λ, while the other two changes tend to increase the growth rate. These latter behaviours dominate with the growth rate increasing

ΔT	Λ	$\theta_{L\infty}$	$\mathcal{S}_t$	λ	Lqd. frac. at surface	High por. %	Ice depth, cm 1 d.	10 d.	60 d.
5^oC	0.6	0.6	16.7	0.55	0.5	100	5.9	19	46
10^oC	0.3	0.8	8.3	0.74	0.27	54	7.8	25	60
20^oC	0.15	0.9	4.1	0.93	0.14	34	9.8	31	76

Table 3.2: Results from calculations using parameter values appropriate for sea ice growth, and three different temperature ranges. ΔT is the imposed temperature range between the initial temperature of 0^oC and the lower cooling temperature, T_c. This primary control parameter for these calculations. The liquidus gradient, Λ, initial liquidus temperature, $\theta_{L\infty}$, and Stefan number, $\mathcal{S}_t$, are calculated for the imposed temperature range and an initial liquidus temperature $T_{L\infty} = -2^oC$. The next columns are the calculated mushy layer growth rate and the liquid fraction at the surface, which will also be the minimum liquid fraction. The percentage of the depth which has a high liquid fraction, $\chi > 50\%$, is shown to indicate the size of the interfacial region. Finally, the ice depth after 1, 10, and 60 days of growth are given in centimetres.

by approximately 50% for 10^oC compared to 5^oC, and roughly doubling for 20^oC compared to 5^oC.

We can also learn useful information about the structure of sea ice. The values of Λ and $\theta_{L\infty}$ combine to give values of $\mathcal{C} = \Lambda/\theta_{L\infty} = 1, 0.38$ and 0.17 for $\Delta T = 5^oC$, 10^oC, and 20^oC respectively. These are all within half an order of magnitude from $\mathcal{C} = 0.3$ which marks the centre of the transition between the Stefan and high liquid fraction limits. We therefore expect these results and those for realistic sea ice systems to span the transition region. Indeed, with the smallest temperature difference, 5^oC, the ice is porous ($\chi > 0.5$) throughout the whole depth, although this is still too solid for the high liquid fraction approximation ($\chi \sim 1$) to apply. For $\Delta T = 10^oC$ only half of the ice has a high porosity and the ice is only one quarter liquid at the surface. With $\Delta T = 20^oC$, the surface is now six-sevenths solid and only a third of the depth has a high porosity, however we are still not in a regime where the Stefan limit is a good approximation.

These results therefore indicate that a larger temperature difference results in more ice formation, and more solidification occurring within the ice itself, but that sea ice systems will lie within the transitional regime where neither the high-liquid-fraction or Stefan approximations can be accurately applied.

Wettlaufer et al. (1997) again provides a useful experimental comparison, describing in detail the solidification of a 70psu salt solution cooled from -2^oC to -20^oC, and

measuring 6.4 ± 0.2cm of ice growth after 400min. The model presented in this section predicts an ice depth of 5.9cm, which is still a slight underestimation of the measured depth, but a considerable improvement on the prediction of 5.1cm given by the simplified model in §3.1.2c. As previously suspected, this system is simply too far outside the range of applicability for the simple model to provide useful predictions, with $\mathcal{C} = \Lambda/\theta_{L\infty} = 0.37$ placing the system in the middle of the transitional regime. The agreement could likely be improved further by including unequal thermal properties, which expected to increase the growth rate (see §3.1.2a).

3.2.3 Summary and Discussion

In this section we have considered the growth rates and liquid fraction profiles for a mushy layer grown from a perfectly conducting upper boundary with appreciable changes in the liquid fraction of the mush. This expands the results from the simplified model in §3.1 and we find that the increase in growth rate for increased $\theta_{L\infty}$ or decreased $\mathcal{S}_t$ hold generally, not just in the high liquid fraction regime.

As well as the high liquid fraction limit, a Stefan limit was also found with a smooth transition between the two centring on $\Lambda/\theta_{L\infty} \approx 0.3$. The ratio $\mathcal{C} = \Lambda/\theta_{L\infty}$ has also been identified as controlling the solid fraction profiles in previous studies such as Worster (1991, 2000). When $\Lambda \gg \theta_{L\infty}$, $\mathcal{C}$ is much larger than one and we are in the high liquid fraction regime of the simplified model. However, when $\Lambda \ll \theta_{L\infty}$, $\mathcal{C}$ approaches 0 and the system approaches the two-phase Stefan problem for a pure fluid. In this limit, which we refer to as the *Stefan limit*, the liquid fraction is close to zero throughout most of the mushy layer, effectively forming a pure solid, and the salinities are very high, except in a small interfacial region where most of the internal solidification occurs. The size of this mushy interfacial region depends on the liquid gradient, but for $\theta_{L\infty} = 0.5$ and $\mathcal{S}_t = 4.0$, it's size is given by 4.0Λ, although these matching values are a numerical coincidence.

I also found that the dependence of the growth rate on the Stefan number obeys the same functional form, regardless of the initial liquidus temperature or liquidus gradient, with this behaviour described by (3.2.5). In this functional relationship, the Stefan number is multiplied by a multiplicative prefactor, which can be roughly approximated by (3.2.6). The prefactor indicates the relevant significance of latent heat release at constant Stefan number, due to the varying amount of internal solidification as Λ and $\theta_{L\infty}$ are varied. Increasing $\theta_{L\infty}$ and decreasing Λ both decrease the prefactor because these changes result in more internal solidification,

and hence latent heat release.

When realistic parameter values were used for the calculations, a colder cooling temperature results in increased growth rate and a deeper ice-ocean interface. There was also greater solidification within the ice itself for colder cooling temperatures, with the surface liquid fraction and depth of the high porosity region both decreasing, but the system remained between the Stefan regime and the high liquid fraction regime in all three calculations. We were able to use the more complex model presented in this section to significantly improve our prediction for the ice depth in the experimental conditions of Wettlaufer et al. (1997).

3.3 Mush with Imperfect Boundary Conduction

We now consider the case of imperfect boundary conduction, as represented by (2.3.2l) with a finite Biot number. Unlike the infinite Biot number case, the temperature at the surface of the mushy layer responds to the change in thermal forcing on a finite timescale, given by $1/\mathcal{B}_i{}^2$, rather than instantaneously. This represents a substantial departure from previous studies of mushy layer growth, either in this setting or in the directional solidification problem,

3.3.1 Method

We will use two different methods to investigate the effects of imperfect boundary conduction. The first extends the simplified model of §3.1.1 for finite Biot numbers and is discussed in §3.3.1b, while the second uses a direct numerical integration of the dynamical equations, and is discussed in §3.3.1c. However, we first discuss the relevance of the self-similarity transformation with imperfectly conducting boundaries.

3.3.1a Self-Similarity and Imperfect Cooling

The self-similarity transformation is a very powerful tool for studying mushy growth in the perfectly conducting limit but it relies on an infinite Biot number. For finite Biot number, we now have two variables in our self-similar coordinate system, $\tilde{z}$ as defined earlier and the self-similar Biot number, $\tilde{\mathcal{B}}_i = \mathcal{B}_i\sqrt{t}$, which means that the time derivative now transforms as:

$$\frac{\partial}{\partial t} = \frac{\tilde{\mathcal{B}}_i}{2t}\frac{\partial}{\partial \tilde{\mathcal{B}}_i} - \frac{\tilde{z}}{2t}\frac{\partial}{\partial \tilde{z}}.$$

The resulting system of equations will therefore be a system of partial differential equations in the two independent variables, $\tilde{z}$ and $\tilde{\mathcal{B}}_i$, which is no longer a simplification to the system so is not helpful for solving the equations. We will therefore solve the dynamical equations in the (z,t) coordinates.

However, we will transform our results into the self-similar coordinates for analysis, since this allows us to remove time as a parameter. We note that this is equivalent to comparing the results at $t=1$, and the evolution of the physical systems are represented by a time-evolving self-similar Biot number and thermal diffusion length scale.

3.3.1b Simplified Model Extension

When formulating the simplified model for imperfect boundary conduction, we follow §3.1.1 up until the self-similarity transform at the start of §3.1.1b. Instead, we substitute in the Biot-number-dependent cooling profile (2.5.1) into the dynamical equations (3.1.1, 2.3.4a, & 2.4.2) and boundary conditions (2.3.2a,e,j&l). This leads to a slightly modified form of (3.1.4), with the temperature profiles given by:

$$\theta\left(z\leq h\right)=A\Upsilon\left(z,t,\kappa^m,\mathcal{B}_i\right), \tag{3.3.1a}$$

$$\theta\left(z\geq h\right)=1-\frac{1-A\Upsilon\left(h,t,\kappa^m,\mathcal{B}_i\right)}{1-\Upsilon\left(h,t,1,\mathcal{B}_i\right)}\left(1-\Upsilon\left(z,t,1,\mathcal{B}_i\right)\right), \tag{3.3.1b}$$

$$\begin{aligned}\theta_L\left(z\geq h\right)=&\,\theta_{L\infty}\\&-\frac{\theta_{L\infty}-A\Upsilon\left(h,t,\kappa^m,\mathcal{B}_i\right)}{1-\Upsilon\left(h,t,\frac{1}{\mathcal{L}_e},\mathcal{B}_i\right)}\left(1-\Upsilon\left(z,t,1/\mathcal{L}_e,\mathcal{B}_i\right)\right).\end{aligned} \tag{3.3.1c}$$

As before, the interface flux conditions (2.3.2g) can be used to eliminate A and solve for $h\left(t\right)$, which is given implicitly by:

$$\begin{aligned}\theta_{L\infty}\left[\frac{\operatorname{erfcx}\left(\frac{h}{2\sqrt{t}}\right)}{\operatorname{erfcx}\left(\frac{h}{2\sqrt{t}}+\tilde{\mathcal{B}}_i\sqrt{t}\right)}-1\right]-\left(1-\theta_{L\infty}\right)\left[\frac{\operatorname{erf}\left(\frac{h}{2\sqrt{\kappa^m t}}\right)\exp\left(\frac{h}{2\sqrt{\kappa^m t}}\right)^2}{\operatorname{erfcx}\left(\frac{h}{2\sqrt{\kappa^m t}}+\mathcal{B}_i\sqrt{\kappa^m t}\right)}+1\right]\\=\left[\frac{\operatorname{erfcx}\left(\frac{h}{2}\sqrt{\frac{\mathcal{L}_e}{t}}\right)}{\operatorname{erfcx}\left(\frac{h}{2}\sqrt{\frac{\mathcal{L}_e}{t}}+\mathcal{B}_i\sqrt{\frac{t}{\mathcal{L}_e}}\right)}-1\right]\end{aligned} \tag{3.3.2}$$

The term on the right-hand side of this equation vanishes in the absence of salt diffusion ($\mathcal{L}_e\to\infty$) and we can remove time from this expression with the

substitutions $\lambda = h/\sqrt{t}$ and $\tilde{\mathcal{B}}_i = \mathcal{B}_i\sqrt{t}$. We also reintroduce the diffusivity factor $m = 1/\sqrt{\kappa^m}$ to simplify notation.

$$\theta_{L\infty}\left[\frac{\operatorname{erfcx}\left(\frac{\lambda}{2}\right)}{\operatorname{erfcx}\left(\frac{\lambda}{2}+\tilde{\mathcal{B}}_i\right)}-1\right] = (1-\theta_{L\infty})\left[\frac{\operatorname{erf}\left(m\lambda/2\right)\exp\left(m\lambda/2\right)^2}{\operatorname{erfcx}\left(\frac{m\lambda}{2}+\frac{\tilde{\mathcal{B}}_i}{m}\right)}+1\right]. \quad (3.3.3)$$

As before, this expression is solved used MATLAB's `fzero` routine.

3.3.1c PDE method

In the absence of salt diffusion, it is possible to numerically integrate the mushy layer equations for finite Biot numbers using MATLAB's `pdepe` partial differential equation routine, which is based on algorithms by Skeel and Berzins (1990). We will refer to this method as the *PDE method*.

To formulate this method, we take the mushy layer equations for temperature (2.3.4a) and salinity (2.4.1) and use them to the eliminate solidification terms from the problem, under the assumption of no fluid flow or salt diffusion:

$$\left(1+\frac{\mathcal{S}_t\Lambda\overline{S}}{\left(\Lambda+\theta_{L\infty}-\theta\right)^2}\right)\frac{\partial\theta}{\partial t} = \nabla^2\theta, \quad (3.3.4)$$

where we have also used the Lever rule (2.3.6b) to eliminate the liquid fraction. This is a simple diffusion equation for θ with a variable heat capacity. With no salt diffusion or fluid flow, $\overline{S} = 1$ throughout and the only dynamic variable present is the temperature.

The PDE method solves this equation and (2.3.4a with $\chi = 1$) directly in a finite depth box with the different dynamics in the mushy and liquid domains handled by providing the routine with a mass function (for the heat capacity) that behaves differently for $\theta < \theta_{L\infty}$ and $\theta > \theta_{L\infty}$. The integration is performed for a constant Biot number, $\mathcal{B}_i$, from a uniform state up until a set final time, which is chosen to ensure that the results are not affected by the finite depth of the box. Box depths were at least 20 times the mushy layer depth.

To extract the dependence of the dimensionless mushy layer thickness, λ, on $\tilde{\mathcal{B}}_i$ from an integration, the time-dependent interface position, $h(t)$ is calculated for a range of times between a chosen start time and the end of the run. The start time is chosen to ensure that the solution has good spatial resolution over the range of depths where θ varied significantly and at least 20-50 points within the mushy layer.

For this range of times, we can calculate the self-similar interface position, λ, and the corresponding self-similar Biot number, $\tilde{\mathcal{B}}_i$, at each time step. To ensure that the full range of $\tilde{\mathcal{B}}_i$ is covered, a number of simulations are run with different values of $\mathcal{B}_i$ and the results combined.

I also benchmarked the code by using this method to solve for perfectly conducting conditions to check for consistency with the shooting method, and by replacing the fully mushy dynamics with the simplified dynamics to compare the results against those from the simplified model of §3.1.1 and §3.3.1b.

3.3.2 Results

My investigation into the effects of imperfect conduction will start by considering the short-time behaviour and the onset of solidification, which will be delayed due to the time taken to cool the top boundary below the initial liquidus temperature. I will then consider the medium-time behaviour, with the long-time behaviour given by a self-similar, perfectly conducting system. Finally, I will compare these model results to the experimental results of Notz and Worster (2008).

3.3.2a Solidification Lag

The first effect of imperfect thermal conduction can be seen by considering the temperature profile:

$$\Upsilon\left(\tilde{z},1,1,\tilde{\mathcal{B}}_i\right)=\operatorname{erf}\left(\frac{\tilde{z}}{2}\right)+\exp\left(\frac{-\tilde{z}^2}{4}\right)\operatorname{erfcx}\left(\frac{\tilde{z}}{2}+\tilde{\mathcal{B}}_i\right), \qquad \text{(2.5.1 revisited)}$$

as quoted by Carslaw and Jaeger (1959) and introduced in §2.5. This gives a surface temperature before solidification of:

$$\Upsilon\left(0,1,1,\tilde{\mathcal{B}}_i\right)=\operatorname{erfcx}\left(\tilde{\mathcal{B}}_i\right).$$

We can invert this surface temperature equation to find the Biot number at which freezing will first occur for a given initial liquidus temperature, and this self-similar *freezing Biot number* is shown in figure 3.14. The freezing Biot number decreases as the initial liquidus temperature increases because less cooling is required for solidification to start.

When $\theta_{L\infty}$ approaches 1, the fluid starts very close to its initial liquidus temperature and can begin to solidify with very little cooling, and the freezing Biot number diverges to 0 as freezing can begin immediately. However, when $\theta_{L\infty}$ approaches 0,

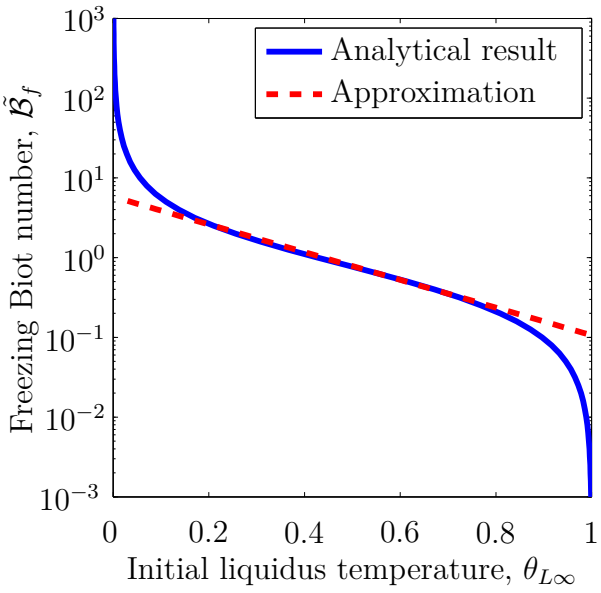

Figure 3.14: The self-similar *freezing Biot number*, at which solidification first occurs, against the initial liquidus temperature. The analytical solution is shown in blue and the approximation $\tilde{\mathcal{B}_f} = 5.5\,\exp\left(-4\,\theta_{L\infty}\right)$ in red.

---

the fluid starts very far from its initial liquidus temperature and requires a rapid rate of cooling or a long time to begin to solidify, and the freezing Biot number diverges to infinity. For the central range, where $0.2 \lesssim \theta_{L\infty} \lesssim 0.8$, the freezing Biot number is roughly exponential in $\theta_{L\infty}$ and can be well approximated by:

$$\tilde{\mathcal{B}_f} = 5.5\,\exp\left(-4\,\theta_{L\infty}\right),$$

which has a root-mean-square error of 10%.

This lag in surface temperature continues once solidification begins, as shown in figure 3.15 which illustrates the structure of a mushy layer in the high liquid fraction regime varying with self-similar Biot number and depth. Since the self-similar Biot number increases with time, this graph can also be considered as showing the time-evolution of the imperfectly cooled mushy layer, and we see three distinct periods to the evolution.

For $\tilde{\mathcal{B}_i} \leq 0.21$, the surface temperature of the fluid has not yet reached the initial liquidus temperature and no solidification can occur. At the other end of the spectrum when $\tilde{\mathcal{B}_i}$ is large ($\gtrsim 100$, in this setup) the structure of the ice becomes independent of the Biot number and therefore is independent of time (apart from the stretch to the physical vertical coordinate, $\hat{z} = \tilde{z}\sqrt{\kappa\hat{t}}$). The mush has therefore

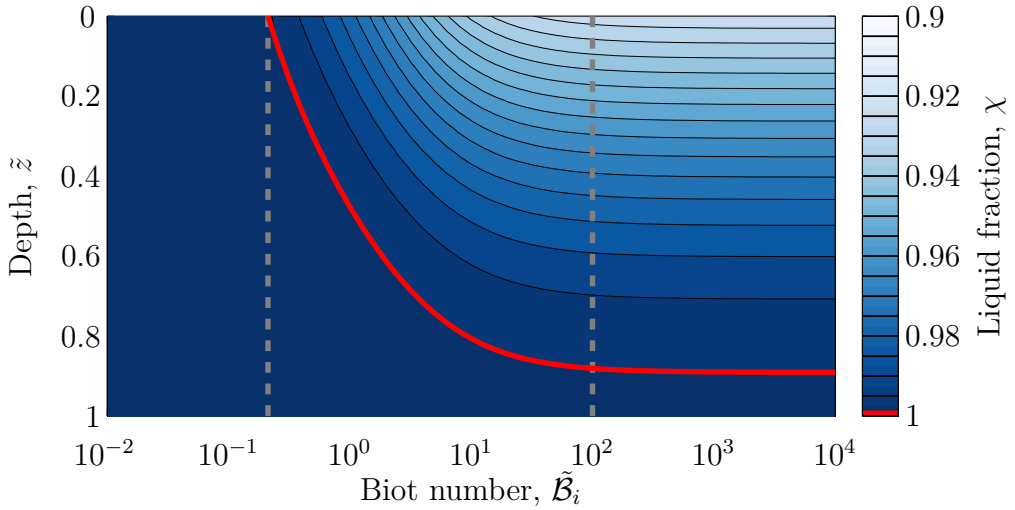

Figure 3.15: The evolution of a mushy layer in the high liquid fraction regime against Biot number for $\Lambda = 10$, $\theta_{L\infty} = 0.8$, and $\mathcal{S}_t = 100$, with the mush-liquid interface shown in red and three distinct periods visible. No solidification for $\tilde{\mathcal{B}}_i \leq 0.21$, an adjustment region for $0.21 \leq \tilde{\mathcal{B}}_i \lesssim 100$ and a self-similar region for $100 \lesssim \tilde{\mathcal{B}}_i$.

reached the self-similar regime where it can be well approximated by the perfectly conducting models.

3.3.2b Investigating the Adjustment Period

In between these two periods ($0.21 \leq \tilde{\mathcal{B}}_i \lesssim 100$ here) we have a period where the mush has begun to form, but has not yet reached the self-similar limiting case and imperfect conduction effects are important, which we will refer to as the *adjustment period*. The evolution of this period manifest itself in two significant ways. Firstly, the surface temperature, and hence liquid fraction, are still approaching their limiting values, meaning that there will be a discrepancy between the surface temperature of the mush and the air temperature, and that further internal solidification will occur near to the surface. Secondly, the thickness of the mushy layer is smaller than expected from the perfectly conducting models, but the instantaneous physical growth rate of the mush is increased relative to the physical growth rate with perfect conduction. This is because the internal ice is warmer and has a lower solid fraction, so the energy requirement to propagate this as a self-similar state is reduced and more energy can be removed from the adjacent fluid. In this example, the adjustment period spreads over three orders of magnitude for $\tilde{\mathcal{B}}_i$, which corresponds to six orders of magnitude for time and will therefore be a very significant stage of the mushy layer development.

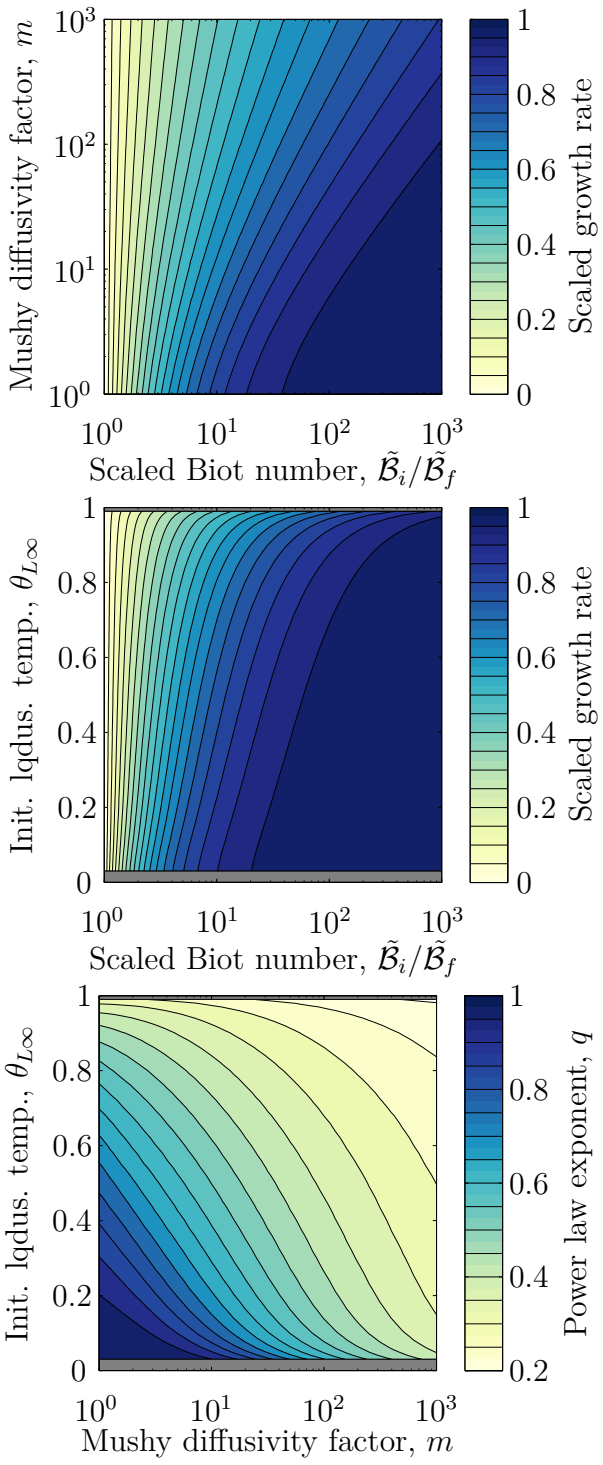

Figure 3.16: Scaled mushy layer growth rates, $\lambda\left(\tilde{\mathcal{B}}_i\right)/\lambda(\infty)$, against scaled Biot number, $\tilde{\mathcal{B}}_i/\tilde{\mathcal{B}}_f$, and (a, top) mushy diffusivity factor, $m = \sqrt{1+\mathcal{S}_c}$, with $\theta_{L\infty} = 0.7$, (b, middle) initial liquidus temperature, with $m = 6.3$. The size of the adjustment period increases as either m or $\theta_{L\infty}$ increases. This is demonstrated in (c, bottom) which plots the exponent q from (3.3.5) for a range of m and $\theta_{L\infty}$ values. The exponent is a measure of 'decay' rate of the growth rate towards the self-similar limit, and hence also a measure of the size of the adjustment period.

To investigate this adjustment period we turn to figure 3.16. The first two panels plot the growth rates against Biot number and either mushy diffusivity factor, $m = \sqrt{1 + \mathcal{S}_c}$, or initial liquidus temperature, $\theta_{L\infty}$. To allow like-for-like comparisons, growth rate data is scaled by the growth rate for infinite Biot number, and the Biot number axis is scaled by the freezing Biot number.

Close to the first freezing, the growth rate can be modelled as:

$$\lambda\left(\tilde{\mathcal{B}}_i\right) = \lambda\left(\infty\right)\left(1 - \left(\frac{\tilde{\mathcal{B}}_f}{\tilde{\mathcal{B}}_i}\right)^q\right), \tag{3.3.5}$$

where the exponent, q, is the single free parameter and is fitted to the data for each pair of m and $\theta_{L\infty}$. There is no obvious physical justification for this functional form but a preliminary investigation showed that it provides a good match to the data up to $\lambda\left(\tilde{\mathcal{B}}_i\right) = 0.6\ \lambda\left(\infty\right)$, with an average RMS fitting error of 3% and a maximum RMS fitting error of 8%. This is a significant proportion of the adjustment period, although the power law form does not always capture the behaviour for $\lambda\left(\tilde{\mathcal{B}}_i\right) \gtrsim 0.6\ \lambda\left(\infty\right)$ as accurately.

The exponent, q is shown in figure 3.16c against m and $\theta_{L\infty}$. By capturing the curve of the growth rate in the adjustment period and the 'decay' towards the self-similar limit, the exponent in this expression gives a good measure of the size of this period, with a smaller exponent indicating a slower 'decay' and therefore a larger adjustment period.

We can therefore see that increasing the mushy diffusivity factor (increasing $\mathcal{S}_c$) increases the length of the adjustment period, as seen directly in figure 3.16a for $\theta_{L\infty} = 0.7$, and in figure 3.16c with q decreasing as m increases over a range of $\theta_{L\infty}$. By increasing the compositional Stefan number, we are increasing the effective heat capacity of the mushy region and decreasing the effective thermal diffusivity. This decreased ability to transmit heat means that changes take longer to propagate through the mushy layer and the system takes longer to adjust.

Increasing the initial liquidus temperature also increases the size of the adjustment period as seen in figure 3.16b for $m = 6.3$, and in figure 3.16c by q decreasing as $\theta_{L\infty}$ increases. This is because increasing $\theta_{L\infty}$ increases the amount of internal solidification, leading to a greater amount of latent heat released and removed across the boundary. With more latent heat to remove, the boundary will be slower to remove sensible heat and it will take longer to adjust to the long-time self-similar state.

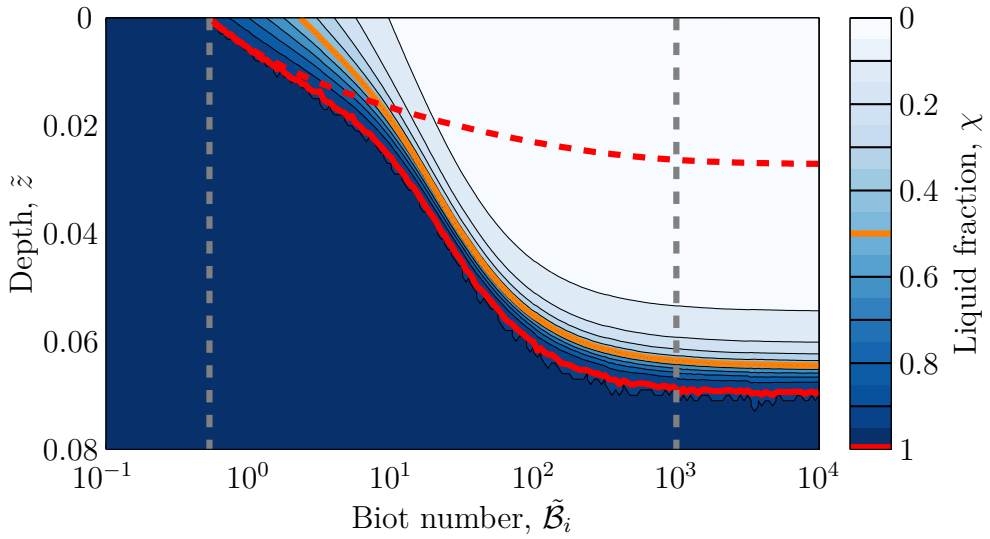

Figure 3.17: The evolution of a mushy layer in the Stefan limit against Biot number for $\Lambda = 0.01$, $\theta_{L\infty} = 0.6$, and $\mathcal{S}_t = 100$, with the mush-liquid interface shown in red and three distinct periods are visible. There is no solidification for $\tilde{\mathcal{B}}_i \leq 0.53$, an adjustment period for $0.53 \leq \tilde{\mathcal{B}}_i \lesssim 1000$ and a self-similar region for $\tilde{\mathcal{B}}_i \gtrsim 1000$. The interface curve no longer shows a uniform concave behaviour, and shows a clear acceleration in growth for $\tilde{\mathcal{B}}_i \sim 10$. For comparison, the growth rate calculated using the simplified model (§3.3.1b) is shown in dashed red.

3.3.2c Imperfect Conduction in the Stefan Regime

In the previous section, we showed that an adjustment period exists before the system reaches its long-time self-similar behaviour, in the high liquid fraction regime. Figure 3.17 plots the mushy layer growth rate and structure against Biot number for a system in the Stefan regime, where the freezing point depression is small compared to the temperature scale, $\Lambda \ll \theta_{L\infty}$, and there is a region of mostly-solid mush (see §3.2.2a). There are a number of similarities to figure 3.15 but also some striking differences.

As before, we note that there is no mushy layer for small Biot numbers, and the mushy layer subsequently adjusts to the self-similar growth pattern slowly over a range of Biot numbers. However, we also observe that there is an acceleration in growth rate during the adjustment period. This acceleration happens as the liquid fraction at the surface decreases and we link this change to the effective mushy heat capacity described in (3.3.4), which can be rewritten as:

$$c_p^{mushy} = 1 + \frac{\mathcal{S}_c \chi^2}{\overline{S}}, \tag{3.3.6}$$

using the Lever rule (2.3.6b) and $\overline{S} = 1$. As the liquid fraction decreases, the effective heat capacity also decreases, allowing for considerably more rapid thermal transport. This leads to faster growth, as seen in §3.1.2a. The effect of this enhanced transport is particularly noticeable when compared to the growth rates calculated using the simplified model for finite $\tilde{\mathcal{B}}_i$, which are shown by the dashed red line, since this model neglects the variation of c_p^{mushy} with χ.

The simplified model has a uniform heat capacity of $1 + \mathcal{S}_c$ and we can see that the growth rates for the full and simplified dynamics diverge significantly once the surface liquid fraction reaches 0.5 and the surface heat capacity has decreased by 25%. From here, the surface liquid fraction and heat capacity decrease further and we see a rapid growth in the low liquid fraction/low heat capacity region which is the driving force behind the increase in the growth rate. The simplified model does not have this variable heat capacity and so does not experience this acceleration.

Another important feature of the Biot-number dependent growth in the Stefan limit is early-time growth. Shortly after first solidification, the whole depth of the mushy layer has a high liquid fraction. A high solid fraction region will develop as time progresses, but its formation is a gradual process and it takes time to develop fully, unlike the instant formation predicted by models with perfect conduction.

Low liquid fraction regions provide considerable resistance to convective overturning and biological growth, which tend to be confined to regions with a large liquid fraction close to the interface. With the whole ice in the high liquid fraction regime at the early stages of growth, there will be a larger region for biological growth and there is potential for convection to be driven over a greater depth.

We note there is a small amount of noise in the interface position (solid red) in figure 3.17. This is due to a known uncertainty inherent in enthalpy methods when determining an interface position on a scale below the grid resolution (Klimeš et al., 2016).

3.3.2d Realistic sea ice growth

To better model realistic ice growth, it was necessary to carry through the phase-weighting of the thermal conductivity and heat capacity from (2.1.6), leading to a modified version of (3.3.4):

$$\left(1 + \left(r_{\rho c_p} - 1\right)(1-\chi) + \frac{\mathcal{S}_t \Lambda \overline{S}}{\left(\Lambda + \theta_{L\infty} - \theta\right)^2}\right) \frac{\partial \theta}{\partial t} = \boldsymbol{\nabla} \cdot \left\{\left[1 + \left(r_k - 1\right)(1-\chi)\right] \boldsymbol{\nabla} \theta\right\}.$$

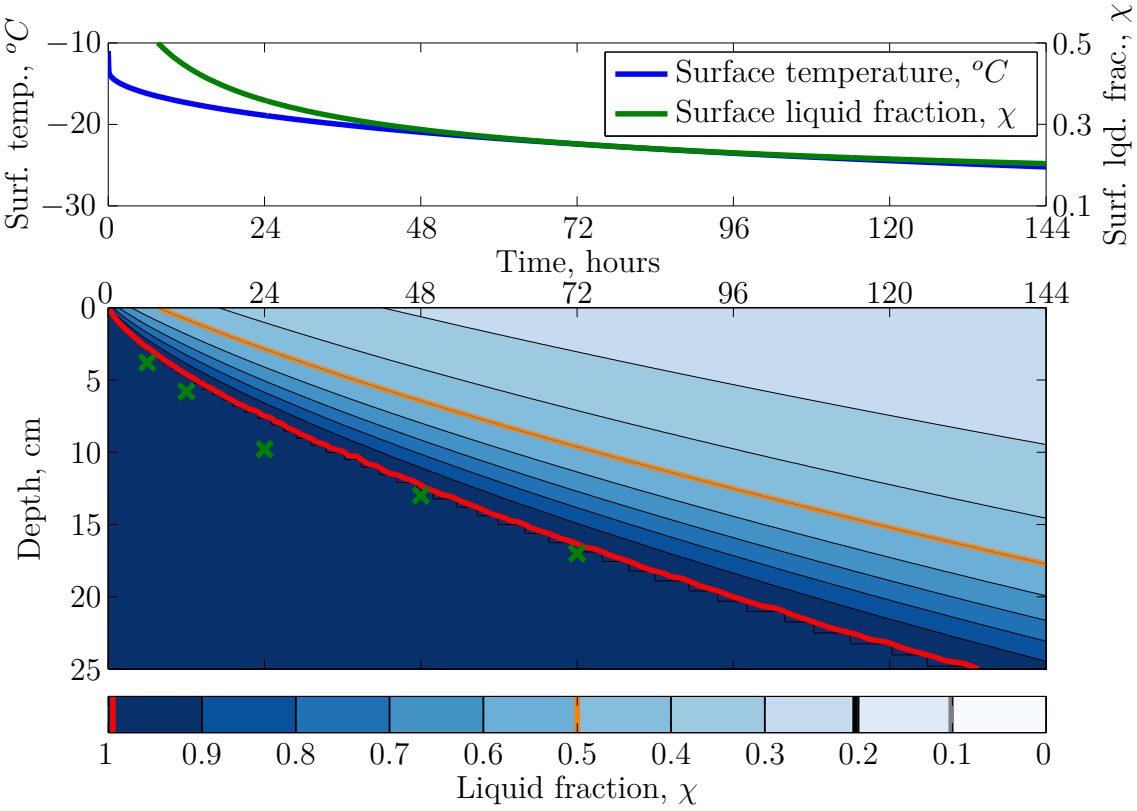

Figure 3.18: (a) Surface temperature and liquid fraction, and (b) liquid fraction profiles from a simulation of experimental conditions in Notz and Worster (2008). Water is cooled from an initial temperature $T_\infty = -1^oC$ by an atmosphere at $T_c = -30^oC$ over six days, with an effective atmospheric conductivity of $\mathfrak{h} = 6.3\text{Wm}^{-2}\text{K}$, corresponding to a wind speed of 2m/s. In (b), the red and orange curves indicate the interface and the $\chi = 0.5$ contour respectively, and depth measurements from Notz and Worster (2008) are shown with green crosses. Both the surface temperature and surface liquid fraction are evolving throughout the simulation with the surface liquid fraction reaching a value of 0.2 (shown on the colour scale in thick black), compared to a long-time limiting value of $\chi = 0.1$ (grey).

Of the two changes introduced here, the effect on the thermal conductivity is the more significant, with $r_k - 1$ six times larger than $r_{c_p} - 1$. The magnitude of the Stefan number also helped reduce the effects of the phase-dependent heat capacity since $\mathcal{S}_t$ is also roughly six times larger than $r_{c_p} - 1$.

We are now in a position to properly simulate realistic sea ice growth and do so in figure 3.18, with comparison to field campaign data from Notz and Worster (2008). The simulation was started with the fluid at a temperature of $T_\infty = -1^oC$ and salinity of $\hat{S}_\infty = 35\text{psu}$. A cooling temperature of $T_c = -30^oC$ was applied and the simulation was run for six days of model time. These numbers lead to

a liquidus gradient $\Lambda = 0.1$, initial liquidus temperature $\theta_{L\infty} = 0.91$, and Stefan number $\mathcal{S}_t = 2.7$. A wind speed of 2m/s in (2.2.5b) leads to a cooling coefficient of $\mathfrak{h} = 6.3\text{Wm}^{-2}\text{K}$.

A good comparison between the model presented in this study and the experimental results of Notz and Worster (2008) can be found by looking at how the ice depth evolves over time. Figure 3.18 shows the modelled ice depth with the red curve, and ice depth measurements from figure 8a of the field measurements of Notz and Worster (2008) with green crosses. There is good agreement between these two sets of results, although without the inclusion of unequal thermal properties, the model underpredicted the depth of the mushy layer.

For $\theta_{L\infty} = 0.91$, the freezing Biot number is $\tilde{\mathcal{B}}_f = 0.0852$ which can be inverted to give a first-freezing time of 350 s or 6 min. This timescale is too short to be noticeable on figure 3.18, which measures time in hours and days. Notz and Worster (2008) did not determine an initial freezing time, although they note that "ice growth started very rapidly".

At the other extreme of time, figure 3.15 suggests self-similar growth is approached when $\tilde{\mathcal{B}}_i \approx 100$, while figure 3.17 suggests $\tilde{\mathcal{B}}_i \approx 1000$. Using the first yields a corresponding time of 4.8×10^8s, or 15 years. This is reflected in figure 3.18a, with both the surface temperature and surface liquid fraction showing clear evolution over the six day period. By the end of the simulation, the temperature at the surface of the ice had dropped to -25^oC, and the liquid fraction had reached $\chi = 0.2$, although the long-time limits would be -30^oC and 0.1 respectively. Figure 3 of Notz and Worster (2008) also notes a decaying surface temperature (measured at 0.5cm) over the six day experiment. However, there is also noise arising from fluctuations in both T_c and u_w, due to changing atmospheric conditions. This will change the atmospheric forcing applied, and variations in the wind speed will affect the cooling rate, but variability in these features is not captured by the model presented by this study.

The results of the simulation differ from the observations of Notz and Worster (2008) in relation to the solid fraction. For the liquidus gradient and initial liquidus temperature, we find that $\mathcal{C} = \Lambda/\theta_{L\infty} = 0.11$. This is in the transitional regime, but on the side of the Stefan regime so there will be appreciable solidification. However, solidification will not be complete anywhere and a significant portion of

the mush will have a high porosity. Figure 3.18b suggests that the high-porosity region occupies at least a third of the full depth throughout the six days and that even at the surface, 20% of the material remains liquid.

In contrast, Notz and Worster (2008) shows faster formation of low-porosity regions and overall greater solidification, with porosities of 0.1 over 3cm after 24h, and very near complete solidification throughout the majority of the layer after two days (Figure 8a). This discrepancy is almost certainly caused by the most important feature missing from this diffusive model: convection. Convection has the effect of removing salt from the growing mushy layer, resulting in greater solidification, and figure 8b of their paper shows a significant decrease in the bulk salinity that closely echos the solid formation. The onset of convection in this setup is discussed in §5.5.

It is interesting to note, however, that the absence of convection does not seem to have significantly impacted our predictions of the ice depth. This is in agreement with the observation by Rees Jones and Worster (2014) that the ice depth is relatively insensitive to the amount of convection which occurs. They suggest this is due to a coincidental balance between two competing effects arising from the fact that convection removes salt and increases solidification. Since the solid phase has a larger thermal conductivity than the liquid phase, this increases thermal transport through the mush and enhances the growth rate. On the other hand, the increased solidification also results in more latent heat release, which inhibits growth.

This section has assumed that congelation ice forms immediately. However, initial ice formation is often in the form of small, isolated crystals known as frazil ice, which gradually coalesce into larger structures (Petrich and Eicken, 2010 and Weeks, 2010). Frazil formation occurs in supercooled water around impurities that act as nucleation sites for the crystals. Pure salt water (without solid impurities) can be supercooled substantially before ice forms, although sea water contains a number of impurities and these allow ice formation with small supercoolings of less than 0.1^oC. The exact process of frazil congelation depends on the sea state and weather conditions, but in calm conditions the crystals can form a thin surface layer of grease ice. In post-mortem cores of sea ice, accumulated frazil shows as a granular ice texture, and the thickness of the granular layer is observed to vary between scales of millimeters and meters (Eicken and Lange, 1989). Crystal nucleation, frazil formation, and congelation are likely to be complicating factors when applying the results of this section to very early growth stages.

3.3.3 Summary and Discussion

In this section we have seen that imperfect thermal conduction leads to a delay in the onset of solidification. Once solidification begins to occur, the mushy layer approaches its long-time liquid fraction structure gradually, with the long-time vertical structure given by the self-similar perfect conduction results. The time over which the gradual shift towards self-similar growth occurs is the *adjustment period*, and a number of factors can affect the length of time it lasts. The length of this adjustment period increases as we increase the initial liquidus temperature, because more latent heat must be removed before the system can reach its long-time structure. It also shrinks as we enhance thermal transport in the mushy layer because changes can propagate through the system faster. This enhancement to the thermal transport can be achieved by decreasing $\mathcal{S}_t$ and reducing the amount of latent heat that is needed for phase changes, or by increasing Λ and decreasing the amount of solidification which occurs.

We also considered the adjustment period of a system in the Stefan limit and found that the growth rate exhibited an acceleration after the initial solid had formed as the surface liquid fraction decreases. The solidification decreases the heat capacity at the surface which in turn increases the rate of thermal transport at the top of the ice and allows faster cooling of lower regions. This behaviour is not present in the high liquid fraction regime where the heat capacity is roughly constant throughout.

Finally, we observed that even in systems in the Stefan limit, for small Biot numbers (and before the acceleration) there is a window when the whole mushy layer is in the high liquid fraction regime temporarily, which will provide a larger environment for biological growth and allow convection over a greater range of depths.

A comparison between our model and the experimental results of Notz and Worster (2008) was fruitful with good agreement between the ice depth found by the two studies. The comparison also highlights the importance of properly modelling the imperfect surface conduction: Both this study and Notz and Worster (2008) saw that the surface temperature was still evolving after six days, indicating that imperfect thermal conduction to the atmosphere was still directly affecting the dynamics. There was a noticable disagreement over the amount of solid formation, but this is likely due to convection removing salt from the experimental system and increasing the amount of solidification.

3.4 Discussion and Conclusions

This chapter has considered the growth and structure of mushy layers before convective onset, with the investigation split into three main parts.

The first section (§3.1) looked at mushy layer growth rates in a regime with high liquid fraction, when $\Lambda \gg \theta_{L\infty}$ and very little solid forms. A simplified dynamical model was implemented that showed increasing the thermal transport in the mushy layer (decreasing m) results in increased ice growth. This effect can be achieved by either decreasing $\mathcal{S}_t$ and the hence amount of latent heat in the system, or by increasing Λ and decreasing the amount of solid which forms. Increasing the initial liquidus temperature also results in faster ice growth as less sensible heat must be removed from a parcel before it can solidify. Salt diffusion in the liquid layer was shown to inhibit ice growth, by creating a compositional boundary layer which parcels must be cooled through before they can solidify, while salt diffusion in the mushy phase enhances ice growth by providing an effective thermal transport.

The next section (§3.2) considered full solidification dynamics and contrasted the high liquid fraction regime with a so-called *Stefan regime*, where the liquidus gradient is much smaller than the initial liquidus temperature, $\Lambda \ll \theta_{L\infty}$. This could represent a system with a low salinity that does not significantly affect the initial liquidus temperature or one with a very large driving temperature difference. The Stefan regime is characterised by high solid fraction over most of the mush depth, but with a thin interfacial region where the majority of the solidification occurs. The relative thickness of the interfacial region depends linearly on the dimensionless liquidus gradient, Λ. A transitional regime exists between the Stefan and high liquid fraction regimes, when most of the mushy layer has a high porosity, but appreciable solid formation occurs at the surface. This regime is roughly centred on $\Lambda = 0.3\theta_{L\infty}$. The variation of the growth rate with the Stefan number, $\mathcal{S}_t$, liquidus gradient, Λ, and initial liquidus temperature, $\theta_{L\infty}$, was shown to collapse onto a well-defined functional form which depends only on growth rate for $\mathcal{S}_t = 0$, and a universal function of the dimensionless group $\mathcal{S}_t {\theta_{L\infty}}^{3/2}/\Lambda^{2/3}$.

The last section (§3.3) considered the effects of imperfect boundary conduction, as described by the Biot number, $\tilde{\mathcal{B}}_i$, which can also be considered a proxy for time. With imperfect conduction, there is no longer instantaneous solidification when cooling begins. Instead solidification starts to occur when the Biot number reaches

the freezing Biot number, which satisfies erfcx $\left(\tilde{\mathcal{B}_f}\right) = \theta_{L\infty}$. After solidification begins, there is an adjustment period when the self-similar ice thickness and amount of solid throughout the layer increase and approach the self-similar solution for large Biot numbers or long times. Using the simplified model, the length of the adjustment period was shown to increase when there is more latent heat in the system. This is the case for a larger Stefan number, which directly represents more latent heat, but also when the initial liquidus temperature, $\theta_{L\infty}$, is higher or liquidus gradient, Λ, is lower, because both of these increase the amount of solidification which occurs. In the Stefan regime, it was also shown that the self-similar growth rate accelerates at the time where appreciable solidification begins to occur at the surface. This is because of the slowing of solidification, and hence latent heat release, in this region, which reduces the effective heat capacity and promotes thermal transport.

Comparisons were also made between the hierarchy of models to growth rates in experiments and for ice growth in the environment. Real sea ice systems have a ratio of Λ to $\theta_{L\infty}$ which places it in the transitional regime with a mostly high liquid fraction, but appreciable solidification at the surface. The model used in §3.2 predicts 76cm of ice growth over 60 days when cooled to -20^oC. Of particular note is the comparison with the observations of Notz and Worster (2008), where good agreement was found between the two sets of results for ice depth. Both results also observed a dynamically evolving surface temperature, as predicted by the imperfect conduction model, but differ on the liquid fraction profiles, potentially due to the effects of convection draining salt and increasing solidification in the observations.

There are a number of avenues for further investigation following this study. The thickness of the high porosity region was characterised for one pair of $\theta_{L\infty}$ and $\mathcal{S}_t$ but an investigation of how the thickness this region varies with these two parameters could provide useful knowledge for studies of convective onset and biological habitats in sea ice. Further investigation would be needed to understand the physical reason for the particular collapse of the growth rates in figure 3.12, and expressed in (3.2.5) & (3.2.6). Finally, there is scope for further characterisation of the adjustment period observed for imperfect conduction, particularly when the long-time system lies in the Stefan regime.

4
Porous Boundary Convection

In this chapter, I will investigate thermal convection in a semi-infinite, uniform porous medium. Thermal and compositional convection have previously been studied in this setting for a perfectly conducting (fixed temperature) upper boundary, as reviewed in §1.4.4. I build on the investigation of Slim and Ramakrishnan (2010), who used an energy stability method to investigate convective onset for a transient boundary layer cooled by a perfectly conducting boundary. I adapt this method to study how changes in the effective boundary conductivity at the surface affect convective onset - an aspect of the problem which has not previously been considered. We will also show that in this system, the effects of thermal properties which differ between the solid and liquid phases but are otherwise constant can be scaled out of the problem when the porosity is uniform. This chapter is based on an edited form of the results described in Hitchen and Wells (2016), published in the Journal of Fluid Mechanics.

4.1 Model

To understand the impact of effective boundary thermal conductivity on convective instability, I consider a simplified system which consists of an infinitely deep, two-dimensional porous medium with temperature-independent thermal properties and uniform porosity, as illustrated in figure 4.1. We consider thermal properties which differ between the solid and liquid phases but show that with a suitable rescaling, this effect has no impact on the dimensionless form of the problem.

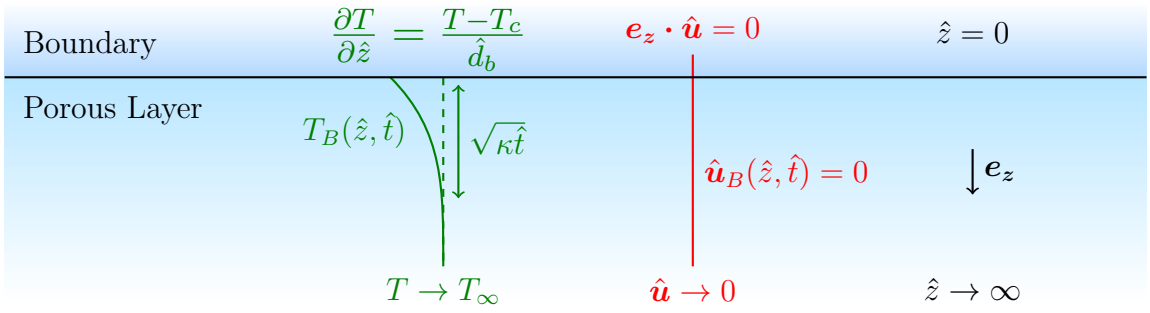

Figure 4.1: A diagram illustrating the model described in the main text. Heat is lost through imperfect thermal conduction, described by (2.2.6), to a heat sink of temperature T_c, which results in an evolving thermal base-state temperature, $\theta_B(\hat{z}, \hat{t})$, that depends on depth $\hat{z}$ and time $\hat{t}$. The evolving base-state forms a diffusive boundary layer of characteristic depth $\sqrt{\kappa \hat{t}}$, where κ is the thermal diffusivity. The base-state velocity, $\hat{\boldsymbol{u}}_B$, is zero everywhere. The other boundary conditions on temperature, T, and velocity, $\hat{\boldsymbol{u}}$, are discussed in the main text, and $\hat{d}_b$ is defined in (2.3.3).

As before, the fluid is initially at rest with an initial temperature of T_∞ everywhere and at time $\hat{t} = 0$, heat loss begins to a heat sink of temperature T_c with the rate of heat loss depending on the temperature difference between the heat sink and the surface of the porous layer:

$$\overline{k} \frac{\partial T}{\partial \hat{z}} = \mathfrak{h} \left(T - T_c \right) \qquad \text{at } \hat{z} = 0. \tag{2.2.6 revisited}$$

To recap, $\mathfrak{h}$ is the heat transfer coefficient which modulates the rate of heat loss from the porous layer and $\overline{k}$ is the combined phase-weighted thermal conductivity of the solid matrix and interstitial fluid.

4.1.1 Dynamical Equations

Modelling thermal convection in a uniform, unreactive porous medium allows us to make a number of simplifications to the mushy layer equations in chapter 2.

With a constant, uniform porosity, we can neglect the effects of latent heat (associated with phase change) on energy conservation and (2.1.5) can be written as:

$$\overline{(\rho c_p)} \frac{\partial T}{\partial \hat{t}} + (\rho c_p)_l \, \hat{\boldsymbol{u}} \cdot \hat{\boldsymbol{\nabla}} T = \overline{k} \hat{\nabla}^2 T,$$

where we have used the fact that $\overline{k}$ is spatially uniform in the final term. This rearranges to give:

$$\frac{\partial T}{\partial \hat{t}} + \omega \hat{\boldsymbol{u}} \cdot \hat{\boldsymbol{\nabla}} T = \kappa \hat{\nabla}^2 T. \tag{4.1.1a}$$

$$\omega = \frac{(\rho c_p)_l}{\chi\,(\rho c_p)_l + \phi\,(\rho c_p)_s}, \qquad \kappa = \frac{\chi k_l + \phi k_s}{\chi\,(\rho c_p)_l + \phi\,(\rho c_p)_s}, \tag{4.1.1b,c}$$

where ω is a new parameter which controls the amount of thermal lag within the system. The definition of κ is different to the definition given previously, which was $k_l/(\rho c_p)_l$, since we have not assumed equal thermal properties.

When non-dimensionalising this equation, we note that we can include any non-unitary thermal lag parameter in the velocity scale without affecting the boundary conditions above, by using a modified non-dimensional velocity $\boldsymbol{u} = \hat{\boldsymbol{u}}\omega\hat{d}/\kappa$. Using this velocity scale and other diffusive scales described in §2.3, the non-dimensional thermal equation is:

$$\frac{\partial\theta}{\partial t} + \boldsymbol{u}\cdot\boldsymbol{\nabla}\theta = \nabla^2\theta. \tag{4.1.2}$$

The fluid flow is governed by Darcy's law (2.1.14) and incompressibility (2.1.2):

$$-\frac{\nu\hat{\boldsymbol{u}}}{\hat{\Pi}(\chi)} = \hat{\boldsymbol{\nabla}}\hat{p} + g\alpha(T - T_c)\boldsymbol{e_z}, \qquad \hat{\boldsymbol{\nabla}}\cdot\hat{\boldsymbol{u}} = 0, \quad \text{(2.1.14 \& 2.1.2 revisited)}$$

where the linear, Boussinesq equation of state (1.2.2) has been substituted into the buoyancy forcing, and the saline buoyancy contribution has been neglected.

We non-dimensionalise (2.1.14) with the new velocity scale and use (2.1.2) to introduce a non-dimensional stream function, $\boldsymbol{u} = \boldsymbol{\nabla}\times\psi\boldsymbol{e_y}$, for 2-D convective rolls. Taking the curl of (2.1.14) then leads to the vorticity equation:

$$\nabla^2\psi = -\mathcal{R}_p\frac{\partial\theta}{\partial x}. \tag{4.1.3}$$

As a result of the inclusion of thermal lag, the Rayleigh number presented here now has a slightly modified definition:

$$\mathcal{R}_p = \frac{g\alpha\Delta T\hat{\Pi}_0\omega\hat{d}}{\kappa\nu}$$

Note that any effects of thermal lag have been scaled out of the non-dimensional problem and will only appear when the results are translated back to dimensional coordinates.

4.1.2 Base-State Solution

In §2.5, I presented the following solution to the thermal diffusion equation (4.1.2) when subject to (2.3.2a) and (2.3.2l):

$$\theta = \theta_B \equiv \operatorname{erf}\left(\frac{z}{2\sqrt{t}}\right) + \exp\left(-\frac{z^2}{4t}\right)\operatorname{erfcx}\left(\frac{z}{2\sqrt{t}} + \mathcal{B}_i\sqrt{t}\right). \tag{4.1.4}$$

where the scaled complementary error function is defined by $\operatorname{erfcx}(y) = \exp(y^2)\operatorname{erfc}(y)$ (Carslaw and Jaeger, 1959). This has two relevant dimensionless length scales - the thermal diffusion length scale, $\sqrt{t}$, which evolves over time, and the cooling length scale, $1/\mathcal{B}_i$. The former of these is simply the dimensionless form of $\sqrt{\kappa\hat{t}}$, while the latter is related to the dimensional boundary cooling lengthscale, $\hat{d}_b$ (2.3.3) and is associated with the effects of imperfect conduction. The solution also has a well defined limit in the case of large Biot number, long times, or large depths:

$$\theta_B \sim \operatorname{erf}\left(\frac{z}{2\sqrt{t}}\right), \qquad \text{for} \qquad \frac{z + 2\mathcal{B}_i\, t}{2\sqrt{t}} \gg 1, \tag{4.1.5}$$

which will be referred to as the conductive limit.

4.2 Stability Analysis

To perform a stability analysis on this base state, we consider general, two-dimensional perturbations, θ_p and ψ_p, satisfying:

$$\theta(x,z,t) = \theta_B(z,t) + \theta_p(x,z,t), \qquad \psi(z,x,t) = \psi_p(x,z,t), \tag{4.2.1a,b}$$

with $\boldsymbol{u}_p = \boldsymbol{\nabla}\times\psi_p\boldsymbol{e_y}$. We use the energy stability method of Slim and Ramakrishnan (2010) to calculate the stability of the system by considering the maximal growth rate of arbitrarily sized perturbations. The method therefore provides a strong lower bound for the stability of the system, with all disturbances decaying below the threshold it provides, and convection permitted above it. For perfectly conducting boundaries, a number of methods have been used to determine the onset of instability, but we note that the these other methods generally assume small linear perturbations which means they may not capture an instability triggered by a finite amplitude perturbation. The popular propagation method (eg. Kim and Choi, 2012) also requires that perturbations spread vertically with the growing thermal diffusion length scale, which may break down here following the introduction of a second length scale, $\hat{d}_b$, to the infinite-depth problem.

However, it is important to remember that the stability bound presented here identifies the first perturbations that are able to grow in amplitude. Determining the time for convective disturbances to develop to a specified finite-amplitude threshold constitutes a different problem, and would depend on both the full details of the initial perturbation and the subsequent time development of these disturbances (see Tilton and Riaz, 2014; Emami-Meybodi et al., 2015).

When interpreting the results we will also make use of relevant linearised dynamics (discussed in §4.2.2) where the perturbations are assumed to be small compared to the base-state.

4.2.1 Energy Stability Method

The main calculations follow the energy stability method of Slim and Ramakrishnan (2010), which I summarise below. This method considers the maximal growth rate of the perturbation-amplitude functional:

$$E_0 = \int_V \frac{\theta_p^2}{2} d^3\boldsymbol{x}.$$

The integration volume, V, includes full depth of the domain and has a suitable width which allows horizontal boundary conditions to cancel, as discussed below. By finding the maximal growth rate of this functional with respect to all possible perturbations θ_p that are constrained by the dynamics in (4.1.2) and (4.1.3), we can determine the non-linear stability of the system with respect to an arbitrary perturbation. I have chosen a functional of θ_p rather than a functional of ψ_p because the equations include no time derivatives of ψ_p. This functional represents a generalised energy, rather than a physical energy. Differentiating E_0 with respect to time and using the energy equation (4.1.2) to eliminate $\partial\theta_p/\partial t$ leads to:

$$\dot{E}_0 = \frac{dE_0}{dt} = \int_V \left[\theta_p \nabla^2 \theta_p - \theta_p \left(\boldsymbol{u}_p \cdot \boldsymbol{\nabla}\right) \theta_B - \left(\boldsymbol{u}_p \cdot \boldsymbol{\nabla}\right) \left(\frac{\theta_p^2}{2}\right)\right] d^3\boldsymbol{x}. \tag{4.2.2}$$

The non-linear term in (4.1.2) gives rise to the non-quadratic final term above. Integrating this term by parts gives:

$$\int_V \boldsymbol{u}_p \cdot \boldsymbol{\nabla} \left(\frac{\theta_p^2}{2}\right) d^3\boldsymbol{x} = \oint_S \boldsymbol{n} \cdot \left[\frac{\theta_p^2}{2} \boldsymbol{u}_p\right] d^2\boldsymbol{x} - \int_V \frac{\theta_p^2}{2} \, \boldsymbol{\nabla} \cdot \boldsymbol{u}_p \, d^3\boldsymbol{x},$$

where S is the surface bounding the volume V. Incompressibility (2.1.2) causes the contribution from the final term to vanish. We focus on systems where the boundary terms also vanish or are negligible, with $\boldsymbol{u}_1 \cdot \boldsymbol{n} = \partial\psi_1/\partial x = 0$ at $z = 0$

and as $z \to \infty$, and then either assuming horizontal periodicity, impermeable or isothermal sidewalls, or a domain of sufficient width for end contributions to be small compared to the full volume integral. Hence, the only non-linear term in the original dynamical equations makes no contribution to the stability of the system and we will obtain the same stability results for linearised and non-linear perturbations.

The growth rate functional is written as:

$$\sigma = \frac{\dot{E}_0 + \dot{E}_1}{2E_0},$$

where $\dot{E}_0/E_0$ is the normalised perturbation growth rate and a new term, $\dot{E}_1/E_0$, is introduced to ensure that any variations on this functional are constrained by the vorticity equation (4.1.3). We add this constraint using a distributed Lagrange multiplier, $\mu_p(\boldsymbol{x}, t)$, with:

$$\dot{E}_1 = \int_V \mu_p \left[\nabla^2 \psi_p + \mathcal{R}_p \frac{\partial \theta_p}{\partial x} \right] d^3\boldsymbol{x}.$$

To find the maximal growth rate $\sigma_{\max}$, we vary σ with respect to θ_p, ψ_p and μ_p resulting in the system:

$$\begin{aligned} \nabla^2 \theta_p - \frac{1}{2} \frac{\partial \theta_B}{\partial z} \frac{\partial \psi_p}{\partial x} - \sigma_{\max} \theta_p &= \frac{\mathcal{R}_p}{2} \frac{\partial \mu_p}{\partial x}, \\ \nabla^2 \psi_p = -\mathcal{R}_p \frac{\partial \theta_p}{\partial x}, \qquad & \nabla^2 \mu_p + \frac{\partial \theta_B}{\partial z} \frac{\partial \theta_p}{\partial x} = 0, \end{aligned} \tag{4.2.3a-c}$$

with boundary conditions on μ_p identical to those on ψ_p.

Despite considering non-linear perturbations, the resulting derived system (4.2.3) is linear and invariant under horizontal translations, and so we assume a horizontally periodic perturbation structure and perform a Fourier decomposition with wavenumber, k, writing:

$$\begin{bmatrix} \theta_p(x,z,t) \\ \psi_p(x,z,t) \\ \mu_p(x,z,t) \end{bmatrix} = \begin{bmatrix} \theta_f(\mathrm{k},z,t) \\ i\mathrm{k}\ \psi_f(\mathrm{k},z,t) \\ i\mathrm{k}\ \mu_f(\mathrm{k},z,t) \end{bmatrix} e^{i\mathrm{k}x}, \tag{4.2.4}$$

where the subscript $_f$ indicates that the variables have been Fourier transformed in the horizontal direction. Roman 'k' represents the wavenumber, and is distinct from italic 'k' that represents the thermal conductivity. The eigenvalue problem (4.2.3) reduces to:

$$\mathsf{A}\boldsymbol{y} - \mathcal{R}_p\, \mathsf{B}\boldsymbol{y} = \sigma_{\max} \mathsf{C}\boldsymbol{y}, \tag{4.2.5a}$$

$$\boldsymbol{y} = \begin{bmatrix} \theta_f \\ \psi_f \\ \mu_f \end{bmatrix}, \qquad \mathsf{A} = \begin{bmatrix} \frac{\partial^2}{\partial z^2} - \mathrm{k}^2 & \frac{\mathrm{k}^2}{2}\frac{\partial \theta_B}{\partial z} & 0 \\ 0 & \frac{\partial^2}{\partial z^2} - \mathrm{k}^2 & 0 \\ \frac{\partial \theta_B}{\partial z} & 0 & \frac{\partial^2}{\partial z^2} - \mathrm{k}^2 \end{bmatrix}, \tag{4.2.5b,c}$$

$$\mathsf{B} = \begin{bmatrix} 0 & 0 & -\frac{\mathrm{k}^2}{2} \\ -1 & 0 & 0 \\ 0 & 0 & 0 \end{bmatrix}, \qquad \mathsf{C} = \begin{bmatrix} 1 & 0 & 0 \\ 0 & 0 & 0 \\ 0 & 0 & 0 \end{bmatrix}. \tag{4.2.5d,e}$$

The boundary conditions are expanded in the same way as the dynamical equations and become:

$$\frac{\partial \theta_f}{\partial z} = \mathcal{B}_i\, \theta_f, \qquad \psi_f = 0, \qquad \mu_f = 0, \qquad \text{at } z = 0 \tag{4.2.6a-c}$$

$$\theta_f \to 0, \qquad \psi_f \to 0, \qquad \mu_f \to 0, \qquad \text{as } z \to \infty. \tag{4.2.6d-f}$$

As a final step, we note that time now only appears explicitly through the θ_B terms and can be removed by transforming to the self-similar coordinates natural to the thermal diffusion problem:

$$\tilde{z} = \frac{z}{\sqrt{t}}, \qquad \tilde{\mathrm{k}} = \mathrm{k}\sqrt{t}, \qquad \tilde{\mathcal{R}}_p = \mathcal{R}_p\sqrt{t}, \qquad \tilde{\mathcal{B}}_i = \mathcal{B}_i\sqrt{t}, \qquad \tilde{\sigma} = \sigma_{\max} t. \tag{4.2.7}$$

This transformation effectively replaces the non-dimensionalisation length $\hat{d}$ with the thermal diffusion length scale $\sqrt{\kappa \hat{t}}$ and leaves the form of (4.2.5) & (4.2.6) unchanged (with each variable replaced by its rescaled counterpart). With the similarity transformation, the base-state temperature profile (4.1.4) becomes:

$$\theta_B = \operatorname{erf}\left(\frac{\tilde{z}}{2}\right) + \exp\left(-\frac{\tilde{z}^2}{4}\right) \operatorname{erfcx}\left(\frac{\tilde{z}}{2} + \tilde{\mathcal{B}}_i\right) \tag{4.2.8}$$

The removal of t via this rescaling has the advantage of reducing the parameter space that needs to be considered when constraining the stability. I calculate the results in these similarity co-ordinates, corresponding to scales measured relative to the instantaneous thickness of the thermal boundary layer, before later translating back to time-independent physical scales. Note also that by performing this transformation after deriving the stability system (4.2.5) we have avoided any *a priori* assumption of self-similar disturbances, so that our energy stability analysis encompasses general two-dimensional disturbances rather than just disturbances confined to spread at the same rate as the boundary layer, as required by the propagation method.

This eigenvalue problem can be solved for the maximal growth rate at a given Rayleigh number, wavenumber and Biot number, with instability allowed if the real part of $\tilde{\sigma}$ is greater than zero. This yields the neutral stability curve $\tilde{\mathcal{R}}_p(\tilde{\mathrm{k}}, \tilde{\mathcal{B}}_i)$ where the real part of the growth rate is equal to zero. If the imaginary part of $\tilde{\sigma}$ is also zero on the neutral stability curve, then the neutral stability curve can be found directly by setting $\tilde{\sigma} = 0$ in (4.2.5) and solving for $\tilde{\mathcal{R}}_p$. Whilst we did not formally prove that the growth rate is purely real, we found in preliminary investigations that there were no complex growth rates for a sample of Biot numbers, $\tilde{\mathcal{B}}_i = 0.05,\ 1,\ 50$, as well as when $\tilde{\mathcal{B}}_i \to \infty$, and that both methods produced the same results for the position of the neutral stability curve. To accelerate the computations, we therefore neglect oscillatory modes and set the growth rate to zero in all subsequent calculations and solve for the neutral stability curve directly.

4.2.2 Linearised dynamics

Having established above that the energy stability method yields the same stability criteria for linear and nonlinear perturbations, we will also make use of linearised dynamics when interpreting our results. We assume that the perturbations in equation (4.2.1) are small compared to the base-state values, and terms that are quadratic in perturbations can be neglected. The linearised forms of (4.1.2) and (4.1.3) are:

$$\frac{\partial \theta_p}{\partial t} + \frac{\partial \theta_B}{\partial z}\frac{\partial \psi_p}{\partial x} = \nabla^2 \theta_p, \qquad \nabla^2 \psi_p = -\mathcal{R}_p \, \frac{\partial \theta_p}{\partial x}.$$

Eliminating θ_p results in:

$$\left(\frac{\partial}{\partial t} - \nabla^2\right) \nabla^2 \psi_p = \mathcal{R}_p \, \frac{\partial \theta_B}{\partial z} \, \frac{\partial^2 \psi_p}{\partial x^2}. \tag{4.2.9}$$

Thus, the linearised perturbation dynamics are driven by the quantity $\mathcal{R}_p \, \partial\theta_B/\partial z$. We will make use of this observation later when interpreting results, noting that the form of this equation is unchanged under the similarity transformation (4.2.7).

4.3 Numerical Method

To solve the eigenvalue problem in (4.2.5), we use a Chebyshev pseudo-spectral discretisation of the three variables, θ_f, ψ_f & μ_f, and the differential operators are rewritten as matrix operators on the Chebyshev modes (see Trefethen, 2000). The discretised form of the boundary conditions (4.2.6) are algebraically rearranged to express the boundary values in terms of the internal values. This is then used to

write an eigenvalue problem for the internal points with eigenfunctions that satisfy both the dynamical equations and boundary conditions.

The eigenvalue problem is solved numerically by the `eig` routine in MATLAB, which uses the QZ algorithm (Horn and Johnson, 1985). When solving for the growth rate, the most positive eigenvalue is selected, where as the least positive eigenvalue is selected when solving for the Rayleigh number. These represent the most unstable modes, with the other eigenvalues represent higher order instability modes.

Convergence testing was performed to ensure that the results are numerically consistent, and independent of both the number of Chebyshev modes used, N_z, and the numerically imposed finite domain depth, $\tilde{H}$, for suitably large $\tilde{H}$. The resolution was increased at fixed $\tilde{H}$ to obtain numerical convergence. This was then repeated at larger $\tilde{H}$ until the resolution-converged values also showed no significant variation with depth. For $\tilde{\mathcal{B}}_i > 1$, good convergence is found using $N_z \geq 40$ and $\tilde{H} \geq 70$. For $\tilde{\mathcal{B}}_i < 1$, a deeper domain and more grid points were needed. For $\tilde{\mathcal{B}}_i = 0.001$, the lowest Biot number investigated, convergence was only found once $N_z \geq 90$ and $\tilde{H} \geq 475$.

4.4 Results

To test the accuracy of our code, I first solved the porous boundary layer convection problem in the limit of a perfectly conducting boundary, with an infinite Biot number. We found the critical wavenumber, $\tilde{\mathrm{k}}_\infty$, and Rayleigh number, $\tilde{\mathcal{R}}_{p\infty}$, to be:

$$\tilde{\mathrm{k}}_\infty = 0.378, \qquad \tilde{\mathcal{R}}_{p\infty} = 6.92,$$

in agreement with the results of Slim and Ramakrishnan (2010), who used an equivalent definition of stability. The results here are also of a similar magnitude to calculations using alternative definitions of stability, (for a review, see Tilton et al., 2013, or table 1.2 of this work). Note that the fixed dimensionless wavenumber $\tilde{\mathrm{k}}_\infty$ and Rayleigh number $\tilde{\mathcal{R}}_{p\infty}$ result from the similarity transformation (4.2.7), and lead to time-dependence in physical co-ordinates. Reversing the transformation leads to a dynamic stability criteria compared to the fixed physical scales.

The Biot number appears in the upper boundary conditions (2.3.2l) and in the base-state temperature profile (4.2.8). In addition to the full system calculations, I ran two additional sets of diagnostic simulations as sensitivity studies to isolate

the impacts of $\tilde{\mathcal{B}}_i$-dependent changes of potential energy in the background profile, and $\tilde{\mathcal{B}}_i$-dependent modulation of the perturbation boundary conditions. The *profile effects* set, denoted by superscript ^{p}, uses a conductive boundary condition, $\theta_f = 0$ at $z = 0$, for the perturbation but the full $\tilde{\mathcal{B}}_i$-dependent base-state temperature profile (4.2.8). Meanwhile the *boundary effects* set, denoted by superscript ^{b}, uses the conductive limit of the base-state temperature profile, $\theta_B \sim \mathrm{erf}\,(\tilde{z}/2)$, but maintaining the full $\tilde{\mathcal{B}}_i$-dependent boundary condition for the perturbation. These two extra sets are not intended to represent physically realisable configurations, but instead provide diagnostic insight into the mathematical scalings obtained.

Figure 4.2a shows how the Rayleigh number at neutral stability, with $\tilde{\sigma} = 0$, varies with wavenumber, $\tilde{\mathrm{k}}$, and Biot number, $\tilde{\mathcal{B}}_i$, along with showing the critical wavenumbers, $\tilde{\mathrm{k}}_c$. Figure 4.2b shows the variation of the resulting critical Rayleigh numbers, $\tilde{\mathcal{R}}_{pc}$, with $\tilde{\mathcal{B}}_i$. It is clear that decreasing the Biot number monotonically increases the critical Rayleigh number for the full system (figure 4.2b), while the effect on the critical wave number is more complex with an increase when compared to the conductive limit for $\tilde{\mathcal{B}}_i > O(1)$ and a decrease for $\tilde{\mathcal{B}}_i < O(1)$ - see figure 4.2a. There are two distinct regimes for large and small Biot numbers, which are emphasised using a change of scale at $\tilde{\mathrm{k}} = 0.3$ in figure 4.2a and $\tilde{\mathcal{R}}_{pc} = 12.5$ in figure 4.2b. We find no indication of any secondary minima in the stability curves, $\tilde{\mathcal{R}}_{pc}(\tilde{\mathrm{k}})$, for each $\tilde{\mathcal{B}}_i$.

The structure of the instability differs in these two limits, as illustrated in figure 4.3. For large Biot numbers, the unstable convective cells are narrower and do not penetrate as deeply as the cells for low Biot numbers. By normalising the perturbations such that the integrated amplitude over all three perturbation variables is equal to 1, we can also see that the thermal variations and velocities have significantly larger amplitude when the Biot number is large. This suggests that the instability will be more intense in this regime but less disperse. This conclusion is also supported by looking at the growth rates, $\tilde{\sigma}$, at the critical wavenumber and with a Rayleigh number equal to double the critical value. When $\tilde{\mathcal{B}}_i = 100$, this non-dimensional growth rate is 0.35, while for $\tilde{\mathcal{B}}_i = 0.022$ it is 0.016 which suggests that after onset of instability, the disturbance will initially develop more rapidly at large Biot numbers than it will for small Biot numbers. However, determining the long-time development will require a study of the time-dependent evolution of perturbations to confirm whether such trends continue.

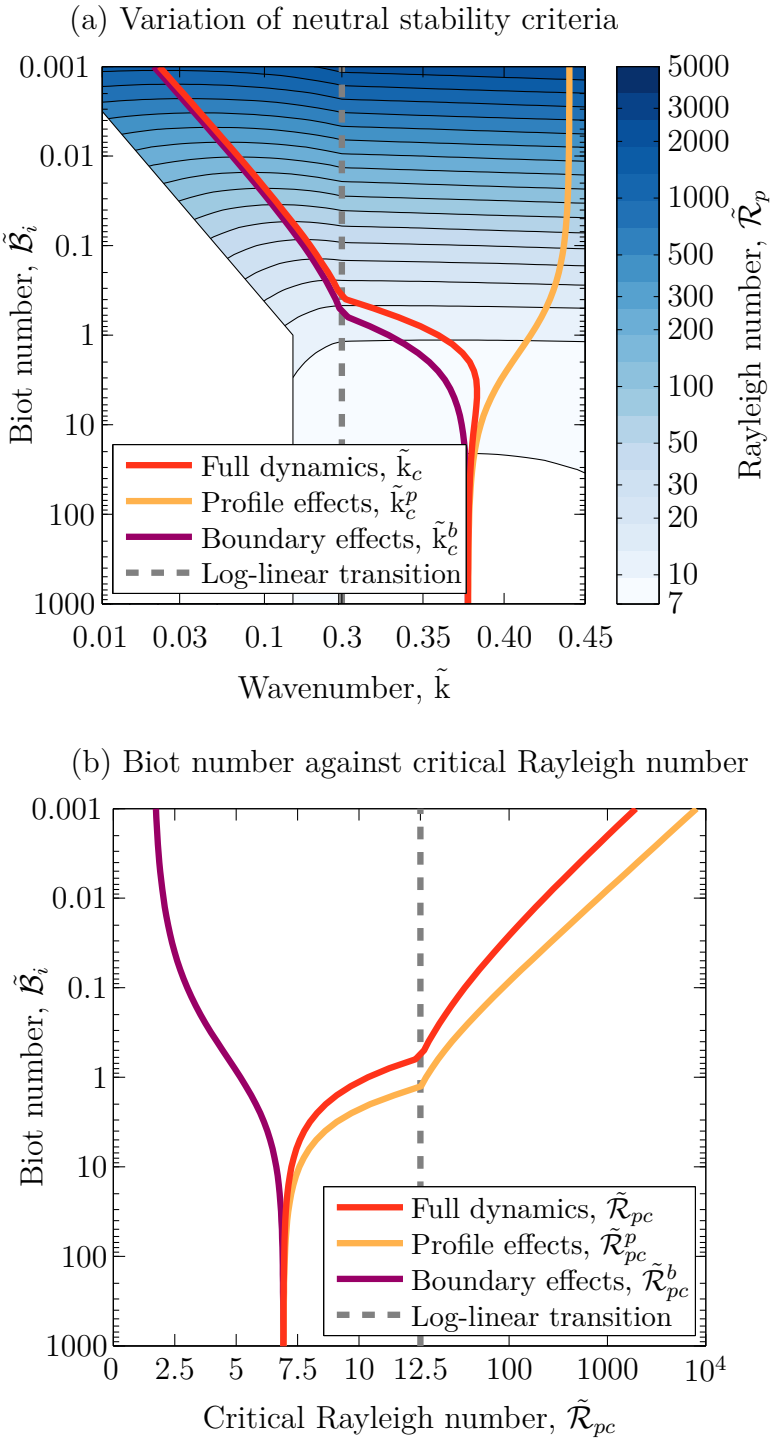

Figure 4.2: Stability properties against Biot number. (a) The colour scale shows the Rayleigh number at neutral stability as a function of wavenumber and Biot number. Overlayed are the critical wavenumbers of the three calculation sets described in the text. To aid viewing of the different limits, the wavenumber is displayed on a logarithmic scale for $\tilde{\mathrm{k}} < 0.3$ and linear scale for $\tilde{\mathrm{k}} > 0.3$, with the transition marked by a dashed line. (b) The critical Rayleigh number varies with Biot number. The data is shown on a linear scale for $\tilde{\mathcal{R}}_{pc} < 12.5$ and a logarithmic scale for $\tilde{\mathcal{R}}_{pc} > 12.5$.

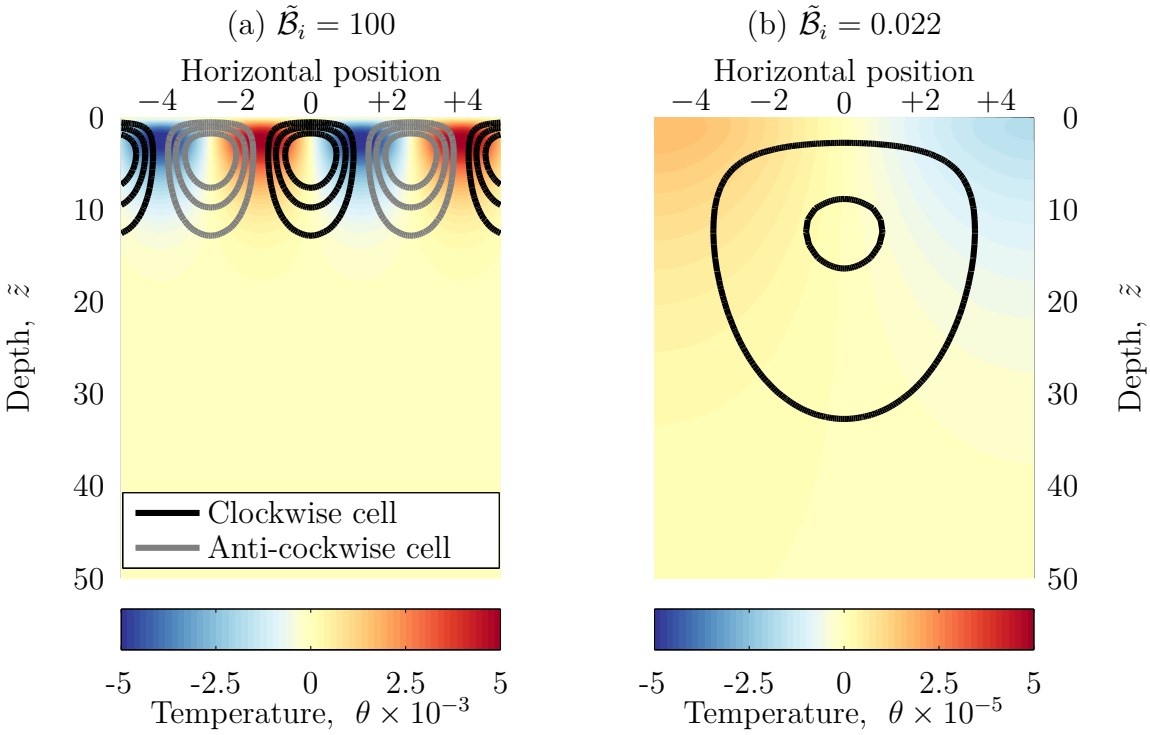

Figure 4.3: Representative convective instability structure for (a) a high Biot number and (b) a low Biot number. The colour scale shows the thermal variation with hot regions coloured red and cold regions coloured blue. Stream lines are also shown with clockwise cells in black and anti-clockwise cells in grey, with $\psi_f = \pm 0.03$, ± 0.06 and ± 0.09 contours plotted. The same vertical and horizontal scales are used in the two panels and the instability continues periodically beyond the region shown, with alternating directions of neighbouring convection cells.

4.4.1 High Biot Number Limit

Boundaries that can rapidly remove heat from a medium have a large Biot number and behave as good effective conductors, with an infinite Biot number representing a perfectly conducting boundary. Behaviour in the large Biot number limit, $\tilde{\mathcal{B}}_i \gg 1$, is dominated by the limiting case of a perfectly conducting boundary (discussed above) with only small $\tilde{\mathcal{B}}_i$-dependent variations. To illustrate the underlying scalings, figures 4.4a and 4.4b show compensated plots taking the deviation from the perfectly conducting limit and scaling by the Biot number, plotting $\tilde{\mathcal{B}}_i(\tilde{\mathcal{R}}_{pc} - \tilde{\mathcal{R}}_{p\infty})$ for the compensated critical Rayleigh number and $\tilde{\mathcal{B}}_i(\tilde{\mathrm{k}}_c - \tilde{\mathrm{k}}_\infty)$ for the compensated critical wavenumber. We observe that both groupings tend to a constant value for large Biot numbers. The critical Rayleigh number and critical wavenumber

therefore behave as:

$$\tilde{\mathcal{R}}_{pc} \sim \tilde{\mathcal{R}}_{p\infty} + \frac{3.25}{\tilde{\mathcal{B}}_i}, \quad \tilde{\mathcal{R}}^p_{pc} \sim \tilde{\mathcal{R}}_{p\infty} + \frac{6.35}{\tilde{\mathcal{B}}_i}, \quad \tilde{\mathcal{R}}^b_{pc} \sim \tilde{\mathcal{R}}_{p\infty} - \frac{3.10}{\tilde{\mathcal{B}}_i}, \quad \text{for } \tilde{\mathcal{B}}_i \gg 1, \tag{4.4.1a-c}$$

$$\tilde{\mathrm{k}}_c \sim \tilde{\mathrm{k}}_\infty + \frac{0.054}{\tilde{\mathcal{B}}_i}, \qquad \tilde{\mathrm{k}}^p_c \sim \tilde{\mathrm{k}}_\infty + \frac{0.088}{\tilde{\mathcal{B}}_i}, \qquad \tilde{\mathrm{k}}^b_c \sim \tilde{\mathrm{k}}_\infty - \frac{0.034}{\tilde{\mathcal{B}}_i}, \quad \text{for } \tilde{\mathcal{B}}_i \gg 1, \tag{4.4.2a-c}$$

corresponding to the full calculation, profile effects and boundary effects in each of (4.4.1a-c) and (4.4.2a-c). These trends remain accurate for $\tilde{\mathcal{B}}_i \gtrsim 5$. We also note that in both cases the sum of the deviations caused by the profile effects only, plus the deviations caused by the boundary effects only is very similar to the deviation of the full system:

$$\Delta\tilde{\mathcal{R}}_{pc} = \tilde{\mathcal{R}}_{pc} - \tilde{\mathcal{R}}_{p\infty} \approx \Delta\tilde{\mathcal{R}}^p_{pc} + \Delta\tilde{\mathcal{R}}^b_{pc}, \qquad \Delta\tilde{\mathrm{k}}_c = \tilde{\mathrm{k}}_c - \tilde{\mathrm{k}}_\infty \approx \Delta\tilde{\mathrm{k}}^p_c + \Delta\tilde{\mathrm{k}}^b_c.$$

This suggests that non-linear interactions between the changes in the base-state profile and perturbation boundary condition are negligible when the Biot number is large.

The $O(1/\tilde{\mathcal{B}}_i)$ deviations found in this limit can be considered as a first-order expansion in the small parameter $1/\tilde{\mathcal{B}}_i$ around the perfectly conducting limit, $\tilde{\mathcal{B}}_i \to \infty$. This is also reflected in the profiles of θ_f, ψ_f and μ_f having only small deviations from the conducting limit (not shown here). The observed signs of the deviations are explained as follows. For large Biot numbers, the thermal forcing term identified previously in (4.2.9) is approximately:

$$\tilde{\mathcal{R}}_p \frac{\partial\theta_B}{\partial\tilde{z}} = \frac{\tilde{\mathcal{R}}_p}{\sqrt{\pi}} \exp\left(-\frac{\tilde{z}^2}{4}\right)\left[1 - \frac{\tilde{z}}{2\tilde{\mathcal{B}}_i} + O\left(\frac{1}{\tilde{\mathcal{B}}_i^2}\right)\right], \qquad \text{for } \tilde{\mathcal{B}}_i \gg 1.$$

When the Biot number decreases from the perfectly conducting limit, the thermal forcing decreases because the potential energy available for convection has been reduced. This change in the background profile necessarily causes an increase in the critical Rayleigh number, $\Delta\tilde{\mathcal{R}}^p_{pc} > 0$, but it also affects the critical wavenumber by changing the vertical distribution of the available energy. By decreasing the energy available at depth to a greater extent than the energy available close to the boundary, the change in forcing confines the convection to a shallower layer near the surface. In turn, this is consistent with a smaller convective wavelength and larger wavenumber, $\Delta\tilde{\mathrm{k}}^p_c > 0$, when viewed as relative fractions of the corresponding diffusion length scale of the growing boundary layer.

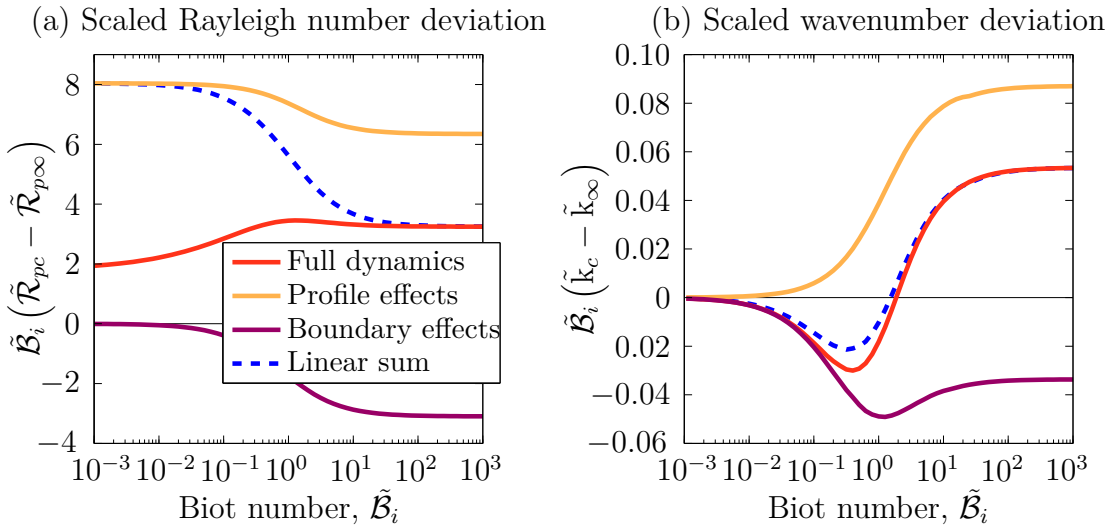

Figure 4.4: Scaled deviations from the perfectly conducting limit: (a) $\tilde{\mathcal{B}}_i(\tilde{\mathcal{R}}_{pc} - \tilde{\mathcal{R}}_{p\infty})$ for the compensated critical Rayleigh number, and (b) $\tilde{\mathcal{B}}_i(\tilde{\mathrm{k}}_c - \tilde{\mathrm{k}}_\infty)$ for the compensated critical wavenumber. The scaled deviation of both the Rayleigh number and wavenumber asymptote to a constant value for large Biot numbers. In this limit, the deviation for the full system (red) matches a linear sum (dashed blue) of the deviation caused by the profile effects (orange), and the deviation caused by the boundary effects (purple). At small Biot numbers, $\tilde{\mathcal{B}}_i(\tilde{\mathcal{R}}_{pc} - \tilde{\mathcal{R}}_{p\infty})$ again tends to a constant (but different) value for the full dynamics and profile effects.

However, the Biot number dependence of the perturbation boundary condition causes the opposite effect, as shown by the scaling of the boundary effects simulations. The change in boundary condition allows the energy close to the upper boundary to be more effectively utilised by permitting modes to develop with non-zero thermal variation on the upper boundary. This tends to decrease the critical Rayleigh number, $\Delta\tilde{\mathcal{R}}^b_{pc} < 0$. It is also consistent with a tendency for stronger and deeper-penetrating convection, leading to larger convective cells with a longer wavelength and smaller wavenumber, $\Delta\tilde{\mathrm{k}}^b_c < 0$ compared to the boundary layer depth. Barletta et al. (2015) noted a similar effect for steady-state convection in a finite horizontal domain. As the Biot number decreases they observed that the critical Rayleigh number and critical wavenumber also decrease as the boundary conditions become less restrictive on the allowable perturbations (Note that their parameters a_i and b_i $(i = 1, 2)$ are equivalent to $1/\mathcal{B}_i$).

The combined effect of these profile and boundary effects is an increase in both the critical Rayleigh number and critical wavenumber compared to the perfectly conducting limit. This suggests that the changes caused by the available potential energy in the background profile are more significant than the modification to the

heat-flux boundary conditions on the growing perturbations.

The above results have considered the impact of the effective boundary conductivity on wavenumbers and Rayleigh numbers scaled relative to the time-dependent thermal diffusion timescale $\sqrt{\kappa \hat{t}}$. We can invert the scaling behaviour in equation (4.4.1a-c) to find the physical instability time of the system:

$$\hat{t}_i = 47.9\ \hat{t}_p \left[1 + 0.136\ \mathcal{R}_B + O\left(\mathcal{R}_B\right)^2\right], \qquad \text{for} \quad \mathcal{R}_B \ll 1. \tag{4.4.3}$$

where the buoyancy time scale is $\hat{t}_p = \hat{d}_p^2/\kappa$, and we define the effective boundary Rayleigh number as the ratio of boundary-cooling and buoyancy lengthscales,

$$\mathcal{R}_B = \frac{\mathcal{R}_p}{\mathcal{B}_i} = \frac{g\alpha\Delta T\hat{\Pi}_0\omega k}{\kappa\nu\mathfrak{h}} = \frac{\hat{d}_b}{\hat{d}_p}. \tag{4.4.4}$$

The instability time (4.4.3) is dominated by the buoyancy time scale $\hat{t}_p$. As the heat transfer coefficient increases, $\mathfrak{h} \to \infty$, the boundary length scale correspondingly decreases, $\hat{d}_b \to 0$, and the time of instability reduces to the time found by Slim and Ramakrishnan (2010). For finite $\mathfrak{h}$, $\hat{d}_b$ is non-zero and convective instability is delayed in a way that depends on the boundary Rayleigh number (4.4.4). Larger values of $\mathcal{R}_B$ correspond to increasingly imperfect cooling and convection is delayed by a greater amount. The conductive limit corresponds to $\mathcal{R}_B \to 0$, and the subsequent expansion (4.4.3) in small $\mathcal{R}_B$ is accurate to within 10% for $\mathcal{R}_B \lesssim 14.4$.

We can also find the physical wavenumber at the moment of convective instability:

$$\hat{\mathrm{k}}_i = \frac{0.0546}{\hat{d}_p}\left[1 - 0.0206\ \mathcal{R}_B + O\left(\mathcal{R}_B\right)^2\right]. \qquad \text{for } \mathcal{R}_B \ll 1. \tag{4.4.5}$$

The dominant length scale in this limit is therefore the buoyancy length scale $\hat{d}_p$. We note that this approximation is accurate to within 10% of the true value for $\mathcal{R}_B \lesssim 4.8$, which is a smaller range of $\mathcal{R}_B$ than for (4.4.3). Intriguingly, we see that whilst (4.4.2a-c) predicts that boundary conductivity effects increase the wavenumber scaled relative to the thermal diffusion length, there is still a net decrease in the physical wavenumber observed at the time of convective instability. This is a consequence of the delayed instability time described in (4.4.3). Thus the trend of wavenumber variation is now monotonic for all values of $\mathcal{R}_B$. The delay of instability allows growth of a thicker diffusive boundary layer before convection is triggered. Combined with the relative changes in the distribution of available potential energy across the boundary layer depth, and modulation of

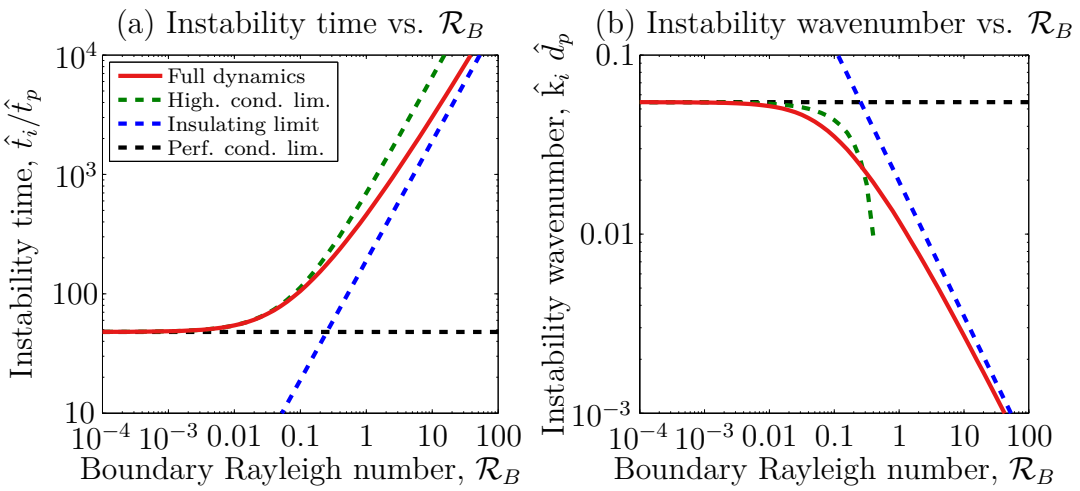

Figure 4.5: These two graphs show the variation of (a) the physical instability time and (b) most unstable wavenumber with the boundary Rayleigh number, $\mathcal{R}_B = \frac{g\alpha\Delta T\Pi_0\lambda^*}{\kappa\nu h}$, comparing the full dynamics to the limiting trends given in equations (4.4.3) and (4.4.5) for the highly conducting limit and (4.4.6) and (4.4.7) for the insulating limit. The perfectly conducting limit is given by (4.4.3) and (4.4.5) with $\mathcal{R}_B = 0$.

growing perturbations by surface boundary conditions, the net effect is an increase of the physical wavelength of the perturbation expected at the moment of instability.

In figure 4.5, we illustrate the full behaviour of the onset time (scaled by the buoyancy time), $\hat{t}_i/\hat{t}_p$, and onset wavenumber (scaled by the buoyancy length), $\hat{\mathrm{k}}_i\ \hat{d}_p$. We also plot the limiting behaviour found in (4.4.3) and (4.4.5) for the highly conducting limit, and those for the insulating limit which is discussed in the next section. Note that the non-monotonic variation found for the self-similar wavenumber (figure 4.2a) does not appear in the physical onset wavenumber, (figure 4.5b), as discussed above.

4.4.2 Low Biot Number Limit

In the low Biot number limit, the upper boundary is a poor thermal conductor and thus heat removal is much slower. The limiting case of $\tilde{\mathcal{B}}_i = 0$ represents a perfectly insulating boundary with no cooling and no convection. Behaviour for $\tilde{\mathcal{B}}_i \ll 1$ shows very different scaling to the high Biot number regime.

Figure 4.4a shows that the scaled deviations for both $\tilde{\mathcal{R}}_{pc}$ and $\tilde{\mathcal{R}}^p_{pc}$ tend to a constant value for $\tilde{\mathcal{B}}_i \ll 1$, consistent with the profile effects controlling the behaviour of the full dynamics, while the deviation for $\tilde{\mathcal{R}}^b_{pc}$ goes to zero. As $\tilde{\mathcal{B}}_i \to 0$, we note that

$\tilde{\mathcal{B}}_i\tilde{\mathcal{R}}_{p\infty} \to 0$ and hence the asymptotic behaviour is consistent with:

$$\tilde{\mathcal{R}}_{pc} \sim \frac{1.9}{\tilde{\mathcal{B}}_i}, \qquad \tilde{\mathcal{R}}^p_{pc} \sim \frac{8.0}{\tilde{\mathcal{B}}_i}, \qquad \text{for } \tilde{\mathcal{B}}_i \ll 1.$$

The dominating influence of the profile effects on the stability criteria suggests that the instability is controlled by the amount of potential energy available for convection with little dependence on the perturbation boundary conditions. This scaling can be explained by approximating the thermal forcing term in (4.2.9) for small Biot numbers:

$$\tilde{\mathcal{R}}_p \, \frac{\partial \theta_B}{\partial \tilde{z}} \sim \tilde{\mathcal{R}}_p \, \tilde{\mathcal{B}}_i \, \text{erfc}\left(\frac{\tilde{z}}{2}\right), \qquad \text{for } \tilde{\mathcal{B}}_i \ll 1.$$

Clearly, the vertical structure of the forcing is independent of the Biot number (leading to the constant critical wavenumber for the profile effects) but the amplitude of the forcing has a linear dependence on $\tilde{\mathcal{R}}_p \, \tilde{\mathcal{B}}_i$. We therefore expect that the critical Rayleigh number should scale as $\tilde{\mathcal{R}}_{pc} = O(1/\tilde{\mathcal{B}}_i)$, as observed. Hence in the limit of poor thermal transport by the boundary, convection is suppressed because the available potential energy in the background profile is reduced.

This argument might suggest the introduction of a local Rayleigh number, $\mathcal{R}_{pl} \propto \tilde{\mathcal{R}}_p \, [1 - \theta(0,t)]$, which is dependent on the time-evolving temperature difference within the porous media rather than the externally-imposed constant temperature difference ΔT. This local Rayleigh number is an analogue to the Biot-modified Rayleigh number of Kubitschek and Weidman (2003) for a fixed depth, steady-state system. However, whilst such a modification would capture the correct form of Biot-number dependence by accounting for variation in the global critical Rayleigh number caused by changes to the surface temperature, it does not determine the correct numerical prefactor. There are still $\mathcal{B}_i$-dependent variations in $\mathcal{R}_{pl}$ which arise from the changing perturbation boundary conditions and from the changing vertical forcing structure. This second effect does not appear in Kubitschek and Weidman (2003) because their base-state temperature profile has a linear vertical structure which is unchanged by variations in the Biot number. The time-dependent nature of the local Rayleigh number used here means that it requires more careful interpretation than the global Rayleigh number, but might be useful for order of magnitude estimates when considering applications of the results.

We can invert these scalings to find the dimensional convective instability time:

$$\hat{t}_i \sim 1.9 \, \mathcal{R}_B \, \hat{t}_p = 1.9 \left(\hat{t}_p \hat{t}_b\right)^{1/2} = 1.9 \frac{\hat{d}_b \hat{d}_p}{\kappa}, \qquad \text{for } \mathcal{R}_B \gtrsim 1.0 \times 10^5. \quad (4.4.6)$$

The leading-order scaling of the instability time in this nearly-insulating limit depends on the diffusion time scale over a distance given by the geometric mean of the boundary-cooling length scale $\hat{d}_b$ and the buoyancy length scale $\hat{d}_p$. This contrasts with the high Biot number limit, where we found that the dependence on $\hat{d}_b$, and hence on the rate of heat transfer $\mathfrak{h}$, is only through weak higher-order corrections in the effective boundary Rayleigh number $\mathcal{R}_B$. The transition towards this limit for $\mathcal{R}_B \gg 1$ is illustrated in figure 4.5a.

Despite the perturbation boundary conditions playing no significant role in controlling the instability time, they intriguingly are significant for selecting a preferred wavelength. Figure 4.2a shows that the scaling of the critical wavenumber is consistent between the full dynamics and the boundary effects simulations, but differs substantially from the scaling found for the profile effects simulations. The observed asymptotic trends are:

$$\tilde{\mathrm{k}}_c \sim 0.73\sqrt{\tilde{\mathcal{B}}_i}, \qquad \tilde{\mathrm{k}}_c^b \sim 0.67\sqrt{\tilde{\mathcal{B}}_i}, \qquad \text{for } \tilde{\mathcal{B}}_i \ll 1.$$

Expressing this in dimensional coordinates leads to:

$$\hat{\mathrm{k}}_c \sim 0.73\sqrt{\frac{1}{\hat{d}_b\sqrt{\kappa\hat{t}}}},$$

which indicates that the critical wavenumber scales inversely with the geometric mean of the two thermal length scales in the problem, namely the thermal diffusion length scale, $\sqrt{\kappa\hat{t}}$, and the boundary cooling length scale, $\hat{d}_b$, the latter of which contains the effects of the heat transfer coefficient, $\mathfrak{h}$.

At the physical instability time (4.4.6), this wavenumber becomes:

$$\hat{\mathrm{k}}_i \sim \frac{0.62}{\mathcal{R}_B{}^{3/4}\,\hat{d}_p} = \frac{0.62}{\hat{d}_b{}^{3/4}\,\hat{d}_p{}^{1/4}}, \qquad \text{for } \mathcal{R}_B \gtrsim 3.1\times 10^4. \tag{4.4.7}$$

Thus there is stronger dependence of the critical wavenumber on boundary conductivity effects, scaling as $\hat{d}_b{}^{-3/4}$ and therefore $\mathfrak{h}^{3/4}$, than on the buoyancy effects, scaling as $\hat{d}_p{}^{-1/4}$. The transition towards the scaling (4.4.7) for the insulating limit is illustrated in figure 4.5b.

4.5 Conclusion

This chapter has investigated the convective stability of a growing thermal boundary layer in a semi-infinite porous medium cooled from above via exchange with a heat sink with imperfect thermal transport. The system stability depends on the dimensionless Biot number, $\tilde{\mathcal{B}}_i$, which characterises the ratio of the effective thermal conductivity of heat exchange with the surface heat sink, compared to thermal conduction in the porous media. Stability also depends on a porous medium Rayleigh number, $\tilde{\mathcal{R}}_p$, representing the relative strength of buoyancy forcing versus dissipative mechanisms. Both $\tilde{\mathcal{B}}_i$ and $\tilde{\mathcal{R}}_p$ increase with time as the thermal boundary layer (and hence available potential energy) grows.

I have identified two distinct regimes of behaviour. For large Biot numbers, efficient cooling produces a boundary condition behaving similarly to a perfect conductor. For small Biot numbers, the boundary condition behaves like a poor conductor. In the large Biot number regime, $\tilde{\mathcal{B}}_i \gg 1$, we observe $O(1/\tilde{\mathcal{B}}_i)$ deviations from the perfectly conducting limit ($\tilde{\mathcal{B}}_i \to \infty$) which has been previously studied in some detail (e.g. Slim and Ramakrishnan, 2010; Tilton et al., 2013). The net deviation causes a weak increase in stability, and is consistent with a competition between reduction of available potential energy by vertical confinement of the background profile, and the tendency of the modified perturbation boundary condition to reduce stability by allowing greater variation in surface temperature (see Barletta et al., 2015). For smaller Biot numbers, the reduction in available potential energy strongly dominates and leads to a substantial increase in the critical Rayleigh number, which scales as $\tilde{\mathcal{R}}_{pc} \sim 1.9/\tilde{\mathcal{B}}_i$ for $\tilde{\mathcal{B}}_i \ll 1$. Hence the convective stability of a growing boundary layer is enhanced if the supply of potential energy is decreased by imperfect heat transfer to the neighbouring medium. This leads to a delay in the instability compared to settings with perfectly conducting boundaries that have a temperature difference of $T_\infty - T_c$ within the porous layer. In the limit of poor boundary conductivity, one might interpret the scaling with Biot-number in terms of a modified criterion with instability occurring when a local Rayleigh number, based on the temperature difference across the porous medium rather than the externally-imposed temperature difference, exceeds a constant value. This local Rayleigh number would depend on the surface temperature of the porous layer, which is an intrinsic part of the problem that evolves in time. To determine the prefactor accurately, one also needs to account for changes in the perturbation boundary condition and vertical structure of the forcing.

The most unstable wavenumber also varies depending on the rate of boundary cooling, with the viewpoint depending on the particular non-dimensionalisation considered. When scaled relative to the time-dependent diffusion length $\sqrt{\kappa \hat{t}}$ the most unstable dimensionless wavenumber shows non-monotonic variation with the Biot number. As $\tilde{\mathcal{B}}_i$ is reduced from the perfectly conducting limit of $\tilde{\mathcal{B}}_i \to \infty$, the dimensionless wavenumber first increases, consistent with enhanced vertical confinement of the background profile generating shallower convection cells with shorter wavelengths as a fraction of the diffusion length $\sqrt{\kappa \hat{t}}$. The dimensionless wavenumber eventually begins to decrease as $\tilde{\mathcal{B}}_i$ is decreased further and approaches an asymptotic behaviour of $\tilde{\mathrm{k}}_c \sim 0.73\sqrt{\tilde{\mathcal{B}}_i}$ for $\tilde{\mathcal{B}}_i \ll 1$. This leads to larger, deeply penetrating convective cells with longer wavelengths when the surface cooling is inefficient and acts like a poor conductor. However, when calculating dimensional wavenumbers, the above relative effects must be combined with the impact of cooling rate on the onset of convective instability. Slower cooling results in delayed instability and growth of a thicker diffusive boundary layer. The net effect of delayed instability and the changes relative to the boundary-layer depth is a monotonic decrease in the dimensional wavenumber as the cooling rate is reduced.

The physical instability times found, and corresponding wavenumbers, agree with the results of previous studies when the heat transfer coefficient is infinite, $\mathfrak{h} \to \infty$, and otherwise depend on a boundary Rayleigh number, $\mathcal{R}_B$ defined in (4.4.4) which represents the ratio of buoyancy effects to viscous dissipation and thermal dissipation through exchange with the overlying heat sink. The boundary Rayleigh number $\mathcal{R}_B$ can be interpreted as the ratio of two lengthscales. The boundary cooling length scale $\hat{d}_b = k/\mathfrak{h}$ describes a characteristic scale for heat transfer within the domain with conductivity k driven by surface cooling with heat transfer coefficient $\mathfrak{h}$. The buoyancy length scale $\hat{d}_b = \kappa\nu/g\alpha\Delta T\hat{\Pi}_0\omega$ describes a natural scale for convective motion before a buoyant perturbation is dissipated within the porous medium. When the boundary acts as a relatively good conductor, the leading-order scaling of the instability time $\hat{t}_i \propto \hat{t}_p$ is controlled by the porous medium buoyancy timescale. Deviations of $\hat{t}_i$ from this conducting limit are characterised by a Taylor expansion (4.4.5) in terms of $\mathcal{R}_B$, which is a small parameter in this limit. When the overlying heat sink acts as a relatively poor conductor, we see different behaviour with $\hat{t}_i \propto \mathcal{R}_B\ \hat{t}_p = \hat{d}_b\hat{d}_p/\kappa$ depending on both the boundary-cooling and buoyancy scales. The wavelength at the moment of instability also shows similar behaviour, scaling with the buoyancy length scale for highly conducting boundaries, but for near-insulating boundaries the most unstable wavelength scales with the

combination $\mathcal{R}_B{}^{3/4}\hat{d}_p = \hat{d}_b^{3/4}\hat{d}_p^{1/4}$ of boundary-cooling and buoyancy length scales. Thus we expect much longer wavelength convective features to be favoured at the moment of instability when boundary heat transfer is relatively poor. These results for boundary-layer convection in a porous medium echo results for Rayleigh-Bénard convection in a pure fluid of fixed depth with poorly conducting boundaries (Hurle et al., 1967).

In this chapter, I have discussed how the boundary conductivity can affect the onset of stability in a uniform porous medium cooled from above and showed there are three ways this can contribute to the stability. Firstly, the decreasing surface temperature means that the total energy available increases over time (increasing $\tilde{\mathcal{B}}_i$), creating tendency towards instability as time progresses. Next, the increasing boundary resistance as $\tilde{\mathcal{B}}_i$, and hence time, increases creates an opposing tendency towards stability, as noted by Barletta et al. (2015) and others. Finally, the evolving structure of the temperature profile also impacts the stability and, in this setup, contributes a tendency to instability as $\tilde{\mathcal{B}}_i$ and time increase. This information will be very useful in the next chapter where we consider convection in a mushy layer, and consider the effects of imperfect thermal conduction by the surface boundary as part of our investigation. The results also have a number of physical implications for geophysical settings, with key applications including carbon sequestration (Hassanzadeh et al., 2006; Slim and Ramakrishnan, 2010) and ground water convection (van Dam et al., 2009).

5
Mushy Layer Convection

This chapter investigates the convective onset in transient sea ice growth, by characterising the stability properties of a mushy layer growing from a fixed boundary over a range of parameters. For convection to be possible, the total density change from the combination of cooling and salt rejection must be positive for cooling from above, or negative for cooling from below. Because the thermal and saline fields are coupled through the liquidus relationship, the contribution from one of the fields may be convectively stable on its own, provided the destabilising contribution from the other field is suitably strong. Convection can occur in salt- or sea water cooled from the upper surface, when the effects of both the cooling and the salt rejection associated with solidification act to increase the density and destabilise the fluid. As another example, when $H_2O - NH_4Cl$ is solidified from below, the thermal field is stabilising, but the removal of dense NH_4Cl molecules leads to a destabilising saline field which is strong enough to overcome the thermal stabilisation. Recall that double diffusive effects are not possible in the mushy layer because temperature and salinity are coupled.

Building on the broad investigation of mushy layer growth and structure in chapter 3, this chapter will perform a linear stability analysis on temperature and liquid fraction profiles found in chapter 3, and draw on some of the discussion therein when describing the results found. The analysis in this chapter has a number of crucial differences to that of chapter 4, most notably the presence of the saline field and a variable background porosity, but those discussions will also contribute to the consideration of imperfect boundary conduction in §5.5. The main dynamical

parameters will be considered over a broad range of values to provide a systematic understanding of the results and their dependence on the physical conditions, with specific examples discussed to give a physical grounding.

Convection in mushy layers has been the subject of many studies, as reviewed in §1.4.5 and §1.4.6. The majority of these studies focus on convection in the directional solidification setting where material is pulled through two heat exchangers at a constant rate, with Worster (1992b) being a particularly important study in this area. This chapter will consider convection in the transient growth setting, rather than this constant growth setting. The different growth behaviour between these two settings means that stability results are not directly transferrable, although we anticipate similar general themes. There are also some noticeable differences with the previous studies of convection in a transient growth setting, through the use of variable permeability (previously only considered by Hwang, 2013), different stability methods, and the consideration of imperfect boundary conduction.

The next section describes the linear analysis method used. After that, §5.2 describes the effects on the convective onset of varying the dimensionless liquidus gradient. This was shown in chapter 3 to have a significant impact on the porosity, temperature, and salinity profiles of the mushy layer before convection begins. A comparison is also made with the experimental results of Wettlaufer et al. (1997) in §5.2.1. The previous results reveal that convective confinement occurs and this is discussed in §5.3. The effect of the Stefan number on convective instability, through its effects on the background temperature and liquid fraction profiles, is considered in §5.4. Section §5.5 explores the effects of imperfect boundary conduction, as measured by the Biot number, including a discussion of convective onset for initial sea ice growth in the environmental conditions observed by Notz and Worster (2008) (§5.5.1). Finally, there is a summary of the results in §5.6.

5.1 Linearised Perturbation Equations

The reactive nature of the mushy layer equations and the solidification feedbacks means that an energy stability analysis, as described in §4.2.1 for an unreactive porous medium, is not straightforward. Instead, I will be using the frozen time method, alternatively called the quasi-static stability analysis (QSSA), to find the linear stability criteria of a mushy layer, This assumes that perturbations are small enough that any terms non-linear in the perturbations are zero and that the base

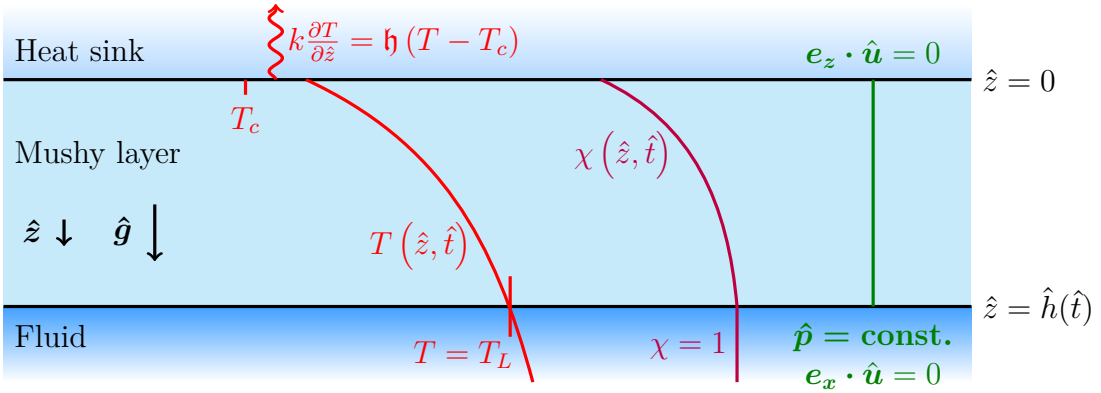

Figure 5.1: A diagram of the setup for the linear stability calculations showing the base state temperature, liquid fraction and velocity profiles in the mushy layer, along with their associated boundary conditions. The liquid salinity is not shown but is coupled to the temperature through the liquidus relationship (2.3.6a). Similarly, the surface liquid fraction can be calculated from the surface temperature using the Lever rule (2.3.6b). The liquid phase is not included in the linear stability calculations explicitly, but is parameterised in line with Emms and Fowler (1994) as described in the main text

state evolves at a much slower rate than the perturbation timescale, such that it can be considered static, or 'frozen'. A diagram of the setup for these calculations is shown in figure 5.1.

From chapter 2, the dynamical equations describing conservation of heat, salt, momentum, and mass for the mushy layer are given by:

$$\frac{\partial\theta}{\partial t} + \boldsymbol{u}\cdot\boldsymbol{\nabla}\theta + \mathcal{S}_t\frac{\partial\chi}{\partial t} = \nabla^2\theta, \qquad \text{(2.3.4a revisited)}$$

$$\chi\frac{\partial\theta}{\partial t} + \boldsymbol{u}\cdot\boldsymbol{\nabla}\theta - (\Lambda + \theta_{L\infty} - \theta)\frac{\partial\chi}{\partial t} = \frac{1}{\mathcal{L}_e}\boldsymbol{\nabla}\cdot[\chi\boldsymbol{\nabla}\theta], \qquad \text{(2.4.1 revisited)}$$

$$\boldsymbol{u} = -\mathcal{R}_p\chi^3\left[\hat{\boldsymbol{\nabla}}p + \left(1 + \frac{\beta^*}{\Lambda}\right)\theta\boldsymbol{e_z}\right], \qquad \text{(2.3.12 revisited)}$$

$$\boldsymbol{\nabla}\cdot\boldsymbol{u} = 0, \qquad \text{(2.1.2 revisited)}$$

where (2.3.6a) has been used to describe the saline field in terms of the thermal field. The χ^3 term in (2.3.12) was not present in the previous chapter and comes from the permeability of the ice, (2.1.15). The surface conditions are given by the linearised energy balance and a no normal fluid flux condition:

$$\frac{\partial\theta}{\partial z} = \mathcal{B}_i\theta, \qquad \boldsymbol{e_z}\cdot\boldsymbol{u} = 0, \qquad \text{when } z = 0. \qquad \text{(2.3.2l\&n revisited)}$$

Following the example of Emms and Fowler (1994), I will treat the mush-liquid interface as an isothermal, constant pressure boundary:

$$\theta = \theta_{L\infty}, \qquad \boldsymbol{e_x} \cdot \boldsymbol{u} = 0, \qquad \text{when } z = h. \tag{5.1.1a,b}$$

This is based on the knowledge that the temperature must be equal to the liquidus temperature at the boundary, and the use of scaling arguments to characterise weak convection in the liquid phase as a constant pressure condition. The horizontal flow condition (5.1.1b) follows from the constant pressure condition by considering the horizontal component of Darcy's law (2.3.12). I am also assuming that both boundaries remain flat and that there is no salt diffusion.

Assuming a 2D convection pattern, incompressibility (2.1.2) is used to introduce the stream function $\boldsymbol{u} = \boldsymbol{\nabla} \times \psi \boldsymbol{e_y}$, and this results in a system with three fields: θ, ψ, and χ. These are then expanded as base states and perturbations:

$$\begin{aligned}
\theta(x,z,t) &= \theta_B(z,t) + \epsilon\theta_p(x,z,t),\\
\chi(x,z,t) &= \chi_B(z,t) + \epsilon\chi_p(x,z,t),\\
\psi(x,z,t) &= \epsilon\psi_p(x,z,t),
\end{aligned}$$

where ϵ is the small perturbation amplitude and the base-state stream function is uniformly zero. The base-state equations of $O(1)$ yielded by this substitution recover those solved in chapter 3, while the linear perturbation equations found by gathering terms of $O(\epsilon)$ are:

$$\frac{\partial\theta_p}{\partial t} + \frac{\partial\theta_B}{\partial z}\frac{\partial\psi_p}{\partial x} + \mathcal{S}_t\frac{\partial\chi_p}{\partial t} = \nabla^2\theta_p, \tag{5.1.2a}$$

$$-\mathcal{R}_p\left(1 + \frac{\beta^*}{\Lambda}\right)\frac{\partial\theta_p}{\partial x} = \boldsymbol{\nabla}\cdot\left[\frac{1}{{\chi_B}^3}\boldsymbol{\nabla}\psi_p\right], \tag{5.1.2b}$$

$$(\Lambda + \theta_{L\infty} - \theta_B)\frac{\partial\chi_p}{\partial t} - \theta_p\frac{\partial\chi_B}{\partial t} - \chi_p\frac{\partial\theta_B}{\partial t} - \chi_B\frac{\partial\theta_p}{\partial t} = \frac{\partial\theta_B}{\partial z}\frac{\partial\psi_p}{\partial x}, \tag{5.1.2c}$$

where (5.1.2b) arises from taking the curl of Darcy's law (2.3.12) and we have neglected salt diffusion, $\mathcal{L}_e \to \infty$. As in §4.2.1, we now perform a Fourier decomposition with wavenumber, k, and assume an exponential growth rate of σ:

$$\begin{bmatrix} \theta_p(x,z,t) \\ \psi_p(x,z,t) \\ \chi_p(x,z,t) \end{bmatrix} = \begin{bmatrix} \theta_f(\mathrm{k},z) \\ i\mathrm{k}\ \psi_f(\mathrm{k},z) \\ \chi_f(\mathrm{k},z) \end{bmatrix} e^{i\mathrm{k}x}e^{\sigma t}. \tag{5.1.3}$$

Using this, (5.1.2) yields a matrix eigenvalue problem for either σ or $\mathcal{R}_p$, when the other is provided:

$$\mathsf{A}\boldsymbol{y} - \mathcal{R}_p\,\mathsf{B}\boldsymbol{y} = \sigma\mathsf{C}\boldsymbol{y}, \tag{5.1.4a}$$

$$\boldsymbol{y} = \begin{bmatrix} \theta_f \\ \psi_f \\ \chi_f \end{bmatrix}, \qquad \mathsf{A} = \begin{bmatrix} \partial^2/\partial z^2 - \mathrm{k}^2 & \mathrm{k}^2\,\partial\theta_B/\partial z & 0 \\ 0 & \frac{\partial}{\partial z}\left(\frac{1}{{\chi_B}^3}\frac{\partial}{\partial z}\right) - \mathrm{k}^2/{\chi_B}^3 & 0 \\ -\frac{\partial\chi_B}{\partial t} & \mathrm{k}^2\frac{\partial\theta_B}{\partial z} & -\frac{\partial\theta_B}{\partial t} \end{bmatrix}, \tag{5.1.4b,c}$$

$$\mathsf{B} = \begin{bmatrix} 0 & 0 & 0 \\ -(1+\beta^*/\Lambda) & 0 & 0 \\ 0 & 0 & 0 \end{bmatrix}, \qquad \mathsf{C} = \begin{bmatrix} 1 & 0 & \mathcal{S}_t \\ 0 & 0 & 0 \\ \chi_B & 0 & -(\Lambda + \theta_{L\infty} - \theta_B) \end{bmatrix}. \tag{5.1.4d,e}$$

Anderson and Worster (1996) observed an oscillatory mode instability (with $\mathbf{Im}\{\sigma\} \neq 0$) in the directional solidification setting when both $\mathcal{S}_t$ and $\mathcal{C}$ are large. However, this mode was not always present and when it was, it represented only a small adjustment to the direct stability threshold. It is also computationally more efficient to solve for the neutral stability curve, $\mathcal{R}_c(\mathrm{k})$, rather than for the growth rate, $\sigma(\mathcal{R}_p, \mathrm{k})$, and then extracting the neutral stability curve. With those facts in mind, I will solve (5.1.4) directly with $\sigma = 0$ and neglecting any potential oscillatory modes, noting that if one were to exist, it might affect the precise values of $\mathcal{R}_c$ and k_c, but would be unlikely to affect their scalings.

An important feature of (5.1.4) is that the first two rows become independent of χ_f when $\sigma = 0$, which means that for investigations of the neutral stability curve, we only need to consider θ_f and ψ_f when finding $\mathcal{R}_c$, further enhancing computational efficiency. The implication of this is that solidification does not play an active role in the direct linear stability of the mushy layer and the liquid fraction only responds passively to the thermal and advective perturbations.

We can also absorb the buoyancy factor in B into the Rayleigh number by following Worster (1991) and using the mushy Rayleigh number, $\mathcal{R}_m$, and the corresponding mushy convective length, $\hat{d}_m$:

$$\mathcal{R}_m = \left(1 + \frac{\beta^*}{\Lambda}\right)\mathcal{R}_p = \frac{g\,(\alpha + \beta/\Gamma)\,\Delta T\hat{\Pi}_0\hat{d}}{\kappa\nu}, \qquad \hat{d}_m = \frac{\kappa\nu}{g\,(\alpha + \beta/\Gamma)\,\Delta T\hat{\Pi}_0}. \tag{2.3.13a,b revisited}$$

As discussed in §2.3, this new Rayleigh number now measures the buoyancy contributions from both the thermal and saline fields over the range of temperatures

in the system, and the convective length $\hat{d}_m$ is a measure of the distance a buoyancy anomaly will propagate through a mushy layer before it dissipates.

The transformed boundary conditions become:

$$\frac{\partial \theta_f}{\partial z} = \mathcal{B}_i \theta_f, \qquad \psi_f = 0, \qquad \text{at } z = 0, \tag{5.1.5a,b}$$

$$\theta_f = 0, \qquad \frac{\partial \psi_f}{\partial z} = 0, \qquad \text{at } z = h. \tag{5.1.5c,d}$$

Time only appears in the reduced forms of (5.1.4) and (5.1.5) through the base-state temperature and liquid fraction, θ_B and χ_B, but we showed in chapter 3 that these profiles can be calculated in self-similar coordinates using the variables $\tilde{z}$ and $\tilde{\mathcal{B}}_i$. We therefore repeat the self-similarity transformation used in §4.2.1:

$$\tilde{z} = \frac{z}{\sqrt{t}}, \qquad \tilde{\mathrm{k}} = \mathrm{k}\sqrt{t}, \qquad \tilde{\mathcal{R}}_m = \mathcal{R}_m \sqrt{t}, \qquad \tilde{\mathcal{B}}_i = \mathcal{B}_i \sqrt{t}, \qquad \text{(4.2.7 revisited)}$$

which we noted is equivalent to changing the length scale of the problem from the fixed length $\hat{d}$ to the time-evolving thermal diffusion length scale $\sqrt{\kappa \hat{t}}$. This transformation leaves the structure of (5.1.4) and (5.1.5) unchanged.

Finally, we note that varying parameters such as the liquidus gradient will change the depth of the mushy layer. This changing vertical extent will have a well understood impact on the convective instability, with the critical Rayleigh number increasing in inverse proportion to the layer depth. To allow us to see past this effect, it is useful to define the *scaled Rayleigh number* and the corresponding wavenumber:

$$\tilde{\mathcal{R}}^*_m = \lambda \tilde{\mathcal{R}}_m = \frac{g\,(\alpha + \beta/\Gamma)\,\Delta T \hat{\Pi}_0 \hat{h}(\hat{t})}{\kappa \nu} = \frac{\hat{h}(\hat{t})}{\hat{d}_m}, \qquad \tilde{\mathrm{k}}^* = \tilde{\mathrm{k}}\ \lambda = \hat{\mathrm{k}}\ \hat{h}(\hat{t}), \tag{5.1.6a,b}$$

where λ is the self-similar interface position/growth rate defined in chapter 3. Since the self-similarity transformation and rescaling only affect the depth used in the Rayleigh number, the convective length is unaffected and given by (2.3.13b).

A reduced eigenvalue system is found by setting $\sigma = 0$ in (5.1.4) and (5.1.5). Following §4.3, the discretised boundary condition operators are used to express the boundary values as linear combinations of the profile values at internal grid points. These conditions are then used to eliminate the boundary values from the eigenvalue problem, leaving a problem for the internal values only. The solutions to this problem satisfy both the dynamical and boundary equations and they are found

numerically using the using the `eig` routine in MATLAB. This yields the Rayleigh number needed for convection a given wavenumber, and for each calculation a suitable range of wavenumbers is considered to find the global minimum, known as the critical Rayleigh number.

5.2 Impact of the Liquidus Gradient on Stability

The first part of our investigation will focus on the effect that the liquidus gradient, Λ, has on the convective instability. Following the introduction of the mushy Rayleigh number (2.3.13), the liquidus gradient does not appear in either (5.1.4) or (5.1.5) explicity, but it will affect both θ_B and χ_B. We aim to see how the changes to the internal structure controlled by Λ impact the stability of the mushy layer. Varying Λ will also affect the growth rate, but we will use the scaled Rayleigh number, $\tilde{\mathcal{R}}_m^*$, which already accounts for the impact of the growth rate. In §3.2.2a we saw that the mushy layer is highly porous throughout for large values of Λ, with $\chi \to 1$ as $\Lambda \to \infty$. In contrast, for small values of Λ, we found that most of the mush has a very low liquid fraction with a small interfacial region containing most of the porosity variation. The initial liquidus temperature used in this section will be $\theta_{L\infty} = 0.8$ unless stated otherwise, which corresponds roughly to water at 0^oC being cooled to -20^oC, and in this section we will assume perfect boundary conductivity, $\tilde{\mathcal{B}}_i \to \infty$.

Figure 5.2 shows the variation of the critical scaled Rayleigh number and wavenumber as the liquidus gradient and Stefan number are varied, although detailed discussion of the Stefan number behaviour will be deferred until §5.4. There is a sharp increase in both critical Rayleigh number and wavenumber as the liquidus gradient is decreased, with the Rayleigh number increasing over several orders of magnitude and the wavenumber increasing over one order of magnitude. These increases are well described by the trends:

$$\tilde{\mathcal{R}}_m^* \approx 49 + \frac{15}{\Lambda^2}, \qquad \mathrm{k}_c^* \approx 2.4 + \frac{0.27}{\Lambda}, \tag{5.2.1a,b}$$

which are illustrated in figure 5.3. These trends are approximations which are independent of Stefan number. However, they provide a good match to the data and the maximum error of the Rayleigh number trend is 59.0% with a root-mean-square error of 26.8%, while the maximum error of the wavenumber trend is 23.3% with a root-mean-square error of 4.1%. We later present explanations for these scalings which are independent of the value chosen for $\theta_{L\infty}$. While the shape of these trends

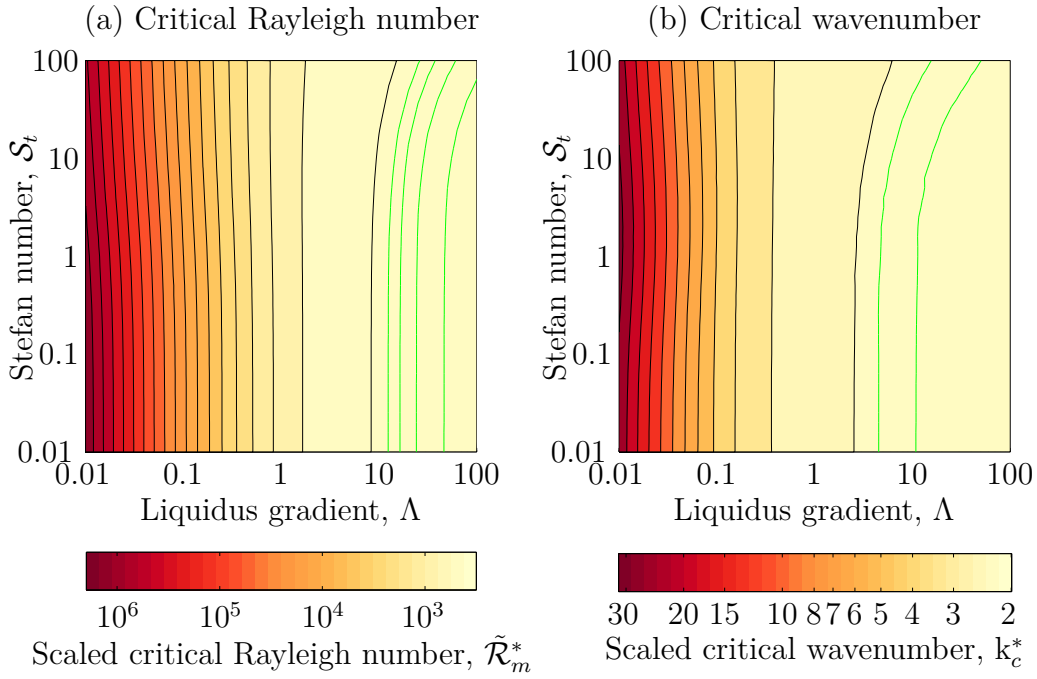

Figure 5.2: *(a)* Critical Rayleigh numbers for the mushy layer, $\tilde{\mathcal{R}}_m^*$, against liquidus gradient, Λ, and Stefan number, $\mathcal{S}_t$, calculated when $\theta_{L\infty} = 0.8$. The black contours are spaced at intervals of $10^{0.2}$ and the green contours are at 45, 46, 47, and 48. The critical Rayleigh number increases sharply as the liquidus gradient is decreased, which is discussed in the main text. *(b)* The corresponding critical wavenumbers for the mushy layer, k_c^*, over the same range of liquidus gradient and Stefan number. The black contours are now at intervals of $10^{0.1}$ and the green contours are 2.4 and 2.45. The wavenumbers also increases as the liquidus gradient decreases.

---

will remain unchanged as $\theta_{L\infty}$ varies, the numerical values needed, and the overall accuracy, may be different.

This result echos that of Hwang (2013), which were obtained using the propagation method that assumes self-similar perturbations. Hwang (2013) observed a large increase in Rayleigh number and a moderate increase in wavenumber as the concentration ratio, $\mathcal{C}$, decreases below 1, with both tending to a constant value for large values of $\mathcal{C}$. Hwang (2013) hypothesises that this behaviour is due to the presence of a low porosity region for small $\mathcal{C}$ which confines the convection although does not investigate this further. To investigate this phenomenon, figure 5.4 shows the convection, liquid fraction, and permeability profiles for three different values of liquidus gradient.

The largest liquidus gradient shown is $\Lambda = 3.02$, which with $\theta_{L\infty} = 0.8$ corresponds to $\mathcal{C} = \Lambda/\theta_{L\infty} = 3.77$. Here, the system is in the high-liquid fraction regime, with

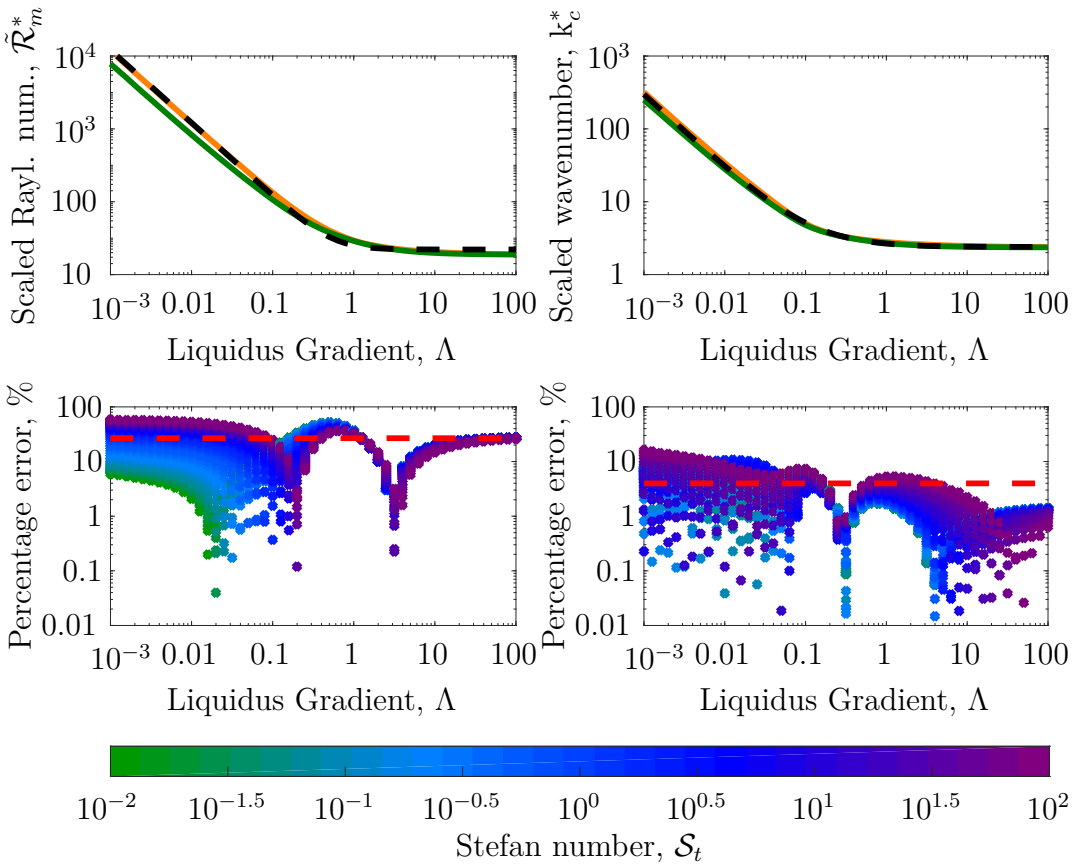

Figure 5.3: *(Left, top)* The critical Rayleigh numbers, $\tilde{\mathcal{R}}_m^*$, against liquidus gradient, Λ, for Stefan numbers in the range $10^{-2} \leq \mathcal{S}_t \leq 10^3$ and $\theta_{L\infty} = 0.8$, calculated in coordinates scaled such that the depth of of the mushy layer is 1. The upper and lower bounds of the data are shown in orange and green respectively, while the dashed black curve shows the empirical fit given by equation (5.2.1a). *(Left, bottom)* The fractional errors of the calculated results compared to the empirical fit with the colour scale indicating the Stefan number and the RMS error of 26.8% is highlighted in red. *(Right)* The same graphs, but for the critical wavenumber. The fit is now given by (5.2.1b) and the RMS error is 4.1%.

$\chi > 0.79$ throughout, and the permeability is similarly high ($\Pi > 0.49$). In this regime, the convection penetrates the full depth of the mushy layer and the cells are relatively wide compared to the thickness of the layer.

The middle row shows $\Lambda = 0.25$, which gives $\mathcal{C} = \Lambda/\theta_{L\infty} = 0.38$ and is in the transitional regime with some appreciable solid formation close to the upper boundary ($\chi_B(0) = 0.27$). This is reflected in the convection pattern with the convection confined further away from the upper boundary than in figure 5.4a, and focussed more in the lower part of the domain. The convective cells also narrow slightly relative to the layer thickness.

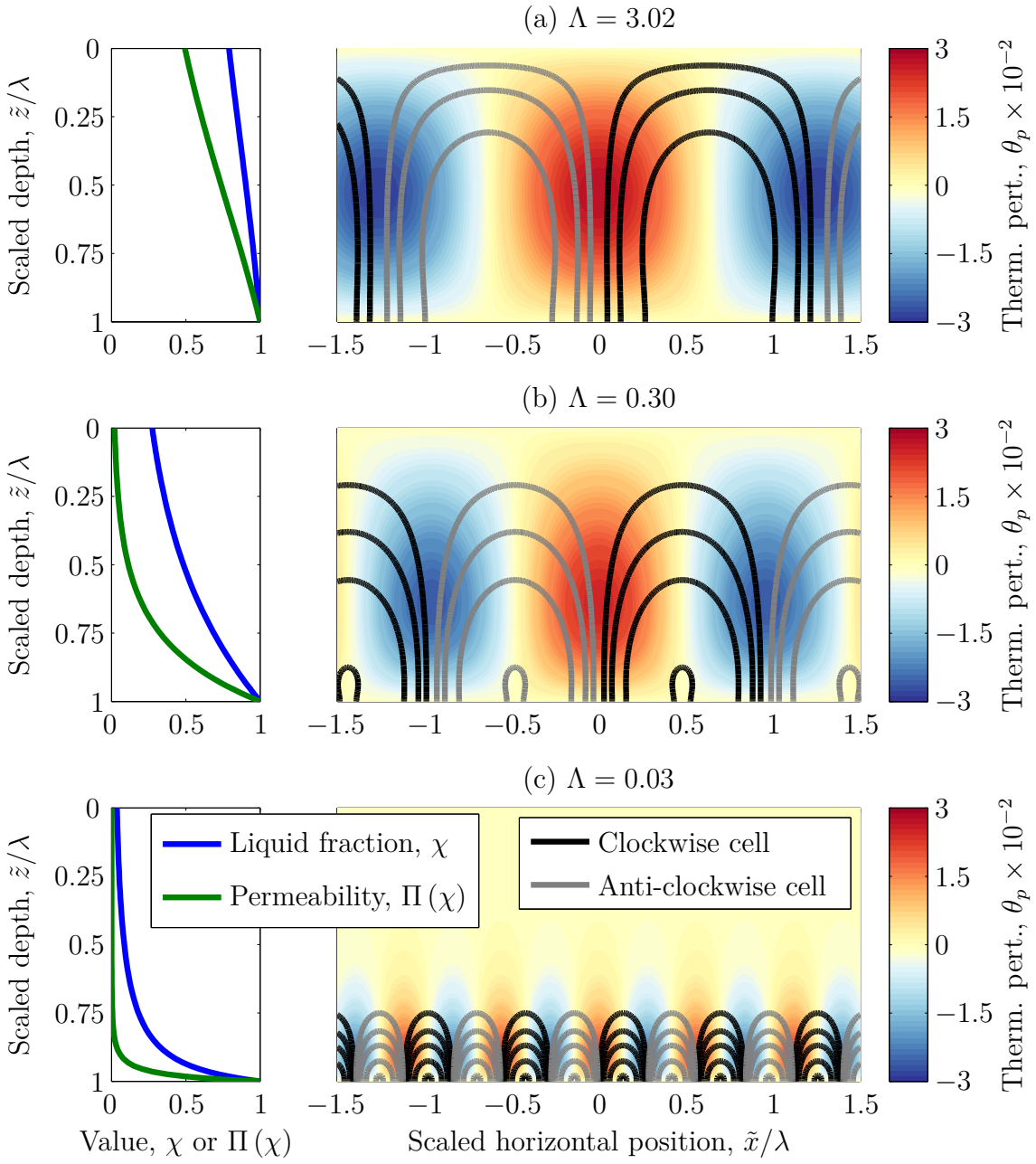

Figure 5.4: *(Left)* Liquid fraction and permeability profiles - blue and green respectively - for $\theta_{L\infty} = 0.8$, $\mathcal{S}_t = 0$, and three different values of Λ, 3.02, 0.30, and 0.03. *(Right)* Convection graphs showing the QSSA instability profiles for the three cases. The thermal perturbations are shown by the colour scale. Stream function contours are shown at 0.02, 0.05, 0.1, 0.2 and 0.3, with black contours representing clockwise circulation and grey contours representing anti-clockwise circulation.

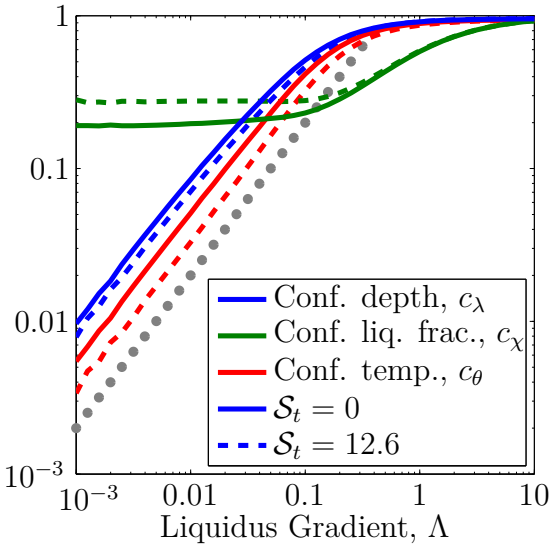

Figure 5.5: The confinement depth (blue), confinement liquid fraction (green), and confinement temperature (red) are plotted against the liquidus gradient, Λ, for two values of the Stefan number, $\mathcal{S}_t = 0$ (solid) and $\mathcal{S}_t = 12.6$ (dashed). Also shown in dotted grey is the one-to-one trend line. The method of calculation for these properties is described in the main text.

Finally, the last set of figures shows $\Lambda = 0.025$, with $\mathcal{C} = \Lambda/\theta_{L\infty} = 0.04$, which is well into the earlier-defined Stefan regime. Here, the top of the mushy layer has a large solid fraction and a low permeability, while the high porosity mush is focused in a thin interfacial region. The convective cells are heavily confined to this interfacial region, and there is very little fluid motion in most of the domain, although thermal variations do spread slightly further than the velocity.

As a measure of this convective confinement, we calculate the scaled depth at which the stream function drops below 10% of its maximum value and refer to this as the *confinement depth*, c_λ. We also calculate the liquid fraction at the confinement depth (*confinement liquid fraction*, c_χ) and fraction of the temperature range which is between the confinement depth and mush-liquid interface (*confinement temperature*, c_θ). These three diagnostic properties are shown in figure 5.5 for a range of liquidus gradients and two Stefan numbers.

For large values of the liquidus gradient, the confinement depth tends to a value close to one, which represents convection through the full depth (by definition, c_λ will not reach one since $\psi = 0$ at the surface). For smaller values with $\Lambda \ll 1$, the confinement varies linearly with the liquidus gradient, indicating that in the Stefan regime convection is being confined to a region of the mushy layer with a relative

depth proportional to Λ.

The confinement liquid fraction tends to a constant value as Λ decreases, with a limit of $\chi \approx 0.2$ for $\mathcal{S}_t = 0$ and $\chi \approx 0.3$ for $\mathcal{S}_t = 12.6$. Fluid motion is therefore being capped at the same liquid fraction for a large range of Λ and cannot substantially penetrate into the low liquid fraction region which exists above this contour. We saw in figure 3.8b and (3.2.4) that the relative depth of the high porosity interfacial region, f_χ as introduced in §3.2.2a, is proportional to Λ. There are therefore clear parallels between the size of the high porosity region and the proportion of the mushy layer which convects, with figure 5.4 also showing us that these two features are co-located.

The combination of a preference for convection to occur with a roughly square aspect ratio and the convective confinement to a region with a relative thickness proportional to Λ means that we expect a wavelength proportional to Λ, when scaled relative to the mushy layer thickness. Wavenumbers are inversely proportional to their corresponding wavelengths and $\tilde{\mathrm{k}}^*$ is measured relative to the mushy layer thickness, so we recover a scaling of $\tilde{\mathrm{k}}^* \propto 1/\Lambda$ for small liquidus gradients, as seen in (5.2.1b). The vertical confinement also contributes a factor of $1/\Lambda$ to the low liquidus gradient scaling of the Rayleigh number in (5.2.1a), but we also need to account for the confinement temperature. To a first approximation, the temperature profile in the mushy layer is roughly linear so the temperature difference across part of the layer will be proportional to the thickness of the slice. Fluid motion is confined to a layer with a thickness proportional to Λ which means that the temperature difference driving the convection (the confinement temperature) will also be proportional to Λ, as seen in figure 5.5. Since the amount of forcing has decreased by factor of Λ, the system is more stable and the critical Rayleigh number will increase in inverse proportion to the decrease in energy, leading to the second factor of $1/\Lambda$ in (5.2.1a).

The results from this section can also be used to predict convective onset in terms of the convective length scale, $\hat{d}_m$, of the mushy layer. Combining (5.1.6) and (5.2.1), we find that:

$$\hat{h}_c \approx \hat{d}_m \left(49 + \frac{15}{\Lambda^2}\right), \qquad \hat{\mathrm{k}}_c \approx \frac{2.4 + 0.27/\Lambda}{\hat{d}_m \left(49 + 15/\Lambda^2\right)}, \tag{5.2.2a,b}$$

where $\hat{h}_c$ is the critical mushy layer thickness, and convection will start when the mushy layer has grown to this depth. This initial convection will occur at a

wavenumber approximated by $\hat{\mathrm{k}}_c$. The trends described in (5.2.1) are approximately independent of Stefan number but we note that the 27% error on the Rayleigh number trend and 4.1% error on the wavenumber trend will propagate through these estimates.

5.2.1 Comparison with Wettlaufer et al. (1997)

In §3.1.2c and §3.2.2d, we compared our models of mushy layer growth with the results of Wettlaufer et al. (1997) and found reasonable agreement between the two sets of results when we considered the full solidification dynamics (§3.2.2d). Wettlaufer et al. (1997) also present an estimate of convective onset in their experiments, which can be used to test the predictions of this section.

Wettlaufer et al. (1997) describe in most detail an experiment with 70psu salt water cooled from -2^oC to -20^oC, for which they observe convective onset "after about 200 minutes, when the mushy layer was about 5cm deep", with convective onset being measured by a change in salinity at the bottom of the tank. These parameters give non-dimensional values of $\Lambda = 0.33$, $\theta_{L\infty} = 0.78$, and $\mathcal{S}_t = 4.6$ and the stability calculations yield $\tilde{\mathcal{R}}_m^* = 240$ and $\tilde{\mathrm{k}}^* = 3.2$. To convert these to a physical critical depth and a critical wavelength, we use (2.3.13b) and a permeability reference of $\hat{\Pi}_0 = 2 \times 10^{-8}\mathrm{m}^{-2}$ (Freitag, 1999) to calculate the mushy convective length, $\hat{d}_m = 7.1 \times 10^{-3}$mm. From (5.1.6), the critical depth is then $\hat{h}_c = 1.7$mm, the critical wavelength is $2\pi/\hat{\mathrm{k}}_c = 3.3$mm, and convective onset is predicted to occur 27s after cooling begins.

This is obviously substantially different from the observations, but a number of factors could be at play. Firstly, the exactly location of their salinity measurements is unclear (although the authors do state they believe the salinity to be vertically uniform throughout their observation) so it is possible convection has started prior to the time quoted by Wettlaufer et al. (1997), but has not yet propagated down to an observable depth. Simiarly, the nature of the measurements is very different - our calculations give the moment a mushy layer could become linearly unstable while the observations require finite amplitude convection to have a noticable impact on the liquid layer. There may well be a lag between a linear instability being triggered and the instability growing to the point where it can be observed experimentally. It is also possible that some of the numbers used in the calculation of the convective depth are not appropriate for comparison to the experimental setting. The data

contributing to Λ, $\theta_{L\infty}$, and $\mathcal{S}_t$ are well defined by the experimental conditions but some of the properties contributing to $\hat{d}_m$ are less clearly defined.

Properties such as the thermal and saline expansivities, α and β, are known to have a temperature dependence, as does the thermal diffusivity, κ, and viscosity, ν, although such variations are modest. A more likely source of error is the permeability, with a value of $\hat{\Pi}_0 = 2 \times 10^{-8}\text{m}^2$ used in the calculations above. This value is widely accepted and originally comes from experiments by Freitag (1999), but measuring the permeability of sea ice is difficult since the material is reactive so the act of measurement will change the microstructure. Recently, Rees Jones and Worster (2014) attempted to model the permeability in the experiments of Wettlaufer et al. (1997), and suggested that a reference permeability of $\hat{\Pi}_0 = 2.24 \times 10^{-9}\text{m}^2$ provided a better match to the data. Using this alternative value gives a new mushy convective lengthscale of 6.3×10^{-2}mm, which then yields a critical depth of 1.5cm, an onset time of 30min, and an onset wavelength of 3.2cm. The critical depth and onset times are notably closer to the observed values, but the wavelength is now larger than their observed channel separation of $\sim$ 1cm. This revised estimate of permeability predicts a convective onset depth and wavelength which are on the same order of magnitude to the observed desalination and brine channel formation, but with some quantative difference in the values. One possible reason for this quantitative discrepancy may be the non-linear evolution of the system after the initial instability, with the formation of brine channels being an intrinsically non-linear process.

5.3 Understanding Convective Confinement

To investigate convective confinement further, we turn to the correlation between the half-solidification depth, f_χ, and the confinement depth, c_λ. The former of these metrics tells us the fraction of the mushy layer depth that has a high porosity, while the latter gives the fraction of the depth where convection is occuring. We anticipate these two metrics to be correlated for small Λ, and this is indeed shown by figure 5.6a.

The strength of the relationship depends on the values of Λ and $\theta_{L\infty}$, and the data is separated into four groups to help illustrate this and other effects, as described in table 5.1. Groups 1 and 3, which have small liquidus gradients, show a very strong linear correlation between the two metrics, running roughly parallel to the $c_\lambda \propto f_\chi$ indicator. Group 2 has a large liquidus gradient but a small initial liquidus temperature and also shows a clear correlation between the metrics, however for

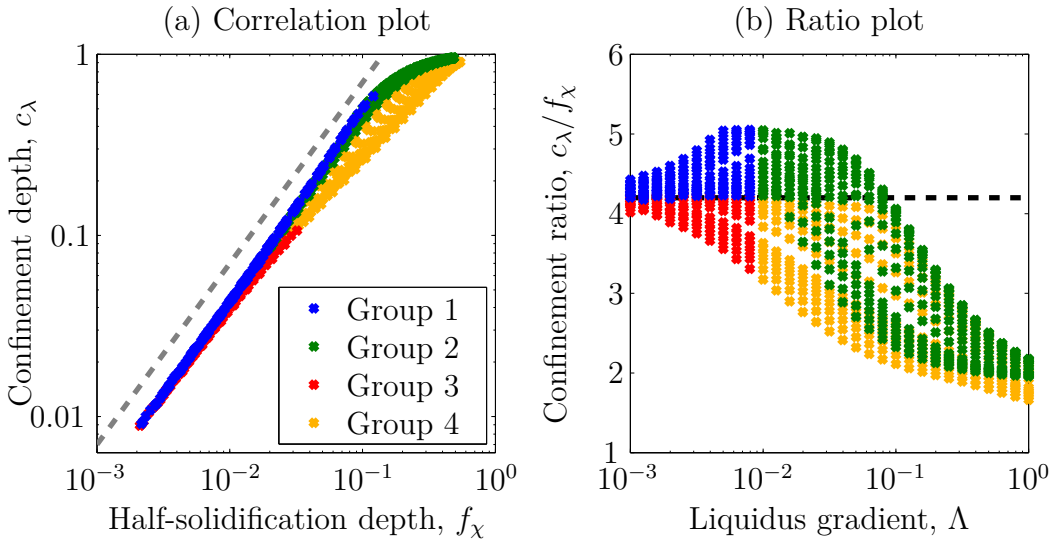

Figure 5.6: (a) The confinement depth, c_λ, plotted against half-solidification depth, f_χ, to indicate the level of correlation between the two metrics. Data is grouped according to Λ and $\theta_{L\infty}$ as described in table 5.1. There is a clear relationship between the two, and the trend $c_\lambda \propto f_\chi$ is shown in dashed grey for comparison. (b) The ratio of confinement depth to half-solidification depth, c_λ/f_χ, plotted against liquidus gradient, Λ. This ratio tends to a value of 4.2 (dashed black) in the limit of small Λ, with a small dependence on $\theta_{L\infty}$.

	$\Lambda \leq 10^{-2}$	$\Lambda > 10^{-2}$
$\theta_{L\infty} \leq 0.65$	Group 1 (blue)	Group 2 (green)
$\theta_{L\infty} > 0.65$	Group 3 (red)	Group 4 (yellow)

Table 5.1: The groupings used in the figures of §5.3 to break down the results. The $\theta_{L\infty}$ values for the groupings are based on the behaviour of f_χ and c_λ. For $\theta_{L\infty} \leq 0.65$ and small Λ, both the half solidification depth, f_χ, and the confinement depth, c_λ, decrease as the initial liquidus temperature, $\theta_{L\infty}$. For $\theta_{L\infty} \geq 0.7$, f_χ and c_λ increase as $\theta_{L\infty}$ increases. The exact change in behaviour occurs somewhere between these values. The split on the liquidus gradient is used to separate the more regular behaviour for very small values of Λ, and the more disperse results for larger values of Λ as the metrics begin to saturate.

large values of Λ the group moves away from a linear relationship as both the confinement depth and the half-solidification depth start to saturate. Group 4, which has a large liquidus gradient and a large initial temperature, does not show the strong correlation seen in the other groups but still follows the general trends.

To help understand how the size of the high porosity region (as measured by f_χ) affects the vertical extent of convection, c_λ, figure 5.6b plots the ratio c_λ/f_χ against the liquidus gradient, Λ. The ratios clearly tend to a limiting value close to 4.2 as $\Lambda \to 0$, with $\theta_{L\infty}$ possibly having a small effect on the limiting value. For $\theta_{L\infty} > 0.6$,

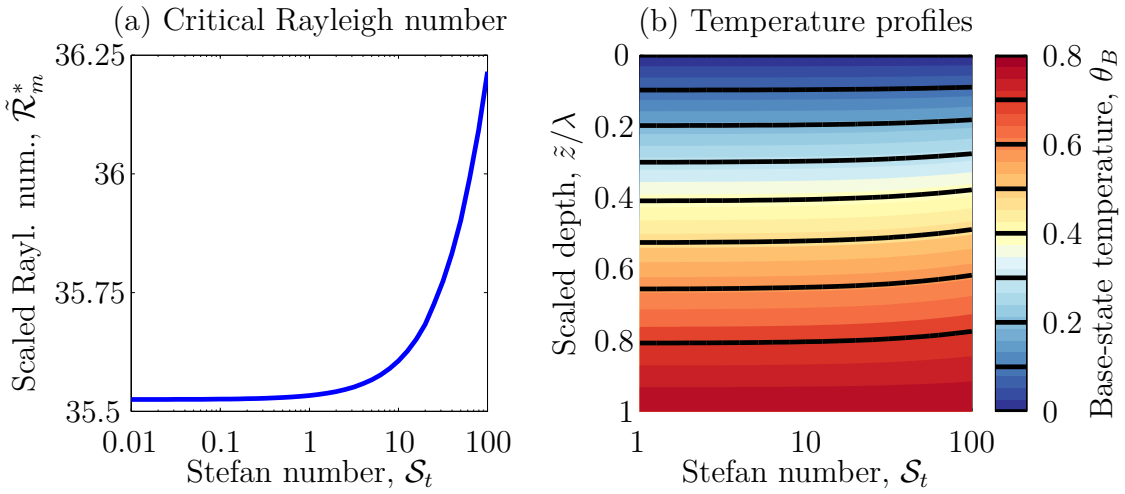

Figure 5.7: (a) The scaled critical Rayleigh number against Stefan number for $\Lambda = 100$ and $\theta_{L\infty} = 0.8$. Stefan numbers greater than one cause a small increase in the value of $\tilde{\mathcal{R}}^*_m$. (b) The corresponding base-state temperature profiles against Stefan number. The depth axis has been scaled by the mushy layer depth to highlight changes in the vertical structure. For large Stefan numbers, the temperature contours curve slightly upwards.

$c_\lambda/f_\chi < 4.2$ and convection concentrates more in the high-porosity region than it does for the limiting case. Conversely, for $\theta_{L\infty} \leq 0.6$, $c_\lambda/f_\chi > 4.2$ and there is a relatively wider spread into the low-porosity region compared to the limit. The mechanism behind this is unclear but it is possible the increased thermal forcing as $\theta_{L\infty}$ increases makes it energetically favourable to drive convection in a smaller region. This smaller region would experience a lesser fraction of the total forcing but also less resistance, compared to a larger region which would experience more of the total forcing but also more resistance.

5.4 Effects of the Stefan number

We now consider the effects of varying the Stefan number, $\mathcal{S}_t$, on the stability of the mushy layer. The Stefan number characterises the amount of latent heat in the system, relative to the amount of specific heat. As with Λ, $\mathcal{S}_t$ does not explicitly appear in the reduced eigenvalue problem (5.1.4 & 5.1.5) when solving for $\tilde{\mathcal{R}}^*_m$ with $\sigma = 0$, but will affect both θ_B and χ_B. These effects were not described in §3.2.2c when considering the impact of $\mathcal{S}_t$ on the growth rate, but a qualitative description will be presented here where relevant to the discussion.

In the high liquid fraction regime, increasing the Stefan number results in a small, but noticeable, increase in the scaled Rayleigh number. This is shown in figure 5.7a

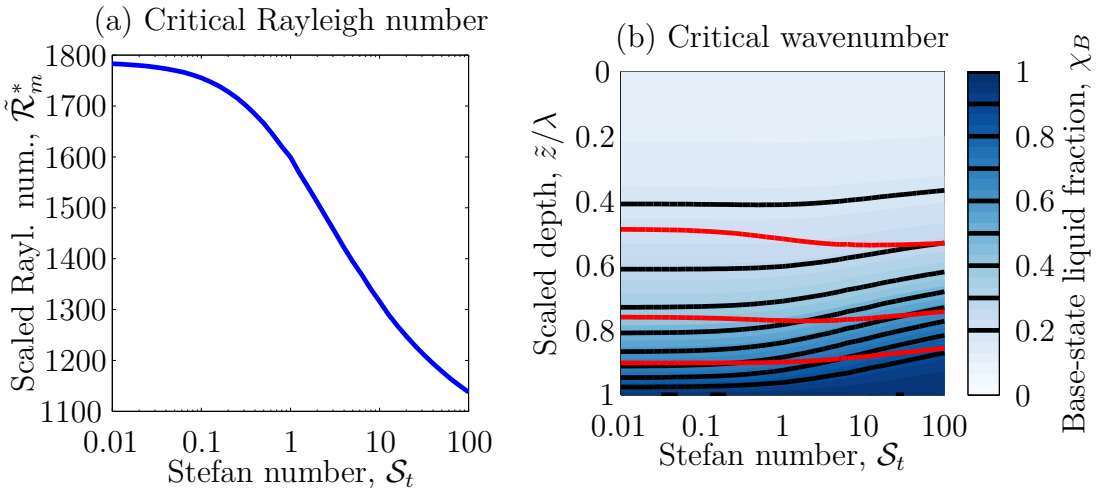

Figure 5.8: (a) The scaled critical Rayleigh number against Stefan number for $\Lambda = 0.1$ and $\theta_{L\infty} = 0.8$. Increasing the Stefan number causes an appreciable decrease in the value of $\tilde{\mathcal{R}}_m^*$. (b) The corresponding base-state liquid fraction profiles against Stefan number. Curves respresenting (from the top down) 10%, 50%, and 90% of the maximum stream function are shown in red. Note that the 10% contour is also used in the definition of the confinement depth, c_λ. The depth axis has been scaled by the mushy layer depth to highlight changes in the vertical structure. A larger Stefan number results in a larger high-porosity region close to the interface, with the stream function variation localising and moving upwards.

for $\Lambda = 100$ where $\tilde{\mathcal{R}}_m^*$ increases by 2% as $\mathcal{S}_t$ increases from 0.01 to 100. With such a large liquidus gradient, the porosity is greater than 0.99 throughout the depth of the mushy layer regardless of Stefan number, but there are some modest changes to the base-state temperature profile for large Stefan numbers, as shown in figure 5.7b. As the Stefan number increases, more latent heat is released when solidification occurs and the effective heat capacity of the mushy layer is increased. There is more solidification close to the surface than there is towards the interface, so there is a greater release of latent heat closer to the surface than at depth. This results in slower thermal transport through the surface layer and less cooling at depth, because the thermal energy cannot be removed as efficiently. The temperature profile therefore becomes less linear, with the gradient sharpening closer to the surface and flattening closer to the interface, as indicated by the upward curve of temperature contours in figure 5.7b. Thermal forcing is proportional to the temperature gradient and is concentrated closer to the no normal flow boundary at the surface, which is more restrictive than the constant pressure boundary at the interface, increasing the boundary resistance experienced by the flow and increasing the scaled Rayleigh number.

By contrast, in the Stefan regime with small Λ and low porosity over much of the depth, there is a significant decrease in scaled Rayleigh number as the amount of latent heat in the system increases (figure 5.8a). Here a liquidus gradient of $\Lambda = 0.1$ was chosen, which is relatively high for a system in the Stefan limit but provides better illustrations. With this setup, the scaled Rayleigh number decreases by approximately a third as the Stefan number increases from 0.01 to 100. As seen in the high liquid fraction regime, the thermal forcing will shift slightly upwards but this effect on the scaled Rayleigh number is relatively small compared to the changes that arise from the base-state liquid fraction profile. Figure 5.8b shows a clear thickening of the high-porosity interfacial region as the Stefan number increases, which results from the warming of the mushy layer at depth, combined with the Lever rule (2.3.6b). This decreases the scaled Rayleigh number because there is less resistance to flow over a greater range of depths at the base of the mushy layer.

However, the increased Stefan number also results in more localisation of the flow to within this enlarged high-porosity region. This can be seen in the stream function contours shown in figure 5.8b, which reveal an interesting balance. Flow over a smaller vertical extent experiences less resistance than flow which spreads further and penetrates into the low-porosity region. However, flow over a greater vertical extent experiences a greater temperature difference and so has more energy available to drive convection. As the Stefan number begins to increase, the increasing porosity close to the interface reduces the resistance to flow in this region, and so it becomes favourable to focus convection over a smaller vertical extent, albeit with less thermal forcing. For $\mathcal{S}_t > 10$, the 50% and 90% stream function contours show a small upward shift in figure 5.8b. This is because the growing high-porosity region means it is favourable for the cores of the convective cells (which are in this high-porosity region) to expand and encompass a greater range of temperature. The 10% stream function contour does not show the same behaviour because it is still localising towards this region to reduce resistance. When the Stefan number increases further, the increased size of the high-porosity region makes it favourable for the vertical extent of convection to increase again so that it encompasses a greater range of temperatures again. The increased localisation with increased Stefan number also manifests itself in figure 5.5 as a higher confinement liquid fraction and a lower confinement depth when the Stefan number is increased from 0 to 12.6.

5.5 Effects of Imperfect Boundary Conduction

In chapter 4, we saw there were three ways that the Biot number could affect the stability of a system with uniform porosity: by changing the temperature range in the fluid, by changing the structure of the thermal forcing, and by changing the boundary resistance applied to the thermal perturbation. Additionally, the evolving Biot number will affect the porosity of the mushy layer, with lower porosities forming as the Biot number grows (see §3.3.2). To investigate how these four effects affect the stability of a mushy layer, we will focus on examples in both of the high liquid fraction and Stefan regimes, before considering the setting observed by the field experiments of Notz and Worster (2008).

For the high liquid fraction regime, we consider a system with $\Lambda = 10$, $\theta_{L\infty} = 0.8$, and $\mathcal{S}_t = 100$, with the liquid fraction profiles for such a system shown against Biot number in figure 3.15. We saw that such a system initially freezes with a Biot number of $\tilde{\mathcal{B}_f} = 0.21$ and reaches a self-similar state for $\tilde{\mathcal{B}_i} \gtrsim 100$, corresponding to late times because the self-similar Biot number, $\tilde{\mathcal{B}_i} = \mathcal{B}_i\sqrt{t}$, increases over time. However, between these extremes there are significant changes to the growth and structure of the mushy layer as the effects of the cooling propagate through the system.

In figure 5.9, the scaled Rayleigh number, $\tilde{\mathcal{R}}^*_m$, and wavenumber for this system are plotted against Biot number in blue. With imperfect thermal conduction from the boundary, the surface temperature evolves over time and the temperature difference across the mushy layer grows as $\tilde{\mathcal{B}_i}$ increases. To see the effects of this changing temperature difference, and to isolate it from structural and perturbation boundary condition changes, figure 5.9 also shows the evolution of a local Rayleigh number in green. As in §4.4.2, the local Rayleigh number:

$$\tilde{\mathcal{R}}^*_{m,l} = \frac{g\left(\alpha + \beta/\Gamma\right)\left(T_{L\infty} - T(0)\right)\hat{\Pi}_0\hat{h}}{\kappa\nu}, \tag{5.5.1}$$

is defined using the temperature difference across the mushy layer, $T_{L\infty} - T(0)$, rather than the temperature difference across the full system, $\Delta T = T_\infty - T_c$. The global Rayleigh number, $\tilde{\mathcal{R}}^*_m$, has a minimum of 42.2 as $\tilde{\mathcal{B}_i} \to \infty$, and increases up to 1400 when $\tilde{\mathcal{B}_i} = 0.25$ before diverging to infinity as $\tilde{\mathcal{B}_i} \to \tilde{\mathcal{B}_f}$. In contrast, the local Rayleigh number, $\tilde{\mathcal{R}}^*_{m,l}$, has a maximum of 33.8 as $\tilde{\mathcal{B}_i} \to \infty$ and decreases to a limit of 18.4 as $\tilde{\mathcal{B}_i} \to \tilde{\mathcal{B}_f}$. The variation of the local Rayleigh number is minimal compared to that of the global Rayleigh number, indicating that the changing

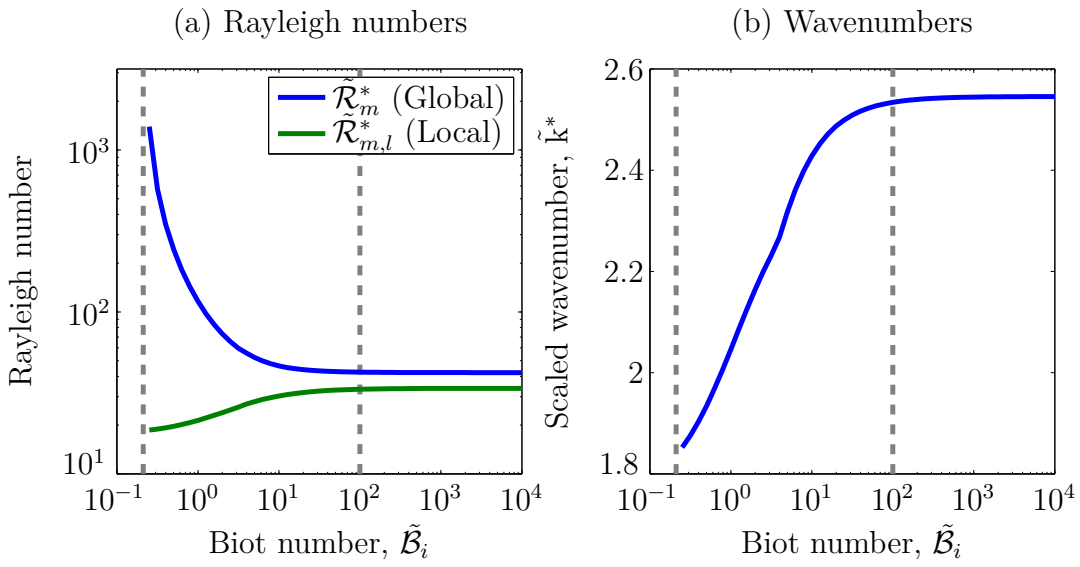

Figure 5.9: (a) Critical Rayleigh numbers and (b) critical wave numbers against Biot number for $\Lambda = 10$, $\theta_{L\infty} = 0.8$, and $\mathcal{S}_t = 100$. These conditions are the same as for those in figure 3.15, and place the system well into the high liquid fraction regime, with $\chi > 0.92$ for all $\tilde{\mathcal{B}}_i$. Two different definitions for the Rayleigh number are used. In blue is the 'global' Rayleigh number, $\tilde{\mathcal{R}}^*_m$, defined in (5.1.6a) is defined in terms of the temperature difference across the whole system and using the mushy layer depth as the lengthscale. The 'local' Rayleigh number, $\tilde{\mathcal{R}}^*_m$, in green is defined using the temperature difference across the mushy layer only (5.5.1). This difference in temperature scale does not affect the wavenumber. Shown in dashed grey are the first solidification at $\tilde{\mathcal{B}}_i = 0.21$ and the approximate transition from the adjustment period to the self-similar period at $\tilde{\mathcal{B}}_i \sim 100$.

---

thermal range is the most significant effect of varying the Biot number.

It is interesting to consider how the other three factors affect the local Rayleigh number. We know from figure 3.15 that the liquid fraction is uniformly one at first freezing and develops vertical structure over time as the surface solidifies. Decreased porosity at the surface decreases the permeability and increases the resistance to flow, providing a tendency for the critical Rayleigh number to increase. However, with a minimum liquid fraction of $\chi = 0.9$ there is no substantial convective confinement and this tendency is small. Similarly, figure 4.2b showed that decreasing the Biot number applied to a thermal perturbation decreases the critical Rayleigh number for thermal convection in a porous medium. This is because a smaller Biot number decreases the resistance from the boundary, as seen by a number of previous studies such as Kubitschek and Weidman (2003) and Barletta et al. (2015). Finally, the thermal gradients will be more uniform when the ice initially forms but at later times the temperature profile will become more non-linear with a sharper gradient

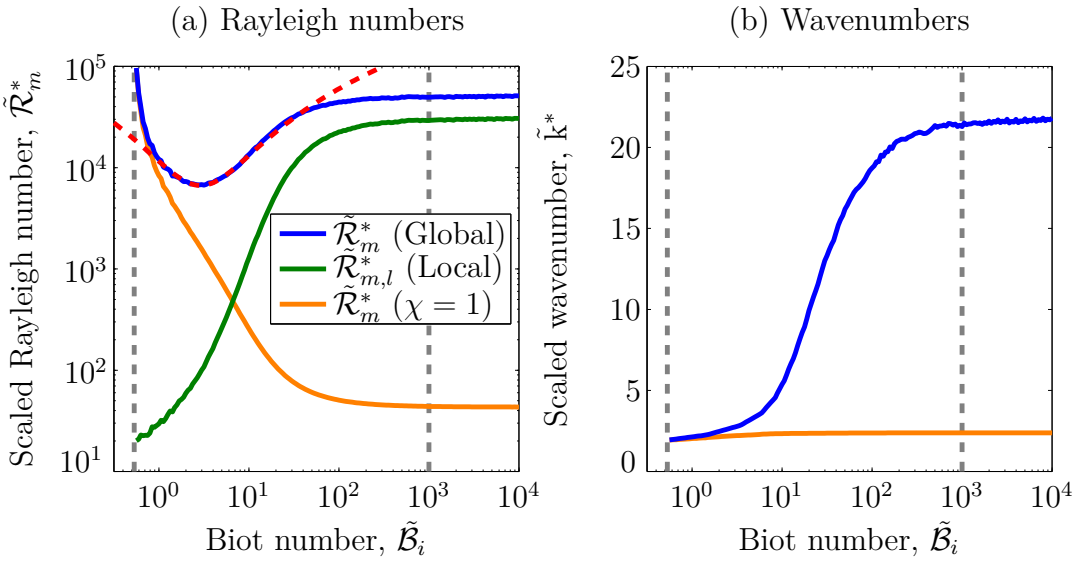

Figure 5.10: (a) Critical Rayleigh numbers and (b) critical wave numbers against Biot number for $\Lambda = 0.01$, $\theta_{L\infty} = 0.6$, and $\mathcal{S}_t = 300$. These conditions are the same as for those in figure 3.17, and place the system well into the Stefan regime, with a large region of low porosity. Two different definitions for the Rayleigh number are used. In blue is the 'global' Rayleigh number defined in (5.1.6a) is defined in terms of the temperature difference across the whole system while the 'local' Rayleigh number in green is defined in terms of the temperature difference across the mushy layer only (5.5.1). The global critical Rayleigh number and wavenumber are also calculated with a uniform porosity, and shown in orange for comparison. Shown in dashed grey are the first solidification at $\tilde{\mathcal{B}}_i = 0.53$ and approximate transition from the adjustment period to the self-similar period at $\tilde{\mathcal{B}}_i \sim 1000$. Due to low-level noise in the interface position being amplified by the stability calculations, λ was smoothed with a running average before being used in the stability analysis.

near the surface and a shallower gradient at depth. Figure 5.7 demonstrated that a more non-linear temperature profile tends towards an increased Rayleigh number, so changes to the thermal structure will also result in an increased Rayleigh number as the Biot number increases. Changes to the liquid fraction structure, perturbation stress, and thermal structure all act to the increase the local Rayleigh number as the Biot number increases, as indicated by the green curve in figure 5.9a. However, these changes are not significant enough to overcome the reduction in the global Rayleigh number caused by increased thermal forcing, as shown by the blue curve also in figure 5.9a.

We next consider the Stefan regime, which has $\Lambda \ll \theta_{L\infty}$ and relatively low liquid fractions. Figure 5.10 shows the effects of imperfect conduction in this regime, with $\Lambda = 0.01$, $\theta_{L\infty} = 0.6$, and $\mathcal{S}_t = 300$. The liquid fraction profiles for this setup are shown in figure 3.17 and show a large low porosity region which begins to form for

$\tilde{\mathcal{B}}_i \geq 2.3$ and eventually occupies roughly 90% of the mushy layer. In this instance, the porosity of the system has a significant impact on the stability of the system due to convective confinement. While in figure 5.9a, the local Rayleigh number, $\tilde{\mathcal{R}}^*_{m,l}$, roughly doubled between first growth at small $\tilde{\mathcal{B}}_i$ and the self-similar limit for large $\tilde{\mathcal{B}}_i$, in figure 5.10a it increases over three orders of magnitude. This is in contrast to the Rayleigh number calculated with the full temperature range but a uniform porosity, which is shown in orange and is initially close to the scaled Rayleigh number, $\tilde{\mathcal{R}}^*_m$, but rapidly drops two and a half orders of magnitude. The critical wavenumber increases by an order of magnitude in figure 5.10b indicating a dramatic narrowing of the convective cells relative to the mushy layer depth. By noting the preference for square aspect ratios in convective patterns, this is further evidence of the convective confinement becoming more significant as the Biot number increases.

The critical Rayleigh number for the system, $\tilde{\mathcal{R}}^*_m$ (blue), is therefore being set by two competing effects. As the Biot number increases, the increasing temperature difference across the mushy layer increases the thermal forcing and therefore increases the amount of energy available to drive convection. This acts to decrease the global critical Rayleigh number. On the other hand, increased solidification increases the resistance to flow and the growth of the low porosity region significantly affects the vertical extent of the convection. A balance forms between these two effects which results in a minimum in the scaled Rayleigh number, $\tilde{\mathcal{R}}^*_m$, at $\tilde{\mathcal{B}}_i \approx 2.9$, with the behaviour around the minimum given empirically by:

$$\tilde{\mathcal{R}}^*_m = 6700 + 4300 \left[\ln \left(\frac{\tilde{\mathcal{B}}_i}{2.9} \right) \right]^2 , \tag{5.5.2}$$

which is a quadratic curve with a logarithmic independent variable, and was fitted with a least-squares method. Comparing this with figure 3.17, we see that the minimum occurs when $\chi(0) = 0.42$ and $\theta(0) = 0.58$. Recalling that $\theta_{L\infty} = 0.6$, the temperature difference across the mushy layer only represents 2% of the total temperature difference, $T_\infty - T_c$, at this point but with a very small liquidus gradient ($\Lambda = 0.01$), this nevertheless corresponds to appreciable solidification at the surface which will start restricting convective flow.

5.5.1 Comparison with Notz and Worster (2008)

We now consider conditions appropriate for the experimental results in Notz and Worster (2008), as previously discussed in §3.3.2d. This study reports on field observations of initial ice growth in a hole cut into land-fast sea ice in Svalbard. The temperature, liquid fraction and bulk salinity where measured in two experiments lasting six and four days respectively, although we will only draw on data from the first, longer experiment. They observed sea water with a salinity of $\hat{S}_\infty = 35$psu being cooled from $T_\infty = -1^oC$ to $T_c = -30^oC$, which gives the dimensionless parameters $\Lambda = 0.10$, $\theta_{L\infty} = 0.91$ and $\mathcal{S}_t = 2.9$. We will primarily use the more established value for the permeability reference, $\hat{\Pi}_0 = 2 \times 10^{-8}\text{m}^2$ (Freitag, 1999), which yields a convective lengthscale of $\hat{d}_m = 4.4 \times 10^{-3}$ mm. However, we will also discuss how the results change with the newer value proposed by Rees Jones and Worster (2014), $\hat{\Pi}_0 = 2.2 \times 10^{-9}\text{m}^2$, which yields a longer convective length of $\hat{d}_m = 3.9 \times 10^{-2}$ mm.

Figure 5.11 plots the critical depth for this setup against Biot number, found by rearranging (5.1.6a) to give $\hat{h}_c$. While this setup is in the transitional regime rather than the pure Stefan regime, we still observe the non-monotonic behaviour in the scaled Rayleigh number and critical depth. In this instance, the minimum scaled Rayleigh number is 600, corresponding to a critical depth of 2.6mm, which occurs when $\tilde{\mathcal{B}}_i = 0.6$ and just after half of the surface layer has solidified, $\chi = 0.44$, with a surface temperature of 0.78. The scaled Rayleigh number then rises to a long-time limit of 1300, which is equivalent to a depth of 5.7mm.

We can also calculate the time-evolving depth trajectories by combining and dimensionalising (3.1.3) and (4.2.7d) to yield:

$$\hat{h}\left(\tilde{\mathcal{B}}_i\right) = \hat{d}_b \; \tilde{\mathcal{B}}_i \; \lambda\left(\tilde{\mathcal{B}}_i\right), \qquad \hat{d}_b = \frac{k_l}{\rho_a c_{pa} C_s u_w}. \tag{5.5.3a,b}$$

where the boundary cooling length scale is $\hat{d}_b$ and I have assumed that heat losses are dominated by sensible heat transfer. Of the parameters contributing to the boundary length scale the wind speed, u_w, is most likely to vary and affect the cooling rate. Increasing the wind speed decreases the boundary cooling length and lowers the ice depth for a given $\tilde{\mathcal{B}}_i$. This does not indicate less ice at a given time since $\hat{d}_b$ also affects the mapping from $\tilde{\mathcal{B}}_i$ to physical time.

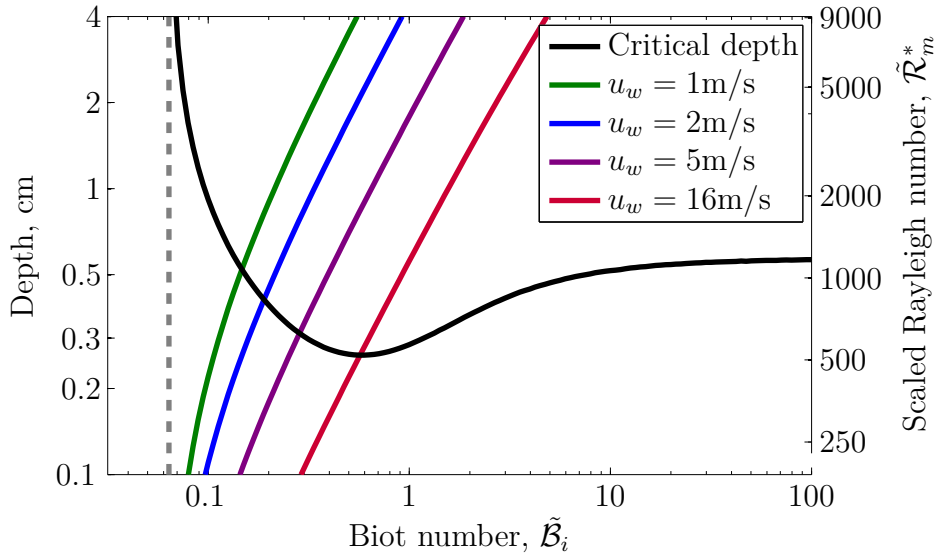

Figure 5.11: The critical depth, $\hat{h}_c$, (black) and time-evolving ice depth, $\hat{h}$, (coloured) for four different surface wind speeds against self-similar Biot number, $\tilde{\mathcal{B}}_i = \sqrt{\kappa \hat{t}}/\hat{d}_b$. Shown on the alternate vertical scale is the scaled Rayleigh numbers corresponding to these ice depths, which is related to the main scale through (5.1.6a), using $\hat{\Pi}_0 = 2\times10^{-8}\text{m}^2$. The self-similar Biot number, $\tilde{\mathcal{B}}_i$, can be converted to physical times using $\tilde{\mathcal{B}}_i = \sqrt{\kappa \hat{t}}/\hat{d}_b$, with $\hat{d}_b$ inversely proportional to wind speed, u_w. The ice depths monotonically increase with Biot number, and hence time, but the critical depth exhibits the non-monotonic variation first observed in figure 5.10 for the Stefan regime which arises from the formation of a low porosity region and subsequent convective confinement.

We note that since $\hat{h}_c$ has a minimum, there will be an 'optimal' cooling rate where the growing ice depth intercepts the minimum of $\hat{h}_c$ and the mushy layer becomes linearly unstable with the least possible ice growth. To investigate this, figure 5.11 also shows the time-evolving trajectories of ice depth for four different surface wind speeds which are consistent with the range observed by Notz and Worster (2008). At the low, but physically reasonable, wind speeds considered here, increasing the wind speed decreases the depth at which the mushy layer becomes unstable. This can be seen by the critical depth and the physical growth trajectories intercepting at a lower point. The trend continues up to wind speeds of 16m/s where the intercept occurs at the minimum of the critical depth curve, and represents the 'optimal' rate of cooling. Increasing the wind speed further will delay the convective onset until the ice has reached a greater depth.

Calculating the Biot number at which $\hat{h}$ intercepts $\hat{h}_c$ gives the onset time, $\hat{t}_i = (\hat{d}_b\tilde{\mathcal{B}}_i)^2/\kappa$, and the wavelength of convection, $2\pi\hat{h}_c/\text{k}^*_c$. These are shown in figure 5.12 for a range of realistic wind speeds. Whilst an increase in the wind speed increases

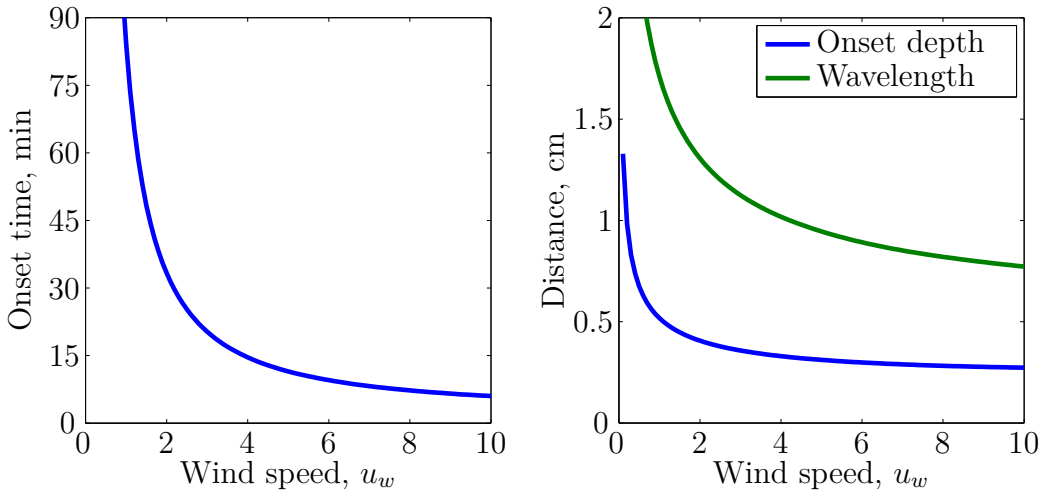

Figure 5.12: (a) The onset time and (b) onset depth (blue) and half-wavelength (green) against wind speed. These results have been calculated for 35psu sea water cooled from -1^oC to -20^oC, with a permeability of $\hat{\Pi}_0 = 2 \times 10^{-8}\mathrm{m}^2$ and all other properties taking their standard values. Faster wind speeds result in convective onset occurring sooner, with thinner ice and at shorter wavelengths.

---

the value of $\tilde{\mathcal{B}}_i$ needed for convective onset, the actual onset time decreases as the wind speed increases and is well described by:

$$\hat{t}_i = \left(120 + 360\left(\frac{\mathrm{m/s}}{u_w}\right)^{1.3}\right)\mathrm{s},$$

which was fitted by a least-squares method and has less than a 1% error between 1m/s and 10m/s. This occurs because higher wind speeds allow faster heat transfer from the surface, which enhances the cooling of the mushy layer. As a result, the mushy layer grows faster and reaches the critical depth sooner, with the critical depth itself also lowered by the increasing wind speed. Increasing the wind speed also decreases the wavelength of convective patterns which form, in a way which closely follows the decreasing critical depth. This wavelength is given by:

$$\frac{2\pi}{\hat{\mathrm{k}}} = 1.7\mathrm{cm}\left(\frac{\mathrm{cm/s}}{u_w}\right)^{0.34},$$

with an error of $< 2\%$.

In §3.3.2d, we predicted that Notz and Worster (2008) would observe first solidification approximately 6 min after the start of the experiment. From figure 5.12 and an average observed wind speed of 2m/s, we can predict that convective onset would occur 33min after the start of the experiment, which is also 27min after the

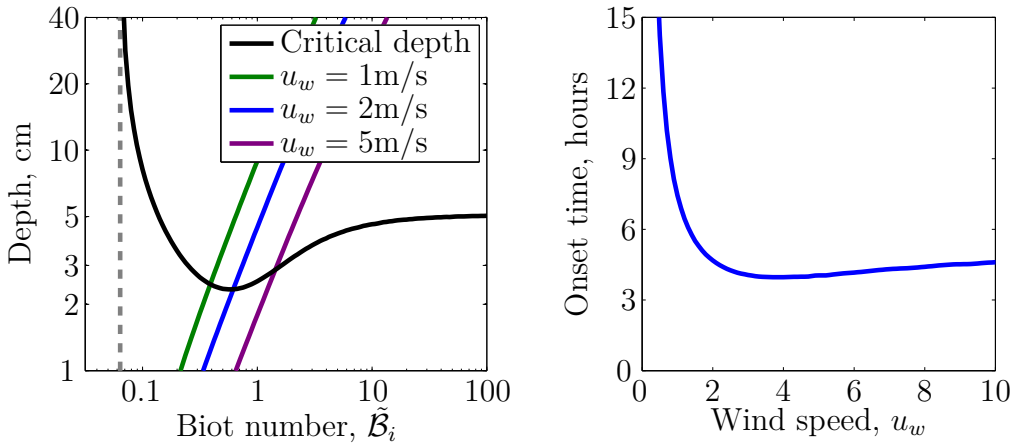

Figure 5.13: *(Left)* The critical depth, $\hat{h}_c$, and three ice growth trajectories, $\hat{h}(\hat{t})$, against Biot number, $\tilde{\mathcal{B}}_i$, recreating figure 5.11 with $\hat{\Pi}_0 = 2.2 \times 10^{-9}\text{m}^2$ (Rees Jones and Worster, 2014) instead of $\hat{\Pi}_0 = 2 \times 10^{-8}\text{m}^2$ (Freitag, 1999). The critical depth curve is now a order of magnitude higher and the 'optimal' wind speed for convective onset at the minimum critical depth is now 2m/s. *(Right)* The onset time, $\hat{t}_i$, against wind speed, u_w, calculated with the new permeability value. Convective onset is significantly delayed compared to the traditional permeability value and now exhibits a minimum at $\sim$ 4m/s.

first solidification. At this time, the mush would be 4mm thick and the convection would have a wavelength of 1.3cm. Their results show a noticeable decrease in the bulk salinity after six hours, indicating that convection has started in the first six hours of ice growth, but they did not resolve shorter timescales. After six hours, the ice had reached a depth of $\sim$ 4cm.

Figure 5.13a considers the same system but calculated with a permeability value of $\hat{\Pi}_0 = 2.2 \times 10^{-9}\text{m}^2$ (Rees Jones and Worster, 2014) rather than the value used previously, $\hat{\Pi}_0 = 2 \times 10^{-8}\text{m}^2$ (Freitag, 1999). The critical Rayleigh number is unchanged but the critical depth curve is now an order of magnitude higher, with a minimum value of 2.3cm, rather than 2.6mm. This also affects the intercept points where the ice growth trajectories cross the critical depth curve, with 2m/s now being the 'optimal' wind speed for convective onset with the minimum of ice growth, where 16m/s was the value previously given. We note that 2m/s is the average wind speed observed by Notz and Worster (2008) during their experiment.

Since the ice must grow significantly deeper before convective onset, figure 5.13b shows much higher onset times than figure 5.12a, with onset times increasing from 10s of minutes to about 10 hours. Intriguingly, there is now a minimum onset time at $\sim$ 4m/s beyond which the onset time increases slightly with increased wind speed.

This behaviour is also observed for the higher permeability, but requires hurricane-strength wind speeds of ~ 35m/s, and the resulting sea state likely prohibits the application of the model presented here. The minimum onset time is not coincident with the minimum critical depth, but instead appears to be coincident with the inflection point in $\hat{h}_c(\tilde{\mathcal{B}}_i)$. A possible explanation is that the tendency for onset times to increase with the critical depth is initially offset by higher growth rates for higher wind speeds, so less time elapses before the ice reaches the (higher) critical depth. As the wind speeds increase further, the effect on the growth rate decreases at a greater rate than the effect on the critical depth, so the onset time begins to increase again.

Using the new permeability value, we can also offer alternative predictions for convective onset in the conditions observed by Notz and Worster (2008). Using a wind speed of ~ 2m/s, we now predict that convective onset would begin after 4h40min, with a wavelength of 6cm and an ice depth of 2.3cm.

Finally, we note that as $\tilde{\mathcal{B}}_i \to \infty$ and we approach the self-similar limit, λ will tend to a constant value in (5.5.3a) so the physical ice depth will continually increase as $\tilde{\mathcal{B}}_i$ diverges. The critical depth tends to a constant value for $\tilde{\mathcal{B}}_i \to \infty$ so the physical ice depth will always intercept the critical depth and the mushy layer will always lie in the convectively unstable region above the black curve in figure 5.12 (or figure 5.13a). However, the non-monotonic variation of the critical depth raises the possibility that the growth trajectories, $\hat{h}(\tilde{\mathcal{B}}_i)$, might intercept the critical depth, $\hat{h}_c(\tilde{\mathcal{B}}_i)$, at three points, rather than just one. Physically, this would represent a system which initially becomes unstable as the temperature difference across the mushy layer grows without significant solidification. Further solidification, particularly at the surface, would make convection unviable for linear perturbations by increasing the resistance to flow. Finally, the growing ice depth reduces the ability of thermal diffusion to stabilise the fluid and the high-porosity interfacial region becomes unstable again. However, I was unable to find such a trajectory for the setup presented here with a constant $\hat{d}_b$ so further investigation would be needed over a wider range of parameters to demonstate that such a configuration is possible (or otherwise). In any case, the initial period of convection may alter the bulk salinity and structure of the mushy layer to the extent that the convective shut down does not occur.

5.6 Summary and Conclusions

In this chapter, I have performed a linear stability analysis for the onset of convection in a transiently growing mushy layer, considering the impact of the temperature and liquid fraction profiles calculated in chapter 3. Following earlier studies of convection in mushy layers, such as Emms and Fowler (1994), the interface was treated as an isothermal, constant pressure boundary. The scaled Rayleigh number, $\tilde{\mathcal{R}}_m^* = g(\alpha + \beta/\Gamma)\hat{\Pi}_0\hat{h}(\hat{t})/\kappa\nu$, was found and used to obtain the critical depth, $\hat{h}_c$, through knowledge of the other properties. Similarly, the corresponding wavenumber, $\tilde{\mathrm{k}}^* = \hat{\mathrm{k}}\hat{h}(\hat{t})$, was also found and can be combined with the critical depth to give the onset wavelength.

The investigation showed that the dimensionless liquidus gradient, Λ, has a significant impact on the stability of the system, with the behaviour of the critical Rayleigh number given by $\tilde{\mathcal{R}}_m^* = 49 + 15/\Lambda^2$, and the critical wavenumber by $\tilde{\mathrm{k}}^* = 2.4 + 0.27/\Lambda$, for non-dimensional initial liquidus temperature of $\theta_{L\infty} = 0.8$ and independent of Stefan number, $\mathcal{S}_t$, which measures the ratio of latent to specific heat. These increases had been observed previously by Hwang (2013), but had not been characterised quantitatively. When the liquidus gradient is large, the freezing point depression is much larger than the range of temperatures in the system. The liquid fraction is close to one throughout and convection can penetrate the full depth of the mushy layer. However, for small liquidus gradients (the Stefan regime) the system is comparatively fresh and a large low porosity region forms, which severely increases the resistance to flow and results in a critical Rayleigh number $\propto 1/\Lambda^2$. Convection is unable to penetrate this low porosity region and so is confined to the interfacial region, which has a fractional thickness proportional to Λ, with a similar fraction of the total temperature difference. This confinement explains the increase in wavenumber, $\tilde{\mathrm{k}}^*$, for small Λ, since convection has a preference for square aspect ratios. The vertical extent of the flow is being reduced, so the convective cells narrow. The scaling of the critical Rayleigh number, $\tilde{\mathcal{R}}_m^*$, is explained by a combination of the reduced vertical extent and the reduced temperature range across the thinner convective cell. It was also shown, in §5.3, that an increase in the initial liquidus temperature results in more flow localising towards the high-porosity interfacial region but the reason for this is unclear.

I showed that the effect of the Stefan number on convective instability depends on the dimensionless liquidus gradient. When the liquidus gradient is large and

the mushy layer has a high liquid fraction throughout its depth there is a modest increase in the critical Rayleigh number as $\mathcal{S}_t$ increases. This is because increasing the Stefan number focusses the thermal forcing nearer to the restrictive no-flow surface condition and away from the liberal constant pressure interface condition. In contrast, when the liquidus gradient is small and the system is in the Stefan regime there is a significant decrease in the critical Rayleigh number for larger $\mathcal{S}_t$. The largest effect comes from the liquid fraction profiles, because increasing the Stefan number increases the size of the high porosity region close to the interface. This promotes convection by reducing the resistance to flow. This effect is much larger than that caused by the changing temperature profiles.

When considering the effects of imperfect conduction, we demonstrated that changes to the internal temperature difference across the mushy layer and to the porosity structure are far more significant than changes to the temperature structure or thermal boundary resistance. Increasing the temperature difference across the mushy layer directly increases the amount of potential energy available to drive convection and leads to a corresponding decrease in the critical Rayleigh number. In the high liquid fraction regime, there is no significant change in liquid fraction as $\tilde{\mathcal{B}}_i$ is varied and the temperature difference between the surface layer and the interface is the main driver of change to $\tilde{\mathcal{R}}_m^*$. However, in the Stefan and transitional regimes, changes to the liquid fraction become significant and an initially uniform layer develops low porosity regions which greatly increase the resistance to flow. The increased resistance to flow and resulting convective confinement increases the amount of forcing needed to drive convection through the lower porosity regions. It also requires a more substantial thermal gradient to accumulate sufficient potential energy across the smaller high porosity regions to trigger convection. This causes an increase in the global critical Rayleigh number as $\tilde{\mathcal{B}}_i$ increases, which competes with the lower surface temperature and greater thermal forcing. As a result of this balance, $\tilde{\mathcal{R}}_m^*$ shows non-monotonic behaviour as $\tilde{\mathcal{B}}_i$ increases, in contrast to the monotonic variation when Λ is large and internal solidification is relatively weak. The Rayleigh number, $\tilde{\mathcal{R}}_m^*$, exhibits a minimum that occurs when the temperature difference across the mushy layer is 2% of the total temperature range, and also roughly corresponded with the surface liquid fraction dropping below 0.5. The non-monotonic behaviour of $\tilde{\mathcal{R}}_m^*$ (and hence $\hat{h}_c$) combined with the steady growth of the physical ice depth, $\hat{h}(\hat{t})$ raises the possibility that certain conditions could exhibit a convective shut-down and restart. This could occur if the critical depth increases faster than the physical ice depth after an initial onset, but further investigation is

needed to determine if this is possible.

Specific calculations were also performed for the conditions observed by the field experiments of Notz and Worster (2008). For an ice permeability of $2 \times 10^{-8}\mathrm{m}^2$ and wind speeds less than 16m/s, increasing the wind speed results in a lower critical depth for the onset of convection, because the faster winds cause more rapid cooling of the mushy layer. The Biot numbers at onset increase with the wind speed but this nevertheless translates to earlier convective onset since the larger wind speed drives rapid growth. I determined an empirical scaling law for this decrease in the onset time with wind speed, along with a corresponding scaling law for the convective wavelength. Increasing the wind speed reduces the wavelength at convective onset roughly in proportion to the decreasing critical depth. However, for much larger wind speeds, we observe a more complex non-monotonic variation of the onset time with wind speed. This becomes particularly significant when a lower estimate of the permeability, $2.2 \times 10^{-9}\mathrm{m}^2$ (Rees Jones and Worster, 2014), is used, where the minimum onset time occurs for a wind speed of 4m/s.

For the conditions observed by Notz and Worster (2008) with a 2m/s wind speed and a permeability of $2 \times 10^{-8}\mathrm{m}^2$, we predict that convection will start 33min after the start of cooling (27min after first solidification), with a wavelength of 1.3cm and an ice depth of 4mm. Using an alternative permeability of $2.2 \times 10^{-9}\mathrm{m}^2$, suggested by Rees Jones and Worster (2014), we make an alternative prediction of convective onset after 4h40min with a wavelength of 6cm and an ice depth of 2.3cm. Both predictions are within the bound of $<$ 6hour from the original study. In both cases, the prediction for ice depth is very small, and it is possible the ice has not yet suitably coalesced for this model to be applicable (see §3.3.2d), or that the assumptions of the continuum approximation are not valid.

Comparisons were also made to the data of Wettlaufer et al. (1997) who characterised the onset of finite-amplitude convection in growing mushy layers by measuring the salinity of the underlying fluid and the characteristic spacing between channels. The model presented here predicts onset depth, time, and wavelength to within an order of magnitude of the observations when a permeability reference of $2.2 \times 10^{-9}\mathrm{m}^2$ is used, but quantitative agreement is not strong. While uncertainty in the material properties may contribute to this, it is more likely that the linear stability analysis is less appropriate for capturing brine channel formation. The frozen time method analyses linear instability, and does not capture any non-linear dynamics. It is

therefore unable to determine the existence or otherwise of subcritical stability branches, which are known to exist in the directional solidification setting (Amberg and Homsy, 1993). Nevertheless, the linear analysis has provided new physical insight into the general processes which control stability, and should accurately characterise instability on supercritical branches.

6
Discussion and Conclusions

Sea ice is a vital part of polar climates and ecosystems (introduction, chapter 1). It moderates the exchange of thermal energy between the ocean and the atmosphere and provides a biological habitat for species ranging from algae within the ice, to marine mammals and birds. The seasonal cycle of brine rejection during ice growth, and freshwater release during ice melt, impacts ocean mixing and circulation. For example, brine rejection contributes to the generation of the cold halocline in the Arctic, which traps heat at depth, and the formation of bottom water at both poles.

Sea water is a *multi-component alloy* containing many different chemical species (§1.2.2), and sea ice growth results in a mixture of solid crystals and concentrated brine in the interstitial pores (§1.3). This mixture is known as a *mushy layer* (Worster, 1992a), corresponding to a reactive porous medium in local thermodynamic equilibrium. The local temperature and liquid salinity are constrained by a *liquidus relationship* (1.2.1), with solidification or melting occurring in response to any local disequilibrium. Once solidification begins, cooling increases the fraction of solid ice crystals such that the salinity of the remaining brine increases to restore equilibrium. Hence, cold, saltier fluid closest to the sea ice surface has greater density than the comparatively warm, fresh fluid in the underlying ocean. The resulting unstable density gradient can drive convection through the ice pore space and leads to the rejection of concentrated brine into the ocean. This convection is resisted by thermal dissipation (through diffusion) and viscous drag from the walls of the pores (§1.4). Importantly, the viscous forces depend on the permeability of the ice, and hence the porosity, which means that the internal solidification of the ice can play a major

role in controlling the stability of the interstitial fluid.

This thesis has aimed to gain insight into the early transient growth and internal structure of sea ice, and to understand the initial onset of convection through a combination of broad parameter investigations and comparison with specific physical examples. To build insight into the relevant processes, I have considered three settings. I started with an investigation of a mushy layer growing diffusively to determine how the growth rate and internal structure are affected by changes to the initial and external conditions, including the imposed temperature range and the rate of heat loss at the ice surface. I then considered the impact of imperfect thermal conduction on thermal convection in a deep, unreactive, porous layer to understand how this can affect convection in a boundary layer. Building on these two studies, I studied how the internal structure of the ice and external cooling rate can affect the onset of convection in a growing mushy layer. While the primary motivation is sea ice development, the general approach means that the results are relevant to other applications in Earth sciences and engineering that feature reaction or convection in porous media.

The mushy layer equations (chapter 2, following Worster, 1992a) were used to model sea ice growth and five non-dimensional parameters particularly pertinent to our discussion were identified:

- The dimensionless liquidus gradient, $\Lambda = \Gamma \hat{S}_\infty/(T_\infty - T_c)$, characterises the relative size of the freezing point depression, $\Gamma \hat{S}_\infty$, to the driving temperature range, $\Delta T = T_\infty - T_c$.

- The dimensionless initial liquidus temperature, $\theta_{L\infty} = (T_{L\infty} - T_c)/\Delta T$, measures the temperature difference across the mushy layer relative to the temperature difference across the full system.

- The Stefan number, $\mathcal{S}_t = L/c_p \Delta T$, describes the amount of latent heat in the system compared to the specific heat content.

- The self-similar Biot number, $\tilde{\mathcal{B}}_i = \mathfrak{h}\sqrt{\kappa \hat{t}}/k$, measures the effective thermal conductivity of the surface boundary, with $\mathfrak{h}$ representing the strength of thermal processes removing heat from the system. It is measured relative to the thermal diffusion lengthscale, which means that it will increase as time increases and the thermal diffusion lengthscale grows.

- The self-similar Rayleigh number, $\tilde{\mathcal{R}}_p = g\,(\alpha + \beta/\Gamma)\,\Delta T \hat{\Pi}_0 \sqrt{\kappa \hat{t}}/\kappa\nu$, describes the strength of buoyancy forcing in the system relative to the amount of the dissipation. This combination is also defined in terms of the thermal diffusion length scale so will also increase as time passes.

6.1 Summary of Key Results

6.1.1 Diffusive Growth of a Mushy Layer

The first branch of research presented in this thesis considered the growth and porosity structure of a mushy layer prior to the onset of convection and how this is affected by the initial and external conditions, as well as the rate of heat loss across an imperfectly conducting boundary. Whilst diffusive growth has previously been studied in some settings, I have performed a systematic investigation that provides new insight into the evolving internal structure of the ice, the effect of salt diffusion on growth, and the impact of imperfect surface cooling.

Using a simple model which assumes that the solid fraction is small (§3.1.1), I demonstrated that increasing the dimensionless initial liquidus temperature or decreasing the amount of latent heat in the system increases the mushy layer growth rate (figure 3.1). Increasing the dimensionless initial liquidus temperature reduces the amount of sensible heat which must be removed from the system before it can begin to solidify, which means it is easier for a parcel to start solidifying and the mushy layer can grow faster. In contrast, increasing the amount of latent heat in the system decreases the amount of sensible heat which can be removed and so inhibits ice growth. The growth rates were also shown to be well approximated by (3.1.8) (see figure 3.2), which is subtly different to the result of Emms and Fowler (1994) (3.1.7).

Salt diffusion in the liquid and mushy phases was shown to impact the mushy layer growth rates (§3.1.2b). Including salt diffusion in the liquid phase tends to decrease the growth rate, with the effect most pronounced when $\theta_{L\infty}$ is smaller. This occurs because the salt forms a compositional boundary layer with a depressed local liquidus temperature, which parcels must be cooled through before they solidify. By decreasing the temperature at the interface, the compositional boundary layer effectively decreases $\theta_{L\infty}$ and this effect is most noticeable when $\theta_{L\infty}$ is small. When $\theta_{L\infty}$ is smaller, the energy removed from the mushy layer represents a smaller fraction of the total so changes to the energy budget in the liquid will have a larger

impact on the growth rate. This makes the freezing point depression from salt diffusion more significant. In contrast, Salt diffusion in the mushy phase tends to enhance the growth rate, with the effects more pronounced when latent heat is more significant. This is because salt diffusion creates an effective thermal transport, with downward salt motion causing local solidification and dissolution as the system relaxes to local thermodynamic equilibrium. The result is an effective flux of solid and latent heat upwards. Of these two effects, the mushy phase contribution is more important over regions of parameter space appropriate to sea ice. The net impact on the growth rate is modest but not negligible (figures 3.4 and 3.5, as well as §3.1.2c).

A more complex model that accounts for appreciable solidification (§3.2.1) was used to determine how the liquidus gradient and Stefan number influence the growth rate and solidification. The dimensionless liquidus gradient only significantly affects the growth rate when $\Lambda \gg 1$ (figure 3.6). This is because the relevant Stefan number shifts from the 'standard' Stefan number $\mathcal{S}_t = L/c_p\Delta T$ to the *compositional Stefan number* $\mathcal{S}_c = \mathcal{S}_t/\Lambda = L/c_p\Gamma\hat{S}_\infty$ as Λ increases, representing a transition from a thermally-controlled system to a compositionally-controlled system.

There are also changes in the liquid fraction structure within the ice accompanying this change in growth rate behaviour, with a dependence on the ratio, $\Lambda/\theta_{L\infty}$ indentified. The combination $\mathcal{C} = \Lambda/\theta_{L\infty}$ has been used by previous studies to describe this ratio (Worster, 1991). For large dimensionless liquidus gradients, $\Lambda \gg \theta_{L\infty}$, the liquid fraction is high throughout the mushy layer (figure 3.8a). The salinity changes needed to maintain local thermodynamic equilibrium are small compared to the initial salinity, so very little solid can form before the salinity has increased sufficiently to restore equilibrium. However, for small dimensionless liquidus gradients, $\Lambda \ll \theta_{L\infty}$, there is appreciable solidification over much of the depth (figure 3.8a). Because of the constraint of local thermodynamic equilibrium, large salinity changes are needed to match the temperature variations and significant solid formation can occur before the salinity inhibits further solidification. The mushy layer can be considered as a large region of very high solid fraction, with a small region localised near the mush-liquid interface where most of the internal solidification occurs. The fraction of the depth occupied by this interfacial region is proportional to the dimensionless liquidus gradient, Λ, (eq. 3.2.4 and figure 3.8b), with the thickness tending to zero as the liquidus gradient also approaches zero. In this extreme limit, the problem approaches that of the Stefan problem, where are

pure substance is solidified and forms a planar interface. I therefore describe the $\Lambda \ll \theta_{L\infty}$ limit as the *Stefan regime*. The regimes are defined fully in table 3.1.

The investigation also showed (§3.2.2c) that the growth rates, $\lambda(\mathcal{S}_t)$, can be roughly approximated by $\lambda(0)\, M\left({\theta_{L\infty}}^{3/2}/\Lambda^{2/3}\ \mathcal{S}_t\right)$ (figure 3.12, with eqs. 3.2.5 and 3.2.6). Here, the amplitude of the curve, $\lambda(0)$ is the growth rate for $\mathcal{S}_t = 0$, and $M(\mathcal{S}_t)$ is given by solving the corresponding Stefan problem for solid growth in a pure fluid. The approximation for the scaling factor, $p \approx {\theta_{L\infty}}^{3/2}/\Lambda^{2/3}$ (3.2.6), is a good match to the emperical results (figure 3.13) and measures the relative amount of latent heat release on the growth rate, at constant Stefan number. Increasing the liquidus gradient decreases this scaling factor, which makes any latent heat release less significant and so increases the growth rate. Increasing the initial liquidus temperature increases the scaling factor, which makes latent heat release more significant, but does not necessarily translate to a decreased growth rate since $\theta_{L\infty}$ also affects the amplitude of the growth rate, $\lambda(0)$.

I also considered the effects of imperfect thermal conduction on the growth of a mushy layer (§3.3.2). Slow surface cooling delays the onset of solidification (figure 3.14), and there is a subsequent adjustment period between this first solidification and the mushy layer approaching a self-similar state (figures 3.15 and 3.17). In the high liquid fraction regime, $\Lambda \gg 0.3\theta_{L\infty}$, the size of this adjustment period was shown to increase as either the mushy diffusivity factor, $m = \sqrt{1+\mathcal{S}_c}$, or initial liquidus temperature increases (figure 3.16, as characterised by eq. 3.3.5). In the Stefan regime, $\Lambda \ll 0.3\theta_{L\infty}$, we saw a delay in the appearance of the low-porosity region and an acceleration in the growth rate corresponding to its late formation. This is particularly significant because it means that the whole of the mushy layer will have a high porosity for suitably short times, regardless of final state, and was of importance later in §5.5 when considering convective instability.

Comparisons were made to the experimental results of Wettlaufer et al. (1997) (§3.2.2d) and Notz and Worster (2008) (§3.3.2d). Modelled ice depths were approximately 10% lower than those observed by Wettlaufer et al. (1997), with equal thermal properties used in this comparison. Much better agreement was found when comparing ice depths with Notz and Worster (2008) using unequal thermal properties. This suggests unequal thermal properties are important for faithfully reproducing observations. The comparison with Notz and Worster (2008) also indicated that imperfect conduction effects are significant on the timescales

involved in sea ice growth, with the modelled surface temperature continuing to evolve over the six day period and showing a similar underling trend to that observed, although missing the temporal fluctuations of conditions present in the environment. Qualitative comparison suggested that the model presented in this work underestimated the amount of internal solidification which occurs, but we note this is likely due to convective salt drainage which is neglected in our diffusive model.

6.1.2 Convection in a Deep Porous Layer

The second branch of research (chapter 4) considered the onset of convection in a suddenly cooled porous layer and how this convective onset is affected by changing the effective thermal conductivity of the boundary. To do this, I focused on a deep porous medium with a uniform permeability (neglecting the solidification dynamics of mushy layers) in order to build fundamental insight into how the Biot number can affect stability. The results could also be used in geophysical applications, such as carbon sequestration, groundwater convection, or industrial applications.

Following Slim and Ramakrishnan (2010), an energy stability method was used to assess stability, with the method giving the maximum possible growth rate for a perturbation that obeys the dynamical equations. The linearised dynamical equations were also used in interpreting the results. In this setting, changing the Biot number, $\tilde{\mathcal{B}}_i$, can affect the system in two primary ways. Firstly, it directly alters the boundary conditions (4.2.6a), and hence changes the amount of resistance the boundary imparts on the perturbation. Secondly, it alters the base-state temperature profile which is driving the convection (2.5.1). In particular, this second contribution changes the temperature difference within the fluid, since the surface temperature decreases as $\tilde{\mathcal{B}}_i$ increases, and also changes the temperature structure.

I found that decreasing the effective thermal conductivity of the overlying heat sink (decreasing $\tilde{\mathcal{B}}_i$) causes an increase in the critical Rayleigh number (figure 4.2b), meaning that it is harder to drive convection with smaller cooling rates or at shorter times. This effect is primarily due to the changing background profile and most notably, the changing temperature difference across the fluid. For very small Biot number, we recover $\tilde{\mathcal{R}}_p \propto 1/\tilde{\mathcal{B}}_i$ because the temperature range in the fluid and hence the amount of potential energy in the system is proportional to the Biot number. Changes to the temperature structure and the perturbation boundary conditions are also contributing factors. The former of these acts to increase the critical Rayleigh

number by shifting the distribution of available energy closer to the surface, limiting the vertical extent of the convection. However, the latter acts to decrease the critical Rayleigh number by reducing the resistance from the boundary, as seen in a fixed depth setting by Barletta et al. (2015) and others. Of these two effects, the profile changes have a greater impact for large Biot numbers, but the boundary condition changes have a greater impact for small Biot numbers. The critical Rayleigh number can also be inverted to find the physical onset time (figure 4.5a) with the onset time always increasing as the boundary Rayleigh number, $\mathcal{R}_B = \mathcal{R}_p/\mathcal{B}_i = g\alpha\Delta T\hat{\Pi}_0 k/\kappa\nu\mathfrak{h}$ (4.4.4), increases. Unlike $\tilde{\mathcal{B}}_i$ and $\tilde{\mathcal{R}}_p$, this combination is independent of time and it indicates how far buoyancy anomalies can propagate relative to the boundary lengthscale, $\hat{d}_b = k_l/\mathfrak{h}$. Decreasing the boundary lengthscale represents a more efficient heat sink at the upper boundary, and hence increases the Biot number, $\tilde{\mathcal{B}}_i$, and decreases $\mathcal{R}_B$. Limiting approximations to the onset time are given in (4.4.3) and (4.4.6).

The critical wavenumber also depends on cooling efficiency. Decreasing the effective conductivity of the boundary initially caused a small increase in critical wavenumber, $\tilde{\mathrm{k}}_c$ (scaled by the diffusion lengthscale), before the wavenumber decreases as the Biot number decreased for small $\tilde{\mathcal{B}}_i$ (figure 4.2a). The initial increase is due to the changes in temperature structure moving the distribution of available energy closer to the surface, which limits the vertical extent of convection and results in a slight narrowing of convective cells. The boundary conditions act to decrease the wavenumber throughout, and while they are not significant enough to overcome the changes due to the profile structure for $\tilde{\mathcal{B}}_i \gg 1$, they become the dominating factor for $\tilde{\mathcal{B}}_i \ll 1$, leading to $\tilde{\mathrm{k}}_c \sim 0.73\sqrt{\tilde{\mathcal{B}}_i}$. In this regime, the convective cells are much wider and deeper than for large Biot numbers (figure 4.3) but the mechanism responsible for these changes eluded explanation. The physical onset wavenumber, $\hat{\mathrm{k}}_i$, always decreases as $\mathcal{R}_B$ increases (figure 4.5b), regardless of the non-monotonic behaviour of the scaled wavenumber, $\tilde{\mathrm{k}}_c$. This is due to the increased onset time allowing the thermal diffusion lengthscale to grow more, decreasing $\tilde{\mathrm{k}}_c$ faster than the non-monotonic behaviour increases it. Limiting approximations for $\hat{\mathrm{k}}_i$ are given in (4.4.5) and (4.4.7).

This investigation has shown us that the effects of imperfect boundary conduction can have a noticeable impact on the stability of porous layers, both by changing the amount and distribution of potential energy available, and by changing the resistance experienced from the boundary.

6.1.3 Convection in Growing Mushy Layers

The final branch of research investigated convective onset in growing mushy layers cooled from above, making use of a linear stability analysis and parametrising the underlying liquid layer through an isothermal, mush-liquid boundary at constant pressure. To remove the effects of the changing growth rates, the Rayleigh number and wavenumber were rescaled using the mushy layer thickness, rather than the thermal diffusion lengthscale (5.1.6).

When considering the stability properties as a function of the dimensionless liquidus gradient, I found that both the critical Rayleigh number and critical wavenumber tend to constant values for large dimensionless liquidus gradients, but increase sharply as the dimensionless liquidus gradient decreases for small Λ (figures 5.2 and figure 5.3). In the high liquid fraction regime, the porosity becomes increasingly uniform as Λ increases and the temperature also tends to a constant structure, resulting in the stability properties approaching a corresponding asymptotic limit. However, in the Stefan regime, most of the mushy layer has a low porosity with a high resistance to flow. Convection is confined to the small high porosity region of thickness Λ. With order-one aspect ratio convective cells, this yields $\tilde{\mathrm{k}}_c \propto 1/\Lambda$ for $\Lambda \ll 1$ (5.2.1b). Reducing the thickness of the convective cells by a factor of Λ also reduces the temperature difference across the convection pattern by a factor of Λ. These factors combine to give the $\tilde{\mathcal{R}}_m^* \propto 1/\Lambda^2$ behaviour in the Stefan regime (5.2.1a). The resulting changes to the convective patterns as the liquidus gradient increases are shown in figure 5.4.

I also demonstrated that the effect of the Stefan number on convection depends on the value of the dimensionless liquidus gradient. For large values of the dimensionless liquidus gradient, an increase in the Stefan number increases the critical Rayleigh number (figure 5.7a). This is because an increase in the Stefan number results in more latent heat release near the upper surface, which slows thermal transport through from the lower ice and concentrates the thermal gradients near the surface (figure 5.7b). The resulting perturbation is focussed near the surface where it interacts more strongly with the restrictive no-normal flow boundary and less strongly with the more liberal constant-pressure boundary. This increases the boundary resistance to convection and increases stability. For small values of the liquidus gradient, increasing the Stefan number has the opposite effect and decreases the Rayleigh number (figure 5.8a). The focussing of temperature gradients near the upper ice surface results in a relative warming of the mushy layer close to the

mush-liquid interface, which increases the liquid fraction (figure 5.8b) and reduces the resistance to flow in the lower ice. This enhances the tendency for convection.

To investigate the effects of imperfect thermal boundary conduction, I considered case studies in both the high liquid fraction regime and the Stefan regime. In the high liquid fraction regime, the critical Rayleigh number decreases as the Biot number (and hence time) is increased and there is a small increase in the critical wavenumber (figure 5.9). The decreasing Rayleigh number is primarily due to the gradual cooling of the surface over time, which results in an increasing temperature difference across the mushy layer and increased thermal forcing as time progresses. There is also a small contribution from the changing boundary conditions, temperature profile, and liquid fraction profile (see local Rayleigh number, figure 5.9a), which act together to increase the resistance to convection and increase the wavenumber. The behaviour is noticeably different in the Stefan regime where increasing the Biot initially causes $\tilde{\mathcal{R}}_m^*$ to decrease, before it increases back up towards a limit (figure 5.10a). This is accompanied by a much more dramatic increase in the critical wavenumber (figure 5.10b). In the Stefan regime, the mushy layer starts off with high porosity throughout its depth, before developing the low-porosity region in the upper portion of the ice at later times (figure 3.17). The porosity is initially high throughout the ice so there is little resistance to flow, but the temperature difference across the layer is also small so there is little forcing. At early times, the increase of the temperature difference over time has the greater affect on the stability, leading to a decrease in $\tilde{\mathcal{R}}_m^*$ as $\tilde{\mathcal{B}}_i$ and time increase. At later times, the low-porosity region forms and begins to restrict convective flow to the high porosity interfacial region. This restriction on the flow then begins to dominate the dynamics and causes the later increase in $\tilde{\mathcal{R}}_m^*$ over time. For the setup presented, the balance between the two competing effects occurs when $\tilde{\mathcal{B}}_i = 2.9$ and the minimum critical Rayleigh number is 6700, which occurred just after the surface liquid fraction had dropped below 50%. As the low porosity region develops, it causes convective confinement near the mush-liquid interface, which causes an increase in the critical wavenumber, with the convective cells limited in vertical extent and maintaining an order-one aspect ratio.

We finished with a discussion of convection during ice growth in the field, focussing on conditions observed by Notz and Worster (2008), which provides insight into sea ice growth. The critical Rayleigh number, $\tilde{\mathcal{R}}_m^*$, varies non-monotonically with Biot number, $\tilde{\mathcal{B}}_i$, which means that the critical thickness for convective onset also varies

non-monotically over time (figure 5.11). The minimum critical Rayleigh number occurs for $\tilde{\mathcal{B}}_i = 0.6$. By plotting ice growth trajectories, it was shown that increasing the wind speed decreases the critical ice thickness at which convection will start, for wind speeds up to a threshold which varies from 2m/s to 16m/s, depending on the permeability estimate used. Beyond this threshold, the critical ice thickness will increase as the wind speed increases. Converting the onset ice thicknesses into times, reveals that higher wind speeds (greater cooling) result in convective onset occurring sooner (figure 5.12a), although there is again a threshold in wind speed where upon the onset time increases with wind speed again (figure 5.13a). This threshold for the onset time is different (and roughly double) the threshold for the onset depth, and also depends on the permeability used. The onset wavelengths showing a similar behaviour to the critical onset time (figure 5.12b). Using a permeability of $2.2 \times 10^{-9}\text{m}^2$ (Rees Jones and Worster, 2014), convective onset for the observed wind speed of 2m/s would be predicted to occur after 4h40min, when the ice would be 2.3cm thick.

6.1.4 Overall Summary

This thesis has investigated the growth and convective onset of mushy layers over a wide range of parameters. Of the various non-dimensional parameters investigated, the dimensionless liquidus gradient and the Biot number were found to be the most dynamically significant.

The dimensionless liquidus gradient measures the relative sizes of the thermal and salinity scales and was shown to significantly affect the amount of internal solidification which occurs and the localisation of the high-porosity region, with two limiting regimes explored and a transitional region between the them. This control over the internal solidification often controls the response of the system to changes in other parameters, most notably the Stefan number. For the initial growth of sea ice, the dimensionless liquidus gradient is likely to fall in the transitional region where the low-porosity region has begun to form, but a significant proportion of the ice retains a high porosity.

The Biot number is a measure of the effective thermal conductivity of the surface boundary, relative to the rate of thermal conduction within the system. During the transient growth considered here, it depends on the thermal diffusion lengthscale and therefore increases with time. Imperfect conduction results in slow cooling of the surface layer and a surface temperature which evolves over time. This impacts

both the ice depth and internal solidification with less ice and less solidification at short times than would be expected for a perfectly conducting boundary. The changing structure also impacts the onset of convection, with the early period of low internal solidification providing an optimal window for convective onset. Comparison with conditions from field observations revealed these effects to have a noticeable influence on the growth and development of sea ice in a natural setting. The Biot number can also impact convective onset by changing the boundary resistance which perturbations experience, and this was shown to have a large effect on the wavenumber in deep, uniformly porous system.

6.2 Implications

This study has provided insight into how the growth, structure, and convective onset of mushy layers are affected by changing conditions, and the results have wide ranging implications for sea ice and beyond.

I have shown that the porosity structure of the ice varies with the external conditions and this has direct implications for the mechanical properties of the sea ice. It will also affect the electromagnetic properties of the sea ice, such as its permittivity, which is used for in situ measurements and remote sensing (Petrich and Eicken, 2010). There will also be an effect on the exchange of chemical tracers, such as dissolved gasses, between the ocean and the atmosphere (Weeks, 2010). I have developed understanding of the extent of the high-porosity skeletal layer, which is a known feature of sea ice and provides a habitat for algae and other species (Krembs et al., 2001). Chapter 3 focussed on ice grown diffusively and continuously from a fixed boundary, but the key physical concepts are transferrable and might also be applied to ice growth after or between convective episodes. For example, desalinated sea ice would behave similarly to ice grown with a reduced initial salinity $\hat{S}_\infty$, which would decrease Λ and result in increased internal solidification and a smaller high-porosity region. Accounting for spatially and temporally varying $\hat{S}_\infty$ represents an interesting challenge, that is currently pursued with parameterised models (see review by Worster and Rees Jones, 2015).

My results for convective onset are qualitatively consistent with observations of convection in the high porosity region at the base of the ice (e.g. Notz and Worster, 2008, 2009) and have a number of implications. Firstly, it is often argued that a percolation threshold controls the restriction of fluid flow through the ice (Golden

et al., 2007). For liquid fractions below $\chi = 0.05$, the pores become too disconnected for fluid motion to occur. However, I have demonstrated that convective confinement can be alternatively explained by simple thermodynamic behaviour that results in a localisation of high permeability, and that meaningful convection ceases before the porosity drops to 0.05. The results also provide insight for parametrisations of convection by providing theoretical support for the idea that convection will be most active where a localised Rayleigh number exceeds some threshold (Worster and Rees Jones, 2015). Finally, convection is also necessary to keep life within the ice supplied with vital nutrients (Vancoppenolle et al., 2013). My results for convective onset shed light on when this process can be expected to start and how far it will penetrate into the ice, thus giving some indication of the regions which can be biologically active.

There are also wider implications for geophysical and industrial settings. For industrial solidification, it is desirable to control the material properties and in particular to minimise defects, which often arise from convection in the melt (Copley et al., 1970). My results could be used to help tune the cooling conditions and quench times to maximise uniformity and minimise the potential for convection, or otherwise controlling the relative fraction of the two components. The discussion of convection in reactive media undergoing phase changes is also helpful in geological settings, such as cooling magma chambers (Worster et al., 1990), or potentially the edge of the Earth's inner core (Bergman and Fearn, 1994). Finally, chapter 4 on convection in unreactive porous media also has geophysical applications and could be used to better understand carbon sequestration (Hassanzadeh et al., 2006), or ground water convection (van Dam et al., 2009).

6.3 Suggestions for Future Work

There are a number of ways the understanding from the diffusive solidification model can be enhanced. While quantitative scalings were identified for the growth rate as a function of $\mathcal{S}_t$, Λ and $\theta_{L\infty}$ and explained qualitatively, the physical origin of the approximate scaling exponents in the grouping $\mathcal{S}_t\ {\theta_{L\infty}}^{3/2}/\Lambda^{2/3}$ remains unclear. Given the complex internal structures discussed in chapter 3, it is also surprising that a single functional form collapses the growth rate data over such a wide range of Λ and $\theta_{L\infty}$. Finally, there is scope for better a characterisation of the scalings for the adjustment period for imperfect boundary conduction, particularly surrounding

the acceleration in growth rate observed in the Stefan regime.

Incremental advances could be made in the realism of the sea ice growth model, such as systematically exploring the impact of unequal thermal properties, which was demonstrated to affect the growth rate. Analysis with the simple model showed that salt diffusion has a modest effect on the growth rate and including this feature in the more complex model could reveal interesting behaviour, at the cost of greater computational complexity in the numerical method. It should be noted that the inclusion of salt diffusion predicts a fully solid layer at the surface, which has interesting implications for tracer transport, since it would form an impermeable barrier. The model also considered thermal forcing which remained constant over the time period investigated, but it could also be informative to consider a linearly decreasing heat sink temperature, sinusoidal variation around some low average, or forced by a spectrum of temporal fluctuations to build insight into the significance of variability in the environmental conditions.

The convection model used has some limitations, which were shown most clearly in the comparison to Wettlaufer et al. (1997). A particular weakness was the inability of the linear analysis to capture subcritical and non-linear behaviour, which are known to be relevant to channel formation. Modelling subcritical behaviour would either require a weakly non-linear analysis (such as that performed by Amberg and Homsy, 1993, for steady-state growth) or direct numerical simulation. A preliminary attempt at the latter was made as part of this investigation, but I found that the accurate computation of stability boundaries requires high resolution in order to resolve small deflections to the mush-liquid interface. This results in significant computational expense to produce the necessary ensembles of simulations and so was not pursued further here but may be an interesting opportunity for future development. Finite-amplitude methods, such as the energy method used in chapter 4, are also a possible route for investigation if the mushy layer equations can be manipulated into an appropriate form.

While less relevant to sea ice dynamics, there are also a number of ways that the investigations of convection in a deep, unreactive porous medium (chapter 4) could be pursued further. On a theoretical level, the mechanism which produces the scaling $\tilde{\mathrm{k}}_c \propto \sqrt{\tilde{\mathcal{B}}_i}$ is unclear and understanding this could help shed further light on the nature of the problem. Similarly, considering a permeable or semi-permeable upper boundary in conjunction with the imperfectly conducting boundary will

provide some indication of how well the results of Barletta et al. (2015) translate to this new setting. More practically, it would be interesting to examine the evolution of convection after the onset of instability. This could be pursued by direct numerical simulation and would also allow investigation of properties such as the Nusselt number, which measures the rate of heat transfer by convection.

Appendices

A Nomenclature

This section is intended as a reference guide to the nomenclature used by this thesis. Symbols are grouped according to their definitions.

A.1 Modifiers

$\hat{X}$	Where a quantity, X, is represented in both dimensional and dimensionless values, a hat indicates that X has dimensions. Quantities without a hat are dimensionless.
$\tilde{X}$	Where a quantity is described or measured in both the lab coordinates and self-similar coordinates, a tilde indicates measurement in the self-similar coordinates.
X_l	Denotes that X is measured in the liquid phase.
X_s	Denotes that X is measured in the solid phase.
X_a	Denotes that X is measured in the atmosphere.
$\overline{X}$	Indicates that X is phase-weighted, $\overline{X} = \chi X_l + \phi X_s$, where χ is the liquid fraction and ϕ is the solid fraction.
r_X	Denotes the ratio of X in the solid phase to the liquid phase, $r_X = X_s/X_l$.
X_B	Denotes the base state profile of X.
X_p	Denotes a perturbation profile of X.
X_f	Denotes a Fourier-transformed perturbation profile of X.

A.2 Physical Quantities

α	Thermal expansivity.
β	Saline expansivity.
C_s	Sensible heat transfer shape coefficient.
c_p	Specific heat capacity.
D	Salt diffusivity.
g	Acceleration due to gravity.
$\mathfrak{h}$	Thermal transfer coefficient for surface cooling.
k	Thermal conductivity.
κ	Thermal diffusivity.
L	Latent heat.
Γ	Physical liquidus gradient.
ρ	Density.
u_w	Atmospheric wind speed.
ν	Viscosity.

A.3 Coordinates, Physical Lengths and Physical Times

$\hat{d}$	The length scale used to non-dimensionalise lengths and times.
t	Time since onset of cooling. Dimensional form: $\hat{t} = t\hat{d}^2/\kappa$.
x	Horizontal position. Dimensional form: $\hat{x} = \hat{d}x$. Made self-similar by $x = \tilde{x}\sqrt{t}$.
z	Depth. Dimensional form: $\hat{z} = \hat{d}z$. Made self-similar by $z = \tilde{z}\sqrt{t}$
$\boldsymbol{\nabla}$	Vector derivative operator. Dimensional form: $\hat{\boldsymbol{\nabla}} = 1/\hat{d}\ \boldsymbol{\nabla}$.
$\boldsymbol{e_x}$	Horizontal unit vector.
$\boldsymbol{e_y}$	In-to-page unit vector.
$\boldsymbol{e_z}$	Vertical unit vector.
$\boldsymbol{n}$	Unit vector in the normal direction.
$\hat{b}$	A nominal domain depth, large enough to be considered infinite for all practical purposes.
h	The depth of the interface between mush and liquid. Dimensional form: $\hat{h} = \hat{d}h$.

λ Self-similar interface position. Also referred to as the *growth rate* since $\partial h/\partial t = \lambda/2\sqrt{t}$ for self-similar growth.
Defined by: $h = \lambda\sqrt{t}$.

$\hat{h}_c$ The critical mushy layer depth for linear convective instability.

$\hat{t}_i$ The critical time for onset of convection.

A.4 Profiles and Reference Values

χ Liquid fraction.

ϕ Solid fraction.

T Dimensional temperature. (N.B. No hat)

T_c The temperature of the surface heat sink.

T_∞ The initial temperature, and temperature of deep fluid.

ΔT The temperature difference across the domain, $T_\infty - T_c$.

T_S Temperature of the surface of the mushy layer.

T_{la} Temperature of the lower atmosphere.

T_{ua} Temperature of the upper atmosphere.

θ Dimensionless temperature.
Dimensional form: $T = \Delta T\theta + T_c$.

T_L Dimensional liquidus temperature.

$T_{L\infty}$ Dimensional liquidus reference temperature (Dimensionless form in §A.5).

θ_L Dimensionless liquidus temperature.
Dimensional form: $T_L = \Delta T\theta_L + T_c$.

$\hat{S}_\infty$ The initial salinity, and salinity of deep fluid.

S Salinity.
Dimensional form: $\hat{S} = \hat{S}_\infty S$.
Used as the salinity scale.

$\Delta\hat{S}$ An arbitrary salinity scale. Used when $\hat{S}_\infty$ is inappropriate.

H Enthalpy.
Dimensional form: $\hat{H} = c_{pl}\,(H\Delta T - T_c)$

$\boldsymbol{u}$ Velocity vector.
Dimensional form: $\hat{\boldsymbol{u}} = \kappa/\hat{d}\ \boldsymbol{u}$.

ψ Stream function.
Dimensional form: $\hat{\psi} = \kappa/\hat{d}^2\ \psi$.

p Pressure.
Dimensional form: $\hat{p} = \rho_0 g\alpha\Delta T\hat{d}\,(p - zT_c/T_\infty)$.

$\hat{\Pi}_0$ Dimensional permeability reference value.

Π Permeability.
Dimensional form: $\hat{\Pi} = \hat{\Pi}_0 \Pi$.

μ A lagrange multiplier field.

A.5 Dimensionless Quantities and Characteristic Lengths

$\mathcal{R}_a$ Thermal Rayleigh number for a liquid material.

$\hat{d}_c$ The convective length scale associated with thermal convection in a liquid.

$\hat{t}_c$ The convective time scale associated with thermal convection in a liquid.

$\mathcal{R}_p$ Thermal Rayleigh number for a porous material.
Made self-similar by $\tilde{\mathcal{R}}_p = \mathcal{R}_p \sqrt{t}$ (also applies to derived quantities).

$\hat{d}_p$ The convective length scale associated with thermal convection in a porous medium.

$\hat{t}_p$ The convective time scale associated with thermal convection in a porous medium.

$\mathcal{R}_m$ Thermohaline Rayleigh number for a porous medium or mushy layer.

$\hat{d}_m$ The convective length scale associated with thermohaline convection in a porous medium.

$\hat{t}_m$ The convective time scale associated with thermohaline convection in a porous medium.

$\mathcal{R}_c$ Critical thermal Rayleigh number for a porous material.

$\mathcal{R}_{p\infty}$ Thermal Rayleigh number for a porous material with infinite Biot number.

$\mathcal{R}_B$ Thermal Rayleigh number defined on the boundary length scale.

$\mathcal{R}_{pl}$ 'Local' thermal Rayleigh number for a porous material, defined using only the temperature range within the porous layer.

$\tilde{\mathcal{R}}^*_m$ 'Scaled' thermohaline Rayleigh number, defined using the thickness of the mushy layer.

$\tilde{\mathcal{R}}^*_{m,l}$ 'Scaled' 'local' thermohaline Rayleigh number, defined using the thickness of the mushy layer and the temperature range within the mushy layer.

k Convective wavenumber.

k_c Critical convective wavenumber.

k_∞ Critical convective wavenumber for infinite Biot number.

$\tilde{\mathrm{k}}^*$	Convective wavenumber, relative to the mushy layer depth.
Λ	Dimensionless liquidus gradient.
$\theta_{L\infty}$	Dimensionless liquidus reference. Dimensional form: $T_{L\infty} = \Delta T \theta_{L\infty} + T_c$.
$\mathcal{B}_i$	Biot number. Made self-similar by $\tilde{\mathcal{B}}_i = \mathcal{B}_i \sqrt{t}$.
$\tilde{\mathcal{B}}_f$	Self-similar Biot number at first freezing.
$\hat{d}_b$	Boundary cooling length scale associated with the Biot number.
$\hat{t}_b$	Boundary cooling time scale associated with the Biot number.
$\mathcal{S}_t$	Stefan number.
$\mathcal{S}_c$	Compositional Stefan number.
$\mathcal{D}_a$	Darcy number.
$\mathcal{L}_e$	Lewis number.
s	The saline diffusivity factor, $s = \sqrt{\mathcal{L}_e}$.
$\mathcal{P}_r$	Prandtl number.
κ^m	Ratio of the thermal diffusivity in mushy layer relative to standard thermal diffusivity.
m	The mushy diffusivity factor, $m = 1/\sqrt{\kappa^m}$.
β^*	Compressibility ratio.
ω	Thermal lag parameter.
$\mathcal{C}$	Concentration ratio / "curly C".
θ_∞	Dimensionless superheat.

A.6 Miscellaneous

F_{LW}^{out}	Outbound, longwave radiative flux.
F_{LW}^{in}	Inbound, longwave radiative flux.
F_{SW}	Net, shortwave radiative flux.
F_{SH}	Sensible heat flux.
F_{LH}	Latent heat flux.
F_C	Conductive thermal flux (in mushy layer).
F_O	Oceanic heat flux
F_{Sal}	Surface salt flux.
σ_{sb}	Stefan-Boltzmann constant.
ϵ	Longwave radiative emissivity.
Υ	Function representing the general solution to the fixed chill diffusion equation with imperfect conduction.

$\bar{\Upsilon}$	A reduced form of the diffusion equation general solution for $t = 1$ and $\mathcal{B}_i \to \infty$.
A	A parameter used in constructing the simple model of diffusive growth.
t_{sa}	The time scale for salt addition to the domain through the surface boundary.
f_χ	Fraction of the depth with $\chi > 0.5$, measured from the interface.
p	The parameter used for fitting Stefan curves.
$M(\mathcal{S}_t)$	The functional form of the Stefan curves.
q	A parameter used for measuring the size of the adjustment region for diffusive growth with imperfect conduction.
$\hat{V}$	The volume that the domain occupies.
$\partial\hat{V}$	The surface of the domain.
σ	Growth rate of perturbation or energy functional.
$\sigma_{\max}$	Maximal growth rate of energy functional.
c_λ	The confinement depth, at which convection becomes negligible.
c_χ	The confinement liquid fraction, defined as the liquid fraction at the confinement depth.
c_θ	The confinement temperature, defined as the temperature at the confinement depth.

Bibliography

Ryan P. Abernathey, Ivana Cerovecki, Paul R. Holland, Emily Newsom, Matt Mazloff, and Lynne D. Talley. Water-mass transformation by sea ice in the upper branch of the Southern Ocean overturning. *Nature Geosci*, 9(8):596–601, aug 2016. ISSN 1752-0894. doi: 10.1038/ngeo2749.

Kenneth S. Alexander, Marek Biskup, and Lincoln Chayes. Colligative Properties of Solutions: I. Fixed Concentrations. *Journal of Statistical Physics*, 119(3):479–507, May 2005. ISSN 1572-9613. doi: 10.1007/s10955-005-3016-2.

Gustav Amberg and G. M. Homsy. Nonlinear analysis of buoyant convection in binary solidification with application to channel formation. *Journal of Fluid Mechanics*, 252:79–98, 1993. doi: 10.1017/S0022112093003672.

D. M. Anderson and M. G. Worster. A new oscillatory instability in a mushy layer during the solidification of binary alloys. *J. Fluid Mech.*, 307:245–267, 1996.

Edgar L. Andreas. Estimation of Mass and Heat Fluxes Over Arctic Leads. *Monthy Weather Rev.*, 108:2057–2063, December 1980.

Kevin R. Arrigo, Thomas Mock, and Michael P. Lizotte. Primary Producers and Sea Ice. In Thomas and Dieckmann (2010), chapter 8.

A. Assur. Composition of sea ice and its tensile strength. *U.S. Army Snow, Ice, and Permafrost Research Establishment*, 1960.

Pascale Aussillous, Andrew J. Sederman, Lynn F. Gladden, Herbert E. Huppert, and M. Grae Worster. Magnetic resonance imaging of structure and convection in solidifying mushy layers. *J. Fluid Mech.*, 552:99–125, 2006. doi: 10.1017/S0022112005008451.

A. Barletta and L. Storesletten. Onset of convective rolls in a circular porous duct with external heat transfer to a thermally stratified environment. *International Journal of Thermal Sciences*, 50(8):1374–1384, 2011. doi: 10.1016/j.ijthermalsci.2011.03.010.

A. Barletta and L. Storesletten. Effect of a finite external heat transfer coefficient on the Darcy-Bénard instability in a vertical porous cylinder. *Phys. Fluids*, 25(4), 2013. doi: 10.1063/1.4799253. 044101.

Antonio Barletta, Peder A. Tyvand, and Heidi S. Nygård. Onset of thermal convection in a porous layer with mixed boundary conditions. *Journal of Engineering Mathematics*, 91(1):105–120, 2015. doi: 10.1007/s10665-014-9745-y.

Gordon S. Beavers and Daniel D. Joseph. Boundary conditions at a naturally permeable wall. *Journal of Fluid Mechanics*, 30(1):197–207, 1967. doi: 10.1017/S0022112067001375.

Michael I. Bergman and David R. Fearn. Chimneys on the Earth's inner-outer core boundary? *Geophysical Research Letters*, 21(6):477–480, 3 1994. ISSN 1944-8007. doi: 10.1029/94GL00028.

Bodil A. Bluhm, Rolf R. Gradinger, and Sigrid B Schnack-Schiel. Sea Ice Meio- and Macrofauna. In Thomas and Dieckmann (2010), chapter 10.

M. A. Brandon, F. R. Cottier, and F. Nilsen. Sea ice and oceanography. In Thomas and Dieckmann (2010), chapter 3.

M. I. Budyko. The effect of solar radiation variations on the climate of the Earth. *Tellus*, 21(5):611–619, 1969. ISSN 2153-3490. doi: 10.1111/j.2153-3490.1969.tb00466.x.

S. L. Butler. Effective transport rates and transport-induced melting and solidification in mushy layers. *Physics of Fluids*, 23(1):016602, 2011. doi: 10.1063/1.3541840.

Jean-Paul Caltagirone. Stabilty of a Saturated Porous Layer Subject to a Sudden Rise in Surface Temperature: Comparison Between the Linear and Energy Methods. *The Quarterly Journal of Mechanics and Applied Mathematics*, 33 (1):47–58, 1980. doi: 10.1093/qjmam.

H. S. Carslaw and J. C. Jaeger. *Conduction of Heat in Solids*. Oxford University Press, 1959.

Jinlong Chao, Chengyu Liu, Yingjun Xu, Wei Gu, Ying Li, and Feng Xie. Multi-angular thermal infrared emission characteristics of Bohai Sea ice based on in situ measurements. *Journal of Glaciology*, 61(229):864–874, 2015. doi: 10.3189/2015JoG14J143.

F. Chen and C. F. Chen. Onset of finger convection in a horizontal porous layer underlying a fluid layer. *ASME Transactions Journal of Heat Transfer*, 110: 403–409, May 1988. doi: 10.1115/1.3250499.

Falin Chen and C. F. Chen. Experimental investigation of convective stability in a superposed fluid and porous layer when heated from below. *Journal of Fluid Mechanics*, 207:311–321, 1989. doi: 10.1017/S0022112089002594.

Falin Chen and C. F. Chen. Convection in superposed fluid and porous layers. *Journal of Fluid Mechanics*, 234:97–119, 1992. doi: 10.1017/S0022112092000715.

A. O. P. Chiareli and M. Grae Worster. On measurement and prediction of the solid fraction within mushy layers. *J. Crystal Growth*, 125:487–494, 1992. doi: 10.1016/0022-0248(92)90288-T.

A.O.P. Chiareli, Herbert E. Huppert, and M.Grae Worster. Segregation and flow during the solidification of alloys. *Journal of Crystal Growth*, 139(1):134–146, 1994. ISSN 0022-0248. doi: 10.1016/0022-0248(94)90038-8.

J. C. Comiso. Variability and trends of the global sea ice cover. In Thomas and Dieckmann (2010), chapter 6.

S. M. Copley, A. F. Giamei, S. M. Johnson, and M. F. Hornbeck. Origin of freckles in unidirectionally solidified castings. *Metallurgical Transactions*, 1:2193–2204, 1970. doi: 10.1007/BF03037879.

Finlo Cottier, H. Eicken, and P. Wadhams. Linkages between salinity and brine channel distribution in young sea ice. *Journal of Geophysical Research: Oceans*, 104(C7):15859–15871, 1999. ISSN 2156-2202. doi: 10.1029/1999JC900128.

Gerhard S. Dieckmann and Hartmut H. Hellmer. The Importance of Sea Ice: An Overview. In Thomas and Dieckmann (2010), chapter 10.

J.M. Dixon and F.A. Kulacki. Mixed convection in fluid-superposed porous layers. Part 1. Analysis. *International Journal of Heat and Mass Transfer*, 109:1289–1300, 2017a. ISSN 0017-9310. doi: 10.1016/j.ijheatmasstransfer.2017.01.123.

J.M. Dixon and F.A. Kulacki. Mixed convection in fluid superposed porous layers. Part 2: Experiments. *International Journal of Heat and Mass Transfer*, 109: 1301–1306, 2017b. ISSN 0017-9310. doi: 10.1016/j.ijheatmasstransfer.2017.02.028.

J.R. Dormand and P.J. Prince. A family of embedded Runge-Kutta formulae. *Journal of Computational and Applied Mathematics*, 6(1):19–26, 1980. doi: 10.1016/0771-050X(80)90013-3.

Elizabeth E. Ebert and Judith A. Curry. An intermediate one-dimensional thermodynamic sea ice model for investigating ice-atmosphere interactions. *Journal of Geophysical Research: Oceans*, 98(C6):10085–10109, 1993. ISSN 2156-2202. doi: 10.1029/93JC00656.

Hajo Eicken and Manfred A. Lange. Development and properties of sea ice in the coastal regime of the southeastern weddell sea. *Journal of Geophysical Research: Oceans*, 94(C6):8193–8206, 1989. doi: 10.1029/JC094iC06p08193.

H.d Emami-Meybodi, H. Hassanzadeh, C. P. Green, and J. Ennis-King. Convective dissolution of CO2 in saline aquifers: Progress in modeling and experiments. *International Journal of Greenhouse Gas Control*, 40:238–266, 2015. doi: 10.1016/j.ijggc.2015.04.003.

P. W. Emms and A. C. Fowler. Compositional convection in the solidification of binary alloys. *J. Fluid Mech.*, 262:111–139, 1994.

J. Ennis-King, I. Preston, and L. Paterson. Onset of convection in anisotropic porous media subject to a rapid change in boundary conditions. *Phys. Fluids*, 17, 2005. doi: 10.1063/1.2033911. 084107.

D. L. Feltham, M. G. Worster, and J. S. Wettlaufer. The influence of ocean flow on newly forming sea ice. *Journal of Geophysical Research*, 107(C2), 2002.

D. L. Feltham, N. Untersteiner, J. S. Wettlaufer, and M. G. Worster. Sea ice is a mushy layer. *Geophys. Res. Letters*, 33, 2006. doi: 10.1029/2006GL026290.

Daniel L. Feltham and M. Grae Worster. Flow-induced morphological instability of a mushy layer. *Journal of Fluid Mechanics*, 391:337–357, 1999. doi: 10.1017/S002211209900539X.

George E. Forsythe, Michael A. Malcolm, and Cleve B. Moler. *Computer Methods for Mathematical Computations*. Prentice Hall Professional Technical Reference, 1977. ISBN 0131653326.

Theodore D. Foster. Stability of a Homogeneous Fluid Cooled Uniformly from Above. *The Physics of Fluids*, 8(7):1249–1257, 1965. doi: 10.1063/1.1761393.

A. C. Fowler. The formation of freckles in binary alloys. *IMA J. App. Maths*, 35: 159–174, 1985.

J. Freitag. Untersuchungen zur Hydrologie des arktischen Meereises - Konsequenzen fur den kleinskaligen Stofftransport (in German). *Berichte zur Polarforschun*, 1999.

Nicholas R. Gewecke and Tim P. Schulze. Solid–mush interface conditions for mushy layers. *Journal of Fluid Mechanics*, 689:357–375, 2011. doi: 10.1017/jfm.2011.420.

K. M. Golden, H. Eicken, A. L. Heaton, J. Miner, D. J. Pringle, and J. Zhu. Thermal evolution of permeability and microstructure in sea ice. *Geophysical Research Letters*, 34(16), 2007. ISSN 1944-8007. doi: 10.1029/2007GL030447. L16501.

William G. Gray. A derivation of the equations for multi-phase transport. *Chemical Engineering Science*, 30(2):229–233, 1975. ISSN 0009-2509. doi: 10.1016/0009-2509(75)80010-8.

P.M Gresho and R.L Sani. The stability of a fluid layer subjected to a step change in temperature: Transient vs. frozen time analyses. *International Journal of Heat and Mass Transfer*, 14(2):207–221, 1971. ISSN 0017-9310. doi: 10.1016/0017-9310(71)90090-1.

Christian Haas, Andreas Pfaffling, Stefan Hendricks, Lasse Rabenstein, Jean-Louis Etienne, and Ignatius Rigor. Reduced ice thickness in Arctic Transpolar Drift favors rapid ice retreat. *Geophysical Research Letters*, 35(17):n/a–n/a, 2008. ISSN 1944-8007. doi: 10.1029/2008GL034457. L17501.

H. Hassanzadeh, M. Pooladi-Darvish, and D. W. Keith. Stability of a fluid in a horizontal saturated porous layer: effect of non-linear concentration profile, initial, and boundary conditions. *Transp. Porous Med.*, 65:193–221, 2006. doi: 10.1007/s11242-005-6088-1.

R. N. Hills, D. E. Loper, and P. H. Roberts. A Thermodynamically Consistent Model of a Mushy Zone. *The Quarterly Journal of Mechanics and Applied Mathematics*, 36(4):505, 1983. doi: 10.1093/qjmam.

Joseph Hitchen and Andrew J. Wells. The impact of imperfect heat transfer on the convective instability of a thermal boundary layer in a porous media. *Journal of Fluid Mechanics*, 794:154–174, 2016. doi: 10.1017/jfm.2016.149.

Roger A. Horn and Charles R. Johnson. *Matrix Analysis*. Cambridge University Press, 1985. ISBN 978-0-521-83940-2.

C. W. Horton and F. T. Rogers. Convection Currents in a Porous Medium. *Journal of Applied Physics*, 16(6):367–370, 1945. doi: 10.1063/1.1707601.

E. C. Hunke, D. Notz, A. K. Turner, and M. Vancoppenolle. The multiphase physics of sea ice: a review for model developers. *The Cryosphere*, 5(4):989–1009, 2011. doi: 10.5194/tc-5-989-2011.

Herbert E. Huppert. The fluid mechanics of solidification. *Journal of Fluid Mechanics*, 212:209–240, 1990. doi: 10.1017/S0022112090001938.

Herbert E. Huppert and M. Grae Worster. Dynamic solidification of a binary melt. *Nature*, 314:703–707, 1985. doi: 10.1038/314703a0.

D. T. J. Hurle, E. Jakeman, and E. R. Pike. On the solution of the Bénard problem with boundaries of finite conductivity. *Procedings of the Royal Society - Mathematical and Physical Sciences*, 296(1447):469–475, 1967. doi: 10.1098/rspa.1967.0039.

I. G. Hwang and C. K. Choi. Onset of compositional convection during solidification of a two-component melt from a bottom boundary. *J. Crystal Growth*, 267: 714–723, 2004.

I. G. Hwang and C. K. Choi. Onset of convection in a porous mush during binary solidification. *Korean J. Chem. Eng.*, 25(2):199–202, 2008.

I.G. Hwang and C.K. Choi. The onset of mushy-layer-mode instabilities during solidification in ammonium chloride solution. *Journal of Crystal Growth*, 220(3): 326–335, 2000. ISSN 0022-0248. doi: 10.1016/S0022-0248(00)00863-0.

In Gook Hwang. Stability analysis of compositional convection in a mushy layer in the time-dependent solidification system. *Korean Journal of Chemical Engineering*, 30(5):1023–1028, 2013. ISSN 1975-7220. doi: 10.1007/s11814-013-0013-z.

In Gook Hwang and Chang Kyun Choi. Stability of buoyancy-driven convection in directional solidification of a binary melt. *Korean Journal of Chemical Engineering*, 26(4):930–934, Jul 2009. ISSN 1975-7220. doi: 10.1007/s11814-009-0156-0.

Adrian Jenkins. Convection-Driven Melting near the Grounding Lines of Ice Shelves and Tidewater Glaciers. *Journal of Physical Oceanography*, 41(12):2279–2294, 2011. doi: 10.1175/JPO-D-11-03.1.

E.P. Jones, B. Rudels, and L.G. Anderson. Deep waters of the Arctic Ocean: origins and circulation. *Deep Sea Research Part I: Oceanographic Research Papers*, 42 (5):737–760, 1995. ISSN 0967-0637. doi: 10.1016/0967-0637(95)00013-V.

R. F. Katz and M. Grae Worster. Simulation of directional solidification, thermochemical convection, and chimney formation in a Hele-Shaw cell. *J. Comp. Phys*, 227(23):9823–9840, 2008. doi: 10.1016/j.jcp.2008.06.039.

Min Chan Kim and Chang Kyun Choi. Linear stability analysis on the onset of buoyancy-driven convection in liquid-saturated porous medium. *Physics of Fluids*, 24(4), 2012. doi: 10.1063/1.3703330.

Lubomír Klimeš, Tomáš Mauder, Pavel Charvát, and Josef Štětina. An accuracy analysis of the front tracking method and interface capturing methods for the solution of heat transfer problems with phase changes. *Journal of Physics: Conference Series*, 745(3):032136, 2016.

C. Krembs, T. Mock, and R. Gradinger. A mesocosm study of physical-biological interactions in artificial sea ice: effects of brine channel surface evolution and brine movement on algal biomass. *Polar Biology*, 24(5):356–364, May 2001. ISSN 1432-2056. doi: 10.1007/s003000000219.

J.P. Kubitschek and P.D. Weidman. Stability of a fluid-saturated porous medium heated from below by forced convection. *International Journal of Heat and Mass Transfer*, 46(19):3697–3705, 2003. doi: 10.1016/S0017-9310(03)00168-6.

R. Kwok and D. A. Rothrock. Decline in Arctic sea ice thickness from submarine and ICESat records: 1958-2008. *Geophysical Research Letters*, 36:L15501, 2009. doi: 10.1029/2009GL039035.

J. S. Langer. Instabilities and pattern formation in crystal growth. *Reviews of Modern Physics*, 52:1–28, January 1980. doi: 10.1103/RevModPhys.52.1.

E. R. Lapwood. Convection of a fluid in a porous medium . *Proc. Cam. Phil. Soc.*, 44:508–521, 1948.

M. Le Bars and M. Grae Worster. Interfacial conditions between a pure fluid and a porous medium: implications for binary alloy solidification. *J. Fluid Mech.*, 550: 149–173, 2006. doi: 10.1017/S0022112005007998.

D. R. Lide, editor. *Handbook of Chemistry and Physics*. CRC Press, 85 edition, 2005.

R. M. Lieb-Lappen and R. W. Obbard. The role of blowing snow in the activation of bromine over first-year Antarctic sea ice. *Atmospheric Chemistry and Physics*, 15(13):7537–7545, 2015. doi: 10.5194/acp-15-7537-2015.

P. F. Linden. Convection in the Environment. In G. K. Batchelor, H. K. Moffatt, and M. G. Worster, editors, *Perspectives in Fluid Dynamics*. Cambridge University Press, 2000. ISBN 0521531691.

Lord Rayleigh. On Convection Currents in a Horizontal Layer of Fluid, when the Higher Temperature is on the Under Side. *Phil. Mag. Series 6*, 1916.

Douglas G. Martinson. Evolution of the southern ocean winter mixed layer and sea ice: Open ocean deepwater formation and ventilation. *Journal of Geophysical Research: Oceans*, 95(C7):11641–11654, 1990. ISSN 2156-2202. doi: 10.1029/JC095iC07p11641.

G. A. Maykut. Energy exchange over young sea ice in the central Arctic. *J. Geophys. Res.*, 83(C7):3646–3658, 1978.

G. A. Maykut and N. Untersteiner. Some results a time-dependent from thermodynamic model of sea ice. *J. Geophys. Res.*, 76:1550–1575, 1971.

C. A. Middleton, C. Thomas, A. De Wit, and J.-L. Tison. Visualizing brine channel development and convective processes during artificial sea-ice growth using Schlieren optical methods. *Journal of Glaciology*, 62(231):1–17, 2016. doi: 10.1017/jog.2015.1.

M. A. Morales Maqueda, A. J. Willmott, and N. R. T. Biggs. Polynya Dynamics: a Review of Observations and Modeling. *Reviews of Geophysics*, 42(1), 2004. ISSN 1944-9208. doi: 10.1029/2002RG000116. RG1004.

J J Moré, B S Garbow, and K E Hillstrom. User guide for MINPACK-1. Technical Report ANL-80-74, Argonne Nat. Lab., Argonne, IL, Aug 1980.

W. W. Mullins and R. F. Sekerka. Stability of a Planar Interface During Solidification of a Dilute Binary Alloy. *Journal of Applied Physics*, 35(2):444–451, 1964. doi: 10.1063/1.1713333.

Jerome A. Neufeld and J. S. Wettlaufer. An experimental study of shear-enhanced convection in a mushy layer. *Journal of Fluid Mechanics*, 612:363–385, 2008. doi: 10.1017/S0022112008003339.

Terren M. Niedrauer and Seelye Martin. An experimental study of brine drainage and convection in Young Sea ice. *Journal of Geophysical Research: Oceans*, 84 (C3):1176–1186, 1979. ISSN 2156-2202. doi: 10.1029/JC084iC03p01176.

D. A. Nield. Onset of thermohaline convection in a porous medium. *Water Resources Res.*, 4(3), 1968.

D. A. Nield. Onset of convection in a fluid layer overlying a layer of a porous medium. *Journal of Fluid Mechanics*, 81(3):513–522, 1977.

D. Notz, J. S. Wettlaufer, and M. Grae Worster. A non-destructive method for measuring the salinity and solid fraction of growing sea ice in situ. *Journal of Glaciology*, 51(172), 2005.

Dirk Notz. *Thermodynamic and fluid-dynamical processes in sea ice.* PhD thesis, University of Cambridge, 2005.

Dirk Notz and M. Grae Worster. In situ measurements of the evolution of young sea ice. *J. Geophys. Res*, 113, 2008. doi: 10.1029/2007JC004333. C03001.

Dirk Notz and M. Grae Worster. Desalination processes of sea ice revisited. *J. Geophys. Res*, 114, 2009. doi: 10.1029/2008JC004885. C05006.

Heidi S. Nygård and Peder A. Tyvand. Onset of Convection in a Porous Box with Partly Conducting and Partly Penetrative Sidewalls. *Transport in Porous Media*, 84(1):55–73, 2010. doi: 10.1007/s11242-009-9484-0.

Nobuo Ono. Specific Heat and Heat of Fusion of Sea Ice. *Physics of Snow and Ice*, 1(1):599–610, 1967.

James E. Overland and Muyin Wang. When will the summer Arctic be nearly sea ice free? *Geophysical Research Letters*, 40(10):2097–2101, 2013. ISSN 1944-8007. doi: 10.1002/grl.50316.

S. S. L. Peppin, Herbert E. Huppert, and M. Grae Worster. Steady-state solidification of aqueous ammonium chloride. *Journal of Fluid Mechanics*, 599:465–476, 2008. doi: 10.1017/S0022112008000219.

Donald K. Perovich, Jacqueline A. Richter-Menge, Kathleen F. Jones, and Bonnie Light. Sunlight, water, and ice: Extreme Arctic sea ice melt during the summer of 2007. *Geophysical Research Letters*, 35(11), 2008. ISSN 1944-8007. doi: 10.1029/2008GL034007. L11501.

Chris Petrich and Hajo Eicken. Growth, Structure and Properties of Sea Ice. In Thomas and Dieckmann (2010), chapter 2.

M. J. D. Powell. A Fortran Subroutine for Solving Systems of Nonlinear Algebraic Equations. In P. Rabinowitz, editor, *Numerical Methods for Nonlinear Algebraic Equations*, chapter 7. Routledge, 1970.

William H. Press, Saul A. Teukolsky, William T. Vetterling, and Brian P. Flannery. *Numerical Recipes in C (2Nd Ed.): The Art of Scientific Computing.* Cambridge University Press, 1992. ISBN 0-521-43108-5.

David W. Rees Jones and M. Grae Worster. Fluxes through steady chimneys in a mushy layer during binary alloy solidification. *Journal of Fluid Mechanics*, 714: 127–151, 2013. doi: 10.1017/jfm.2012.462.

David W. Rees Jones and M. Grae Worster. A physically based parameterization of gravity drainage for sea-ice modeling. *Journal of Geophysical Research: Oceans*, 119(9):5599–5621, 2014. ISSN 2169-9291. doi: 10.1002/2013JC009296.

A. Riaz, M. Hesse, H. A. Tchelepi, and F. M. Orr. Onset of convection in a gravitationally unstable diffusive boundary layer in porous media. *Journal of Fluid Mechanics*, 548:87–111, 2 2006. doi: 10.1017/S0022112005007494.

J. Brent Roberts, Franklin R. Robertson, Carol A. Clayson, and Michael G. Bosilovich. Characterization of Turbulent Latent and Sensible Heat Flux Exchange between the Atmosphere and Ocean in MERRA. *Journal of Climate*, 25(3):821–838, 2012. doi: 10.1175/JCLI-D-11-00029.1.

S.M. Roper, S.H. Davis, and P.W. Voorhees. An analysis of convection in a mushy layer with a deformable permeable interface. *Journal of Fluid Mechanics*, 596: 333–352, 2008. doi: 10.1017/S0022112007009469.

R.L. Sani. *Convective instability* . PhD thesis, Univ. Minn., Minneapolis, 1963.

T. P. Schulze and M. Grae Worster. A time-dependent formulation of the mushy-zone free-boundary problem. *J. Fluid Mech.*, 541:193–202, 2005. doi: 10.1017/S0022112005006221.

Peter Schwerdtfeger. The Thermal Properties of Sea Ice. *Journal of Glaciology*, 4 (36):789–807, 1963. doi: 10.1017/S0022143000028379.

T.G.L. Shirtcliffe, Herbert E. Huppert, and M.Grae Worster. Measurement of the solid fraction in the crystallization of a binary melt. *Journal of Crystal Growth*, 113(3):566–574, 1991. ISSN 0022-0248. doi: 10.1016/0022-0248(91)90092-J.

Robert D. Skeel and Martin Berzins. A Method for the Spatial Discretization of Parabolic Equations in One Space Variable. *SIAM Journal on Scientific and Statistical Computing*, 11(1):1–32, 1990. doi: 10.1137/0911001.

A. C. Slim and T. S. Ramakrishnan. Onset and cessation of time-dependent, dissolution-driven convection in porous media. *Phys. Fluids*, 22, 2010. doi: 10.1063/1.3528009. 124103.

Josef Stefan. Über die Theorie der Eisbildung, insbesondere über die Eisbildung im Polarmeere. *Annalen der Physik und Chemie*, 1891.

Doru Michael Stefanescu. *Eutectic Solidification*, pages 186–209. Springer US, Boston, MA, 2002. ISBN 978-1-4757-6472-7. doi: 10.1007/978-1-4757-6472-7_9.

Melvin E. Stern. The "Salt-Fountain" and Thermohaline Convection. *Tellus*, 12(2): 172–175, 1960. ISSN 2153-3490. doi: 10.1111/j.2153-3490.1960.tb01295.x.

Henry Stommel, Arnold B. Arons, and Duncan Blanchard. An oceanographical curiosity: the perpetual salt fountain. *Deep Sea Research (1953)*, 3(2):152–153, 1956. ISSN 0146-6313. doi: 10.1016/0146-6313(56)90095-8.

Kirstie Stramler, Anthony D. Del Genio, and William B. Rossow. Synoptically Driven Arctic Winter States. *Journal of Climate*, 24(6):1747–1762, 2011. doi: 10.1175/2010JCLI3817.1.

W. J. Sun. *Convective instability in superposed porous and free layers.* PhD thesis, Univ. Minn., Minneapolis, 1973.

Stephen Tait and Claude Jaupart. Compositional convection in viscous melts. *Nature*, 338(6216):571–574, apr 1989. doi: 10.1038/338571a0.

Stephen Tait and Claude Jaupart. Compositional convection in a reactive crystalline mush and melt differentiation. *Journal of Geophysical Research: Solid Earth*, 97 (B5):6735–6756, 1992. ISSN 2156-2202. doi: 10.1029/92JB00016.

P. D. Taylor and D. L. Feltham. A model of melt pond evolution on sea ice. *Journal of Geophysical Research: Oceans*, 109(C12):n/a–n/a, 2004. ISSN 2156-2202. doi: 10.1029/2004JC002361. C12007.

D. N. Thomas and G. S. Dieckmann, editors. Wiley-Blackwell, 2nd edition, 2010.

N. Tilton and A. Riaz. Nonlinear stability of gravitationally unstable, transient, diffusive boundary layers in porous media. *Journal of Fluid Mechanics*, 745: 251–278, 4 2014. doi: 10.1017/jfm.2014.72.

N. Tilton, D. Daniel, and A. Riaz. The initial transient period of gravitationally unstable diffusive boundary layers developing in porous media. *Phys. Fluids*, 25, 2013. doi: 10.1063/1.4821225. 092107.

L. N. Trefethen. *Spectral Methods in MATLAB*. SIAM, 2000.

Cynthia T. Tynan, David G. Ainley, and Ian Stirling. Sea Ice: A Critical Habitat for Polar Marine Mammals and Birds. In Thomas and Dieckmann (2010), chapter 11.

N. Untersteiner. On the mass and heat budget of arctic sea ice. *Archiv für Meteorologie, Geophysik und Bioklimatologie, Serie A*, 12(2):151–182, Jan 1961. ISSN 1436-5065. doi: 10.1007/BF02247491.

G. K. Vallis. *Atmospheric and Oceanic Fluid Dynamics*. Cambridge University Press, Cambridge, UK, 2006.

R. L. van Dam, C. T. Simmons, D. W. Hyndman, and W. W. Wood. Natural free convection in porous media: First field documentation in groundwater. *Geophys. Res. Lett.*, 36, 2009. doi: 10.1029/2008GL036906. L11403.

Martin Vancoppenolle, Klaus M. Meiners, Christine Michel, Laurent Bopp, Frédéric Brabant, Gauthier Carnat, Bruno Delille, Delphine Lannuzel, Gurvan Madec, Sébastien Moreau, Jean-Louis Tison, and Pier van der Merwe. Role of sea ice in global biogeochemical cycles: emerging views and challenges. *Quaternary Science Reviews*, 79:207–230, 2013. ISSN 0277-3791. doi: 10.1016/j.quascirev.2013.04.011.

W. F. Weeks. *On Sea Ice*. Alaska, 2010.

A. J. Wells, J. S. Wettlaufer, and S. A. Orszag. Maximal potential energy transport: A variational principle for solidification problems . *Phys. Rev. Lett.*, 105(254502), 2010. doi: 10.1103/PhysRevLett.105.254502.

A. J. Wells, J. S. Wettlaufer, and S. J. Orszag. Nonlinear mushy-layer convection with chimneys: stability and optimal solute fluxes. *J. Fluid Mech.*, 716:203–227, 2013. doi: 10.1017/jfm.2012.541.

J. S. Wettlaufer, M. Grae Worster, and Herbert E. Huppert. Natural convection during solidification of an alloy from above with application to the evolution of sea ice. *Journal of Fluid Mechanics*, 344:291–316, 1997. doi: 10.1017/S0022112097006022.

J. S. Wettlaufer, M. G. Worster, and H. E. Huppert. Solidification of leads: theory, experiment and field observations. *J. Geophys. Res.*, 105:1123——1134, 2000.

M. G. Worster. *The Dynamics of Mushy Layers*, pages 113–138. Springer Netherlands, 1992a. ISBN 978-94-011-2809-4. doi: 10.1007/978-94-011-2809-4_20.

M. G. Worster. Convection in mushy layers. *Annu. Rev. Fluid Mech.*, 29:91–122, 1997.

M. Grae Worster. Solidification of an alloy from a cooled boundary. *J. Fluid Mech.*, 167:481–501, June 1986. doi: 10.1017/S0022112086002938.

M. Grae Worster. Natural convection in a mushy layer. *J. Fluid Mech.*, 224:335–359, 1991. doi: 10.1017/S0022112091001787.

M. Grae Worster. Instabilities of the liquid and mushy regions during solidification of alloys. *J. Fluid Mech.*, 237:649–669, 1992b.

M. Grae Worster. Solidification of Fluids. In G. K. Batchelor, H. K. Moffatt, and M. G. Worster, editors, *Perspectives in Fluid Dynamics*. Cambridge University Press, 2000. ISBN 0521531691.

M. Grae Worster and David W. Rees Jones. Sea-ice thermodynamics and brine drainage. *Philosophical Transactions of the Royal Society of London A: Mathematical, Physical and Engineering Sciences*, 373(2045), 2015. ISSN 1364-503X. doi: 10.1098/rsta.2014.0166.

M. Grae Worster, Herbert E. Huppert, and R. Stephen J. Sparks. Convection and crystallization in magma cooled from above. *Earth and Planetary Science Letters*, 101(1):78–89, 1990. ISSN 0012-821X. doi: 10.1016/0012-821X(90)90126-I.

D. Y. Yoon and C. K. Choi. Thermal convection in a porous medium subject to isothermal heating. *Korean J. Chem. Eng.*, 1989.

Jiayun Zhou, Bruno Delille, Hajo Eicken, Martin Vancoppenolle, Frédéric Brabant, Gauthier Carnat, Nicolas-Xavier Geilfus, Tim Papakyriakou, Bernard Heinesch, and Jean-Louis Tison. Physical and biogeochemical properties in landfast sea ice (Barrow, Alaska): Insights on brine and gas dynamics across seasons. *Journal of Geophysical Research: Oceans*, 118(6):3172–3189, 2013. ISSN 2169-9291. doi: 10.1002/jgrc.20232.